

The Pennsylvania State University

The Graduate School

Eberly College of Science

**CLASS IC RIBONUCLEOTIDE REDUCTASES: EXPANSION OF THE SUBCLASS
AND INSIGHT INTO THE MULTI-STEP INTER-SUBUNIT RADICAL
TRANSLOCATION MECHANISM**

A Dissertation in

Chemistry

by

Jovan Livada

© 2019 Jovan Livada

Submitted in Partial Fulfillment

of the Requirements

for the Degree of

Doctor of Philosophy

December 2019

The dissertation of Jovan Livada was reviewed and approved* by the following:

Joseph Martin Bollinger, Jr.
Professor of Chemistry and of Biochemistry and Molecular Biology
Dissertation Advisor
Chair of Committee

Squire J. Booker
Howard Hughes Medical Investigator
Professor of Chemistry and of Biochemistry and Molecular Biology
Eberly Distinguished Chair in Science

Alexey Silakov
Assistant Professor of Chemistry

Ming Tien
Professor of Biochemistry and Molecular Biology

Philip C. Bevilacqua
Distinguished Professor of Chemistry and Biochemistry and Molecular Biology
Head of the Chemistry Department

*Signatures are on file in the Graduate School.

ABSTRACT

Ribonucleotide reductases (RNRs) are the only known catalysts that are capable of the life essential conversion of ribonucleotides to deoxyribonucleotides. All RNRs use a transient cysteine radical (C^\bullet) to initiate the catalytic cycle. Based on the method of generation of the C^\bullet , RNRs are divided into three (I, II, III) major classes. Class III RNRs use an Fe_4S_4 cluster in tandem with an S-adenosyl-L-methionine radical activase to install a glycy radical that is stable in anoxic conditions. In class III RNRs this glycy radical is the active oxidant that forms the C^\bullet . The active oxidant in class II RNRs is 5'-deoxyadenosylcob(III)alamin which generates the C^\bullet via the reversible Co-C bond homolytic cleavage. Class I RNRs are the sole focus of this study and they contain two subunits, a smaller β subunit that contains the active oxidant and usually hosts a dimetal center, and the larger α subunit that harbors the substrate binding site and contains the key cysteine residue that is transiently oxidized during catalysis.

All class I RNRs use the active oxidant in their smaller subunit β to transiently oxidize the C^\bullet in the larger subunit α that is ~ 35 Å away. This is a multi-step, long range electron transfer process coupled by a few local proton transfers and mediated by, at a minimum, one tyrosine residue in β and two tyrosine residues in α . Class I RNRs are further subdivided into five subclasses (a-e) that differ in four relevant properties. One, the nature of the active oxidant in β (Y^\bullet , Mn^{IV} or $DOPA^\bullet$), two, the presence of a dimetal cofactor (Fe/Fe, Mn/Mn, Mn/Fe, or none), three, the oxygen species required for the formation of the active oxidant (O_2 or O_2^\bullet), and four, the requirement of an activase protein, NrdI. Archetypical class Ia RNRs generate the active oxidant, Y^\bullet , via the use of a β - Fe^{II}/Fe^{II} cofactor and O_2 . On the other hand, class Ic RNRs, the main topic of this study, use a heterobinuclear β - Mn^{II}/Fe^{II} cofactor that is activated in the reaction with

dioxygen and via the $\beta\text{-Mn}^{\text{IV}}/\text{Fe}^{\text{IV}}$ intermediate form the active cofactor $\beta\text{-Mn}^{\text{IV}}/\text{Fe}^{\text{III}}$, where Mn^{IV} represents the active oxidant.

RNR subclasses Ia, Ib, Id and Ie all have a minimum of three members verified by *in vitro* characterization, while the RNR from *Chlamydia trachomatis* (*Ct*) remains the sole verified example of class Ic ribonucleotide reductases, discovered in 2007. In this work, twelve years later, we have introduced a second class Ic RNR that uses a $\beta\text{-Mn}^{\text{IV}}/\text{Fe}^{\text{III}}$ active cofactor from *Gimesia maris* (*Gm*), a heterotroph found in various aquatic locations around the US. Rapid kinetic methods, stopped-flow and freeze quench, Mössbauer, and electron paramagnetic resonance (EPR) spectroscopies as well as activity assay analysis were all used to characterize *Gm* RNR as a bona fide class Ic RNR. Like *Ct*, *Gm* RNR was shown to possess a branched electron relay pathway in β that consist of two tyrosine residues and one tryptophan. Interestingly, by removing a subclass specific tyrosine residue involved in the cofactor reaction with dioxygen we were able to noticeably increase the rate of catalytic activity. This information sheds light onto the activating and catalytic electron relays in class Ic RNRs.

Sequence similarity network analysis of genes that encode both for RNR α and β subunits indicate clusters of closely coevolved RNRs that belong to both class Ia and class Ic RNR subclasses. *In vitro* characterization of a tentative class Ia RNR from *Methylococcus capsulatus* (*Mc*) confirms that this RNR uses a Fe/Fe cluster to generate the nearby active $\text{Y}\cdot$ oxidant. A closely co evolved RNR whose gene sequence suggests that it belongs to the class Ic RNR subclass from *Salinisphaera hydrothermalis* (*Sh*) was also characterized and confirmed that it forms a $\text{Mn}^{\text{IV}}/\text{Fe}^{\text{III}}$ cofactor and that it uses Mn^{IV} as the active oxidant. Activity assays have shown that both heterologous pairs of α and β subunits of *Mc* and *Sh* RNR are able to perform bidirectional radical translocation. This represents initial evidence that the multi-step, one electron, multiple

proton transfer mechanism between α and β RNR subunits is conserved between the RNR subclasses Ia and Ic. We hypothesize that this mechanism might be conserved in all class I RNRs. Additionally, we concluded that there were no adaptations required, for performing ribonucleotide reduction, made to either subunit to accommodate a complementary subunit from a different subclass except for the evolution of the β subunit to harbor a distinct active oxidant.

The aforementioned multi-step, one electron, multiple proton transfer process is believed to involve a 35 Å distance between the active oxidant in β and the catalysis initiating cysteine residue in α . The active cofactor from the class Ic RNR from *Chlamydia trachomatis* β -Mn^{IV}/Fe^{III} is reduced to an EPR accessible ($S = 1/2$) Mn^{III}/Fe^{III} state in the β subunit and generates a cysteinyl radical in the α active site. The radical in the larger subunit can be trapped via a known mechanism based inactivator, 2'-azido-2'-deoxyuridine-5'-diphosphate (N₃UDP). The resulting reaction accumulates a stable, nitrogen-centered radical (N•) in the active site of α . Using double electron–electron resonance experiments, we have elucidated the distance between the β -Mn^{III}/Fe^{III} cofactor in β and N• in α to be 43 ± 1 Å. This experimental investigation not only provides the first structural information concerning the class Ic RNR holoenzyme complex but also the first direct experimental measurement of the inter-subunit RT distance in any class I RNR.

In class Ia RNRs, the first step of the bidirectional, multi-step, one electron, multiple proton transfer process has been characterized as a proton-coupled-electron-transfer (PCET) reaction where the active oxidant (Y•) is reduced by a nearby organic residue in β and a local proton transfer occurs from the water ligand bound to the β -Fe^{III}/Fe^{III} cofactor onto the radical harboring tyrosine. The presumptive proton transfer step in class Ic, *Ct* RNR, in which reduction of a β -Mn^{IV}/Fe^{III} oxidant to an EPR-active ($S = 1/2$) β -Mn^{III}/Fe^{III} state drives Cys oxidation in α , is not understood. We have used advanced electron paramagnetic resonance spectroscopies as well as density-

functional theory (DFT) calculations to analyze the $\beta\text{-Mn}^{\text{III}}/\text{Fe}^{\text{III}}$ RT product to determine the number and location of its protons. The correlation of our findings in addition to the previous structural characterization of the $\beta\text{-Mn}^{\text{IV}}/\text{Fe}^{\text{III}}$ RT-reactant state led us to identify that the acceptor for the initial proton transfer step in class Ic RNRs is a hydroxide ligand on the Mn^{IV} .

TABLE OF CONTENTS

List of Figures.....	x
List of Tables.....	xiii
List of Equations.....	xiv
Acknowledgments.....	xvi
Chapter 1: Introduction to Ribonucleotide Reductases.....	1
Ribonucleotide reductases: Overall reaction and Applications.....	2
The General Mechanism.....	2
Three Classes of Ribonucleotide Reductases.....	4
Class I Ribonucleotide Reductases: The hallmark RNR from Escherichia coli.....	6
Activation – reaction of <i>Ec</i> - β Fe ^{II} /Fe ^{II} cofactor with O ₂	10
Reaction inhibitors and distance measurements of <i>Ec</i> RNR.....	11
Notion of Reaction Gating and the Structure of the Resting and Product states of Radical translocation in <i>Ec</i> β	15
Class Ib Ribonucleotide Reductase.....	18
Class Ic Ribonucleotide Reductase.....	18
Class Id Ribonucleotide Reductase.....	20
Novel, metal-free Class Ie ribonucleotide reductase.....	23
Sequence similarity network (SSN) of InterPro IPR000358 superfamily that contains all RNR β annotated genes.....	24
Reaction of the β -Fe ^{II} /Fe ^{II} and β -Mn ^{II} /Fe ^{II} cofactors in <i>Ct</i> β with dioxygen.....	26
Electronic structures of β -Mn ^{IV} /Fe ^{IV} and β -Mn ^{IV} /Fe ^{III} cofactors.....	27
Proposed class Ic gene sub-cluster of the small subunit of RNR –Identification and analysis of the class Ic sub-cluster within the Ribonucleotide Reductase small subunit family.....	29

Previous attempts to characterize a second class Ic RNR.....	30
Proposal of the Class Ic and Ia cross-species subunit pairing and characterization of <i>Burkholderia pyrrocinia</i> Ribonucleotide Reductase.....	32
Summary and outlook.....	36
References.....	41
Chapter 2: Characterization and Insight into the Branched Electron Relay Pathways of a Second Class I-c Ribonucleotide Reductase from <i>Gimesia maris</i>.....	59
Abstract.....	60
Introduction.....	61
Experimental Details.....	66
Results and Discussion.....	71
Mössbauer Analysis of the β -Mn ^{IV} /Fe ^{III} product of O ₂ activation in <i>Gm</i> β	82
<i>Gm</i> RNR activity assays.....	84
Spectroscopic evidence of the catalytic activity of <i>Gm</i> RNR.....	85
and Outlook and Discussion.....	87
References.....	93
Chapter 3: Across Species and Subclasses Ribonucleotide Reduction: Insight into the Multi-Step Radical Translocation Mechanism in class I RNRs.....	101
Abstract.....	102
Introduction.....	104
Experimental Details.....	109
Results and Discussion.....	114
The RNR from <i>Methylococcus capsulatus</i> (<i>Mc</i>) is a class Ia RNR representative.....	114
The RNR from <i>Salinisphaera hydrothermalis</i> (<i>Sh</i>) is a bona fide class Ic RNR.....	116
Heterologous catalytic activity of <i>Methylococcus capsulatus</i> and <i>Salinisphaera hydrothermalis</i> Ribonucleotide Reductases.....	120
Discussion and Outlook.....	124
References.....	132
Chapter 4: Direct Measurement of the Radical Translocation Distance in the Class I Ribonucleotide Reductase from <i>Chlamydia trachomatis</i>.....	137
Introduction.....	138

Results and Discussion.....	140
Materials and Methods.....	142
References.....	143
Supporting Information.....	146
Chapter 5: Spectroscopic and Computational Analysis of Proton Transfer in the Turnover-initiating Transient Reduction of the β-Mn^{IV}/Fe^{III} Cofactor of a Class Ic Ribonucleotide Reductase.....	153
Abstract.....	154
Introduction.....	156
Experimental Results and Discussion.....	164
CW EPR Spectrum of the β -Mn ^{III} /Fe ^{III} state.....	164
Analysis of hyperfine parameters of solvent exchangeable hydrons in dinuclear systems.....	166
Observation of a bridging hydron via HYSCORE.....	167
Observation of a terminal hydron via ENDOR.....	170
Structural assignment of the observed hydrons.....	171
Determination of the Heisenberg Exchange Coupling Constant, J, by Spin-lattice-Relaxation/Power-Saturation Measurements	172
Computational Results, and Discussion.....	174
Materials and Methods.....	184
References.....	186
Appendix 5-A: Observation of a strongly coupled ¹⁴N signal probed via Davies ENDOR.....	199
Appendix 5-B: EPR Theory	201
References.....	213
Appendix 5-C: Coordinates of the 6 DFT generated models of the β-Mn^{III}/Fe^{III} cofactor.....	216

LIST OF FIGURES

Chapter 1:

Scheme 1 - General catalytic reaction of all RNRs.....	2
Scheme 2 - General catalytic mechanism of Ribonucleotide Reductases.....	3
Scheme 3 - The three main RNR classes and the five class I subclasses.....	5
Figure 1 - Docking model of the <i>Ec</i> RNR holoenzyme.....	7
Scheme 4 – Activation of <i>Ec</i> β	10
Scheme 5 – Formation mechanism of N^\bullet in α	12
Figure 2 – DEER measured distances in <i>Ec</i> RNR.....	14
Figure 3 – DFT geometries of the initial PCET process of the RT mechanism in <i>Ec</i> RNR.....	15
Figure 4 – DFT calculated Mössbauer parameters of <i>Ec</i> RNR.....	17
Figure 5 – CW EPR spectra of Mn/Mn <i>Fj</i> β	20
Figure 6 – CW EPR spectra of Mn/Fe <i>Fj</i> β	21
Figure 7 - CW EPR spectra of the RT process in <i>Fj</i> RNR.....	22
Figure 8 – Sequence similarity network and alignment of all β RNR gene sequences.....	25
Figure 9 – Activation and Catalysis in <i>Ct</i> RNR.....	26
Figure 10 – Structure of the β -Mn ^{IV} /Fe ^{III} cofactor of <i>Ct</i> RNR.....	28
Figure 11 - CW EPR spectra of the cryoreduced β -Mn ^{IV} /Fe ^{III} cofactor β	30
Figure 12 – Catalytic activity of <i>Bp</i> RNR.....	33
Figure 13 – Iron titration of APO <i>Bp</i> β RNR.....	33
Figure 14 – Tyrosine radical in <i>Bp</i> β RNR.....	34
Figure 15 – Activity assays of <i>Gm</i> RNR.....	36
Figure 16 - CW EPR spectra of the β -Mn ^{III} /Fe ^{III} cofactor generated via the <i>Sh</i> β and <i>Mc</i> α complex.....	37
Figure 17 – Distance between the β -Mn ^{III} /Fe ^{III} cofactor and N^\bullet in <i>Ct</i> RNR.....	38
Figure 18 – Proposed structure of the Mn ^{III} /Fe ^{III} cofactor of <i>Ct</i> RNR.....	39

Chapter 2:

Figure 1 – Sequence similarity network analysis of the Ia and Ic RNR β gene sub-cluster.....	64
Figure 2 – Stopped-flow studies of diiron <i>Gm</i> β reaction with O ₂	73

Figure 3 – Rapid kinetic method analysis of <i>Gm</i> β activation.....	74
Figure 4 – Influence of Ascorbate on <i>Gm</i> β activation.....	76
Figure 5 – Comparison of the activation reaction of <i>Gm</i> β wt and <i>Gm</i> β Y234F variant.....	77
Figure 6 – Global kinetic simulation analysis of the influence of ascorbate on <i>Gm</i> β wt activation.....	79
Figure 7 – Global kinetic simulation analysis of the influence of ascorbate on <i>Gm</i> β Y234F variant activation.....	80
Figure 8 – Proposed activation model of <i>Gm</i> β wt and Y234F variant activation processes in the absence and presence of ascorbate.....	81
Figure 9 – Mössbauer spectroscopy of products of activation of <i>Gm</i> β wt and Y234F variant....	82
Figure 10 – Catalytic activity of <i>Gm</i> β and <i>Gm</i> β Y234F variant with <i>Gm</i> α in the absence and presence of ascorbate.....	84
Figure 11 – Spectroscopic evidence of the catalytic activity of <i>Gm</i> RNR.....	86
Chapter 3:	
Figure 1 – CW EPR spectra of <i>Mc</i> β -Y•.....	114
Figure 2 – Correlation of the catalytic activity of <i>Mc</i> RNR to the amount of Y• in <i>Mc</i> β	115
Figure 3 – Optimized catalytic activity of the <i>Mc</i> $\alpha\beta$ complex.....	115
Figure 4 – Comparison of <i>Sh</i> RNR activity based on the method of <i>Sh</i> β activation.....	116
Figure 5 - Mössbauer spectroscopy of products of activation of <i>Sh</i> β wt.....	117
Figure 6 - Correlation of the catalytic activity of <i>Sh</i> RNR to the amount of total Mn in <i>Sh</i> β	118
Figure 7 - Optimized catalytic activity of the <i>Sh</i> $\alpha\beta$ complex.....	118
Figure 8 - Spectroscopic evidence of the catalytic activity of <i>Sh</i> RNR.....	119
Figure 9 – Catalytic activity of heterologous $\alpha\beta$ pairs of <i>Sh</i> and <i>Mc</i> RNR.....	120
Figure 10 – Evidence of deactivation of <i>Sh</i> β by DT in the reaction with <i>Mc</i> α	122
Figure 11 - Evidence of reactivation of <i>Sh</i> β by HOOH in the reaction with <i>Mc</i> α	123
Figure 12 - Spectroscopic evidence of the catalytic activity of the <i>Sh</i> β and <i>Mc</i> α RNR complex.....	123
Figure 13 – Sequence similarity network analysis of both α and β subunits of prominent, <i>in vitro</i> characterized RNRs.....	126
Figure 14 – C-terminal tail comparisons of <i>Ec</i> , <i>Mc</i> , and <i>Sh</i> RNR β subunits.....	128
Figure 15 – X-ray crystal structure comparisons of <i>Ec</i> and <i>Ct</i> RNR β s.....	130

Chapter 4:

Figure 1 – Structure and function of class I RNRs.....	139
Figure 2 – Pulsed, spin echo detected EPR spectrum of <i>Ct</i> RNR in the presence of N ₃ UDP...140	
Figure 3 – DEER analysis of the distance between the Mn ^{III} /Fe ^{III} cofactor in β and N• in α in <i>Ct</i> RNR.....	141
Figure 4 – Molecular dynamic simulations of the <i>Ct</i> RNR $\alpha_2\beta_2$ complex.....	141
Figure S1 – Schematic representation of DEER distances in Class I RNRs.....	147
Figure S2 – CW EPR spectra of the Mn ^{III} /Fe ^{III} at 15K and of N• at 77K.....	148
Figure S3 – Alternative DEER pump/observed frequency combinations.....	149
Figure S4 – DEER trace simulations using Gaussian distribution models.....	150
Figure S5 – Deviation of the actual geometric distance and the observed dipolar distance as a function of the Mn-Fe vector and vector containing the Mn/Fe cluster and N•.....	151

Chapter 5:

Figure 1 – The proposed structure of the β -Mn ^{IV} /Fe ^{III} cofactor in <i>Ct</i> β	162
Figure 2 – CW EPR spectrum of the RT-product β -Mn ^{III} /Fe ^{III} cofactor in <i>Ct</i> β	164
Figure 3 – Analysis of the hyperfine interaction of solvent exchangeable hydrons in dimetal spin coupled systems.....	166
Figure 4 – HYSCORE spectra of the bridging hydron in the <i>Ct</i> β Mn ^{III} /Fe ^{III} cofactor.....	169
Figure 5 - ENDOR spectra of the terminal hydron in the <i>Ct</i> β Mn ^{III} /Fe ^{III} cofactor.....	170
Figure 6 – Determination of the Heisenberg exchange coupling constant (J) in the <i>Ct</i> β Mn ^{III} /Fe ^{III} cofactor.....	173
Figure 7 – DFT calculated models of the <i>Ct</i> β Mn ^{III} /Fe ^{III} cofactor.....	176
Figure 8 – All activation and catalysis relevant <i>Ct</i> RNR β Mn/Fe cofactor states.....	183

Appendices:

Appendix 5-A Figure 1 - ENDOR spectra of a strongly coupled ¹⁴ N nucleus in the <i>Ct</i> β Mn ^{III} /Fe ^{III} cofactor.....	199
Appendix 5-B Figure 1 – Energy level diagram of simple S=1/2, I=1/2 spin system.....	205
Appendix 5-B Figure 2 – Pulse sequences of most popular pulsed EPR experiments.....	207
Appendix 5-B Figure 3 – Theoretical HYSCORE spectrum.....	209
Appendix 5-B Figure 4 – Basic principles of Davies ENDOR.....	209

LIST OF TABLES

Chapter 1:

Table 1 – Redox protentional analysis of cysteine, tyrosine, and tryptophan residues	9
--------------------------------------------------------------------------------------------	---

Chapter 5:

Table 1 – The division of class I RNRs by the active oxidant, metals in β , dioxygen activation species, and the necessity of a NrdI activase.....	158
----------------------------------------------------------------------------------------------------------------------------------------------------------	-----

Table 2 – List of various DFT calculated and experimentally determined EPR parameters	179
---------------------------------------------------------------------------------------------	-----

LIST OF EQUATIONS

Chapter 2:

Equation 1 – A kinetic system of two parallel, irreversible, first-order reactions.....72

Chapter 5:

Equation 1 –EPR signal intensity related to $P_{1/2}$172

Equation 2 – EPR signal intensity related to $P_{1/2}$ multiplied by \sqrt{P}172

Equation 3 – Relation of $P_{1/2}$ and the Orbach relaxation process.....173

Equation 4 – Dipolar approximation of two individual point-dipolar interactions.....177

Appendix 5-B:

Equation 1 – Spin Hamiltonian.....202

Equation 2 – Effective Spin Hamiltonian202

Equation 3 – g effective in a two spin coupled system.....203

Equation 4 – A_{Mn} effective in a two spin coupled system.....203

Equation 5 – A_{Fe} effective in a two spin coupled system.....203

Equation 6 – c_1 spin projection constant in a two spin coupled system203

Equation 7 – c_2 spin projection constant in a two spin coupled system203

Equation 8 – g effective in a strongly coupled two spin coupled system.....203

Equation 9 – A_{Mn} effective in a strongly coupled two spin coupled system.....204

Equation 10 – A_{Fe} effective in a strongly coupled two spin coupled system.....204

Equation 11 – Hyperfine Hamiltonian.....204

Equation 12 – Isotropic Hyperfine.....204

Equation 13 – Dipolar Hyperfine.....204

Equation 14 – Energy level transition of an $S=1/2$, $I=1/2$ spin system.....206

Equation 15 – Nuclear frequencies of an $S=1/2$, $I=1/2$ spin system206

Equation 16 – Constants related to nuclear frequencies of an $S=1/2$, $I=1/2$ spin system.....206

Equation 17 – Allowed and forbidden transition probabilities of an $S=1/2$, $I=1/2$ spin system..206

Equation 18 – HYSCORE equation of an $S=1/2$, $I=1$ spin system.....208

Equation 19 – Anti-diagonal HYSCORE signal displacement.....208

Equation 20 – Davies ENDOR.....210

Equation 21 – Mims ENDOR.....	210
Equation 22 – Orbach, Raman, and Direct spin-lattice relaxation processes.....	211
Equation 23 – Orbach relaxation process.....	212
Equation 24 – Orbach relaxation process simplified.....	212

ACKNOWLEDGEMENTS

I would like to thank my advisor Marty Bollinger for his endless patience. I would also like to thank him for helping me explore the remarkable and beautiful field of ribonucleotide reductases. I would like to thank my academic advisor Carsten Krebs for upholding the scientific rigor of my work, and for his generosity in editing my thesis chapters. I would like to thank Professor Tyler Grove for teaching me biochemistry and molecular biology during his postdoctoral experience here at Penn State. I would also like to thank professor Alexey Silakov for teaching me EPR spectroscopy during his post-doctoral fellowship at Penn State. I would like to acknowledge the help of professors Scot Showalter and Philip Bevilacqua in obtaining my PhD. Without the help of all of these professors, I would not be the scientist that I am today.

Also, I would not have made it this far if it was not for the emotional support of my mother, Mirjana, father, Zoran, brother, Ivan, wife, Alison, and best friends, Milenko and Richard. Without these individuals, it would not be possible for me to achieve my academic and professional goals. I will be forever grateful to them.

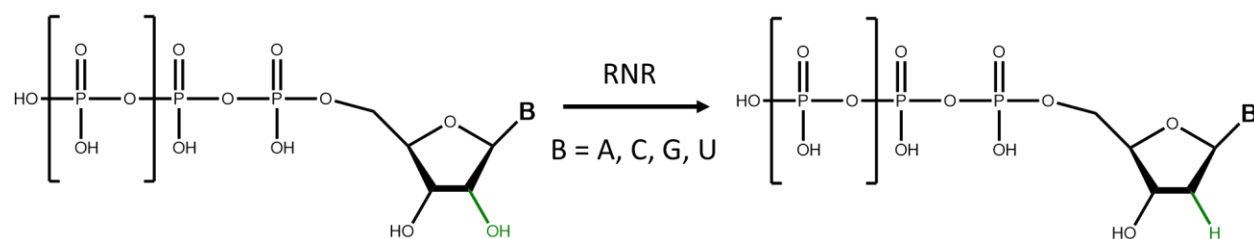
I would like to acknowledge the funding agencies that supported this work. This material is based upon work supported by the National Institute of Health under Award No. 5 R01 GM055365-10 and Award No. 1 R01 GM132653-01. For all materials, except for the embedded journal article, any opinions, findings, and conclusions or recommendations expressed in this publication are those of the authors and do not necessarily reflect the views of the National Institute of Health.

Chapter 1

Introduction to Ribonucleotide Reductases

Ribonucleotide reductases: Overall reaction and Applications

Ribonucleotide reductases (RNRs) catalyze one of the most important cellular chemical reactions – the conversion of ribonucleotides to their deoxy counterparts.¹ These enzymes are ubiquitous to virtually all cellular organisms to date and are responsible for the sole known synthetic pathway of deoxyribonucleotide synthesis and repair. The general reaction of all RNRs



Scheme 1. General RNR reaction

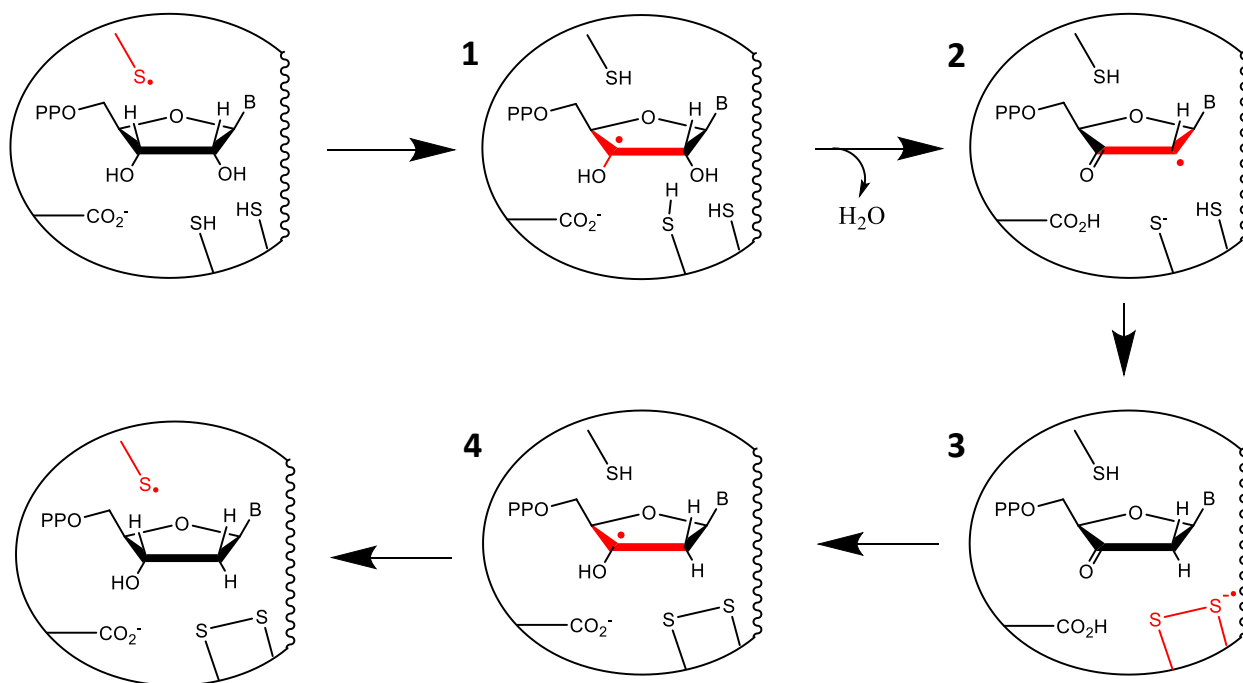
is presented in **Scheme 1**. This reaction is chemically an effective replacement of the 2'-hydroxyl group on the ribose ring with a hydrogen atom (H•). This replacement increases the product stability and provides DNA precursors to cells. Due to their necessity for cell survival, RNRs have been targeted for various anticancer and HIV drugs.

The General Mechanism

The conversion of ribonucleotides to deoxyribonucleotides is currently only known to be achieved via RNRs and via a free-radical mechanism. All RNRs known thus far utilize a transient cysteine thiyl radical (Cys•) buried in the active site of the enzyme to initiate the ribonucleotide reduction. In addition to the aforementioned Cys• radical, Stubbe and coworkers have used different reductants,² and site directed mutagenesis^{3, 4} to identify four more essential cysteines required for RNR activity. One cysteine pair, proximal to the substrate binding site, provides the required reducing equivalents for ribonucleotide reduction, while another pair that is closer to the protein surface is designated to re-reduce the first pair. The second pair of cysteines is re-reduced

by an external reductant, typically thioredoxin or glutaredoxin. The Cys• radical has never been directly observed. However, it has been inferred and hypothesized to be the initiator of the first step in the catalytic mechanism. The RNR active site also contains either a two-cysteine disulfide bridge or uses formate to provide the reducing equivalents for the formation of deoxyribonucleotides.

The ribonucleotide reduction is initiated when Cys• homolytically cleaves the C-H bond at the 3' position of the ribose ring and generates a ribose radical (**1**).⁵ Then, a protonation of 2'-hydroxyl group via a nearby cysteine residue occurs, while a water molecule is eliminated and the



Scheme 2. General catalytic mechanism of ribonucleotide reductases.

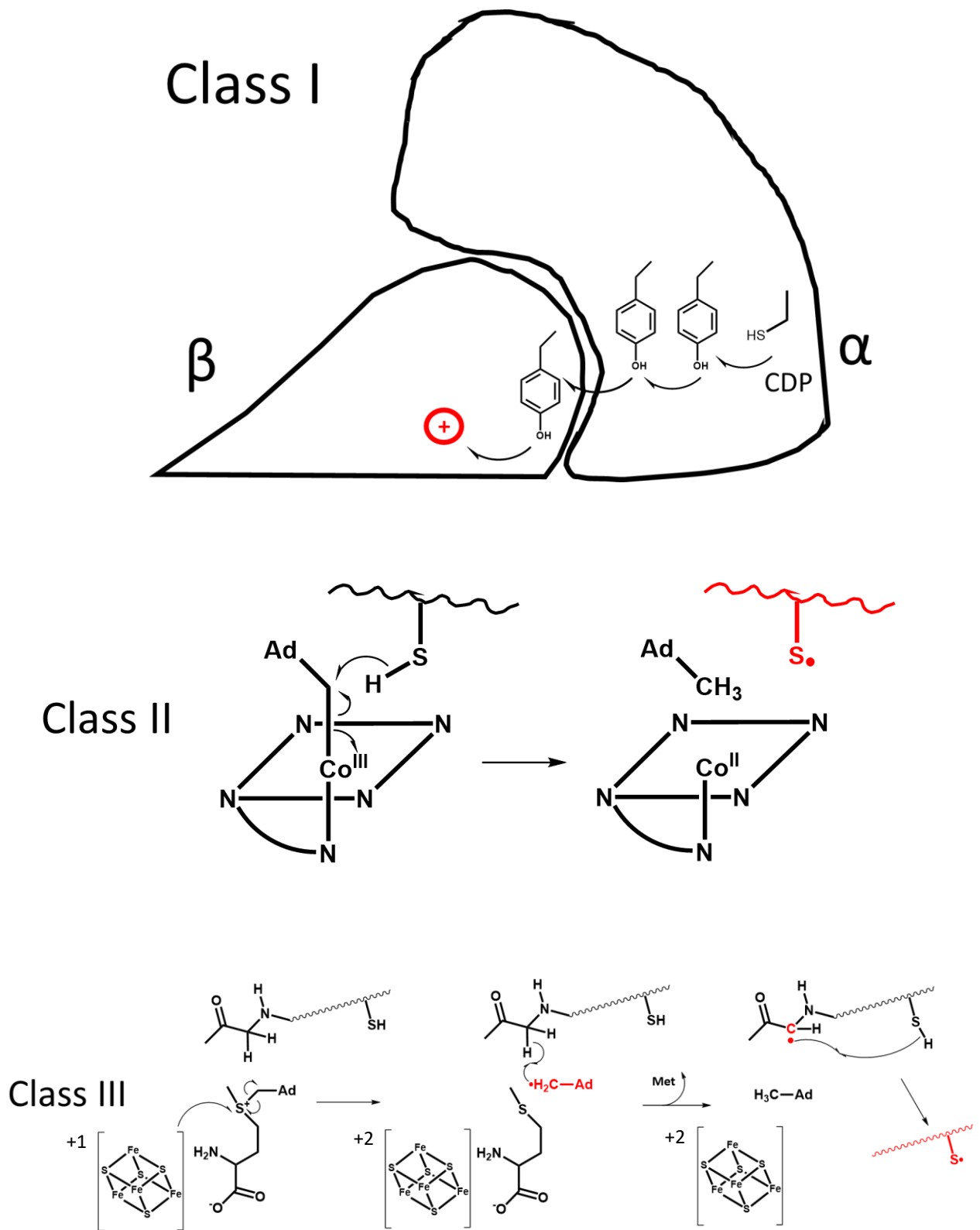
resulting 3'-keto-2'-deoxynucleotide radical is formed (**2**). The subsequent reduction is either performed by two neighboring cysteine residues or formate via a proton coupled electron transfer (PCET) and results in the formation of complex (**3**), a 3'-keto-2'-deoxynucleotide and either a disulfide-radical-anion or carbon dioxide anion radical intermediate. The final steps involve the

generation of a new 3'-nucleotide radical (**4**), the subsequent product formation and the regeneration of the initiator Cys•. This mechanism (**Scheme 2**) was constructed from the various results of mechanism-based inhibitors, site-directed variant proteins, and crystallographic studies.⁶⁻¹⁰

Three Classes of Ribonucleotide Reductases

A stable, oxidized cofactor is required to generate the transient Cys•. Depending on the nature of this stable cofactor, RNRs are classified into three general classes (**Scheme 3**). Additionally, Class I RNR is further classified into several subclasses. Organisms whose genomes contain class I ribonucleotide reductases are strictly aerobes that structurally contain a large (α) and a small subunit (β). This class of enzymes was first discovered by Peter Reichard in the 1950s and is present in all eukaryotes, many bacteria and a number of viruses.^{12, 13} Furthermore, in the past two decades five subclasses of Class I RNRs were distinguished based on the nature of the metal cofactor that lies in β . The original, class Ia harbors a diiron cofactor in β and utilizes a stable tyrosyl radical to initiate ribonucleotide reduction.¹⁴⁻¹⁷ Class Ib is characterized by a dimanganese cofactor and also utilizes a tyrosyl radical¹⁸⁻²¹ but requires a flavoprotein NrdI to generate the tyrosyl radical. Unlike the Ib, class Ic uses a heterodinuclear manganese iron cofactor with no stable radical present. A novel class Id, uses a dimanganese cofactor and requires superoxide for activation,^{22, 23} while class Ie uses a DOPA radical.^{24, 25}

Class II Ribonucleotide Reductases are O₂ independent enzymes that use adenosylcobalamin to generate the cysteine thiol radical and have either monomeric or homodimeric quaternary structure.²⁶⁻³⁰ This class utilizes a mechanism in which the carbon-cobalt bond is homolytically cleaved in adenosylcobalamin thus producing a 5'-deoxyadenosyl radical that directly generates the reaction initiating Cys•.^{26, 31}



Scheme 3: The mechanism of the three main RNR classes.

Unlike the first two RNR classes, Class III Ribonucleotide Reductases are present in anaerobic and facultative organisms. They use a stable glycyl radical (Gly•)^{1, 32} when activated as an initiator of the catalytic cycle. Like class Ia they contain a large subunit (α) and a small subunit (β). However, the Gly• is located in α while β serves a posttranslational generator of the G•.³³⁻³⁵ The smaller subunit is an activase protein. Two other activation parts required for the Gly• generation are a [4Fe-4S] cluster and S-adenosyl methionine (SAM). The [4Fe-4S] cluster is reduced by a flavodoxin reductase system.³⁶ Consequently, the [4Fe-4S] cluster reduces SAM at which point SAM is cleaved into two parts. The first part is the redox inert methionine and the second part is the highly oxidizing 5'-deoxyadenos-5'-yl (5'-dA•) radical. In turn, 5'-dA• abstracts a hydrogen atom from the α carbon of the Gly residue and subsequently produces the stable glycyl radical Gly•. While the class I and II RNRs use thioredoxin or glutaredoxin as reducing agents for the reduction of the disulfide bridge in the active site, Class III instead uses formate to directly reduce the substrate.³⁷

Class I Ribonucleotide Reductases: The hallmark RNR from *Escherichia coli*

The first RNR discovered¹² and the most studied in over 1,500 published articles is the ribonucleotide reductase from the aerobic *Escherichia coli* (Ec 1.17.4.1). The vast majority of what is known in Class Ia RNRs comes from this enzyme, although yeast,^{38, 39} mouse,^{40, 41} and human^{42, 43} RNRs have been studied in some detail as well. Structurally, *Ec* RNR has dimer of dimers $\alpha_2\beta_2$ architecture with several crystal structures solved for both the large⁴⁴ and the small subunit.⁴⁵ So far, the docked holoenzyme has not yet been crystalized. Instead, a docking model⁴⁴ was created

based on both the surface complementarity of the C terminus of the β with a region of the α subunit, and several advanced EPR, double electron-electron resonance (DEER)^{46, 47} studies (**Figure 1**).

The larger subunit (~85 kDa, monomer), R_1 or α , contains the active site that harbors the nucleoside di- or (tri-) phosphates (ND(T)P)s. In addition, the α subunit contains an ATP cone that serves as a binding site of allosteric effectors that dictate substrate selectivity^{1, 44}. Although the *E. coli* RNR only has one ATP cone, the number of cones in Class I RNRs varies between species from one to three cones.⁴⁸ The non-conserved cones can bind ATP, dATP, dTTP or dGTP as an additional on/off switch for catalytic activity. In *Ec* α , dATP binding to another regulatory site in α inhibits overall activity by forming inactive α_6 and $\alpha_4\beta_4$ complexes⁴⁸ and thus, preventing cytotoxic levels of dNDPs⁴⁹. With no allosteric regulation, however, enzymatic activity is very modest⁵⁰.

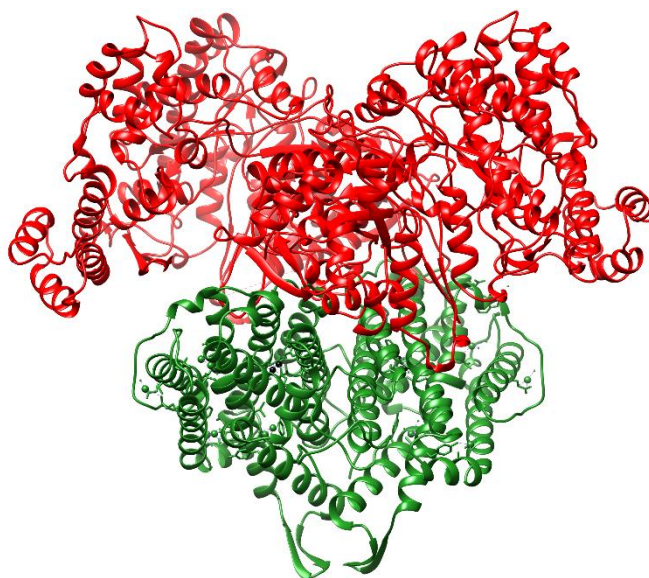


Figure 1. Docking model of the *Ec* RNR holoenzyme. It is generated by putting individual structures of α and β subunits together based on shape complementarity. α_2 is in red while β_2 is in green.

In *Ec* RNR residue numbering, C439 is the aforementioned elusive Cys• that abstracts the H• from the 3' position of the ribose ring, while C225 and C462, located in the active site provide the necessary reducing equivalents. Also, the C754 and C759 residues are required for a re-reduction of the disulfide bond between C225 and C462. The disulfide bond formed between C754 and C759 is re-reduced by an external thioredoxin or glutaredoxin *in vivo*, or via a chemical reductant like dithiothreitol (DTT) or beta mercaptoethanol (BME) *in vitro*.

The smaller subunit, (~43 kDa, monomer) R₂ or β , structurally belongs to the ferritin-like enzyme superfamily containing a four-helix bundle. Buried in these four helices lies a diiron cofactor ligated by two histidines and four carboxylate ligands in addition to oxygen- and solvent-derived oxygenic ligands.⁴⁵ Less than 5 Å away from Fe1 lies the Y122 residue. After the reaction of diferrous (β -Fe^{II}/Fe^{II}) cofactor with oxygen, Y122 is oxidizes to Y122•. That radical is responsible for the subsequent oxidation of C439 during catalysis.^{45, 51}

According to the docking model and several DEER and quantum coherence (DQC) studies^{52, 53}, it is postulated that a ~35 Å distance separates the Y122, the active oxidant, and C439, the reaction initiator. This radical “hole” transfer distance is among the largest observed in a catalytic cycle making this system a unique and exciting topic of study. One question that arose from this system was the mechanism of the radical transfer from the Y• in β to the Cys• in α . It is very unlikely that this transfer happens as a single step based on the Marcus-Levich equation; over 35 Å, the rate of catalysis would be between 10^{-4} and 10^{-9} s⁻¹,⁵⁴ which is considerably slower than the 2-10 s⁻¹ observed rate of catalysis in the *Ec* RNR system.⁵⁵ Therefore, instead of a single step, a multi-step transfer mechanism has been proposed that is mediated via a network of conserved, redox active and hydrogen bonded amino acid residues.⁵⁶⁻⁵⁹ Site directed mutagenesis studies suggested that one other essential residues for catalysis in *Ec* β is Y356. The electron transfer of the electron hole from the β into the α subunit has been characterized as a multi-step, inter-subunit, one electron, multiple proton, radical translocation (RT) mechanism. The residues involved in his mechanism in *Ec* RNR Y122, and Y356 in β and Y731, Y730, and C439 in α . They

are proposed to form intermediate “pathway radicals.” Except for the stable radical harboring Y122, all other transient pathway Y•, C• and possibly W• radicals and are strictly conserved in all

Table 1 The change in redox potential in the cysteine, tryptophan, and tyrosine residues upon (de)protonation. Adapted from ref 101.

Reaction	E° (NHE)/V
RS• → RSH	1.33
RS• → RS ⁻	0.77
WH• ⁺ → WH	1.15
W• → WH	0.9 - 1.05
Y• → YOH	0.83 - 0.94
Y• → YO ⁻	0.65

Legend:

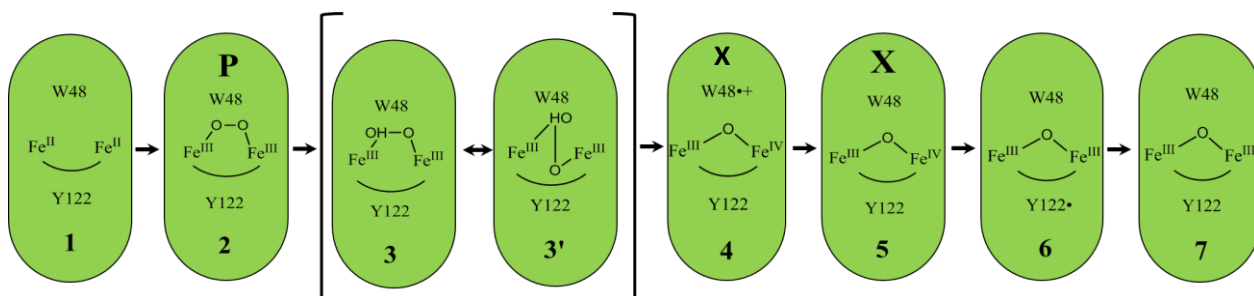
RS• - cysteine radical, RSH - cysteine residue, RS⁻ - cysteine anion,
WH•⁺ - tryptophan cation radical, WH - tryptophan residue,
W• - tryptophan radical, Y• - tyrosine radical,
YH - tyrosine residue, YO⁻ - tyrosine anion

known class I RNRs, where changing any of these residues into its redox inert compliments results in no catalytic activity. In addition to the electron transfer from α to β , it is believed that some individual electron transfer steps are coupled to proton transfer yielding to the so-called proton coupled electron transfer (PCET). **Table 1** illustrates the rise of the redox potential of target amino acid as the

amino acid gets protonated. The RT process itself has not been directly observed.^{60, 61} However, unnatural radical species on the pathway have been seen. The Stubbe and Nocera groups and their collaborators have semi-synthesized 3-nitrotyrosine, various types of fluorotyrosine, 4-aminophenylalanine, and 3,4-dihydroxyphenylalanine. In doing so, they have enabled a depression in the free energy profile of the converted residue and thus, trapped a radical species.⁶¹⁻⁶³

Activation – reaction of *Ec* β with O_2

The activation process of the small subunit of *Ec* RNR has been very well characterized (**Scheme 4**). It involves the reaction of a diferrous cluster with molecular oxygen and the process produces a diferric cluster and a stable nearby tyrosine radical. Once the stable Y^\bullet is formed it can perform multiple turnovers. Therefore, the activation process is only required once for catalysis.



Scheme 4. Details of the reaction of the β - Fe^{II}/Fe^{II} cofactor of *Escherichia coli* RNR with dioxygen.

First, in anaerobic conditions the apoprotein binds β - Fe^{II}/Fe^{II} (**1**). Upon the addition and four electron reduction of molecular oxygen, the resulting cofactor state becomes the β - Fe^{III}/Fe^{III} cofactor and Y122 is oxidized into a tyrosyl radical with an additional electron obtained from various reductants in solution. The detailed mechanism of the diferrous cofactor reaction with oxygen in β has been thoroughly studied. A combination of rapid kinetic methods: stop flow and freeze quench in conjunction with physical methods - EPR and Mössbauer spectroscopies, as well as site directed mutagenesis were all used to elucidate this mechanism.^{60, 64} The first intermediate discovered in the activation process was named **X** and was shown to be kinetically competent to oxidize Y122 in the final and rate determining step.⁶⁵ **X** has been characterized with Mössbauer and ENDOR spectroscopies as a β - Fe^{III}/Fe^{IV} center, with $\delta = 0.56$ mm/s and 0.26 mm/s, and $\Delta EQ = -0.9$ mm/s and -0.6 mm/s for the Fe^{III} and Fe^{IV} sites, respectively.⁶⁶ In a more recent Extended X-Ray Absorption Fine Structure (EXAFS study),⁶⁷ the Fe-Fe distance in **X** was measured to be 2.78 Å, which correlates best with density functional theory (DFT) models that have a water

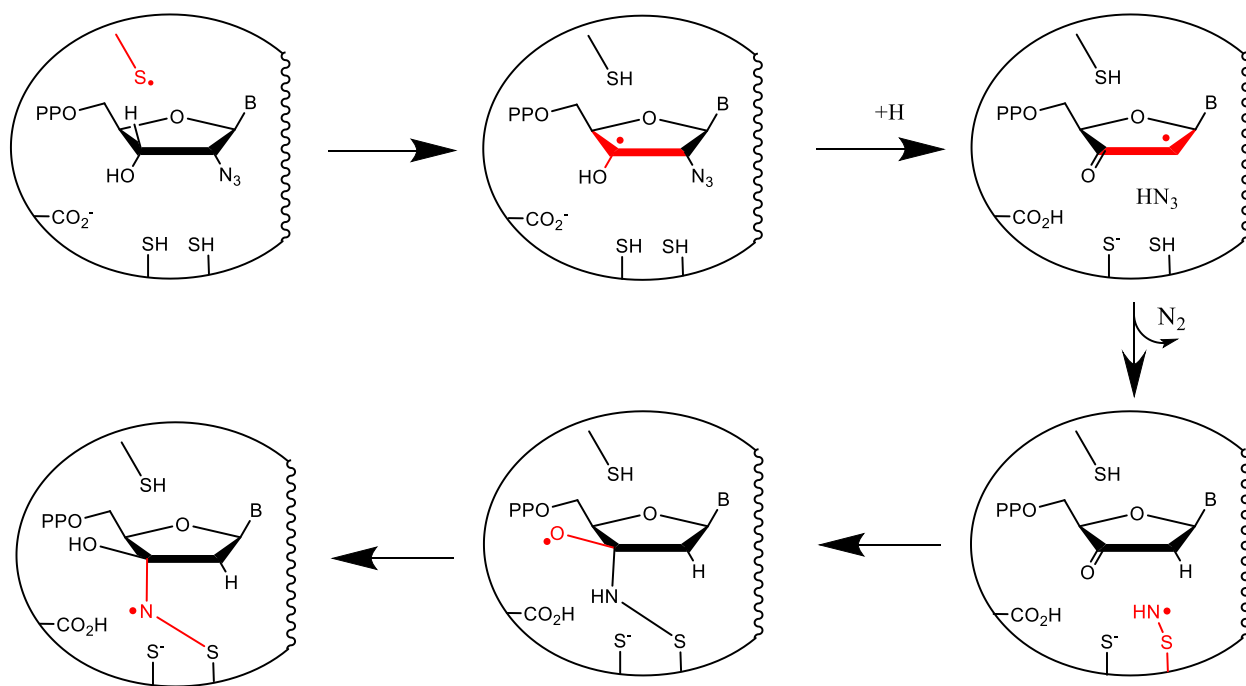
molecule in site **1** and a bis(μ -oxo) core for the structure of **X**. Prior to **X**, however, via several variants studies, three different states of the β cofactor have been identified. The first state that succeeds the β -Fe^{II}/Fe^{II} was characterized as **P_{Ec}** (**2**), a μ -1,2-peroxo- β -Fe^{III}/Fe^{III}, a species that is very similar to the **P** from soluble methane monooxygenase hydroxylase (sMMOH).⁶⁸ After a protonation and fast isomerization of **P_{Ec}**, the [Fe₂O₂]⁴⁺ intermediate state forms (**3**, **3'**). The following O-O cleavage oxidizes both W48 to W48• and β -Fe^{III}/Fe^{III} to **X** (**4**). In the wild type enzyme, W48• is quickly reduced by an external reductant leaving the aforementioned β -Fe^{III}/Fe^{IV}, **X** (**5**). In the next step, **X** oxidizes the nearby tyrosine residue and generates the active state of the cofactor β -Fe^{III}/Fe^{III} coupled to Y122• (**6**). This active state, if left at 25 °C over a period of days will decay to the so called “met,” inactive state of the enzyme, β -Fe^{III}/Fe^{III} and YH (**7**). The maintenance of this activation pathway involves the regeneration of the diferrous state of the cofactor from the inactive met state. This regenerative pathway has been shown to be facilitated by a ferredoxin (flavodoxin) reductase⁶⁹⁻⁷¹, NADPH, FAD, or DTT *in vitro* and by a ferredoxin YfaE *in vivo*.⁷²

Reaction inhibitors and distance measurements of *Ec* RNR

Based on the inhibition strategy, RNR inhibitors have been traditionally classified into three classes. The first prevents the biding of the β_2 and α_2 subunits via a use of a synthetic peptide that can bind to α and thus prevent the formation of the holoenzyme. This inactivation method has been shown to be effective in RNRs from both bacterial, *Escherichia coli*,⁷³ and eukaryotic, *Saccharomyces cerevisiae* and *Mus musculus*⁷⁴ organisms. The second inhibition strategy involves the reduction of the active state of class Ia β , β -Fe^{III}/Fe^{III} and Y•, to the met form. The most typical

one electron reductant studied for this purpose is hydroxycarbamide or hydroxyurea (HU). It has been shown that HU can reduce the Y122• in β_2 in the presence of oxygen.¹⁵ Interestingly, hydroxyurea is able to reduce the transient pathway radicals in β_2 and α_2 at a much higher rate under catalytic condition in the presence of α_2 , the substrate and effector compared to the rate of reduction of Y122• in β_2 alone.^{75, 76}

The third and final type of inhibitor utilizes a wide variety of substrate analogs. With distinct mechanisms in place, all these analogues irreversibly inactivate the reaction. The most well studied examples of these inhibitors include substrate analogs that have one or more modification on the C2 carbon of ribose^{77,78,79,80,81}, 5'-diphosphate^{81, 82}, as well as two notable examples, 2'-deoxy-2',2'-difluorocytidine, which is the drug gemcitabine and 2'-azido-2'-deoxyribonucleotides.^{77, 78, 83, 84} The last inhibitor mentioned is of great importance for the mechanistic studies of all three classes of RNRs because the 2'-azido-substituted substrate analogs



Scheme 5. Mechanism of ribonucleotide reductase on the 2'-azido-2'-deoxynucleotide substrate analog. Adapted from reference 83.

during catalysis generate a new stable nitrogen centered radical while diminishing the concentration of the active oxidant in the reaction. When the azido substrate analog is used in catalysis, within seconds, a formation of a 3'ribose-centered substrate radical occurs in conjunction with loss of the azido moiety as N_3^\bullet or N_3^- .⁸⁵ Within minutes a nitrogen-centered radical forms. This radical is fairly stable in anoxic conditions with a 10-minute half-life at 25 °C. The structure of the N^\bullet has been elucidated where the 3' position of the ribose is covalently attached to α via the N^\bullet to the sulfhydryl of C225 (**Scheme 5**). In addition to giving rise to an EPR signal and indicating RT, 2'-azido-2;-deoxynucleotide analog is considered to be a great candidate for the identification of the active cofactor of any RNR. After the initiation of a catalytic cycle, the active cofactor is one electron reduced. This event can be monitored by a rise of an EPR signal (eg. *Ct* RNR), or by a diminishing EPR signal (eg. *Ec* RNR). Additionally, if the active cofactor contains Fe, this reduction event can be observed by Mössbauer spectroscopy as well. This is a hallmark reaction in this dissertation because all three experimental chapters as well as the published paper in this work include this substrate analog in a small or a great extent. 2'-azido-2;-deoxynucleotides, have been extensively used to generate the nitrogen centered radical in α_2 . In the $\alpha_2\beta_2$ subunit complex, it was shown that only a single pair of α and β are active at a time.⁸⁶ This phenomenon is called half of sites reactivity. Therefore, in *Ec* RNR, when both α and β are present with ATP, and DTT, and azido-NDP the following situation occurs in one pair of α and β monomers, the Y122• in β is reduced and the N^\bullet is formed in α . In the second, non-catalytic pair of α and β , the Y122• remains.

Using DEER spectroscopy, Stubbe and coworkers were able to measure the distance between the Y122• in inactive β , and the N• generated on active α . This kind of distances measured have been named “diagonal” distances because they span both the active and inactive pairs of α and β .⁵³ In addition to the Y122• - N• distance, the diagonal distances between Y122• and a few pathway radicals have also been obtained. To stabilize the otherwise transient pathway radicals, Stubbe and coworkers were able to substitute the tyrosine pathway radical in β with 3-hydroxytyrosine (DOPA•) radical, and pathway radicals in α with 3-aminotyrosine (NH₂Y•) radicals. The radical forms of these amino acid analogs have a lower reduction potential than native tyrosine radicals making them great radical traps.^{61, 87} **Figure 2** illustrates an example of a diagonal distance measurement via DEER spectroscopy in *Ec* RNR.

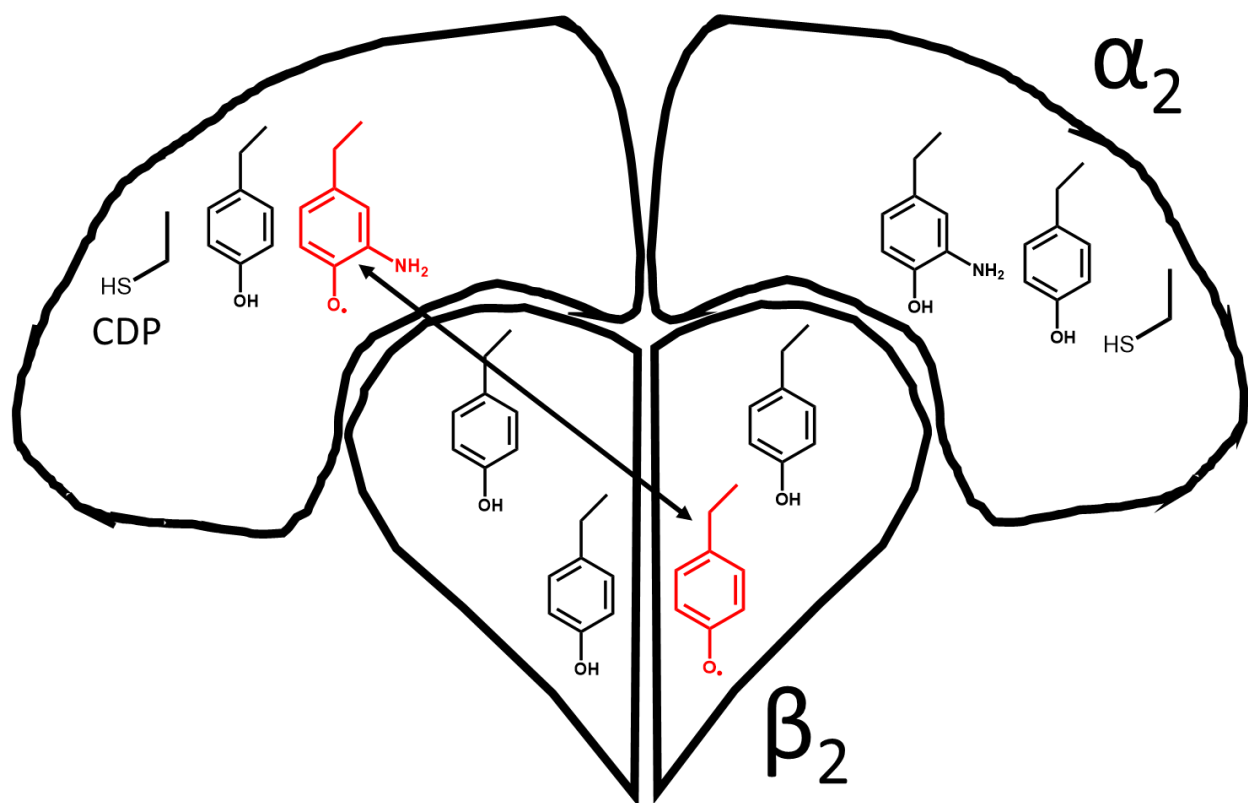


Figure 2. An example of diagonal distance measurements obtained via DEER spectroscopy in *Ec* RNR. Two radical species are required for this kind of measurement. Half-sites reactivity ensures that one β monomer contains the Y•, while in the other monomer the radical is translocated into α . The use of unnatural amino acids enabled radical trapping on the RT pathway thus allowing for DEER measurements.

This EPR method has been widely used to measure 1.5 - 8 nm inter-spin distances in biological systems.^{88, 89} It requires two sources of MW frequency that excite both electron spins. After excitation, time domain data that reflect the electron spin-spin dipole interaction is collected. The strength of this interaction is inversely proportional to the cube of the sought distance between the spins. Tikhonov regularization is usually applied to obtain the desired distributions. In 2015, we have managed to experimentally measure the first inter-subunit radical translocation (RT) distance in any class I RNR. The details of this work have been included in chapter 3.

Notion of Reaction Gating and the Structure of the Resting and Product states of Radical translocation in *Ec* β

One of the most remarkable properties of the small subunit of *Ec* RNR is the stability of Y122•. This radical has been shown to be stable for days at 4 °C.⁹⁰ There is significant evidence in the literature^{75, 76, 91} that suggests that this stability comes from the protein's ability to shield protons⁹² from solution reaching the cofactor, and therefore rising the energy barrier for the tyrosine radical reduction. This protected tyrosine residue, however, needs to be reduced during catalysis.⁵⁵ To explain this phenomenon we have proposed the notion of conformationally gated radical transfer. In *Ec* RNR we have determined that upon RT, an internal proton transfer occurs

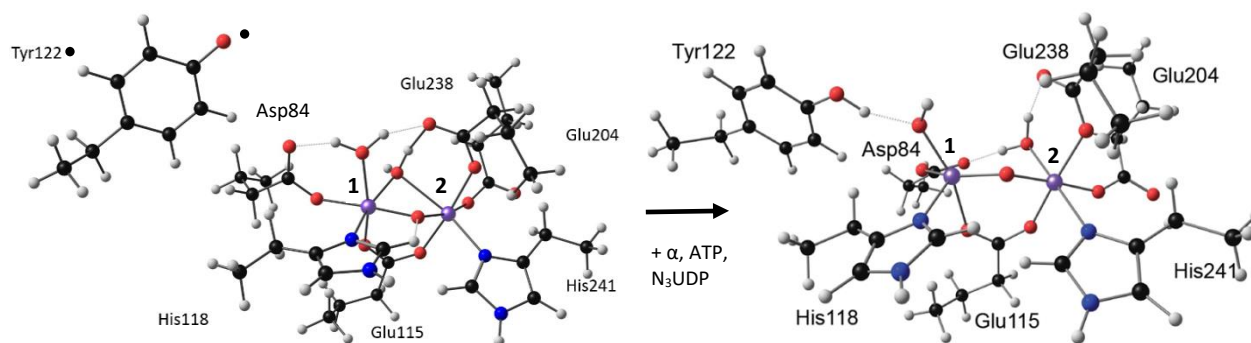


Figure 3. Density functional theory optimized geometries of the resting state of *Ec* RNR β (β -Fe^{III}/Fe^{III}-Y•) and the product RT state (β -Fe^{III}/Fe^{III}-YH) formed upon addition of α , ATP and N₃UDP.

to Y122• and identified the proton donor involved in the gated mechanism (**Figure 3**). In a buffer solution with just β present, the gated mechanism is closed, and it is not thermodynamically favorable for any RT to happen. However, if the substrate is present in conjunction with α subunit the and effector, as a result, a conformation change happens in the small subunit that drives the subsequent proton and electron transfer, thus, transferring a hydrogen atom to the tyrosyl radical.⁹³

In 2013, we have utilized site selective iron labeling, Mössbauer spectroscopy, and DFT methods to show that the proton donor that is involved in the gated mechanism is the water on the

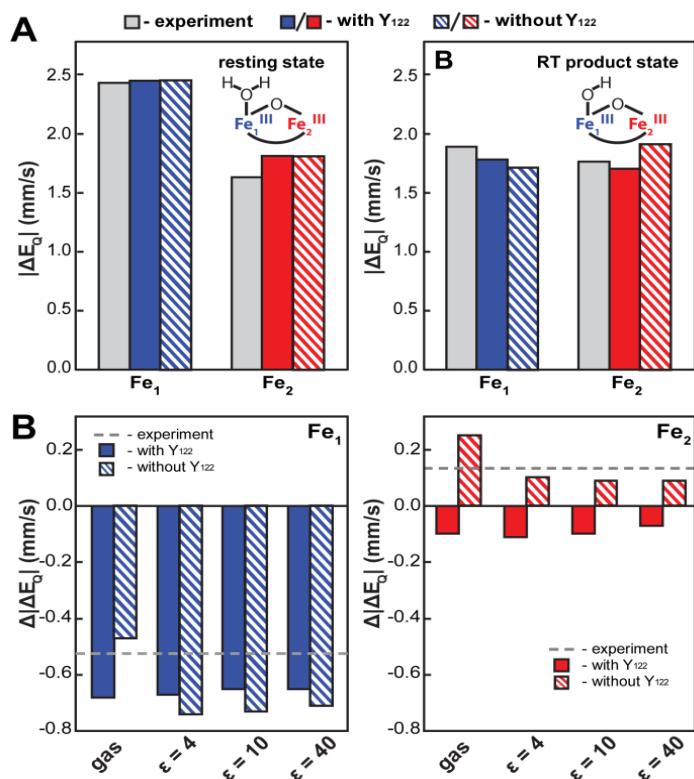


Figure 4. Comparison of the experimental quadrupole splitting (ΔE_Q) parameters for the resting and radical-translocation-product states of the cofactor to the values calculated by DFT. **(A)** Absolute values of ΔE_Q from experiment (gray bars) and the DFT calculations with the COSMO solvation model and $\epsilon = 4$ for models of either the full cofactor including Y122 (solid colored bars) or just the diferric cluster without Y122 (striped colored bars). The blue bars correspond to Fe₁ and the red bars to Fe₂. **(B)** The changes in the absolute values of ΔE_Q associated with the radical-translocation/deprotonation event either from the experiments (dashed gray lines) or from the calculations on the models including (solid bars) or omitting (striped bars) Y122. The color coding is the same as in panel A.

site 1 iron, in Class Ia RNR from *Escherichia coli*. We have compared the Mössbauer parameters of the resting or active state to the RT product state of β and found a profound shift in the ΔE_Q parameter of site 1 from 2.43 to 1.89 mm/s, while the ΔE_Q of iron site 2, as well as the isomer shift parameters of both sites remained largely unaffected. As shown by **Figure 4**, the DFT calculations were able to reproduce this change of the parameters after a reduction of Y122• and a proton transfer from Fe₁-H₂O to Y122•.⁹³ This result thus provided the first evidence that the diiron cluster of this prototypical class Ia RNR functions

not only in its well-known role as generator of the enzyme's essential Y122•, but also directly in

catalysis. The details of the calculations performed in the study are described in the materials and methods section.⁹³

Class Ib Ribonucleotide Reductases

The class Ib ribonucleotide reductase from *Escherichia coli* can initiate reduction of nucleotides to deoxynucleotides with either a $\beta\text{-Mn}^{\text{III}}/\text{Mn}^{\text{III}}\text{-Y}\bullet$ or a $\beta\text{-Fe}^{\text{III}}/\text{Fe}^{\text{III}}\text{-Y}\bullet$ cofactor in the NrdF (β) subunit.²⁰ While $\beta\text{-Fe}^{\text{III}}/\text{Fe}^{\text{III}}\text{-Y}\bullet$ can self-assemble from the diferrous state in NrdF and O_2 , activation of $\beta\text{-Mn}^{\text{II}}/\text{Mn}^{\text{II}}$ NrdF requires a reduced flavoprotein, NrdI. This activator protein was proposed to reduce molecular oxygen to superoxide and aid in the $\text{Mn}^{\text{III}}/\text{Mn}^{\text{III}}\text{-Y}\bullet$ assembly.²⁰ Two crystal structures have been solved for the class Ib *E. coli* RNR, both dimanganese and diiron bound NrdF structures.⁹⁴ The structures reveal different coordination environments, suggesting distinct initial binding sites for the oxidants during cofactor activation.⁹⁴ In addition to the RNR from *E. coli*, RNRs from *Bacillus subtilis*⁹⁵ and *Bacillus cereus*,⁹⁶ have been characterized and shown to be active class Ib RNRs. In contrast, the class Ic RNR currently has only one member from *Chlamydia trachomatis*.

Class Ic Ribonucleotide Reductases

Class Ic RNRs first were recognized in 2000 via multiple sequence alignment analysis of the β subunit.⁹⁷ Two conserved key residues have been identified. The proposed new class of enzymes with the first member being from *Chlamydia trachomatis* (*Ct*) did not possess the previously thought of as an essential, radical harboring Y residue (*Ec* Y122). It was replaced with a redox-inert phenylalanine (*Ct* F127). The aspartate ligand that binds the metal site one (*Ec* D84)

was replaced by a longer side chain containing glutamate (*Ct* E89). Therefore, we annotate the defining residues as D/Y for class Ia RNRs and E/F for class Ic RNRs. The alignment of both the small and large subunits showed that all the other four redox active amino acid residues involved in the radical translocation pathway are present. Initially, it was proposed that the RNR initiator Y^\bullet is located on Y129.⁹⁷ However, when the crystal structure of *Ct* β was solved⁹⁸ it showed unexpected similarity in the helical fold to *Ec* β where F127 occupies the space of Y122 in *E. coli*. No post-translational modifications to F127 were observed⁹⁸ suggesting that this residue is not directly involved in catalysis. It was initially thought that *Ct* RNR utilized a diiron metal center but did not possess a tyrosine radical.⁹⁹ Initial studies showed that like *Ec* β , *Ct* β can bind diiron and react with oxygen to produce the potent oxidant $X_{Ct}, \beta\text{-Fe}^{IV}/\text{Fe}^{III}\text{-}Y^\bullet$. It was proposed that X_{Ct} can initiate the ribonucleotide reduction directly by oxidizing the nearby RT pathway residue.¹⁰⁰ However, the modest amount of dCDP formed never correlated to the amount of X_{Ct} that was accumulated.⁹⁹ Additionally, when the azido UDP reaction was performed and the proportional decay of X_{Ct} was not observed, this diiron generated intermediate was considered catalytically incompetent.¹⁰¹

Not until 2007 was the active cofactor identified in our group. Jiang et al. have shown that *Ct* β does not utilize a diiron cofactor but instead a novel heterobinuclear Mn/Fe cofactor for the initiation of the reduction of NDPs.¹⁰²⁻¹⁰⁴ The RT initiating cofactor was identified as a stable $S_{total} = 1$, $\beta\text{-Mn}^{IV}/\text{Fe}^{III}$ with the Mn^{IV} ion functionally replacing the Y122 \bullet in *E. coli* RNR and providing the initial oxidizing equivalent for RT during catalysis.^{104, 105} The RT product state was determined to be $\beta\text{-Mn}^{III}/\text{Fe}^{III}$ via EPR spectroscopy.

Class Id Ribonucleotide Reductase

A novel, class Id ribonucleotide reductase has recently been discovered both in our laboratory²³ and Swedish group headed by dr. Sjöberg.²² While the Swedish group analyzed an RNR from *Leeuwenhoekiella blandensis*, our group studied an RNR from *Flavobacterium johnsoniae* (*Fj*). While Class Ia and Class Ic RNRs have either a D/Y or E/F cofactor residue dyad respectively, *Fj* is characterized by a mixture of the two by possessing the E/Y dyad. We have identified that this RNR is active with dimanganese and that it requires superoxide for activation. Also, the small subunit has been crystalized and its structure shows a unique solvent exposed metal cofactor due to a disordered helix. It is hypothesized that superoxide can diffuse into the proximity of the metal site via to this opening. One way of generating superoxide in solution is via the

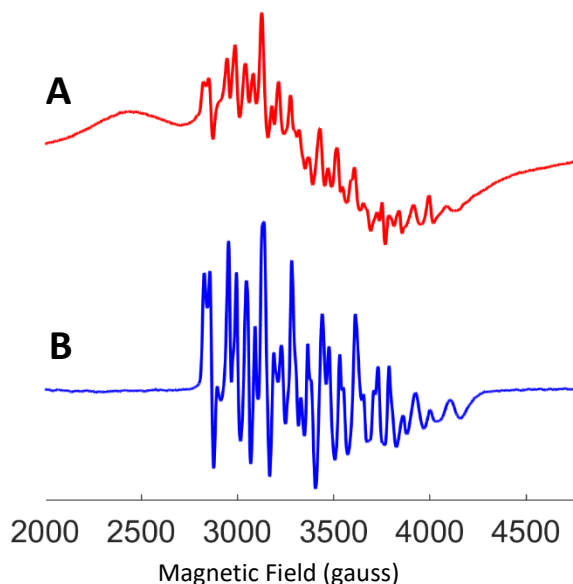


Figure 5 (A) CW EPR spectra of 200 μM *Fj* β_2 with an addition of 1.5 equivalents of manganese per dimer in the presence of oxygen. (B) and the spectrum change upon the addition of 25 mM DTT and a 5 min incubation at room temperature. Spectrometer conditions were: Temperature 10 K, microwave frequency, 9.45 GHz; microwave power, 20 mW; modulation frequency, 100 kHz; modulation amplitude, 10 G; scan time, 180 s; time constant, 180 ms.

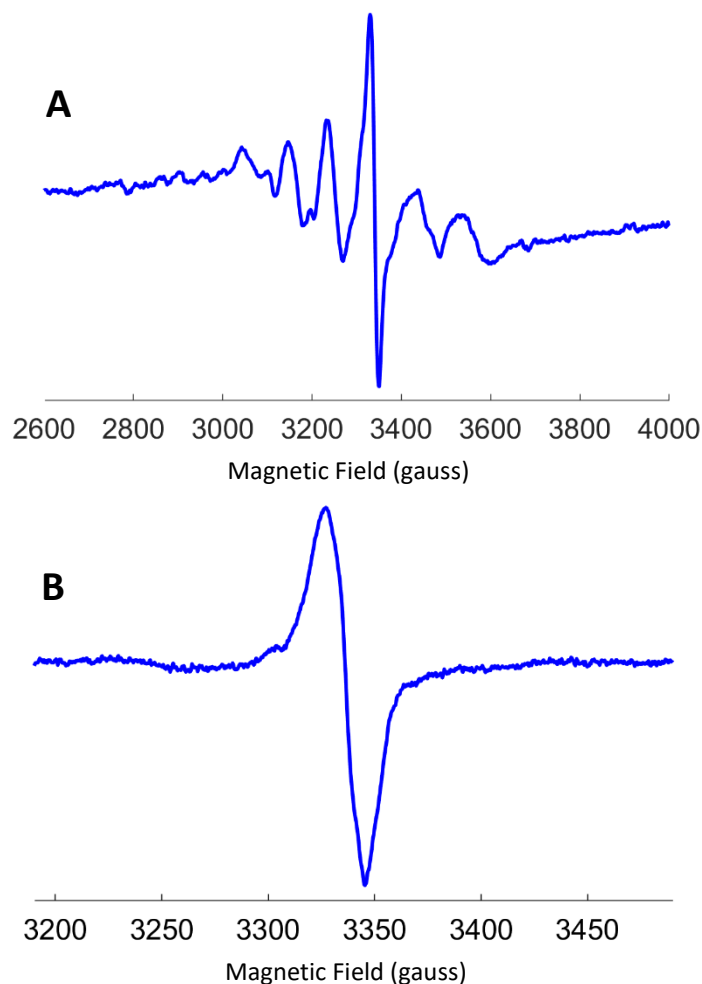


Figure 6. CW EPR spectra of 200 μM *Fj* β_2 with an addition of (A) 1 equivalent of both Mn and Fe per dimer in the presence of oxygen and (B) 2 equivalents of Fe per dimer in presence of oxygen. Spectrometer conditions: Temperature 10 K, microwave frequency, 9.45 GHz; microwave power, 20 μW ; modulation frequency, 100 kHz; modulation amplitude, 10 G; scan time for (A) 180 s, for (B) 30s; time constant, 180 ms.

use of 1,4-Naphthoquinone. Addition of the quinone to the active *Fj* RNR $\alpha\beta$ complex, at 50 μM β_2 has significantly increased activity. There is also evidence that DTT in conjunction with oxygen can generate superoxide. In 1974, it was shown that various dithiols such as dithiothreitol, 2-mercaptoethanol, reduced glutathione, and ethyl mercaptan, via autoxidation can univalently reduce oxygen to superoxide.¹⁰⁶ Upon the addition of DTT in the presence of O_2 (Figure 5), we are able to observe the disappearance of the broad $\beta\text{-Mn}^{\text{II}}/\text{Mn}^{\text{II}}$ signal and a significant increase in intensity of the mixed valent dimanganese signal characterized by a multiline signal

arising from the hyperfine interaction between the two manganese nuclear spins ($I = 5/2$) with the electron spin. This signal shows sharp lines that correspond to the 36 possible EPR transitions due to nuclear 36 nuclear states of the two manganese spins coupled together to the electron spin. The signals arising from these transitions often overlap and only about 12-16 peaks are resolved.¹⁰⁷ Upon detailed spin relaxation studies, our group has determined that there are two multi-line

signals that form upon the reaction of $\beta\text{-Mn}^{\text{II}}/\text{Mn}^{\text{II}}$ with superoxide.²³ One is clearly resolved at 30 K, while at 10 K in addition to the signal observed at higher temperature, another signal arises.

Upon a more detailed analysis, we have determined that both signals likely arise from two distinct $\beta\text{-Mn}^{\text{IV}}/\text{Mn}^{\text{III}}$ species. Which one of these signals correlates to the active cofactor is not yet determined. The EPR signals at 10 K are presented in **Figure 7**.

Although *Fj* β reconstituted with iron was shown to be inactive, the APO protein grown in LB rich medium, after ferrozine chelation, does bind diiron to make the $\beta\text{-Fe}^{\text{III}}/\text{Fe}^{\text{III}}\text{-Y}\cdot$ cofactor (**Figure 6**). In addition to the tyrosine radical, by adding 1 eq. of both Mn and Fe per *Fj* β dimer we have observed a signal that

likely corresponds to an antiferromagnetically coupled $S_{\text{total}} = \frac{1}{2} \beta\text{-Mn}^{\text{III}}/\text{Fe}^{\text{III}}$ state. **Figure 6** illustrates these observations.

One of the key experiments that has helped determine the active cofactor in RNRs is the reaction of α and β with the substrate analog N_3UDP in the presence of the reductant DTT and

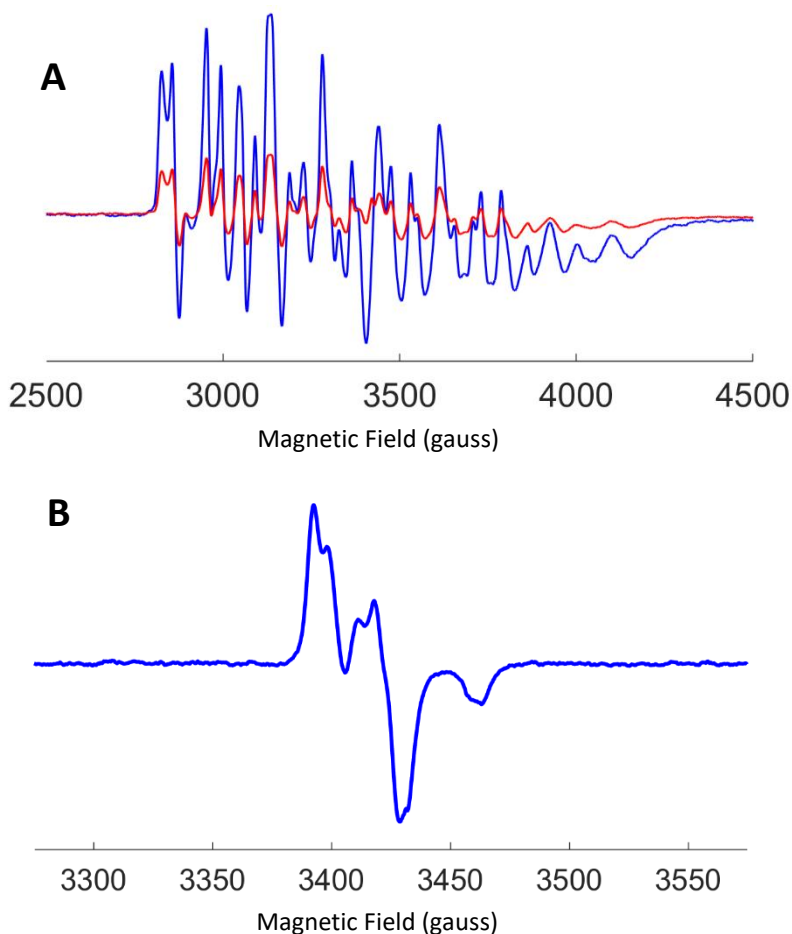


Figure 7. **A)** 10 K CW-EPR spectra of 200 μM *Fj* β_2 activated with NQ and incubated for 2 minutes with DTT, ATP, *Fj* α and N_3UDP (red) and the no azido control (blue). **B)** 100 K CW-EPR spectrum of the nitrogen centered radical. Spectrometer conditions: microwave frequency, 9.45 GHz; microwave power, 20 mW for black and red, 200uW for blue; modulation frequency, 100 kHz; modulation amplitude, 5 G; scan time for black and red 360 s, for blue 60 s; time constant, 180 ms.

effector ATP. The resulting reaction should theoretically show a diminution of the active RT state of the cofactor and the increase of the RT product state, as well as an increase of the nitrogen centered radical in the larger subunit. One of the crucial conditions required for the reproducibility of such experiments in *Fj* RNR was the removal of additional salt and glycerol, as well as a decrease in the buffer concentration in the reaction. With no additional NaCl in solution and with ~50 mM HEPES buffer we have observed a ~35% decrease of the 10 K EPR signal (as compared to a control sample). Upon a longer incubation of the reaction, however, we have observed an increase of the multiline, low temperature, dimanganese signal at 10 K. Since the larger subunit requires DTT for reduction of its disulfide bonds for increased stability, the presence of the dithiol and oxygen in the reaction buffer could generate superoxide in solution. Superoxide could regenerate the active cofactor as observed via the aforementioned dimanganese EPR signal. This further supports our hypothesis that DTT is involved in cofactor activation *in vitro*.

Novel, metal-free Class Ie ribonucleotide reductase

Very recently our group,²⁴ and the group from Sweden²⁵, discovered a novel class Ie RNR that does not seemingly require any metals for ribonucleotide reduction. Unlike any other class I RNRs, it was discovered that the radical initiator in the novel class is a stable radical residing on a modified tyrosyl residue. It was shown that this radical is DOPA•, and that the post translation modification of the tyrosine residue that makes DOPA only occurs if the β is co-expressed with a NrdI activase protein, located nearby in the organism genome.²⁴

Sequence similarity network (SSN) of InterPro IPR000358 superfamily that contains all RNR β annotated genes

There were previous representations of the SSNs of all the RNR β genes given by Rose et al.²³ and Harrison et al.¹⁰⁸ However, in this work, for the first time, we present a complete network of all unique RNR β genes belonging to the InterPro IPR000358 superfamily (**Figure 8**). This means that each node in the network represents a unique RNR gene and that only identical genes share a node. In addition, we have, for the first time, aligned all of the gene sequences that belong to the superfamily. This way, in a rigorous manner, we were able to obtain the number of tentative members of each class I RNR β except for class Ib (and consequently class Ia) RNRs. We have omitted all sequences that contain less than 200 and more than 600 amino acid residues because they likely are not genes that encode for RNR β s, but rather, miss-annotations in the superfamily. The total number of RNR β sequences in our network is 9781. Based on our sequence alignment, we assigned 7380 as tentative class Ia members, 385 as class Ib, 179 as class Ic, 309 as class Id, 188 as class Ie. The rest of the sequences, colored in light blue, were assigned as unknown due to the lack of potential cofactor binding and PCET involving amino acid residues. Tentative class Ie RNR β members were subdivided into two groups, colored in pink and black. The pink colored group contains a valine, proline and lysine (VPK sub-family) while the black colored group contains a glutamine, serine and lysine (QSK sub-family). The aforementioned residues replace the traditionally carboxylate containing residues typically involved in metal binding in conventional RNR β gene sequences. While the VPK containing members of class Ie RNRs have been studied extensively *in vitro*,^{24, 25} we can only speculate that the QSK variants belong to the class Ie RNR subclass and use a DOPA• to initiate ribonucleotide reduction.

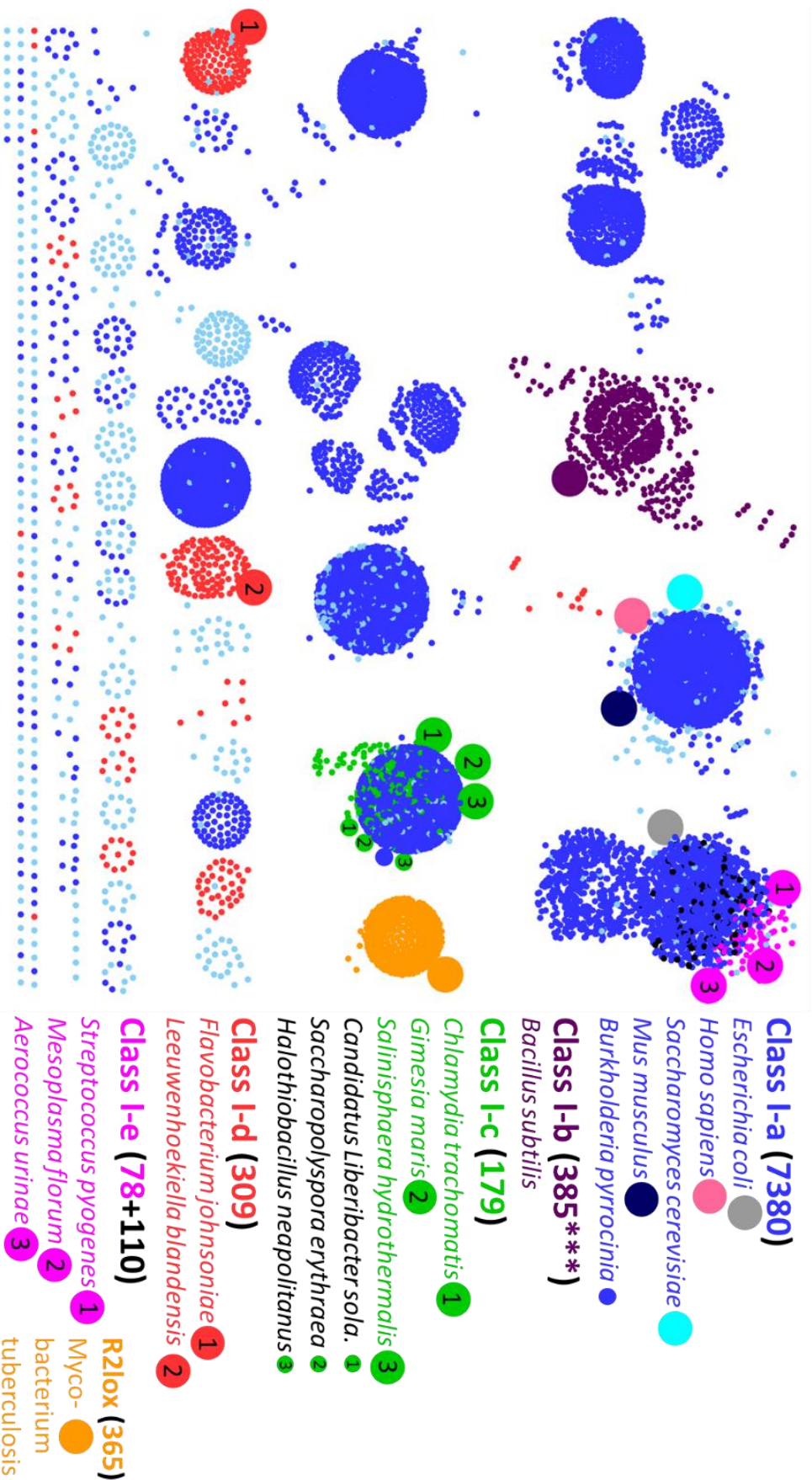


Figure 8. A sequence similarity network of InterPro IPR000358 superfamily of all RNR β subunit genes. The network contains each unique RNR gene and all genetic sequences have been aligned via the MUSCLE alignment package. The legend is color coded for each class I RNR with the notable representatives. *** Class Ib RNRs do not possess a specific defining amino acid residues. Class Ib members were assigned based on the proximity to the *Bacillus Subtilis* RNR β gene. Light blue nodes are RNR β annotated genes that lack one or more essential amino acid residues. The network was generated in May 2017 and visualized via the Cytoscape software package.

Reaction of the β -Fe^{II}/Fe^{II} and β -Mn^{II}/Fe^{II} cofactors in *Ct* β with dioxygen

The reaction of the diiron form of the *Ct* β cofactor with oxygen is very similar to the class Ia *Ec* activation. After the diferrous binding to the apoprotein, the first intermediate on the activation pathway was characterized as μ -1,2-peroxo, or **P_{Ct}**.¹⁰⁹ The next step in the reaction pathway is a homolytic cleavage of the O-O bond that results in the formation of **X_{Ct}** and a tryptophan radical, W51• (analogous to the W48 from *Ec*). This radical is reduced by a solvent exposed Y222 residue giving rise to a tyrosyl radical.¹¹⁰ With an addition of a solvent sourced electron from either ascorbate or Fe^{II}, this residue is reduced leaving the cofactor in the **X_{Ct}** state. The last step of this reaction process is the decay of **X_{Ct}** to the diferric state of the cofactor. This cofactor has been shown to be catalytically incompetent.¹⁰⁴

The catalytically competent cofactor, the heterodinuclear Mn/Fe center, undergoes an activation process in *Ct* RNR. The first step after β -Mn^{II}/Fe^{II} binding to apo- β is a reduction of O₂ and formation of the β -Mn^{IV}/Fe^{IV} intermediate. The next step in the activation process is the one electron reduction of β -Mn^{IV}/Fe^{IV} intermediation that generates the aforementioned W51• that in turn forms the Y222•.¹¹⁰ Just like in the diiron reaction, ferrous or ascorbate from the solvent

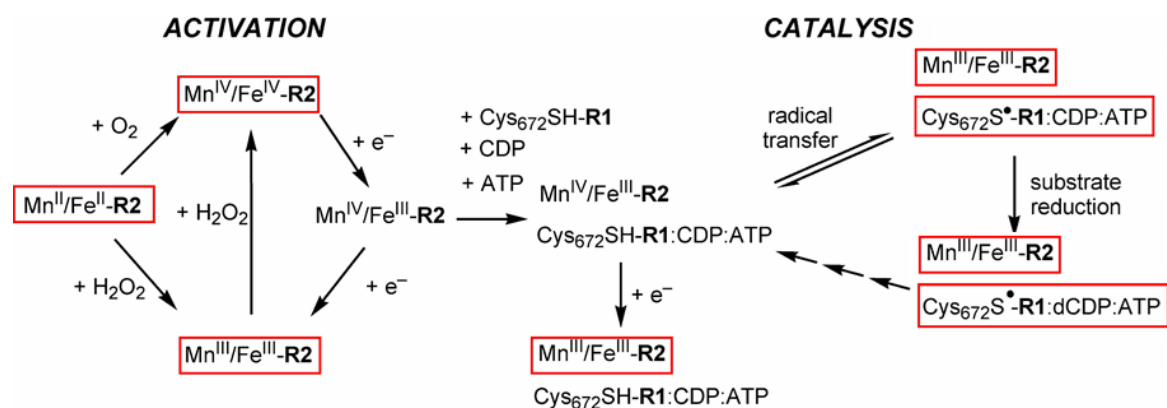


Figure 9. A complete schematic of activation and catalysis of *Ct* RNR. The red boxes around and various states of the cofactor indicate a paramagnetic center that is EPR active. All those states have been detected except for Cys₆₇₂S• in α . Figure courtesy of Carsten Krebs.

provide the last reducing equivalent to reduce Y222 and form the stable active cofactor $\beta\text{-Mn}^{\text{IV}}/\text{Fe}^{\text{III}}$. Our group has also shown that the presence of ascorbate can accelerate the decay of the $\beta\text{-Mn}^{\text{IV}}/\text{Fe}^{\text{IV}}$ intermediate. This acceleration is concentration dependent and ascorbate does not affect the rate of formation of this intermediate.¹¹¹ Another strategy for the generation of the RT resting state is the reaction of the $\beta\text{-Mn}^{\text{II}}/\text{Fe}^{\text{II}}$ with H_2O_2 . It was shown that this reduced state of the cofactor initially forms the $\beta\text{-Mn}^{\text{III}}/\text{Fe}^{\text{III}}$.¹¹² EPR spectroscopy indicated that this state is distinct from the $\beta\text{-Mn}^{\text{III}}/\text{Fe}^{\text{III}}$ RT product state, while with an additional equivalent of hydrogen peroxide the cofactor can be fully oxidized to the $\beta\text{-Mn}^{\text{IV}}/\text{Fe}^{\text{IV}}$ which decays to $\beta\text{-Mn}^{\text{IV}}/\text{Fe}^{\text{III}}$. The most essential details of the O_2 activation and catalysis for the Mn/Fe *Ct* RNR are presented in **Figure 9**.

Electronic structures of $\beta\text{-Mn}^{\text{IV}}/\text{Fe}^{\text{IV}}$ and $\beta\text{-Mn}^{\text{IV}}/\text{Fe}^{\text{III}}$ cofactors

The detailed electronic structure and the protonation states of the solvent and oxygen derived cofactor ligands in $\beta\text{-Mn}^{\text{IV}}/\text{Fe}^{\text{IV}}$ intermediate have been determined in a recent study by the Bollinger/Krebs group.¹¹³ The EXAFS results of both the Mn- and Fe- edge indicated a metal-metal vector of ~ 2.75 Å as well as a “light-atom” scatterer 1.8 Å distant from the iron. In addition, Electron Nuclear Double Resonance (ENDOR) developed by Mims¹¹⁴ revealed an exchangeable deuterium hyperfine coupling of $|T| = 0.7$ MHz. There were no stronger couplings present indicating no possible bridging deuterons. The EXAFS and ENDOR results combined were indicative of a di-(μ -oxo) diamond core structure for the $\beta\text{-Mn}^{\text{IV}}/\text{Fe}^{\text{IV}}$ cofactor with a terminal hydroxide ligand on the manganese, of which the proton is hydrogen-bonded to E89.

The resting (β -Mn^{IV}/Fe^{III}) RT state of the cofactor in *Ct* RNN is arguably the most important one, given its role as the catalytic initiator. Initial structural studies involved EXAFS

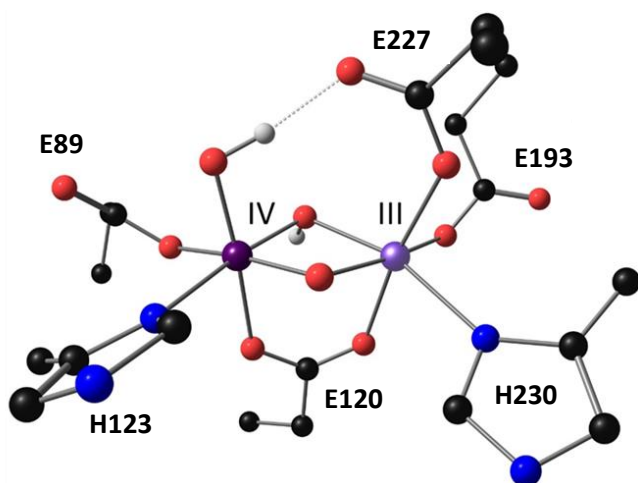


Figure 10. The proposed geometry of the active cofactor β -Mn^{IV}/Fe^{III} from *Ct*. Adapted from reference 119.

spectroscopy that yielded a 2.92 Å metal-metal distance resulting from both the Mn- and Fe- edges.¹¹⁵ The Mn- edge also suggested a short 1.74 Å Mn-O bond. At the time, the assignments of the metals to sites **1** and **2** were unknown and density functional theory models agreed best with six models that included a terminal hydroxo/water in

site one, a μ -oxo, μ -hydroxo bridge between the metals. Whether the hydroxide bridge was cis or trans to the two histidine ligands was not addressed in this study. The Mn/Fe bound crystal structure of β_2 was solved in 2012.¹¹⁶⁻¹¹⁸ The results of these studies showed that X-ray crystallographic anomalous scattering density at site **1** of the active Mn/Fe cofactor was preferentially occupied by Mn. However, the occupancy of site **2** involved both metals to a significant degree, and the low metal occupancy of both sites created difficulties in the positioning of the side chains and bridging ligands in the model. Consequently, assignment of Mn to site **1** still remained uncertain. The most recent study made use of nuclear resonance vibrational spectroscopy (NRVS) and absorption (Abs)/circular dichroism (CD)/ magnetic circular dichroism (MCD), variable temperature, variable field (VTVH) MCD as well as DFT methods, to determine the detailed geometric and electronic structure of the β -Mn^{IV}/Fe^{III} cofactor.¹¹⁹ The numerous aforementioned physical methods in conjunction with DFT indicated that the structure had a solvent terminal hydroxide in site **1** where Mn resides, a μ -oxo, μ -hydroxo bridge between the

metals, and the oxo- bridge is *cis* to the two His ligands (**Figure 10**). The precise location of the terminal hydroxide proton (whether it was facing and hydrogen bonded to E89 or E227) was not explored in this study.

Proposed class Ic gene sub-cluster of the small subunit of RNR – Identification and analysis of the class Ic sub-cluster within the ribonucleotide reductase small subunit family

After the initial discovery of the novel and unique RNR from *Chlamydia trachomatis*, the first in its class, class Ic RNR was hypothesized to contain >25 β proteins.¹⁰³ Each of these hypothetical class Ic members had a phenylalanine instead of a tyrosine and a glutamate instead of the aspartate in the positions that correspond to Y122 and D84 of *Ec* β . These two features will be referred to as the D/Y for class Ia and E/F for class Ic dyads, henceforth. Interestingly, sequence similarity network analysis yielded a set of highly similar sequences that contained both D/Y and E/F dyads, indicating that the cluster was made up of a mixture of class Ia and class Ic RNRs. Another study of this subclass was conducted in 2013¹²⁰ and indicated 100+ hypothetical members with an approximate 1:1 ratio of class Ia/class Ic members. As of May 2017, significantly more genomes have been sequenced and thus we discovered 1110 members of this sub-cluster where 179 belong to the tentative class Ic. As of this date, there are numerous examples of class Ia RNRs,⁴⁸ a few examples of class Ib RNRs,^{95, 96} a few examples of both class Id^{23, 121} and class Ie^{24, 25} RNRs, and a single class Ic RNR. Therefore, an expansion of class Ic RNRs is necessary for the validation of its existence. Even though there have been a few attempts to do so, as of today, *Ct* RNR remains the sole member.

Previous attempts to characterize a second class Ic RNR

The first candidate containing the E/F dyad for the class Ic RNR in our laboratory was taken from the genome of erythromycin-producing bacterium *Saccharopolyspora erythraea* (*Se*).¹²² Both α and β subunit encoding genes were extracted via polymerase chain reaction (PCR) and transferred into a pET28a+ vector. Upon overexpression in *E. coli* and purification, we have shown that *Se* β can assemble a Mn/Fe cofactor.¹²⁰ Stopped-flow and EPR data supported the formation of the β -Mn^{IV}/Fe^{IV} intermediate in the reaction of the Mn/Fe reconstituted *Se* β with dioxygen¹²⁰. The subsequent

formation of the β -Mn^{IV}/Fe^{III} cofactor was confirmed via Mössbauer spectroscopy. In addition, another experiment was performed to verify the

presence of this cofactor. It is known from the *Ct* RNR system that upon ~2 Mrad γ -irradiation of the β -Mn^{IV}/Fe^{III} β @ 77 K, the cofactor reduces to a β -Mn^{III}/Fe^{III} state

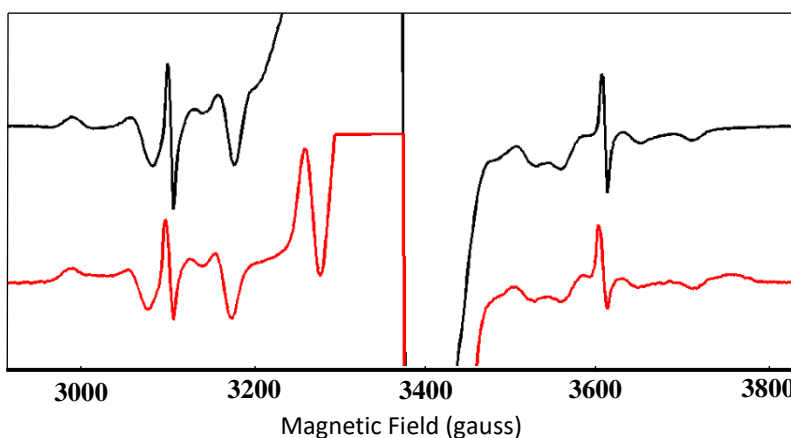


Figure 11. EPR spectra of the β -Mn^{III}/Fe^{III} state of the β cofactor from *Chlamydia trachomatis* (red) and *Saccharopolyspora erythraea* (black). The spectra were generated via ~2 Mrad γ -irradiation at 77K of the β -Mn^{IV}/Fe^{III} active state. The very large and cut off signal centered around $g=2$ arises from the free radical generation of the EPR tube impurities and solvent molecules. Sharp features ~3100 G and ~3600 G correspond to the very strong isotropic hyperfine coupling of H \cdot - another byproduct of irradiation. The outer, visible, Mn based spin packets are strikingly similar to the features of the β -Mn^{III}/Fe^{III} RT product state of *Ct* β . Spectrometer conditions: microwave frequency, 9.45 GHz; microwave power, 20 mW for black and red, 200uW for blue; modulation frequency, 100 kHz; modulation amplitude, 5 G; scan time for black and red 360s, for blue 60s; time constant, 180 ms.

strikingly similar to the RT product β -Mn^{III}/Fe^{III}¹²³ as seen by EPR (**Figure 11**). Catalytic activity of *Se* RNR, however, was shown to be very modest at 19 turnovers in 15 min per β_2 .¹²⁰ Considering such poor ribonucleotide reduction, we were not able to make a definite conclusion whether *Se* RNR is indeed a Mn/Fe dependent class Ic ribonucleotide reductase. Upon further analysis, it was

determined that *Se* genome contains a putative class II RNR as well. It is possible that this ribonucleotide reductase is the catalytically competent one and the tentative Ic RNR we studied has, through evolution, lost its *in vivo* functionality.¹²⁰

To avoid this possibility, the next target for the second class Ic RNR came from *Halothiobacillus neapolitanus* (*Hn*), a sulfur oxidizing chemoautotroph whose genome contained a sole RNR - the one of interest. After the necessary steps required for protein overexpression were taken, *Hn* β was shown to be competent in the Mn/Fe cofactor assembly. Even though we were never able to detect the β -Mn^{IV}/Fe^{IV} intermediate, upon the reaction and incubation of the Mn/Fe *Hn* β cofactor with O₂ and subsequent reduction via sodium dithionite, a β -Mn^{III}/Fe^{III} form was detected via EPR.¹²⁰ This was the main piece of evidence that the small subunit of *Hn* RNR is able to form the active RT state, β -Mn^{IV}/Fe^{III}. Unfortunately, after the addition of α and β , DTT, ATP, and CDP into solution, and after performing mass spectrometric assays, no detectable dCDP was formed. Additionally, the EPR analysis of the sample that contained α and β with N₃UDP, ATP and DTT neither yielded the nitrogen centered radical nor the RT product β -Mn^{III}/Fe^{III} state. In the light of these results, like *Se*, *Hn* RNR was shown not to be a viable candidate for the second class Ic RNR.

In this work, in Chapters II and III, we have identified two class Ic RNRs from *Gimesia maris* and *Salinisphaera hydrothermalis*, respectively, thus firmly establishing the class Ic RNR as a class that uses a β -Mn^{IV}/Fe^{III} cofactor to initiate ribonucleotide reduction.

Proposal of the Class Ic and Ia cross-species subunit pairing and characterization of *Burkholderia pyrocinia* Ribonucleotide Reductase

Once the gene cluster that contained very similar genes that belonged to both class Ia and class Ic ribonucleotide reductases was initially identified, several sequences with striking level of identity (~68%) between putative class Ia and Ic β subunits were uncovered. This intriguing discovery beckoned several questions. Is the only defining characteristic of each class the D/Y and E/F dyad of the small subunit? Do all D/Y β proteins utilize exclusively a diiron cofactor and analogously do all E/F β proteins utilize a Mn/Fe cofactor? Is there any evolutionary adaptation to the large subunit between the Ia and Ic subclasses? Is the RT pathway the same between the subclasses? Is it possible to convert from one class to the other by simply changing the D/Y dyad into E/F to convert a class Ia RNR β into a class Ic RNR β and vice versa? One way to address some of these questions is to attempt the interspecies “subunit swapping” – an experiment where a class Ia β and a class Ic α (and *vice versa*) are mixed with the effector, disulfide reductant and the substrate with the expectation of achieving ribonucleotide reduction. The first pair of RNRs from two different organisms were from *Methylococcus capsulatus* (*Mc*) as a class Ia representative, and *Saccharopolyspora erythraea* (*Se*) as the aforementioned class Ic representative. Both *Mc* β *Se* α and *Se* β *Mc* α combinations were explored. Previous members of the Bollinger/Krebs laboratory have characterized *Mc* as a competent class Ia RNR.¹²⁰ Oxygen activation yielded intermediates \mathbf{P}_{Mc} and \mathbf{X}_{Mc} and resulted in the β -Fe^{III}/Fe^{III}-Y• resting RT state.¹²⁰ *Mc* α • β complex was able to competently perform catalysis with the rate of reduction of 0.18 s⁻¹

per β . The β subunit of *Se* was shown to be inactive both paired with *Se* α and *Mc* α , however, the *Mc* β *Se* α complex was able to achieve multiple turnover. This result demonstrates that there are no modifications required to the larger subunit of a tentative class Ic RNR to make use of a different radical translocation initiating cofactor. However, *Se* ribonucleotide reductase's deficiency in the RT activating ability of the small subunit prevents an absolute assignment of this RNR to class Ic. Therefore, to make any definite conclusions about the evolution and interplay between α and β subunits and classes Ia and Ic, a fully competent second Class Ic RNR is essential. To address this problem, we have implemented three different strategies.

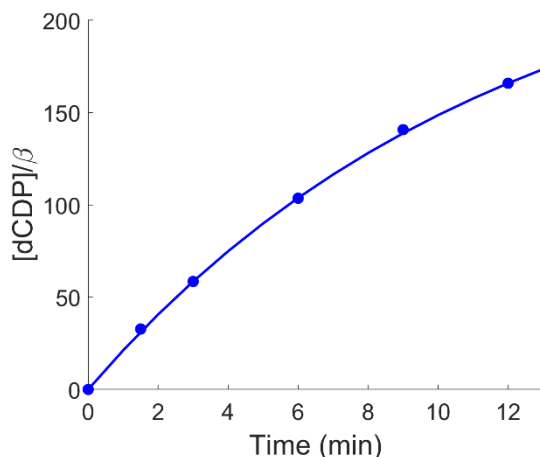


Figure 12. Reaction of the wt *Bp* $\alpha\beta$ subunit complex. The exponential fit produced 0.19 s^{-1} rate of reaction per β . Reaction conditions: 100 μM α_2 , 10 μM β_2 , 40 μM Fe^{II} , 2 mM ATP, 2 mM CDP, 10 mM DTT, Reaction quenched with 2 M formic acid.

The first strategy involved the obtaining of a new class Ia ribonucleotide reductase that is very similar to the well-established class Ic RNR from *Ct*. In 2014, maximum sequence identity

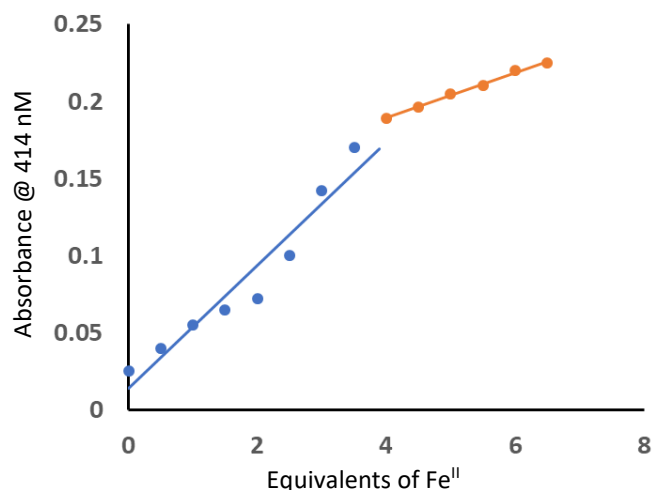


Figure 13. Titration of the apoprotein β_2 from *Burkholderia pyrrocinia* with Fe^{2+} in the absence of a reductant as monitored by the absorbance of the sharp feature of the $\text{Y}\cdot$ at 415 nm.

of the β subunit of 62% compared to *Ct* RNR revealed the best candidate to be the RNR from *Burkholderia pyrrocinia* (*Bp*).¹²⁴ *Bp* is a Gram negative soil bacterium that was discovered in the sputum of patients with cystic fibrosis.¹²⁵ This potential class Ia RNR was the only RNR present in the organism. Genes of both the α and β RNR subunits were

obtained and prepared for protein overexpression. Like *Mc*, *Bp* RNR was shown to be enzymatically competent. Although the activation process was not studied in detail, after addition of diferrous and O₂ to the small subunit, the Fe^{III}/Fe^{III}-Y• state was observed via both absorption and EPR methods (**Figure 14**). In the *Ec* RNR system, Fe²⁺ titration into apoprotein β₂, monitored via the absorption at 410 nm indicated that a critical ratio of Fe²⁺/β₂ was achieved at 4 equivalents of iron binding per β₂ signaling the completion of reconstitution.¹²⁶ We were able to reproduce this result in the *Bp* system as shown in **Figure 13**. After mixing both *Bp* RNR subunits with the addition of the effector ATP, reductant DTT, and substrate CDP, we were able to observe an appreciable rate of ribonucleotide reduction of 0.19 s⁻¹ β⁻¹ (**Figure 12**). In spite of relatively high sequence similarity, the target reactions between *Bp* β and *Ct* α, and *Ct* β and *Bp* α, however, did not yield any detectable levels of dNDPs.

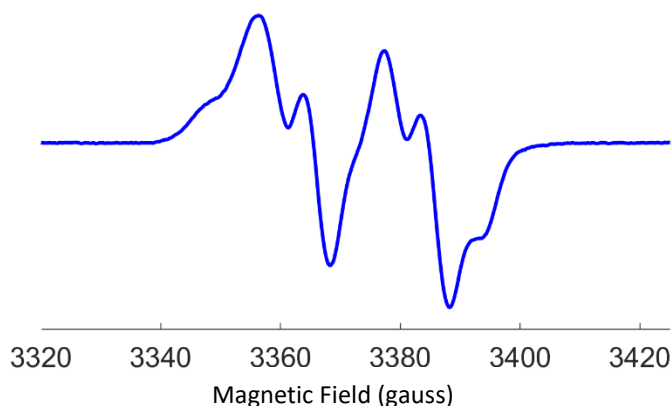


Figure 14. CW-EPR spectrum of the β-Fe^{III}/Fe^{III}-Y• cofactor of *Bp* β. Spectrometer conditions: Temperature 20 K, microwave frequency, 9.45 GHz; microwave power, 2 mW modulation frequency, 100 kHz; modulation amplitude, 10 G; scan time 60 s; time constant, 180 ms.

The second strategy for achieving the “subunit swap” involved the modification of the C-terminal tail of *Ct* β. Our hypothesis was that the 8-12 amino acid residues that follow the last redox active radical translocation residue in the small subunit (Y338 in *Ct*) were key for specific inter-subunit binding. Therefore, we created two variants of *Ct* β that mimic the C-terminus of *Bp* and *Mc* β (named *Ct*_2_*Bp* and *Ct*_2_*Mc*, respectively) with the hope of observing catalysis by reacting *Ct*_2_*Bp* with *Bp* α and *Ct*_2_*Mc* with *Mc* α. This strategy rested on the hypothesis that the only cause of not achieving inter-subunit reactivity in wild type enzymes was due to the lack

of association of the two subunits and that the only key residues responsible of the association follow Y338. Both of the variants of interest are speculated to be able to assemble the active cofactor β -Mn^{IV}/Fe^{III} due to a distinctive color change from colorless to orange upon the addition of Mn and Fe to β in the presence of O₂. However, neither the Ct_2_Bp variant with Bp α nor the Ct_2_Mc variant with Mc α showed any signs of activity. Interestingly, another variant that completely lacked the aforementioned tail (Ct β - Δ (339-346)), after successful activation with O₂ to form β -Mn^{IV}/Fe^{III}, and upon the reaction with wt α showed no CDP conversion to its deoxy-counterpart. In the light of these results we concluded that even though the final 8 C-terminal residues of Ct β are critical for subunit association, their change to mimic the Ia ortholog tails was not enough to achieve the subunit swap. Therefore, there must be other subunit binding or possibly RT related factors that we did not include in our hypothesis.

The third and final strategy we used to attempt the subunit swap was the acquisition of a new class Ic β ortholog whose respective α subunit is most similar to Bp α . At the time, the candidate we chose was from *Candidatus Liberibacter solanacearum* (Lso), a gram-negative, unculturable bacterium that is primarily spread by psyllid insect vectors.¹²⁷ It was of special interest to study the mechanism of its DNA synthesis, because the organism is a fast spreading potato and tomato pathogen.^{128, 129} Unfortunately, after obtaining the gene for the small subunit and overexpressing the protein in *E coli*, the β subunit was not stable in standard buffer conditions at 4 °C, did not show a color change upon the addition of Mn and Fe to β in the presence of O₂, nor was it active with Bp α . Taking these initial results into consideration we did not pursue this project any further.

We have also recently decided to try yet another tentative Ic β RNR for the inter-species subunit swapping. This time we chose the small subunit based on its similarity to the small subunit

of *Bp* (72% identity). Our candidate from *Salinisphaera hydrothermalis* (*Sh*) showed extremely poor activity with Class Ia *Bp* α (~2.8 turnovers per hour per β_2). However, the Mn/Fe reconstituted *Sh* β in tandem with *Mc* α were shown to be catalytically competent. Entire chapter III is dedicated to this remarkable result.

SUMMARY AND OUTLOOK

Characterization and Insight into the Branched Electron Relay Pathways of a Second Class Ic Ribonucleotide Reductase from *Gimesia maris*

The RNR from *Chlamydia trachomatis* has been the only established representative of the class Ic ribonucleotide reductases for over a decade now. Experts in the field of bioinorganic chemistry have brought to question the validity of the existence of the Ic subclass because it rests only on a sole member. In chapter 2, we show that the RNR from *Gimesia maris*, like the RNR from *Chlamydia trachomatis*, is a bona fide member of the subclass Ic RNR. Using EPR and Mössbauer spectroscopy, we were able to confirm that the RNR from *Gimesia maris* uses the β -Mn^{IV}/Fe^{III} as the active cofactor. Additionally, with a rate of reduction of $0.22\text{ s}^{-1}\beta^{-1}$ falling within an order of

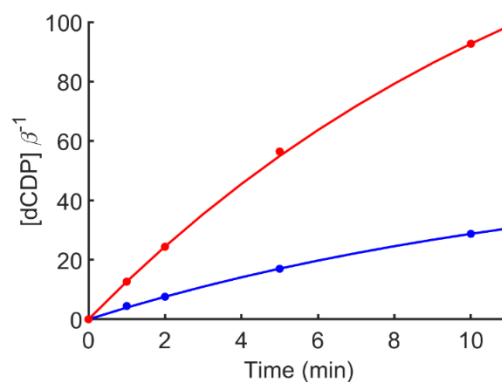


Figure 15. Reaction of the wt *Gm* β and *Gm* α (blue), and *Gm* β Y234F and *Gm* α (red). The exponential fits produced $0.07\text{ s}^{-1}\beta^{-1}$ rate of reaction for *Gm* β wt and $0.22\text{ s}^{-1}\beta^{-1}$ for the *Gm* β Y234F variant. Reaction conditions: $25\text{ }\mu\text{M}$ α_2 , $5\text{ }\mu\text{M}$ β_2 , 2 mM ATP, 1 mM CDP, 10 mM DTT, 10 mM MgCl₂ Reaction quenched with 2 M formic acid.

magnitude compared to other RNR rates,^{55, 104} we can now with great certainty add the RNR from *Gimesia maris* to the class Ic RNRs as a second member.

Across Species and Subclasses Ribonucleotide Reduction: Insight into the Multi-Step Radical Translocation Mechanism in class I RNRs

There are many β -RNR pairs that contain high sequence identity $\sim 60\%$, where one β belongs to a tentative class Ia and the other β belongs to a tentative class Ic RNR. In chapter 3, we were able to show that a class Ic β paired with a class Ia α can competently perform ribonucleotide reduction, and vice versa. To showcase this phenomenon, we have chosen the RNR from *Methylococcus capsulatus* (*Mc*) as the class Ia member and the RNR from *Salinisphaera hydrothermalis* (*Sh*) as the class Ic

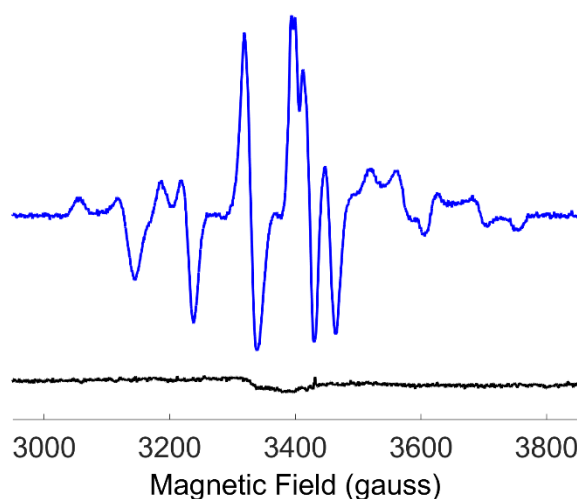


Figure 16. Field swept X-band CW-EPR spectrum of the *Sh* β -Mn^{III}/Fe^{III} RT product state generated in the presence of *Mc* α , DTT, ATP, and N₃UDP.

representative. Activity assays indicated a rate of reduction of $0.14 \text{ s}^{-1} \text{ Y}\cdot^{-1}$ when *Mc* β and *Sh* α were paired, while *Sh* β and *Mc* α pair was able to perform ribonucleotide reduction at a $0.53 \text{ min}^{-1} \text{ Mn}^{-1}$ rate. Additionally, we have established catalytic competency using EPR methods. Sample containing *Sh* β combined with *Mc* α in the presence of ATP, DTT and N₃UDP showed both the six-packet signal that reflects the presence of Mn nuclear spin ($I=5/2$) in the β -Mn^{III}/Fe^{III} as well as the nitrogen centered radical in *Mc* α . The control sample that lacked the substrate analog showed no EPR signals. One conclusion of this study implies that there were no co-adaptations in the α subunit of either class Ia or class Ic RNR that were required for the larger subunit to

accommodate a β subunit from a different subclass and organism. Therefore, while the β subunits have evolved to harbor a different active cofactor, the α subunits have not co-evolved. With this discovery, we could speculate that the well-studied,⁹⁰ intrinsic multi-step radical translocation mechanism that pertains to *E. coli* RNR most likely pertains all class I RNRs.

Direct Measurement of the Radical Translocation Distance in the Class I Ribonucleotide Reductase from *Chlamydia trachomatis*

In the *Ct* RNR, upon radical translocation, two EPR active, $S_{total} = 1/2$, species are created. One is the metal cofactor RT product state, β - Mn^{III}/Fe^{III} , in the smaller subunit, while the other species is the N^\bullet in the larger subunit. In this work,¹³⁰ in chapter 4, we show that the distance between the β - Mn^{III}/Fe^{III} cofactor in β and the nitrogen centered radical in α is 43 ± 1 Å. We achieved this result by using an advanced EPR methods, the double electron-electron resonance experiments (DEER). We have also paired these experimental data with molecular mechanics calculations which supported our experimentally obtained distance. This study provided the first structural data on the *Ct* RNR holoenzyme complex and the first direct experimental measurement of the intra-subunit radical translocation distance in any class I RNR.

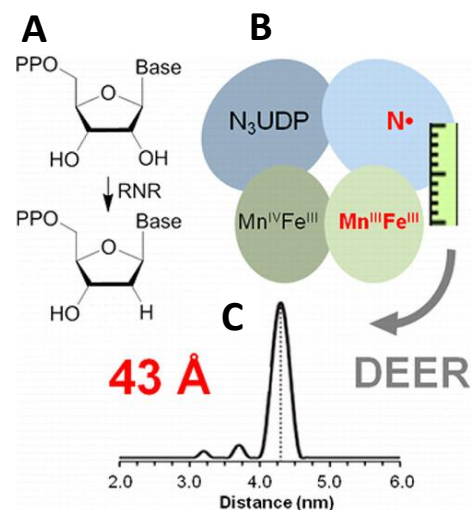


Figure 17. A) The general RNR reaction B) The *Ct* β dimer where one monomer $\alpha\beta$ pair has undergone RT and the Mn^{III}/Fe^{III} cofactor is formed in β along with N^\bullet in α . C) Tikhonov regularization resulting from the time domain processed DEER signal and the resulting distance.

Spectroscopic and Computational Analysis of Proton Transfer in the Turnover-initiating Transient Reduction of the β -Mn^{IV}/Fe^{III} Cofactor of a Class Ic Ribonucleotide Reductase

In chapter 5, using HYSCORE spectroscopy, we were able to determine that there is at least a single bridging oxygen that is protonated in the *Ct* RNR β -Mn^{III}/Fe^{III} cofactor upon radical translocation. Using continuous wave power saturation EPR methods we were also able to determine the exchange J coupling between the manganese and iron in this cofactor. A strong J coupling of ($\sim 100\text{ cm}^{-1}$) was indicative that there was only an oxo bridging ligand between the two metals.

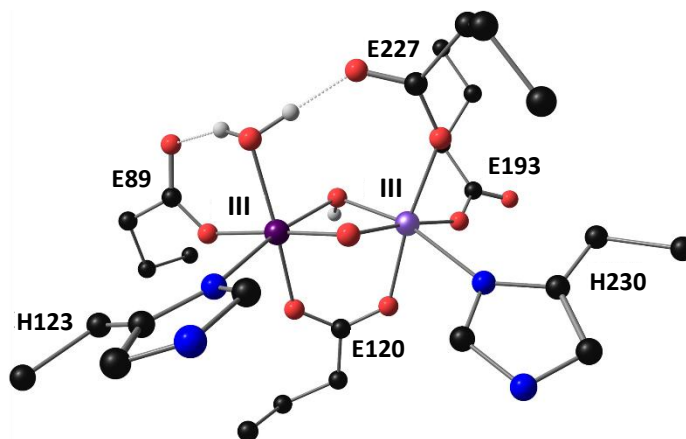


Figure 18. Proposed structure of the RT product state of the metal cofactor in the *Ct* RNR β subunit, β -Mn^{III}/Fe^{III}.

Relatively weak ^1H coupling determined by ENDOR spectroscopy, combined with DFT calculations indicated that the terminal ligand was best described as water with the two protons hydrogen bonded to E89 and E227. With all these results combined, we were able to determine that the RT product state of the dimetal β cofactor from *Chlamydia trachomatis* contains a H_2O -Mn(III)(μ -oxo)(μ -hydroxo)Fe(III) core structure. The comparison of this structure to the core structure of the active cofactor β -Mn^{IV}/Fe^{III} suggests that upon radical translocation and the reduction of the manganese, a proton is transferred onto the terminal hydroxide on site 1. While we have identified the proton acceptor, the proton donor is yet to be determined. From the crystal structure solved (RSCB id: 4D8F) there are no obvious visible proton donor candidates. This could mean that the conformationally gated radical transfer could possibly involve a significant

restructuring of the space surrounding the Mn/Fe cofactor upon the addition of α , the binding of substrate and the allosteric effector.

REFERENCES

1. Nordlund, P.; Reichard, P., Ribonucleotide reductases. *Annu Rev Biochem* **2006**, 75, 681-706.
2. Lin, A. N.; Ashley, G. W.; Stubbe, J., Location of the redox-active thiols of ribonucleotide reductase: sequence similarity between the Escherichia coli and Lactobacillus leichmannii enzymes. *Biochemistry-Us* **1987**, 26 (22), 6905-9.
3. Mao, S. S.; Holler, T. P.; Yu, G. X.; Bollinger, J. M., Jr.; Booker, S.; Johnston, M. I.; Stubbe, J., A model for the role of multiple cysteine residues involved in ribonucleotide reduction: amazing and still confusing. *Biochemistry-Us* **1992**, 31 (40), 9733-43.
4. Mao, S. S.; Johnston, M. I.; Bollinger, J. M.; Stubbe, J., Mechanism-based inhibition of a mutant Escherichia coli ribonucleotide reductase (cysteine-225----serine) by its substrate CDP. *Proc Natl Acad Sci U S A* **1989**, 86 (5), 1485-9.
5. Eklund, H.; Uhlin, U.; Farnegardh, M.; Logan, D. T.; Nordlund, P., Structure and function of the radical enzyme ribonucleotide reductase. *Prog Biophys Mol Biol* **2001**, 77 (3), 177-268.
6. Stubbe, J.; Ackles, D., On the mechanism of ribonucleoside diphosphate reductase from Escherichia coli. Evidence for 3'-C--H bond cleavage. *J Biol Chem* **1980**, 255 (17), 8027-30.
7. Eriksson, M.; Uhlin, U.; Ramaswamy, S.; Ekberg, M.; Regnstrom, K.; Sjoberg, B. M.; Eklund, H., Binding of allosteric effectors to ribonucleotide reductase protein R1: reduction of active-site cysteines promotes substrate binding. *Structure* **1997**, 5 (8), 1077-92.
8. Becker, A.; Fritz-Wolf, K.; Kabsch, W.; Knappe, J.; Schultz, S.; Volker Wagner, A. F., Structure and mechanism of the glycyl radical enzyme pyruvate formate-lyase. *Nature structural biology* **1999**, 6 (10), 969-75.

9. Leppanen, V. M.; Merckel, M. C.; Ollis, D. L.; Wong, K. K.; Kozarich, J. W.; Goldman, A., Pyruvate formate lyase is structurally homologous to type I ribonucleotide reductase. *Structure* **1999**, 7 (7), 733-44.
10. Uhlin, U.; Eklund, H., Structure of ribonucleotide reductase protein R1. *Nature* **1994**, 370 (6490), 533-9.
11. Stubbe, J.; van Der Donk, W. A., Protein Radicals in Enzyme Catalysis. *Chem Rev* **1998**, 98 (2), 705-762.
12. Reichard, P.; Estborn, B., Utilization of desoxyribosides in the synthesis of polynucleotides. *J Biol Chem* **1951**, 188 (2), 839-46.
13. Hammarsten, E.; Reichard, P.; Saluste, E., Pyrimidine Nucleosides as Precursors of Ribonucleic Acid (Pna) Pyrimidines. *Acta Chem Scand* **1949**, 3 (4), 432-433.
14. Reichard, P.; Ehrenberg, A., Ribonucleotide Reductase - a Radical Enzyme. *Science* **1983**, 221 (4610), 514-519.
15. Atkin, C. L.; Thelander, L.; Reichard, P.; Lang, G., Iron and Free-Radical in Ribonucleotide Reductase - Exchange of Iron and Mossbauer-Spectroscopy of Protein-B2 Subunit of Escherichia-Coli Enzyme. *J Biol Chem* **1973**, 248 (21), 7464-7472.
16. Nordlund, P.; Sjöberg, B. M.; Eklund, H., 3-Dimensional Structure of the Free-Radical Protein of Ribonucleotide Reductase. *Nature* **1990**, 345 (6276), 593-598.
17. Stubbe, J., Di-iron-tyrosyl radical ribonucleotide reductases. *Curr Opin Chem Biol* **2003**, 7 (2), 183-188.
18. Cotruvo, J. A.; Stubbe, J., NrdI, a flavodoxin involved in maintenance of the diferric-tyrosyl radical cofactor in Escherichia coli class Ib ribonucleotide reductase. *P Natl Acad Sci USA* **2008**, 105 (38), 14383-14388.

19. Cotruvo, J. A.; Stubbe, J., Mechanism of assembly of the dimanganese(III)-tyrosyl radical cofactor of Escherichia coli class Ib ribonucleotide reductase. *Abstr Pap Am Chem S* **2010**, 240.
20. Cotruvo, J. A.; Stubbe, J., An Active Dimanganese(III)-Tyrosyl Radical Cofactor in Escherichia coli Class Ib Ribonucleotide Reductase. *Biochemistry-Us* **2010**, 49 (6), 1297-1309.
21. Cox, N.; Ogata, H.; Stolle, P.; Reijerse, E.; Auling, G.; Lubitz, W., A Tyrosyl-Dimanganese Coupled Spin System is the Native Metalloradical Cofactor of the R2F Subunit of the Ribonucleotide Reductase of Corynebacterium ammoniagenes. *J Am Chem Soc* **2010**, 132 (32), 11197-11213.
22. Rozman Grinberg, I.; Lundin, D.; Hasan, M.; Crona, M.; Jonna, V. R.; Loderer, C.; Sahlin, M.; Markova, N.; Borovok, I.; Berggren, G.; Hofer, A.; Logan, D. T.; Sjoberg, B. M., Novel ATP-cone-driven allosteric regulation of ribonucleotide reductase via the radical-generating subunit. *Elife* **2018**, 7.
23. Rose, H. R.; Ghosh, M. K.; Maggiolo, A. O.; Pollock, C. J.; Blaes, E. J.; Hajj, V.; Wei, Y.; Rajakovich, L. J.; Chang, W. C.; Han, Y.; Hajj, M.; Krebs, C.; Silakov, A.; Pandelia, M. E.; Bollinger, J. M., Jr.; Boal, A. K., Structural Basis for Superoxide Activation of Flavobacterium johnsoniae Class I Ribonucleotide Reductase and for Radical Initiation by Its Dimanganese Cofactor. *Biochemistry-Us* **2018**.
24. Blaes, E. J.; Palowitch, G. M.; Hu, K.; Kim, A. J.; Rose, H. R.; Alapati, R.; Lougee, M. G.; Kim, H. J.; Taguchi, A. T.; Tan, K. O.; Laremore, T. N.; Griffin, R. G.; Krebs, C.; Matthews, M. L.; Silakov, A.; Bollinger, J. M., Jr.; Allen, B. D.; Boal, A. K., Metal-free class Ie ribonucleotide reductase from pathogens initiates catalysis with a tyrosine-derived dihydroxyphenylalanine radical. *Proc Natl Acad Sci U S A* **2018**, 115 (40), 10022-10027.

25. Vivek Srinivas, H. L., Daniel Lundin, Yuri Kutin, Margareta Sahlin, Michael Lerche, Jürgen Eirich, Rui Branca, Nicholas Cox, Britt-Marie Sjöberg, Martin Högbom, Metal-independent ribonucleotide reduction powered by a DOPA radical in Mycoplasma pathogens. *BiorXiv* **2018**, preprint.
26. Lawrence, C. C.; Stubbe, J., The function of adenosylcobalamin in the mechanism of ribonucleoside triphosphate reductase from *Lactobacillus leichmannii*. *Curr Opin Chem Biol* **1998**, 2 (5), 650-655.
27. Panagou, D.; Blakeley, R. L.; Orr, M. D.; Dunstone, J. R., Cobamides and Ribonucleotide Reduction .9. Monomeric, Allosteric Enzyme with a Single Polypeptide Chain - Ribonucleotide Reductase of *Lactobacillus-Leichmannii*. *Biochemistry-U.S* **1972**, 11 (12), 2378-&.
28. Gleason, F. K.; Frick, T. D., Adenosylcobalamin-Dependent Ribonucleotide Reductase from the Blue-Green-Alga, *Anabaena Sp* - Purification and Partial Characterization. *J Biol Chem* **1980**, 255 (16), 7728-7733.
29. Eliasson, R.; Pontis, E.; Jordan, A.; Reichard, P., Allosteric control of three B-12-dependent (class II) ribonucleotide reductases - Implications for the evolution of ribonucleotide reduction. *J Biol Chem* **1999**, 274 (11), 7182-7189.
30. Booker, S.; Licht, S.; Broderick, J.; Stubbe, J., Coenzyme-B-12 Dependent Ribonucleotide Reductase - Evidence for the Participation of 5 Cysteine Residues in Ribonucleotide Reduction. *Biochemistry-U.S* **1994**, 33 (42), 12676-12685.
31. Stubbe, J. A.; Ackles, D., On the Mechanism of Ribonucleoside Diphosphate Reductase from *Escherichia-Coli* - Evidence for 3'-C-H Bond-Cleavage. *J Biol Chem* **1980**, 255 (17), 8027-8030.

32. Barlow, T., Evidence for a New Ribonucleotide Reductase in Anaerobic Escherichia-Coli. *Biochemical and biophysical research communications* **1988**, 155 (2), 747-753.
33. Gambarelli, S.; Luttringer, F.; Padovani, D.; Mulliez, E.; Fontecave, M., Activation of the anaerobic ribonucleotide reductase by S-adenosylmethionine. *Chembiochem* **2005**, 6 (11), 1960-1962.
34. Logan, D. T.; Andersson, J.; Sjoberg, B. M.; Nordlund, P., A glycyl radical site in the crystal structure of a class III ribonucleotide reductase. *Science* **1999**, 283 (5407), 1499-1504.
35. King, D. S.; Reichard, P., Mass-Spectrometric Determination of the Radical Scission Site in the Anaerobic Ribonucleotide Reductase of Escherichia-Coli. *Biochemical and biophysical research communications* **1995**, 206 (2), 731-735.
36. Bianchi, V.; Eliasson, R.; Fontecave, M.; Mulliez, E.; Hoover, D. M.; Matthews, R. G.; Reichard, P., Flavodoxin is required for the activation of the anaerobic ribonucleotide reductase. *Biochemical and biophysical research communications* **1993**, 197 (2), 792-7.
37. Mulliez, E.; Ollagnier, S.; Fontecave, M.; Eliasson, R.; Reichard, P., Formate Is the Hydrogen Donor for the Anaerobic Ribonucleotide Reductase from Escherichia-Coli. *P Natl Acad Sci USA* **1995**, 92 (19), 8759-8762.
38. Lammers, M.; Follmann, H., Deoxyribonucleotide Biosynthesis in Yeast (*Saccharomyces Cerevisiae*) a Ribonucleotide Reductase System of Sufficient Activity for DNA-Synthesis. *Eur J Biochem* **1984**, 140 (2), 281-287.
39. Perlstein, D. L.; Ge, J.; Nguyen, H. T.; Stubbe, J., Ribonucleotide reductase from yeast: Diiron cluster assembly. *Faseb J* **2000**, 14 (8), A1393-A1393.
40. Fujioka, S.; Silbers, R., Purification and Properties of Ribonucleotide Reductase from Leukemic Mouse Spleen. *J Biol Chem* **1970**, 245 (7), 1688-&.

41. Strand, K. R.; Karlsten, S.; Kolberg, M.; Rohr, A. K.; Gorbitz, C. H.; Andersson, K. K., Crystal structural studies of changes in the native dinuclear iron center of ribonucleotide reductase protein R2 from mouse. *J Biol Chem* **2004**, 279 (45), 46794-46801.
42. Fujioka, S.; Silber, R., Ribonucleotide Reductase in Human Bone Marrow - Lack of Stimulation by 5'-Deoxyadenosyl B12. *Biochemical and biophysical research communications* **1969**, 35 (5), 759-&.
43. Smith, P.; Zhou, B. S.; Ho, N.; Yuan, Y. C.; Su, L.; Tsai, S. C.; Yen, Y., 2.6 angstrom X-ray Crystal Structure of Human p53R2, a p53-Inducible Ribonucleotide Reductase. *Biochemistry-Us* **2009**, 48 (46), 11134-11141.
44. Uhlin, U.; Eklund, H., Structure of Ribonucleotide Reductase Protein R1. *Nature* **1994**, 370 (6490), 533-539.
45. Nordlund, P.; Eklund, H., Structure and Function of the Escherichia-Coli Ribonucleotide Reductase Protein R2. *Journal of molecular biology* **1993**, 232 (1), 123-164.
46. Seyedsayamdost, M. R.; Chan, C. T. Y.; Mugnaini, V.; Stubbe, J.; Bennati, M., PELDOR spectroscopy with DOPA-beta 2 and NH2Y-alpha 2s: Distance measurements between residues involved in the radical propagation pathway of E-coli ribonucleotide reductase. *J Am Chem Soc* **2007**, 129 (51), 15748-+.
47. Kananmascheff, M.; Lee, W.; Nick, T. U.; Stubbe, J.; Bennati, M., Radical transfer in E. coli ribonucleotide reductase: a NH2Y731/R(411)A-alpha mutant unmask a new conformation of the pathway residue 731. *Chem Sci* **2016**, 7 (3), 2170-2178.
48. Jonna, V. R.; Crona, M.; Rofougaran, R.; Lundin, D.; Johansson, S.; Brannstrom, K.; Sjoberg, B. M.; Hofer, A., Diversity in Overall Activity Regulation of Ribonucleotide Reductase. *J Biol Chem* **2015**, 290 (28), 17339-17348.

49. Arts, E. J.; Marois, J. P.; Gu, Z. X.; LeGrice, S. F. J.; Wainberg, M. A., Effects of 3'-deoxynucleoside 5'-triphosphate concentrations on chain termination by nucleoside analogs during human immunodeficiency virus type 1 reverse transcription of minus-strand strong-stop DNA. *J Virol* **1996**, *70* (2), 712-720.
50. Eriksson, S.; Thelander, L.; Akerman, M., Allosteric Regulation of Calf Thymus Ribonucleoside Diphosphate Reductase. *Biochemistry-U.S.* **1979**, *18* (14), 2948-2952.
51. Hogbom, M.; Galander, M.; Andersson, M.; Kolberg, M.; Hofbauer, W.; Lassmann, G.; Nordlund, P.; Lendzian, F., Displacement of the tyrosyl radical cofactor in ribonucleotide reductase obtained by single-crystal high-field EPR and 1.4-angstrom x-ray data. *P Natl Acad Sci USA* **2003**, *100* (6), 3209-3214.
52. Bennati, M.; Weber, A.; Antonic, J.; Perlstein, D. L.; Robblee, J.; Stubbe, J. A., Pulsed ELDOR spectroscopy measures the distance between the two tyrosyl radicals in the R2 subunit of the E-coli ribonucleotide reductase. *J Am Chem Soc* **2003**, *125* (49), 14988-14989.
53. Bennati, M.; Robblee, J. H.; Mugnaini, V.; Stubbe, J.; Freed, J. H.; Borbat, P., EPR distance measurements support a model for long-range radical initiation in E.coli ribonucleotide reductase. *J Am Chem Soc* **2005**, *127* (43), 15014-15015.
54. Jordan, A.; Reichard, P., Ribonucleotide reductases. *Annu Rev Biochem* **1998**, *67*, 71-98.
55. Stubbe, J.; Nocera, D. G.; Yee, C. S.; Chang, M. C. Y., Radical initiation in the class I ribonucleotide reductase: Long-range proton-coupled electron transfer? *Chem Rev* **2003**, *103* (6), 2167-2201.
56. Ekberg, M.; Sahlin, M.; Eriksson, M.; Sjoberg, B. M., Two conserved tyrosine residues in protein R1 participate in an intermolecular electron transfer in ribonucleotide reductase. *J Biol Chem* **1996**, *271* (34), 20655-20659.

57. Ekberg, M.; Potsch, S.; Sandin, E.; Thunnissen, M.; Nordlund, P.; Sahlin, M.; Sjoberg, B. M., Preserved catalytic activity in an engineered ribonucleotide reductase R2 protein with a nonphysiological radical transfer pathway - The importance of hydrogen bond connections between the participating residues. *J Biol Chem* **1998**, 273 (33), 21003-21008.
58. Rova, U.; Goodtzova, K.; Ingemarson, R.; Behravan, G.; Graslund, A.; Thelander, L., Evidence by Site-Directed Mutagenesis Supports Long-Range Electron-Transfer in Mouse Ribonucleotide Reductase. *Biochemistry-Us* **1995**, 34 (13), 4267-4275.
59. Rova, U.; Adrait, A.; Potsch, S.; Graslund, A.; Thelander, L., Evidence by mutagenesis that Tyr(370) of the mouse ribonucleotide reductase R2 protein is the connecting link in the intersubunit radical transfer pathway. *J Biol Chem* **1999**, 274 (34), 23746-23751.
60. Bollinger, J. M.; Tong, W. H.; Ravi, N.; Huynh, B. H.; Edmondson, D. E.; Stubbe, J., Mechanism of Assembly of the Tyrosyl Radical-Diiron(III) Cofactor of Escherichia-Coli Ribonucleotide Reductase .2. Kinetics of the Excess Fe²⁺ Reaction by Optical, Epr, and Mossbauer Spectroscopies. *J Am Chem Soc* **1994**, 116 (18), 8015-8023.
61. Seyedsayamdost, M. R.; Yee, C. S.; Reece, S. Y.; Nocera, D. G.; Stubbe, J., pH rate profiles of FnY356-R2s (n=2, 3, 4) in Escherichia coli ribonucleotide reductase: Evidence that Y-356 is a redox-active amino acid along the radical propagation pathway. *J Am Chem Soc* **2006**, 128 (5), 1562-1568.
62. Yee, C. S.; Seyedsayamdost, M. R.; Chang, M. C. Y.; Nocera, D. G.; Stubbe, J., Generation of the R2 subunit of ribonucleotide reductase by intein chemistry: Insertion of 3-nitrotyrosine at residue 356 as a probe of the radical initiation process. *Biochemistry-Us* **2003**, 42 (49), 14541-14552.

63. Yee, C. S.; Chang, M. C. Y.; Ge, J.; Nocera, D. G.; Stubbe, J., 2,3-difluorotyrosine at position 356 of ribonucleotide reductase R2: A probe of long-range proton-coupled electron transfer. *J Am Chem Soc* **2003**, *125* (35), 10506-10507.
64. Bollinger, J. M.; Krebs, C., Stalking intermediates in oxygen activation by iron enzymes: Motivation and method. *J Inorg Biochem* **2006**, *100* (4), 586-605.
65. Krebs, C.; Chen, S. X.; Baldwin, J.; Ley, B. A.; Patel, U.; Edmondson, D. E.; Huynh, B. H.; Bollinger, J. M., Mechanism of rapid electron transfer during oxygen activation in the R2 subunit of Escherichia coli ribonucleotide reductase. 2. Evidence for and consequences of blocked electron transfer in the W48F variant. *J Am Chem Soc* **2000**, *122* (49), 12207-12219.
66. Sturgeon, B. E.; Burdi, D.; Chen, S. X.; Huynh, B. H.; Edmondson, D. E.; Stubbe, J.; Hoffman, B. M., Reconsideration of X, the diiron intermediate formed during cofactor assembly in E-coli ribonucleotide reductase. *J Am Chem Soc* **1996**, *118* (32), 7551-7557.
67. Dassama, L. M. K.; Silakov, A.; Krest, C. M.; Calixto, J. C.; Krebs, C.; Bollinger, J. M.; Green, M. T., A 2.8 angstrom Fe-Fe Separation in the Fe-2(III/IV) Intermediate, X, from Escherichia coli Ribonucleotide Reductase. *J Am Chem Soc* **2013**, *135* (45), 16758-16761.
68. Lee, S. K.; Lipscomb, J. D., Oxygen activation catalyzed by methane monooxygenase hydroxylase component: proton delivery during the O-O bond cleavage steps. *Biochemistry-US* **1999**, *38* (14), 4423-32.
69. Niviere, V.; Fieschi, F.; Decout, J. L.; Fontecave, M., Is the NAD(P)H:flavin oxidoreductase from Escherichia coli a member of the ferredoxin-NADP⁺ reductase family?. Evidence for the catalytic role of serine 49 residue. *J Biol Chem* **1996**, *271* (28), 16656-61.

70. Fieschi, F.; Niviere, V.; Frier, C.; Decout, J. L.; Fontecave, M., The mechanism and substrate specificity of the NADPH:flavin oxidoreductase from *Escherichia coli*. *J Biol Chem* **1995**, *270* (51), 30392-400.
71. Spyrou, G.; Haggard-Ljungquist, E.; Krook, M.; Jornvall, H.; Nilsson, E.; Reichard, P., Characterization of the flavin reductase gene (*fre*) of *Escherichia coli* and construction of a plasmid for overproduction of the enzyme. *J Bacteriol* **1991**, *173* (12), 3673-9.
72. Wu, C. H.; Jiang, W.; Krebs, C.; Stubbe, J., YfaE, a ferredoxin involved in diferric-tyrosyl radical maintenance in *Escherichia coli* ribonucleotide reductase. *Biochemistry-Us* **2007**, *46* (41), 11577-88.
73. Climent, I.; Sjoberg, B. M.; Huang, C. Y., Carboxyl-Terminal Peptides as Probes for *Escherichia-Coli* Ribonucleotide Reductase Subunit Interaction - Kinetic-Analysis of Inhibition Studies. *Biochemistry-Us* **1991**, *30* (21), 5164-5171.
74. Fisher, A.; Yang, F. D.; Rubin, H.; Cooperman, B. S., R2 C-Terminal Peptide Inhibition of Mammalian and Yeast Ribonucleotide Reductase. *J Med Chem* **1993**, *36* (24), 3859-3862.
75. Karlsson, M.; Sahlin, M.; Sjoberg, B. M., *Escherichia-Coli* Ribonucleotide Reductase - Radical Susceptibility to Hydroxyurea Is Dependent on the Regulatory State of the Enzyme. *J Biol Chem* **1992**, *267* (18), 12622-12626.
76. Jiang, W.; Xie, J. J.; Varano, P. T.; Krebs, C.; Bollinger, J. M., Two Distinct Mechanisms of Inactivation of the Class Ic Ribonucleotide Reductase from *Chlamydia trachomatis* by Hydroxyurea: Implications for the Protein Gating of Intersubunit Electron Transfer. *Biochemistry-Us* **2010**, *49* (25), 5340-5349.

77. Sjöberg, B. M.; Graslund, A.; Eckstein, F., A Substrate Radical Intermediate in the Reaction between Ribonucleotide Reductase from *Escherichia-Coli* and 2'-Azido-2'-Deoxynucleoside Diphosphates. *J Biol Chem* **1983**, 258 (13), 8060-8067.
78. Thelander, L.; Larsson, B., Active-Site of Ribonucleoside Diphosphate Reductase from *Escherichia-Coli* - Inactivation of Enzyme by 2'-Substituted Ribonucleoside Diphosphates. *J Biol Chem* **1976**, 251 (5), 1398-1405.
79. van der Donk, W. A.; Gerfen, G. J.; Stubbe, J. A., Direct EPR spectroscopic evidence for an allylic radical generated from (E)-2'-fluoromethylene-2'-deoxycytidine 5'-diphosphate by *E. coli* ribonucleotide reductase. *J Am Chem Soc* **1998**, 120 (17), 4252-4253.
80. Gerfen, G. J.; van der Donk, W. A.; Yu, G. X.; McCarthy, J. R.; Jarvi, E. T.; Matthews, D. P.; Farrar, C.; Griffin, R. G.; Stubbe, J., Characterization of a substrate-derived radical detected during the inactivation of ribonucleotide reductase from *Escherichia coli* by 2'-fluoromethylene-2'-deoxycytidine 5'-diphosphate. *J Am Chem Soc* **1998**, 120 (16), 3823-3835.
81. Baker, C. H.; Banzon, J.; Bollinger, J. M.; Stubbe, J.; Samano, V.; Robins, M. J.; Lippert, B.; Jarvi, E.; Resvick, R., 2'-Deoxy-2'-Methylenecytidine and 2'-Deoxy-2',2'-Difluorocytidine 5'-Diphosphates - Potent Mechanism-Based Inhibitors of Ribonucleotide Reductase. *J Med Chem* **1991**, 34 (6), 1879-1884.
82. Wang, J.; Lohman, G. J. S.; Stubbe, J., Enhanced subunit interactions with gemcitabine-5'-diphosphate inhibit ribonucleotide reductases. *P Natl Acad Sci USA* **2007**, 104 (36), 14324-14329.
83. Fritscher, J.; Artin, E.; Wnuk, S.; Bar, G.; Robblee, J. H.; Kacprzak, S.; Kaupp, M.; Griffin, R. G.; Bennati, M.; Stubbe, J., Structure of the nitrogen-centered radical formed during

inactivation of E-coli ribonucleotide reductase by 2'-azido-2'-deoxyuridine-5'-diphosphate: Trapping of the 3'-ketonucleotide. *J Am Chem Soc* **2005**, *127* (21), 7729-7738.

84. Ator, M.; Salowe, S. P.; Stubbe, J.; Emptage, M. H.; Robins, M. J., 2'-Azido-2'-Deoxynucleotide Interaction with Escherichia-Coli Ribonucleotide Reductase - Generation of a New Radical Species. *J Am Chem Soc* **1984**, *106* (6), 1886-1887.

85. Salowe, S.; Bollinger, J. M.; Ator, M.; Stubbe, J.; Mccracken, J.; Peisach, J.; Samano, M. C.; Robins, M. J., Alternative Model for Mechanism-Based Inhibition of Escherichia-Coli Ribonucleotide Reductase by 2'-Azido-2'-Deoxyuridine 5'-Diphosphate. *Biochemistry-Us* **1993**, *32* (47), 12749-12760.

86. Sjoberg, B. M.; Karlsson, M.; Jornvall, H., Half-Site Reactivity of the Tyrosyl Radical of Ribonucleotide Reductase from Escherichia-Coli. *J Biol Chem* **1987**, *262* (20), 9736-9743.

87. Seyedsayamdost, M. R.; Xie, J.; Chan, C. T. Y.; Schultz, P. G.; Stubbe, J., Site-specific insertion of 3-aminotyrosine into subunit alpha 2 of E-coli ribonucleotide reductase: Direct evidence for involvement of Y-730 and Y-731 in radical propagation. *J Am Chem Soc* **2007**, *129* (48), 15060-15071.

88. Sahu, I. D.; McCarrick, R. M.; Lorigan, G. A., Use of Electron Paramagnetic Resonance To Solve Biochemical Problems. *Biochemistry-Us* **2013**, *52* (35), 5967-5984.

89. Jeschke, G., DEER Distance Measurements on Proteins. *Annu Rev Phys Chem* **2012**, *63*, 419-446.

90. Minnihan, E. C.; Nocera, D. G.; Stubbe, J., Reversible, Long-Range Radical Transfer in E-coli Class Ia Ribonucleotide Reductase. *Accounts Chem Res* **2013**, *46* (11), 2524-2535.

91. Zlateva, T.; Quaroni, L.; Que, L.; Stankovich, M. T., Redox studies of subunit interactivity in aerobic ribonucleotide reductase from Escherichia coli. *J Biol Chem* **2004**, *279* (18), 18742-7.

92. Bollinger, J. M., Personal Communication. *Penn State University, Chemistry Building* **2017**.
93. Worsdorfer, B.; Conner, D. A.; Yokoyama, K.; Livada, J.; Seyedsayamdost, M.; Jiang, W.; Silakov, A.; Stubbe, J.; Bollinger, J. M., Jr.; Krebs, C., Function of the diiron cluster of Escherichia coli class Ia ribonucleotide reductase in proton-coupled electron transfer. *J Am Chem Soc* **2013**, *135* (23), 8585-93.
94. Boal, A. K.; Cotruvo, J. A.; Stubbe, J.; Rosenzweig, A. C., Structural basis for activation of class Ib ribonucleotide reductase. *Abstr Pap Am Chem S* **2011**, *241*.
95. Zhang, Y.; Stubbe, J., Bacillus subtilis Class Ib Ribonucleotide Reductase Is a Dimanganese(III)-Tyrosyl Radical Enzyme. *Biochemistry-US* **2011**, *50* (25), 5615-5623.
96. Lofstad, M.; Gudim, I.; Hammerstad, M.; Rohr, A. K.; Hersleth, H. P., Activation of the Class Ib Ribonucleotide Reductase by a Flavodoxin Reductase in Bacillus cereus. *Biochemistry-US* **2016**, *55* (36), 4998-5001.
97. Roshick, C.; Iliffe-Lee, E. R.; McClarty, G., Cloning and characterization of ribonucleotide reductase from Chlamydia trachomatis. *J Biol Chem* **2000**, *275* (48), 38111-38119.
98. Hogbom, M.; Stenmark, P.; Voevodskaya, N.; McClarty, G.; Graslund, A.; Nordlund, P., The radical site in chlamydial ribonucleotide reductase defines a new R2 subclass. *Science* **2004**, *305* (5681), 245-248.
99. Voevodskaya, N.; Lendzian, F.; Graslund, A., A stable Fe-III-Fe-IV replacement of tyrosyl radical in a class I ribonucleotide reductase. *Biochemical and biophysical research communications* **2005**, *330* (4), 1213-1216.

100. Voevodskaya, N.; Narvaez, A. J.; Domkin, V.; Torrents, E.; Thelander, L.; Graslund, A., Chlamydial ribonucleotide reductase: Tyrosyl radical function in catalysis replaced by the Fe-III-Fe-IV cluster. *P Natl Acad Sci USA* **2006**, *103* (26), 9850-9854.
101. Jiang, W. FORMATION AND FUNCTION OF A NOVEL HETEROBINUCLEAR MN/FE REDOX COFACTOR IN RIBONUCLEOTIDE REDUCTASE FROM CHLAMYDIA TRACHOMATIS. Penn State, University Park, 2007.
102. Jiang, W.; Yun, D.; Saleh, L.; Bollinger, J. M.; Krebs, C., Formation and Function of the Manganese(IV)/Iron(III) Cofactor in Chlamydia trachomatis Ribonucleotide Reductase. *Biochemistry-Us* **2008**, *47* (52), 13736-13744.
103. Bollinger, J. M.; Jiang, W.; Green, M. T.; Krebs, C., The manganese(IV)/iron(III) cofactor of Chlamydia trachomatis ribonucleotide reductase: structure, assembly, radical initiation, and evolution. *Curr Opin Struc Biol* **2008**, *18* (6), 650-657.
104. Jiang, W.; Yun, D.; Saleh, L.; Barr, E. W.; Xing, G.; Hoffart, L. M.; Maslak, M. A.; Krebs, C.; Bollinger, J. M., A manganese(IV)/iron(III) cofactor in Chlamydia trachomatis ribonucleotide reductase. *Science* **2007**, *316* (5828), 1188-1191.
105. Jiang, W.; Bollinger, J. M.; Krebs, C., The active form of Chlamydia trachomatis ribonucleotide reductase R2 protein contains a heterodinuclear Mn(IV)/Fe(III) cluster with S=1 ground state. *J Am Chem Soc* **2007**, *129* (24), 7504-+.
106. Misra, H. P., Generation of Superoxide Free-Radical during Autoxidation of Thiols. *J Biol Chem* **1974**, *249* (7), 2151-2155.
107. Teutloff, C.; Schafer, K. O.; Sinnecker, S.; Barynin, V.; Bittl, R.; Wieghardt, K.; Lendzian, F.; Lubitz, W., High-field EPR investigations of (MnMnIV)-Mn-II and (MnMnIII)-Mn-

II states of dimanganese catalase and related model systems. *Magnetic Resonance in Chemistry* **2005**, *43*, S51-S64.

108. Amelia O Harrison, R. M. M., Shawn W Polson, K Eric Wommack, Reannotation of the ribonucleotide reductase in a cyanophage reveals life history strategies within the viroplankton. *BiorXiv* **2018**, *PREPRINT*.

109. Saleh, L. OXYGEN ACTIVATION AND ELECTRON TRANSFER IN CLASS I RIBONUCLEOTIDE REDUCTASE. Penn State University, University Park, PA, 16802, 2005.

110. Jiang, W.; Saleh, L.; Barr, E. W.; Xie, J. J.; Gardner, M. M.; Krebs, C.; Bollinger, J. M., Branched activation- and catalysis-specific pathways for electron relay to the manganese/iron cofactor in ribonucleotide reductase from *Chlamydia trachomatis*. *Biochemistry-Us* **2008**, *47* (33), 8477-8484.

111. Jiang, W.; Hoffart, L. M.; Krebs, C.; Bollinger, J. M., A manganese(IV)/iron(IV) intermediate in assembly of the manganese(IV)/iron(III) cofactor of *Chlamydia trachomatis* ribonucleotide reductase. *Biochemistry-Us* **2007**, *46* (30), 8709-8716.

112. Jiang, W.; Xie, J. J.; Norgaard, H.; Bollinger, J. M.; Krebs, C., Rapid and quantitative activation of *Chlamydia trachomatis* ribonucleotide reductase by hydrogen peroxide. *Biochemistry-Us* **2008**, *47* (15), 4477-4483.

113. Martinie, R. J.; Blaes, E. J.; Krebs, C.; Bollinger, J. M.; Silakov, A.; Pollock, C. J., Evidence for a Di-μ-oxo Diamond Core in the Mn(IV)/Fe(IV) Activation Intermediate of Ribonucleotide Reductase from *Chlamydia trachomatis*. *J Am Chem Soc* **2017**, *139* (5), 1950-1957.

114. Mims, W. B., Pulsed Endor Experiments. *Proc R Soc Lon Ser-A* **1965**, *283* (1395), 452-&.

115. Younker, J. M.; Krest, C. M.; Jiang, W.; Krebs, C.; Bollinger, J. M.; Green, M. T., Structural Analysis of the Mn(IV)/Fe(III) Cofactor of Chlamydia trachomatis Ribonucleotide Reductase by Extended X-ray Absorption Fine Structure Spectroscopy and Density Functional Theory Calculations. *J Am Chem Soc* **2008**, *130* (45), 15022-15027.
116. Dassama, L. M. K.; Krebs, C.; Bollinger, J. M.; Rosenzweig, A. C.; Boal, A. K., Structural Basis for Assembly of the Mn-IV/Fe-III Cofactor in the Class Ic Ribonucleotide Reductase from Chlamydia trachomatis. *Biochemistry-Us* **2013**, *52* (37), 6424-6436.
117. Dassama, L. M. K.; Boal, A. K.; Krebs, C.; Rosenzweig, A. C.; Bollinger, J. M., Evidence That the beta Subunit of Chlamydia trachomatis Ribonucleotide Reductase Is Active with the Manganese Ion of Its Manganese(IV)/Iron(III) Cofactor in Site 1. *J Am Chem Soc* **2012**, *134* (5), 2520-2523.
118. Andersson, C. S.; Ohlstrom, M.; Popovic-Bijelic, A.; Graslund, A.; Stenmark, P.; Hogbom, M., The manganese ion of the heterodinuclear Mn/Fe cofactor in Chlamydia trachomatis ribonucleotide reductase R2c is located at metal position 1. *J Am Chem Soc* **2012**, *134* (1), 123-5.
119. Kwak, Y.; Jiang, W.; Dassama, L. M. K.; Park, K.; Bell, C. B.; Liu, L. V.; Wong, S. D.; Saito, M.; Kobayashi, Y.; Kitao, S.; Seto, M.; Yoda, Y.; Alp, E. E.; Zhao, J. Y.; Bollinger, J. M.; Krebs, C.; Solomon, E. I., Geometric and Electronic Structure of the Mn(IV)Fe(III) Cofactor in Class Ic Ribonucleotide Reductase: Correlation to the Class Ia Binuclear Non-Heme Iron Enzyme. *J Am Chem Soc* **2013**, *135* (46), 17573-17584.
120. Zrelak, G. EXPANSION OF THE CLASS IC RIBONUCLEOTIDE REDUCTASE, CONVERSION OF A CLASS IC TO A CLASS IA, AND SUBUNIT SWAPPING BETWEEN THE CLASSES. Penn State University, University Park, PA, 16802, 2013.

121. Rose, H. R.; Maggiolo, A. O.; McBride, M. J.; Palowitch, G. M.; Pandelia, M. E.; Davis, K. M.; Yennawar, N. H.; Boal, A. K., Structures of Class Id Ribonucleotide Reductase Catalytic Subunits Reveal a Minimal Architecture for Deoxynucleotide Biosynthesis. *Biochemistry-US* **2019**, 58 (14), 1845-1860.
122. Oliynyk, M.; Samborsky, M.; Lester, J. B.; Mironenko, T.; Scott, N.; Dickens, S.; Haydock, S. F.; Leadlay, P. F., Complete genome sequence of the erythromycin-producing bacterium *Saccharopolyspora erythraea* NRRL23338. *Nat Biotechnol* **2007**, 25 (4), 447-453.
123. Jiang, W., Unpublished data. *The Pennsylvania State University, University Park, PA, 16801* **2007**.
124. Vandamme, P.; Holmes, B.; Vancanneyt, M.; Coenye, T.; Hoste, B.; Coopman, R.; Revets, H.; Lauwers, S.; Gillis, M.; Kersters, K.; Govan, J. R. W., Occurrence of multiple genomovars of *Burkholderia cepacia* in cystic fibrosis patients and proposal of *Burkholderia multivorans* sp. nov. *Int J Syst Bacteriol* **1997**, 47 (4), 1188-1200.
125. Vandamme, P.; Henry, D.; Coenye, T.; Nzula, S.; Vancanneyt, M.; LiPuma, J. J.; Speert, D. P.; Govan, J. R. W.; Mahenthiralingam, E., *Burkholderia anthina* sp nov and *Burkholderia pyrocinia*, two additional *Burkholderia cepacia* complex bacteria, may confound results of new molecular diagnostic tools. *Fems Immunol Med Mic* **2002**, 33 (2), 143-149.
126. Bollinger, J. M. On the chemical mechanism of assembly of the tyrosyl radical-dinuclear iron cluster cofactor of *E. coli* ribonucleotide reductase. Massachusetts Institute of Technology, Boston, MA, 1993.
127. Antolinez, C. A.; Fereres, A.; Moreno, A., Risk assessment of 'Candidatus *Liberibacter solanacearum*' transmission by the psyllids *Bactericera trigonica* and *B. tremblayi* from Apiaceae crops to potato. *Scientific reports* **2017**, 7, 45534.

128. Mas, F.; Vereijssen, J.; Suckling, D. M., Influence of the Pathogen Candidatus Liberibacter Solanacearum on Tomato Host Plant Volatiles and Psyllid Vector Settlement. *J Chem Ecol* **2014**, *40* (11-12), 1197-1202.
129. Rojas-Martinez, R. I.; Zavaleta-Mejia, E.; Ochoa-Martinez, D. L.; Alanis-Martinez, I.; Garcia-Tapia, F., Association of Candidatus Liberibacter Solanacearum with the Decline of Tomato (*Solanum Lycopersicum* L.). *J Plant Pathol* **2016**, *98* (2), 191-196.
130. Livada, J.; Martinie, R. J.; Dassama, L. M.; Krebs, C.; Bollinger, J. M., Jr.; Silakov, A., Direct Measurement of the Radical Translocation Distance in the Class I Ribonucleotide Reductase from *Chlamydia trachomatis*. *J Phys Chem B* **2015**, *119* (43), 13777-84.

Chapter 2:

Characterization and Insight into the Branched Electron Relay Pathways of a Second Class I-c Ribonucleotide Reductase from *Gimesia maris*

Characterization and Insight into the Branched Electron Relay Pathways of a Second Class I-c Ribonucleotide Reductase from *Gimesia maris*

Jovan Livada,^a Carsten Krebs,^{a,b} and J. Martin Bollinger, Jr.^{a,b}

Departments of ^aChemistry and of ^bBiochemistry and Molecular Biology, Pennsylvania State University, University Park, PA USA 16802.

ABSTRACT

In a class I ribonucleotide reductase (RNR), a one-electron oxidant in the β subunit oxidizes a cysteine $> 30 \text{ \AA}$ away in the α subunit, generating a thiyl radical that initiates turnover by abstracting the substrate's 3' hydrogen. The oxidant in the subclass c ortholog from *Chlamydia trachomatis* (*Ct*) is a $\beta\text{-Mn}^{\text{IV}}/\text{Fe}^{\text{III}}$ cluster; the other known subclasses use $\beta\text{-Mn}^{\text{IV}}/\text{Mn}^{\text{III}}$ clusters (d) and tyrosyl (a and b) or dihydroxyphenylalanyl (e) radicals. The *Ct* RNR cofactor assembles in β by binding of the divalent metal ions, reaction of the $\beta\text{-Mn}^{\text{II}}/\text{Fe}^{\text{II}}$ cluster with dioxygen, and decay of the resultant $\beta\text{-Mn}^{\text{IV}}/\text{Fe}^{\text{IV}}$ intermediate by univalent reduction of the Fe^{IV} site. Whereas multiple orthologs of each of the other subclasses have been characterized *in vitro*, the *Ct* enzyme remains the sole validated representative of subclass c. Importantly, neither the use of the Mn/Fe cofactor *in vivo* nor the physiological imperative for the deployment – uniquely in the Ic subclass – of two different transition metals has been established. Here, we have procured and characterized a second class Ic orthologue, from *Gimesia maris* (*Gm*), to begin to evaluate the generality of the *Ct*-RNR paradigm for the greater subset of hypothetical RNRs with the simple sequence hallmark of the Ic subclass – phenylalanine in place of tyrosine at the position that becomes the radical in the subclass a, b, and e orthologs. The results show that *Gm* RNR can indeed assemble a functional

β -Mn^{IV}/Fe^{III} cofactor by a process similar to the activation of *Ct* β . The surprising augmentation of activity upon removal of a subclass-specific tyrosine residue, shown in *Ct* β to be involved in reduction of the Fe^{IV} site during activation but superfluous for catalysis, sheds light on the nature of the electron-relay processes in activation and catalysis in members of the Ic subclass.

INTRODUCTION

Ribonucleotide Reductases (RNRs) use a free-radical mechanism to catalyze the life essential conversion of ribonucleotides to deoxyribonucleotides.¹ To our knowledge, these enzymes provide the sole source of deoxyribonucleotides required for DNA synthesis and repair. Ribonucleotide reduction is initiated by a transient cysteine thyl radical (C•) that abstracts a hydrogen atom (H•) from the C3' of the substrate.² RNRs are divided into three classes based on the way that the C• is generated. Class III RNRs, in their active form, use a stable glycyl radical³ to initiate ribonucleotide reduction while class II RNRs use adenosylcobalamin⁴ to initiate catalysis. Class I RNRs use an active oxidant in their second subunit annotated as β to initiate radical translocation (RT) and thus form the transient C•, which is generated in the larger, α subunit.⁵ Class I RNR β s are structurally ferritin-like proteins that traditionally bind two metals.⁶ These metals are oxidized when reacted with a form of oxygen to assemble the active state of β . Recently and independently, our group and Sjöberg's group have shown that metals might not be a requirement for the creation of the active state of β in class Ic RNRs.^{7,8}

Class I RNRs are quite diverse and are divided into five subclasses (a-e) based on the following four factors. One, the nature of the active oxidant; Y• in classes Ia and Ib, Mn^{IV} in classes Ic and Id, and DOPA• in class Ie. Two, the presence of a dimetal cluster which might comprise of

iron, manganese, both, or neither metals. Three, the oxidant necessary for activation which is either dioxygen or superoxide. And four, the necessity of an activase protein, NrdI. Class Ia RNR β s use a Fe_2 cluster that is oxidized by dioxygen to form a nearby stable tyrosyl radical with the active cofactor $\beta\text{-Fe}^{\text{III}}/\text{Fe}^{\text{III}}\text{-Y}\bullet$.⁹ Class Ib RNR β s also form a stable tyrosyl radical but use a Mn_2 cluster which is oxidized by superoxide to form the active $\beta\text{-Mn}^{\text{III}}/\text{Mn}^{\text{III}}\text{-Y}\bullet$ cofactor.¹⁰ This sub-class of RNRs also requires a flavin activase, NrdI, for the necessary conversion of dioxygen into superoxide. Class Ic RNR β s do not possess a stable amino acid radical in the active site, but instead, use a heterobinuclear metal center Mn/Fe, that when reacted with O_2 is oxidized into the active cofactor $\beta\text{-Mn}^{\text{IV}}/\text{Fe}^{\text{III}}$.¹¹ Class Id RNR β s require superoxide for activation of their Mn_2 dimetal center. Once oxidized, the metal center becomes the active $\beta\text{-Mn}^{\text{IV}}/\text{Mn}^{\text{III}}$ cofactor;¹² however, unlike class Ib RNR β s, the dimanganese cofactor can scavenge superoxide from solution and does not require an activase protein. Class Ie RNR β s use a DOPA \bullet to initiate ribonucleotide reduction. It is unclear whether class Ie RNR β s require metals for activation. Our group speculated that they use superoxide for both activation and post-translational conversion of a tyrosine residue into DOPA.

Except for class Ic RNRs, all other four class I RNR sub-classes contain several orthologs that were thoroughly characterized *in vitro*. Class Ia RNRs were discovered first¹³ with the most notable examples coming from *Escherichia coli* (*Ec*),¹⁴ *Homo sapiens*,¹⁵ *Mus musculus*,¹⁶ and *Saccharomyces cerevisiae*.¹⁷ Following the 2010 identification of the class Ib sub-class,¹⁸ five other Ib RNRs have been experimentally validated.¹⁹⁻²³ Class Id RNRs have representatives from *Flavobacterium Johnsoniae*,¹² *Leeuwenhoekiella blandensis*,²⁴ and *Actinobacillus ureae*.²⁵ In a span of just a few months, in the scientific literature, three class Ie RNR orthologs have been validated *in vitro*.^{7,8}

Class Ic RNRs use a cofactor that was identified in 2007 in the RNR from *Chlamydia trachomatis* (*Ct*).¹¹ Although genome sequences have revealed dozens of presumptive protein sequences that appear to be Ic RNR- β proteins, to date, only the *Ct* enzyme has been experimentally validated. In the past decade, there have been numerous (50+) publications elucidating the structures and mechanisms of activation and catalysis of the *Ct* RNR class Ic enzyme. To assess whether these mechanistic details pertain to the presumptive larger subclass, rather than to the single validated example, we sought to identify additional members of the subclass that might be amenable to *in vitro* characterization and validation of its *modus operandi*.

To increase our chances at success, we chose a tentative class Ic RNR from *Gimesia maris* whose β subunit is most similar to *Ct* β . All of the tentative class Ic RNR β sequences contain the phenylalanine residues at the position aligning with the radical harboring tyrosines of the class Ia/b RNRs and a glutamate in the place of the unique metal site 1 aspartate ligand of the Ia/b enzymes (e.g. E89 in *Ct* β versus D84 in *Ec* β).^{26, 27} A recently recognized distinct subclass of proteins, denoted R2-like ligand binding oxidases (R2lox),²⁸ also have the E/F dyad and can assemble a Mn/Fe cofactor. However, they lack the subunit interfacial tyrosine residue (Y338 in *Ct* RNR- β) that is essential for catalysis in all known class I RNR- β proteins, a characteristic that definitely distinguishes them from other possible class Ic RNR- β s. Thus the presence of the E/F dyad within protein sequences also possessing all other metal-ligand and radical-translocation-mediating residues may be necessary and sufficient to identify class Ic RNR- β enzymes²⁹. As a first step in evaluating this hypothesis, we sought to identify a second class Ic RNR member for *in vitro* characterization. The apparent class Ic RNR- β sequences, identified by virtue of their > 62% identity to the *Ct* RNR- β sequence and possession of the E/F dyad along with all other metal-ligand and radical-translocation residues cluster together with both other potential class Ic RNR-

βs and some class Ia homologs that all cluster with the minimum alignment score of 100. Upon increasing the minimum alignment score to 145, we unveiled a small, 39-member, sub-cluster that separates from the majority of other RNR gene sequences. This sub-cluster contains 18 genes that belong to the phylum Chlamydiae, 7 to the phylum Planctomycetes, 4 to the phylum Chloroflexi, 3 to the phylum Verrucomicrobia,

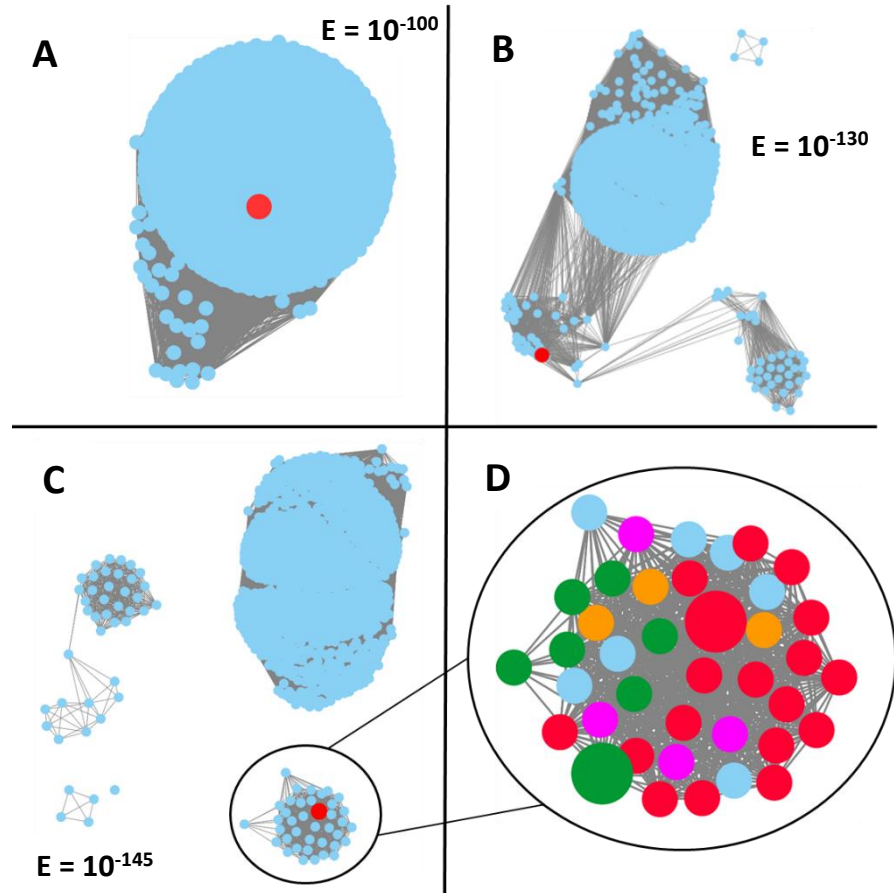


Figure 1. Gene cluster of tentative Class Ia and Class Ic RNR members that includes the RNR from *Chlamydia trachomatis* (large red circle) at the alignment score of 100 and higher (A). At the alignment score of 130 and above, two major sub-clusters separate from the majority, one containing mostly species from the Euryarchaeota phylum and the other mostly from the Chlamydiae phylum (B). At 145 and higher alignment scores, the Chlamydiae species are no longer connected to the majority cluster (C). This small sub-cluster only contains tentative class Ic RNR members and (D) contains 18 Chlamydiae species (red), 7 Planctomycetes species (green), 4 Chloroflexi species (magenta), 3 Verrucomicrobia species (orange), and a few other bacterial species (light blue). The large green circle represents the RNR from *Gimesia maris*.

and a few other bacterial phyla. To guard against the possibility that the RNR of interest might be an evolutionary vestige lacking *in vivo* functionality as a result of the deployment of a different RNR (class I,II, or III) by the host organism, we selected a candidate from an organism possessing only one set of genes for a single class I RNR ortholog and no apparent gene encoding either a class II or a class III RNR. We selected the hypothetical enzyme from *Gimesia maris* (Gm)³⁰

(previously known as *Planctomycetes maris*³¹), an obligatorily aerobic, mesophilic, Gram-negative, heterotroph found in varied aquatic locations around the US.³¹

Previous work on the *Ct* RNR system indicated that the class Ic RNRs are able to form the β -Mn^{II}/Fe^{II} cofactor in anoxic conditions.³² This cofactor in *Ct* β is able to react with dioxygen to form a β -Mn^{IV}/Fe^{IV} intermediate, observed by EPR spectroscopy.³³ The Fe^{IV} of this intermediate undergoes a univalent reduction via the activation electron relay that consists of two amino acids, W58, and the solvent exposed Y222 in *Ct* RNR β . This electron relay was tested via the reaction of the *Ct* β -Fe^{II}/Fe^{II} cofactor with O₂. This reaction monitored by stopped-flow in *Ct* β wt and in a few *Ct* β variants showed the formation of radical species that likely correspond to W58• and Y222•.³⁴ The product of activation, the active β -Mn^{IV}/Fe^{III} cofactor was readily analyzed via Mössbauer spectroscopy.³⁵ LC-MS analysis of activity assays was used to assess the kinetic competency of deoxyribonucleotide production.¹¹ Two other methods were also used to test RT from β into α . The first method involves the use of hydroxyurea (HU) to form the EPR active ($S_{total} = \frac{1}{2}$) cofactor product state β -Mn^{III}/Fe^{III}, in the presence of four other constituents - the α subunit, the effector - adenosine triphosphate (ATP), the disulfide reductant - dithiothreitol (DTT), and the substrate - cytidine diphosphate (CDP).¹¹ The second method also involves the aforementioned constituents except instead of HU and CDP, the substrate analog 2'-azido-2'-deoxynucleoside 5'-diphosphate (N₃UDP) is used to generate the RT cofactor product state β -Mn^{III}/Fe^{III}, as well as a nitrogen centered radical (N•) in α .³⁶ In both cases, the EPR detection of the RT product state β -Mn^{III}/Fe^{III} is indicative of both forward RT (and possible catalytic activity) and the nature of the active cofactor (likely β -Mn^{IV}/Fe^{III}).

In this work, we used rapid kinetic methods that include stopped-flow and freeze-quench techniques, as well as EPR and Mössbauer spectroscopies to assess both the activation process of

Gm β and the catalytic competency of the *Gm* $\alpha\beta$ complex. We found that *Gm* β , like *Ct* β , when anaerobically reconstituted with Mn^{II} and Fe^{II} , and reacted with dioxygen saturated buffer rapidly forms the $\beta\text{-Mn}^{\text{IV}}/\text{Fe}^{\text{IV}}$ intermediate. We were able to observe a pronounced half of sites reactivity in the activation process. We have also found that the second order rate constant in respect to the concentration of ascorbate to the decay of the $\beta\text{-Mn}^{\text{IV}}/\text{Fe}^{\text{IV}}$ intermediate is two orders of magnitude larger for *Gm* β then it is for *Ct* β . Mössbauer spectroscopy revealed signals that indicated the presence of the $\beta\text{-Mn}^{\text{IV}}/\text{Fe}^{\text{III}}$ β cofactor state. *Gm* RNR $\alpha\beta$ complex was able to facilitate multiple turnover deoxyribonucleotide production. Interestingly, the Y234F variant of *Gm* β showed to be ~3.4 times more active than the wild type β in ribonucleotide reduction. We also tested the activation electron pathway in *Gm* β by observing the $\beta\text{-Fe}^{\text{II}}/\text{Fe}^{\text{II}}$ cofactor reaction with O_2 via stopped-flow methods. Results indicated that the *Gm* $\beta\text{-Mn}^{\text{IV}}/\text{Fe}^{\text{IV}}$ cofactor is likely reduced by an electron that is shuttled from reductants in solution via W63 and Y234.

EXPERIMENTAL DETAILS

Overexpression and purification of the α and β RNR proteins

The vectors described above were inserted into the competent BL21(DE3) *E. coli* expression strain cells by heat shock for 45 seconds at 42 °C. The conditions used for the growth of *E. coli* cell strains were 37 °C in LB (Lysogeny broth) medium that contains 35 g/L tryptone, 20 g/L yeast extract, and 5g/L sodium chloride. The growth solution was after an autoclave procedure supplemented with 0.05 g/L kanamycin and grown to an OD_{600} of 0.7-1.0. The cells

were cooled rapidly to 4 °C by incubation on ice for 1 hour upon induced by addition of Isopropyl β -D-1-thiogalactopyranoside (IPTG) in the 50 μ M concentration for the α subunits and 200 μ M for the β subunits. The cells were grown for 16-24 h at 18 °C. The cells were harvested by centrifugation and the cell pellet was frozen in liquid N₂ and stored at -80 °C or immediately used for purification. A typical yield was ~ 6.5g of wet cell paste per liter of culture. If necessary, the frozen cell paste was allowed to thaw in Tris-HCl buffer (pH 7.6, 50 mM) containing 10 mM imidazole, 10% (v/v) glycerol and 0.25 mM PMSF. The cell paste that contained the vectors encoding the α subunits were additionally supplemented with 10 mM DTT. The cells were lysed via the Microfluidizer where the dissolved cell paste was exposed to 15000 kPA pressure 4 times. After lysis, the paste was centrifuged at 10000x g for 20 minutes. The supernatant was poured into a column containing Ni-NTA agarose (Qiagen or Biolabs). 300ml of wash buffer (20 mM imidazole) was applied to the column followed by ~50ml of elution buffer (250 mM imidazole) in order to elute the protein. The protein solution was further concentrated with the use of an ultrafiltration cell with a YM30 membrane (Amicon) to a concentration of ~1mM. All protein solutions were exchanged into 100mM HEPES buffer (pH 7.6, 10% glycerol) via dialysis. All protein solutions used to purify the α subunit contained additional 10 mM DTT to preserve the thiols in their reduced state. If further metal removal was necessary, the purified protein solution was further exposed to 10 mM EDTA for 4 hours and then dialyzed back in to the HEPES buffer that lacked EDTA.

Ferrozine chelating procedure for β subunits.

Typically, the β subunits were found to contain 0.7 and 0.05 equivalents of Fe and Mn respectively by ICP-AES analysis. While the manganese was removed via the EDTA chelation procedure described above the iron bound in the subunits was removed in the following way:³⁷ Fe was first reduced in an anoxic environment to ferrous by a ~1 hour incubation @ 25 °C in the presence of sodium hydrosulfite (60 mM) and methyl viologen (20 μ M). Methyl viologen turned a bright blue color upon reduction by sodium hydrosulfite. Ferrozine was added in about 300-fold stoichiometrical excess. After the addition of ferrozine, the solution turned bright purple. Following a two-hour period of aerobic incubation, the protein solution was poured into a column packed with Sephadex G-50 resin in order to separate the protein from both the “free ferrozine” and the $\text{Fe}^{\text{II}}\text{-(ferrozine)}_3$ complex. This procedure sometimes needed to be applied twice. ICP-AES analysis indicated that there was 0.1 equivalent of iron per β_2 . The protein was frozen at -80 °C for storage.

Protein concentration determination

Absorbance @ 280 nm was monitored by a UV-visible spectrometer (Agilent). Molar absorptivities of all protein solutions were calculated via the Expasy protparam³⁸ software and the method of Gill and von Hippel.³⁹

Activity assay details of β subunits in the presence of excess α

Substrate CDP with the m/z of 402 and the product of ribonucleotide reduction dCDP with the m/z of 386 were both eluted with a mobile phase of a gradient of pure acetonitrile (**1**) and 25 mM ammonium formate (pH 9) (**2**). The elution gradient was the following:

10% **1** for 3 minutes followed by 10-50% **1** over 3 minutes, followed by 50% **1** for another 3 minutes and finally 50-10% **1** over 7 minutes. Both the substrate and the product were detected and quantified by mass spectrometry via the electrospray ionization in the (-) ion mode. The peak ratio of dCDP/(CDP+dCDP) x InitialCDP was used to measure ribonucleotide reduction at one time point. Validate of these assays is presented in detail by Jiang.⁴⁰

Rapid freeze-quench Experiments

The instrument used in this study was from Update Instruments (Madison, MI) with a Model 715A computer controller. Minimum quenching time was ~20 milliseconds. More detail about the instrument and the procedure can be found in the reference by Ravi *et al.*⁹

EPR Spectroscopy

Field swept CW-EPR spectra were recorded on an ESP300 spectrometer (Bruker, Billerica, MA) equipped with an ER 041 MR Microwave Bridge and a 4102ST X-band resonator as described previously.⁴¹ The cryostat responsible for liquid He storage was from Oxford Instruments.

EPR Spectra Simulations

All simulations were performed via the program written by Stefan Stoll (University of Washington) Easyspin.⁴² EPR data analysis was performed using the software KazanViewer written by professor Alexey Silakov (Penn State University).⁴³

Mössbauer Spectroscopy

We recorded Mössbauer spectra on the WEB research (Edina, MN) spectrometers operating in the constant acceleration mode in a transmission geometry. Temperature was held constant at 4.2K. For spectra where the low field of 53 mT was applied, the sample was kept inside a SVT-400 dewar (Janis, Wilmington, MA). Digital Tesla meter (model 132D) was used to record the magnitudes of the static magnetic fields. The probe used in these experiments was a Hall probe LPT 130-20S (Group3 Technologies Inc., Auckland, NZ).

Mössbauer Spectra simulations

WMOSS (Web Research, Edina, MN) was used on Windows 10 with the Windows 95 compatibility mode setting. The fluctuation rate of the electron spin was considered slow in comparison to the ^{57}Fe Larmor frequency in all our simulations.

Sequence Similarity Networks (SSN)

InterPro Database (IPR000358) was used to construct the SSNs that belonged to the β subunit RNR superfamily. As of May 20th 2017, there were 14456 sequences in this family. The networks were generated via the Enzyme Similarity Tool (EFI-EST) web site.⁴⁴ The aforementioned family was used as input. All figures that concern SSN were generated via the Cytoscape software (v3.4.1).

Global kinetic simulations

Global kinetic simulations were all performed via the KinTek software package developed by Kenneth A. Johnson.

RESULTS AND DISCUSSION

ACTIVATION

To test whether the activation electron relay of *Ct* β is unique to *Ct* RNR or if this pathway is conserved in other class Ic RNRs, we examined the reaction of *Gm* β -Fe^{II} with dioxygen. The analogous reaction in wild type *Ct* β , monitored by stopped-flow UV-vis spectroscopy, showed a rapid formation of a tyrosine radical at 420 nm at 32 ms. The same reaction of the Y222F β variant did not show a formation of a Y•, but rather showed a formation of a tryptophan radical (W•) by exhibiting a rapid absorbance at ~ 550 nm. In this reaction, in addition to the formation of these amino acid radicals, *Ct* β also forms the β -Fe^{IV}/Fe^{III} intermediate analogous to **X** in *Ec*,⁴⁵ the **X_{Ct}** in *Ct* β RNR³⁴. It was therefore concluded that the *Ct* β diiron cofactor can receive electrons from various reductants in solution via the activation electron relay that involves the two nearby redox active residues in *Ct* β , W51 and Y222. *Gm* β contains the analogous potentially redox active residues, W63 and Y234. The UV-vis, stopped-flow monitored *Gm* β -Fe^{II} reaction with O₂ showed a broad absorption band ~300-500 nm that included a pronounced shoulder around 370 nm that is characteristic of **X**. The 370 nm signal absorption as a function of time was analyzed via the non-linear regression shown in eq. (1). The equation is characteristic of a system of two parallel, irreversible, first-order reactions:

$$A = A_0 + A_1(1 - e^{-k_1t}) + A_2(1 - e^{-k_2t}) \quad (1)$$

where A is the absorbance of interest, A₀ the absorbance at time zero, k_{1,2} the two rate constants of the irreversible first-order reactions, and A_{1,2} the amplitudes associated with the two rate constants, and t time. The fit yielded a formation rate of $13 \pm 4 \text{ s}^{-1}$ and a decay rate of $0.05 \text{ s}^{-1} \pm 0.02 \text{ s}^{-1}$, both comparable to previously published values of the intermediate **X**.⁴⁶ Previous studies that utilized freeze quench (FQ) EPR methods have characterized **X** with an isotropic EPR singlet at g = 2.0 with the CW-EPR spectrum width of ~60 gauss.⁴⁷ This signal was also observed in *Ct* RNR by FQ-EPR of the diiron form,⁴⁰ as well as by Mössbauer spectroscopy as a side product of the Mn/Fe activation.³³ We have observed an EPR signal spanning ~65 gauss and centered ~g = 2 by analyzing the sample made via a FQ experiment of the reaction of *Gm* β-Mn^{II}/Fe^{II} with O₂ saturated buffer (**Figure 3-B**). Based on the similar formation and decay rates of this species to **X** and **X_{Ct}** and based on the EPR spectrum observed, we assigned this intermediate to **X_{Gm}**. In the reaction of

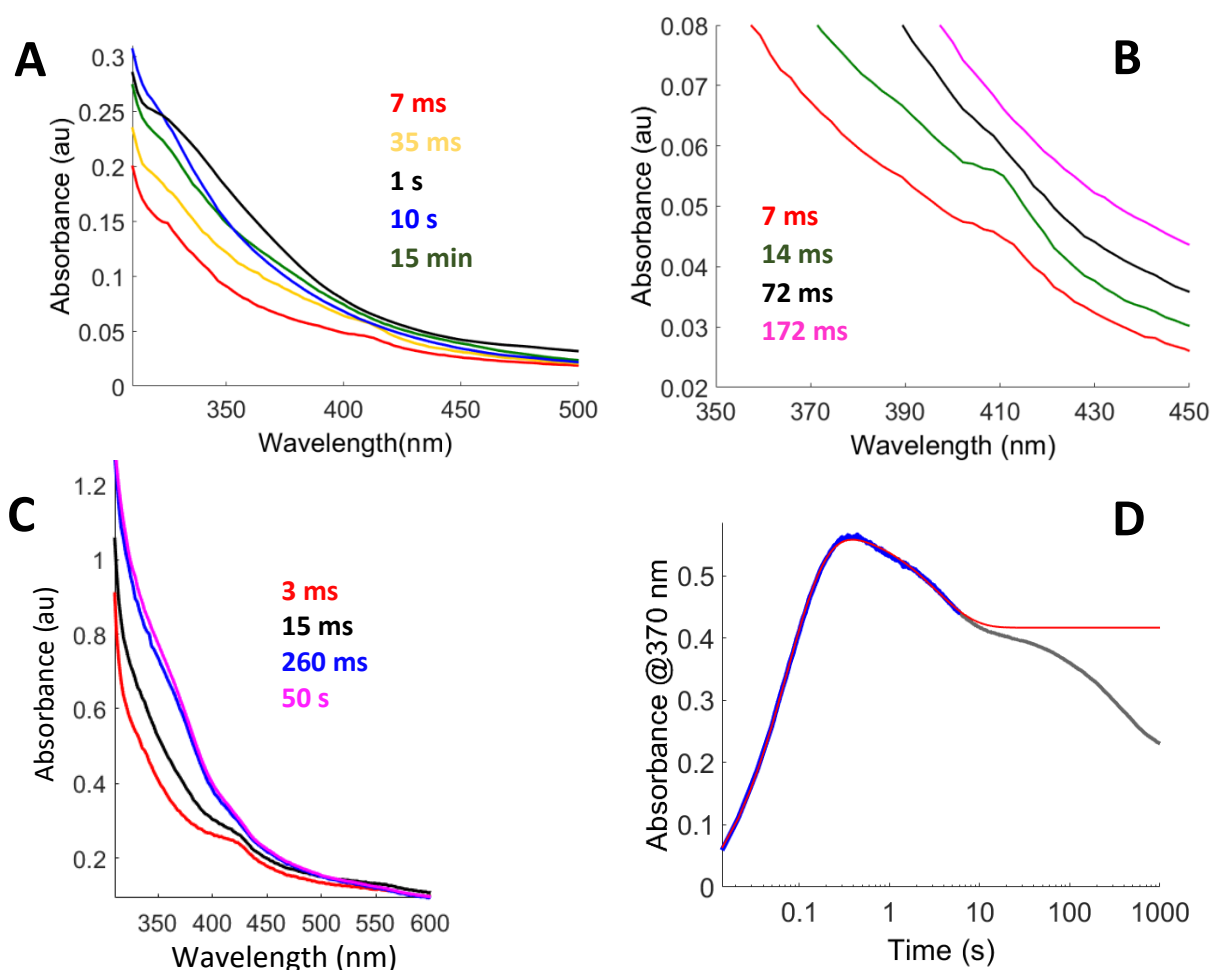


Figure 2. Time dependent UV-VIS absorption spectra of the β -Fe^{II}/Fe^{II} reaction with O₂ saturated buffer. In (A) the 300-450 nm wavelength range depicting the formation and decay of X_{Gm} . In (B) the 380-450 nm range showing the rapid formation and decay of a species centered ~410 nm likely corresponding to Y234•. The individual time traces have been shifted to avoid overlap and for visibility. In (C) the 300-600 nm wavelength range for the diiron reaction with the *Gm* β Y234F variant. In (D) absorbance at 370 nm vs. time. In gray the raw data, in blue the area used for fitting, and in red the kinetic simulation of the blue trace via eq. 1. Due to a second phase of decay at ~10 s the fitting was performed only on the data obtained prior to 10s. Reaction conditions: anaerobic 0.2 mM β_2 with 0.6 mM Fe^{II} was reacted with the equal volume of oxygen saturated buffer at 4 °C.

Ct β -Fe^{II}/Fe^{II} with O₂ as monitored by stopped flow UV-Vis absorbance, our group has previously observed a feature at ~410 nm that was assigned to Y222• of *Ct* RNR- β .³⁴ Similarly, in the reaction of *Gm* RNR β -Fe^{II}/Fe^{II} with dioxygen, we observed an immediate (7 ms) formation of a species that appears at 410 nm and rapidly decays within 170 ms. We have also tested the diferrous reaction of the Y234F β variant with dioxygen with the expectation of not observing the same radical

species as in the wild type reaction. As expected, the reaction did not show the feature that the wild-type enzyme exhibited, but instead, showed a significantly broader (30 vs 10 nm) feature centered ~410 nm. It was previously shown that in the activation of *E. coli* RNR β a transient radical species forms on the subunit interfacial Y356 tyrosine.⁴⁸ Therefore, it is possible that the alternative radical we observed in the *Gm* β Y234F variant is the subunit interfacial Y350•. This hypothesis could be elucidated by analyzing the double variant cofactor *Gm* β -Fe^{II}/Fe^{II} Y234F/Y350F O₂ reaction process, via stopped-flow, UV-vis spectroscopy.

The cofactor oxidation reaction that forms the active cofactor in Ic RNRs is the β -Mn^{II}/Fe^{II} reaction with O₂. In *Gm* β RNR, using stopped-flow UV-vis methods, we observed a rapid

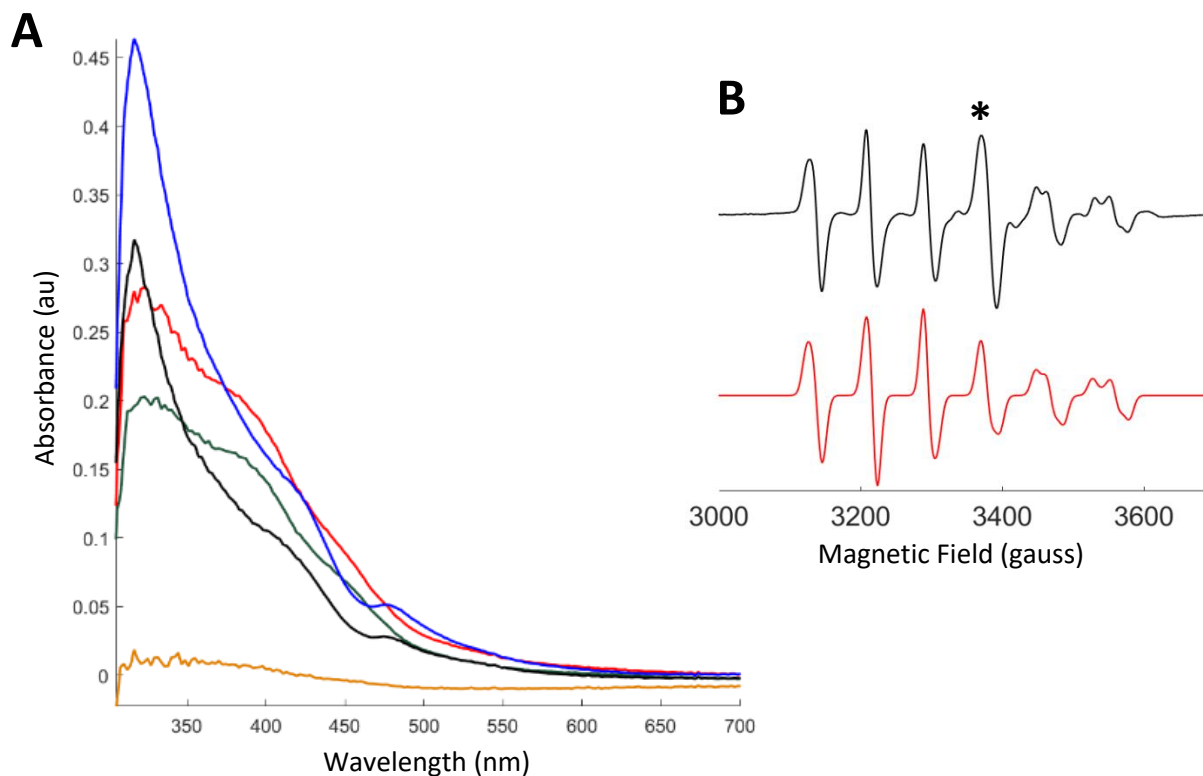


Figure 3. (A) Time dependent UV-VIS absorption spectra of the β -Mn^{II}/Fe^{II} reaction with O₂ saturated buffer. The 300-700 nm wavelength range depicts the formation and decay of the β -Mn^{IV}/Fe^{IV} intermediate. Reaction conditions: anaerobic 0.4 mM β_2 with 0.32 mM Mn^{II} and 0.96 mM of Fe^{II} was reacted with the equal volume of oxygen saturated buffer at 4 °C (B). The 0.5s time point freeze quench CW-EPR spectrum of the β -Mn^{IV}/Fe^{IV} intermediate in black, and the simulation in red Asterisk indicates the location of X_{Gm} . Spectrometer conditions were: Temperature 14K, microwave frequency, 9.44 GHz; microwave power, 20 uW; modulation frequency, 100 kHz; modulation amplitude, 10 G; scantime, 180 s; time constant, 180 ms.

formation and slow decay of a broad feature, centered ~390 nm (**Figure 3-A**). To obtain the rates of formation decay of this intermediate state while minimizing the potential photolytic decay we performed stopped-flow experiments via the photomultiplier tube (PMT) at 390 nm. To probe the nature of the intermediate observed via UV-Vis spectrometry at 390 nm we used freeze quench EPR. EPR analysis of the freeze quench sample showed signals strikingly similar to the β -

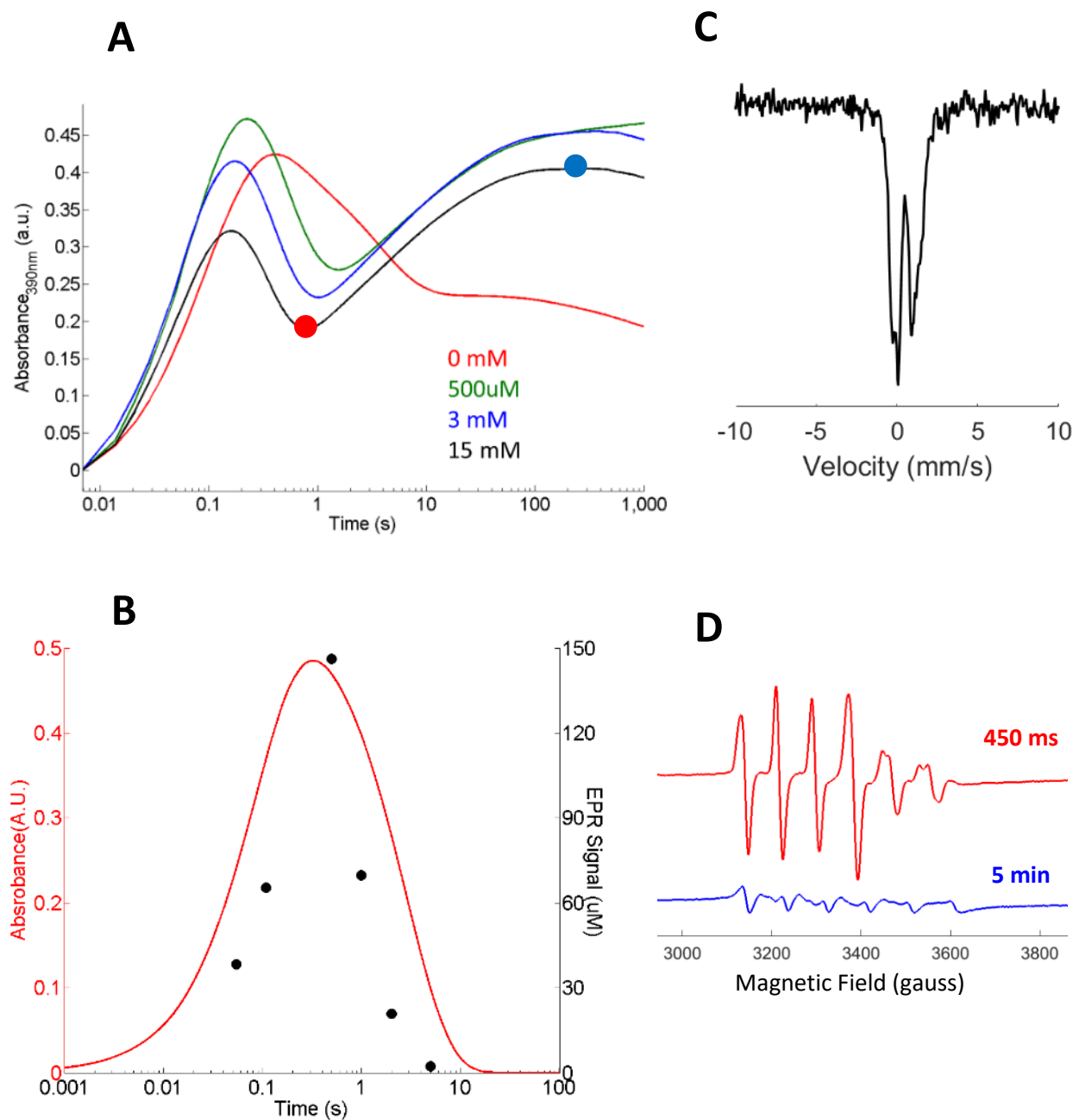


Figure 4. (A) Influence of the concentration of ascorbate on the kinetics of the β -Mn^{IV}/Fe^{IV} intermediate during the activation of *Gm* β -Mn^{II}/Fe^{II} wild type with oxygen at 4°C as observed by stopped-flow PMT 390 nm absorbance. (B) Kinetics of the formation and decay of the *Gm* β -Mn^{IV}/Fe^{IV} intermediate obtained via freeze quench EPR (black dots) and via a simulation of the stopped flow data using eq. 1 (red). General reaction conditions: 400 μ M *Gm* β ₂ containing 2.4 eq. of Mn^{II} and 0.8 eq. of Fe^{II} was rapidly mixed with equal volume O₂ saturated 100mM HEPES buffer. (C) 54 mT Mössbauer spectrum of 1 mM *Gm* β reconstituted with ⁵⁷Fe and ⁵⁵Mn, activated with O₂, and incubated for 15 minutes in the presence of 15 mM ascorbate. (D) Field swept CW-EPR spectra that correlate with the 15 mM stopped-flow data in Figure 4-A (blue and red dot). The red spectrum corresponds to the freeze-quench reaction quenched at 400 ms and the blue spectrum corresponds to the 5-minute hand quench.

Mn^{IV}/Fe^{IV} in *Ct* RNR. Therefore, we concluded that the intermediate is the orthologous cofactor in *Gm* RNR, the β -Mn^{IV}/Fe^{IV} cofactor (**Figure 3-B**). Simulations yielded EPR parameters in reasonable agreement with previously established parameters for the first class Ic enzyme³³ with $g = [2.016, 2.029, 2.026] \pm 0.005$ and the hyperfine tensor of $A_{55\text{Mn}} = [248, 216, 247] \pm 5$ MHz.

We have tested the influence of the presence of ascorbate in the activation reaction of *Gm* β RNR (**Figure 6**). Similarly, to the in *Ct* RNR system, ascorbate did not significantly affect the formation of the *Gm* β -Mn^{IV}/Fe^{IV} intermediate. The slight deviation of the formation rate is likely

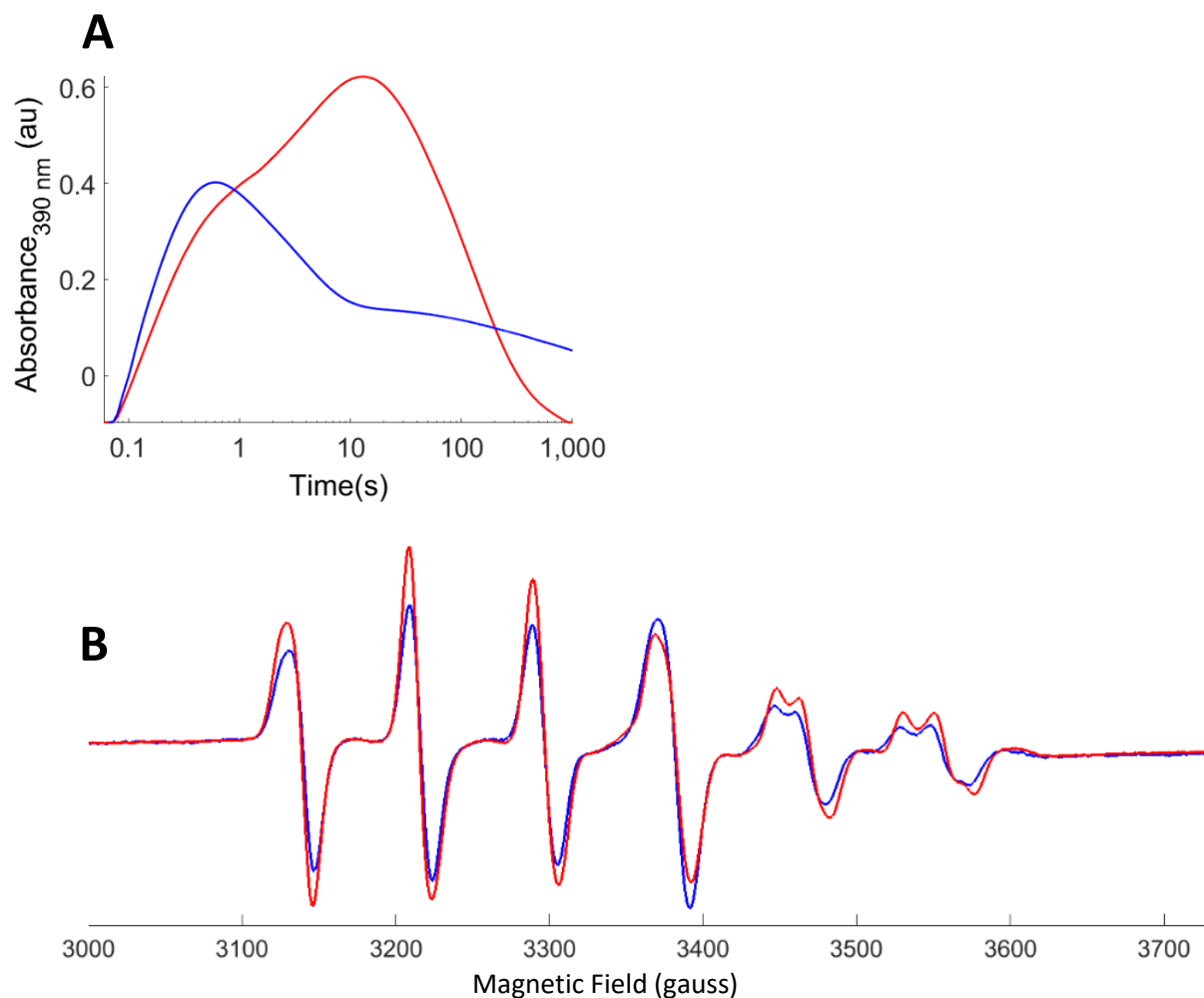


Figure 5. Comparison of the reaction of β -Mn^{II}/Fe^{II} with oxygen saturated buffer in *Gm* wt (blue) and *Gm* Y234F variant (red) via **A**) stopped-flow methods and **B**) via field swept CW-EPR freeze quench. The wild type reaction was freeze-quenched at 400 ms while the variant reaction was freeze-quenched after 11 seconds. The relative ratio of the stopped-flow maxima wt: Y234F is 0.71 and the relative ratio (peak to peak) of the first EPR spin “packet” wt: Y234F is 0.72.

due to small variation of oxygen concentration in the mixing buffer solution. However, ascorbate was shown to accelerate the decay of the intermediate significantly. In addition, we have observed a clear second phase formation starting at ~ 600 ms and ending at ~ 10 minutes. Mössbauer and EPR spectroscopies suggest that these absorption features are not related to any novel iron redox chemistry previously established in *Ct* RNR and do not reflect any novel half-integer spin state species (**Figure 4-C, D**). We have also tested the formation and decay of the $\beta\text{-Mn}^{\text{IV}}/\text{Fe}^{\text{IV}}$ intermediate in both the absence (**Figure 5-A**, red trace) and presence (**Figure 7**) of ascorbate in solution for the *Gm* β Y234F (Y222F cognate in *Ct* RNR) variant. The activation of the Y234F variant measured by the PMT absorption at 390 nm showed a two-phase activation process that yielded about ~1.5x the amount $\beta\text{-Mn}^{\text{IV}}/\text{Fe}^{\text{IV}}$ formed compared to the wild type enzyme. Because of the slow second phase formation in wt and the two-phase formation for

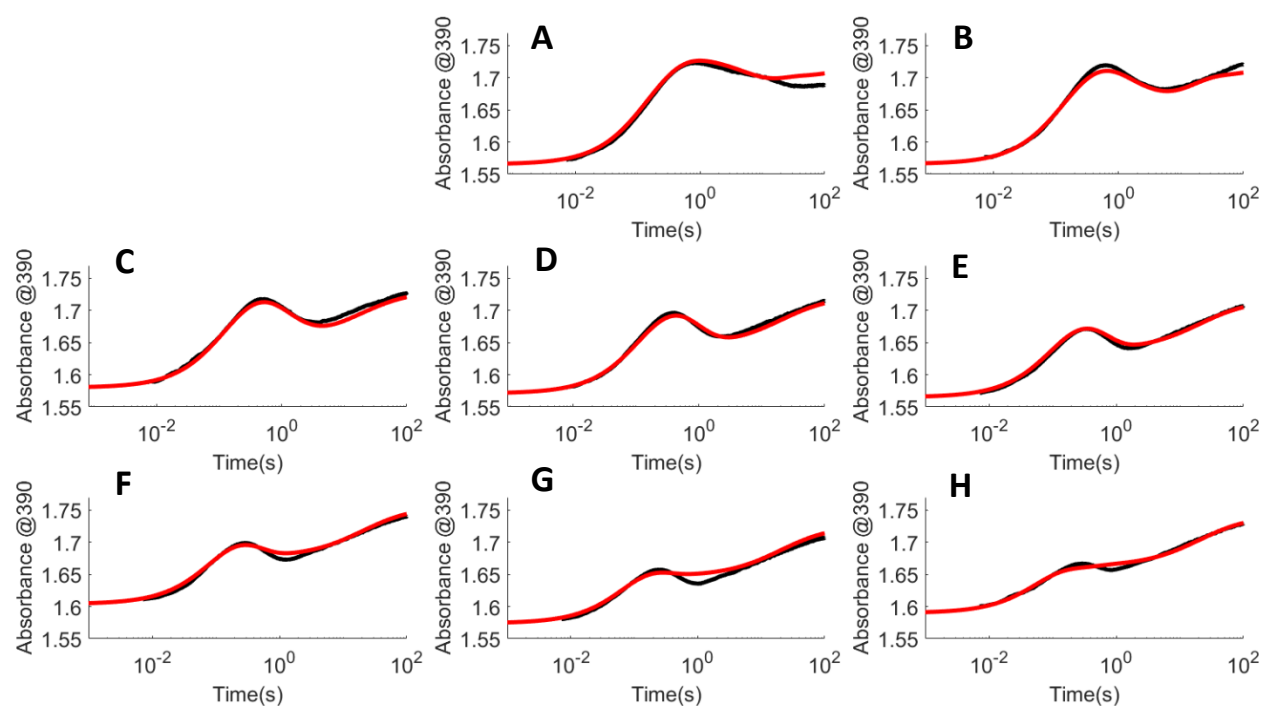


Figure 6. Stopped-flow kinetic traces of the reaction of the wild type *Gm* β with the equal volume of oxygen saturated buffer. Solid red line are the experimental data while the thin red line are the obtained simulations. Different spectra indicate varying concentration of ascorbate. **A)** 0 mM, **B)** 0.3 mM, **C)** 0.6 mM, **D)** 1.2 mM, **E)** 2.4 mM, **F)** 4.8 mM, **G)** 9.6 mM, **H)** 19.2 mM. Reaction conditions: 400 μ M *Gm* β_2 wt was reconstituted with 2.4 eq. of Mn^{II} and 1.1 eq of Fe^{II} under anoxic conditions.

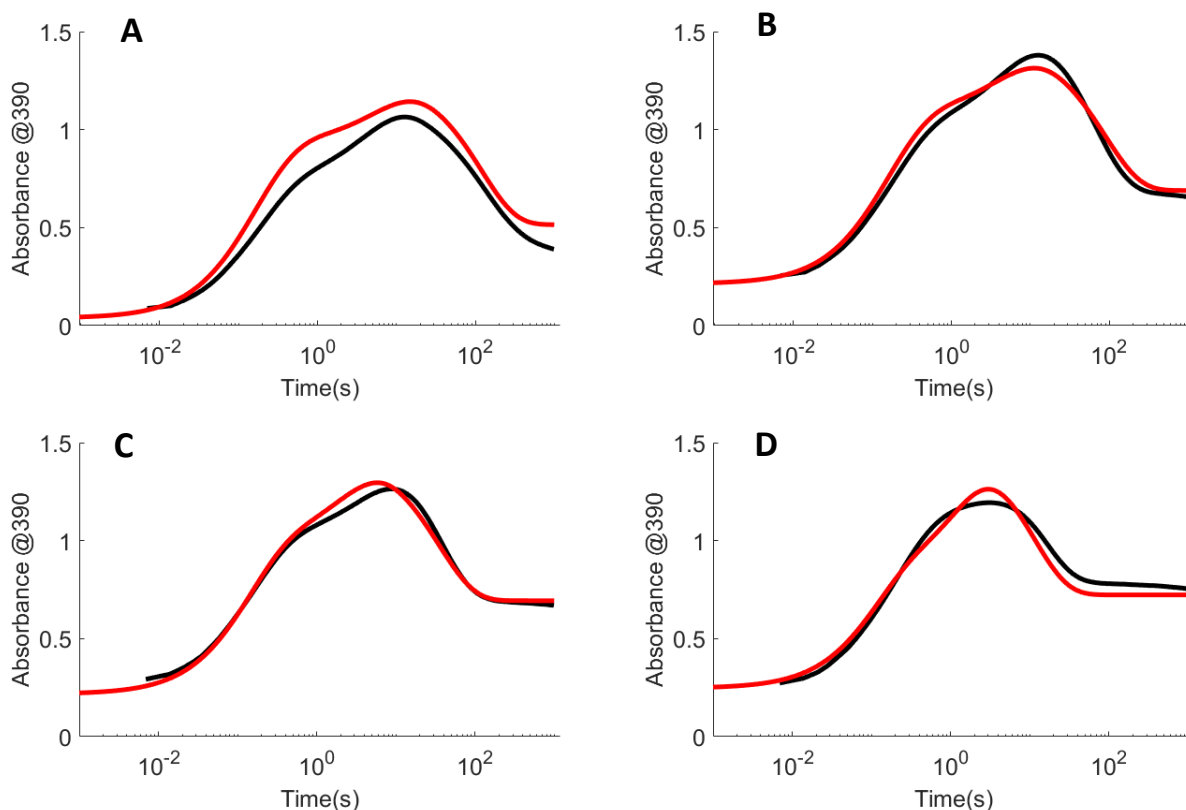
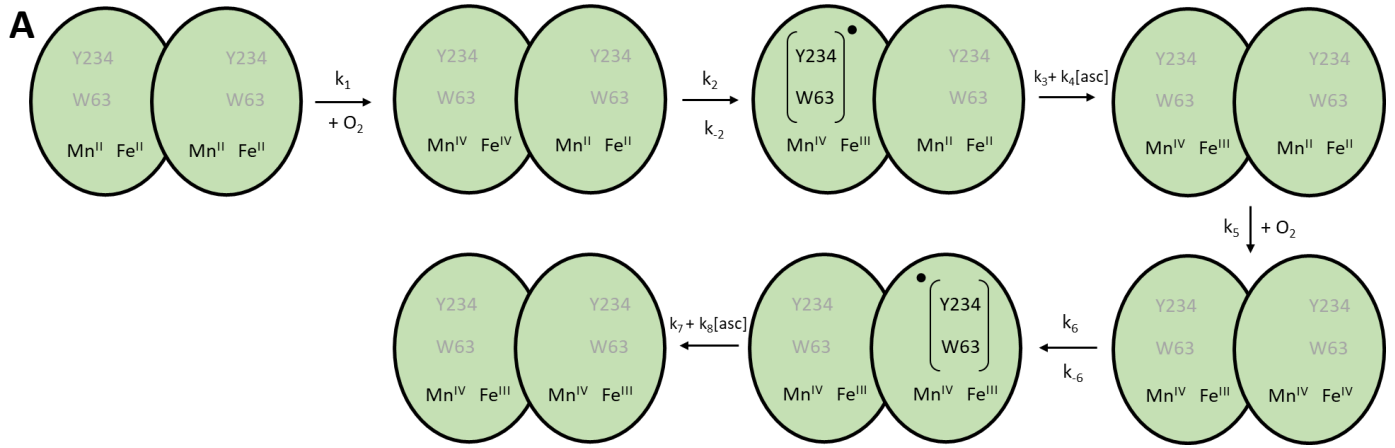


Figure 7. Stopped-flow kinetic traces of the reaction of the *Gm* β Y234F variant with the equal volume of oxygen saturated buffer. Solid red line are the experimental data while the thin red line are the obtained simulations. Different spectra indicate varying concentration of ascorbate: **A)** 0 mM, **B)** 0.5 mM, **C)** 3 mM, **D)** 15 mM. Reaction conditions: 400 μ M *Gm* β_2 variant was reconstituted with 2.4 eq. of Mn^{II} and 1.1 eq of Fe^{II} under anoxic conditions.

the Y234F *Gm* β variant, we have devised a kinetic model that adopts a pronounced half-of-sites reactivity. This model assumes that the second β monomer does not react with O_2 before the first monomer has completed the activation process and presumably formed the $\beta\text{-Mn}^{\text{IV}}/\text{Fe}^{\text{III}}$ cofactor. A graphical representation of this model as well as all rates obtained in the simulations are presented in **Figure 8**. To assess the product of the oxygen activation of the *Gm* β Mn/Fe cofactor, we have employed Mössbauer spectroscopy.



B

	k_1	k_2	k_{-2}	k_3	k_4	k_5	k_6	k_{-6}	k_7	k_8
wild type	8.2×10^{-3}	32.2	282	0.773	1.2×10^{-2}	1.1×10^{-4}	32.2	282	0.773	1.2×10^{-2}
Y234F	7.1×10^{-3}	5.89	859	27.2	2.8×10^{-2}	7.1×10^{-3}	0.27	859	27.2	2.8×10^{-2}

Figure 8. (A) Model used to simulate the rates obtained in the shown table. The model assumes that the second β monomer only reacts after the activation reaction is completed in the first monomer. Rates k_1 , k_5 and rates k_4 , k_8 depend on the concentration of dioxygen and sodium ascorbate in solution, respectively. **(B)** Table containing all the rates obtained in the simulations. Same color table cells indicate that the rates for both monomers in β_2 are equal. Additional parameters: O_2 concentration, 900 μM ; β - Mn^{IV}/Fe^{IV} extinction coefficient for the *Gm* β wt, $4.5 \times 10^{-4} \mu M^{-1} cm^{-1}$, and for *Gm* β Y234F, $2.3 \times 10^{-3} \mu M^{-1} cm^{-1}$; β - Mn^{IV}/Fe^{III} extinction coefficient for the *Gm* β wt, $1.8 \times 10^{-4} \mu M^{-1} cm^{-1}$, and for *Gm* β Y234F, $6.0 \times 10^{-4} \mu M^{-1} cm^{-1}$.

Mössbauer Analysis of the product of O₂ reaction of *Gm* β -Mn^{II}/Fe^{II} with O₂

The EPR detected presence of X_{Gm} and the β -Mn^{IV}/Fe^{IV} intermediate in the freeze quench samples (**Figure 4-A**) of the Mn/Fe reconstituted and O₂ activated *Gm* β indicates that the Mn/Fe

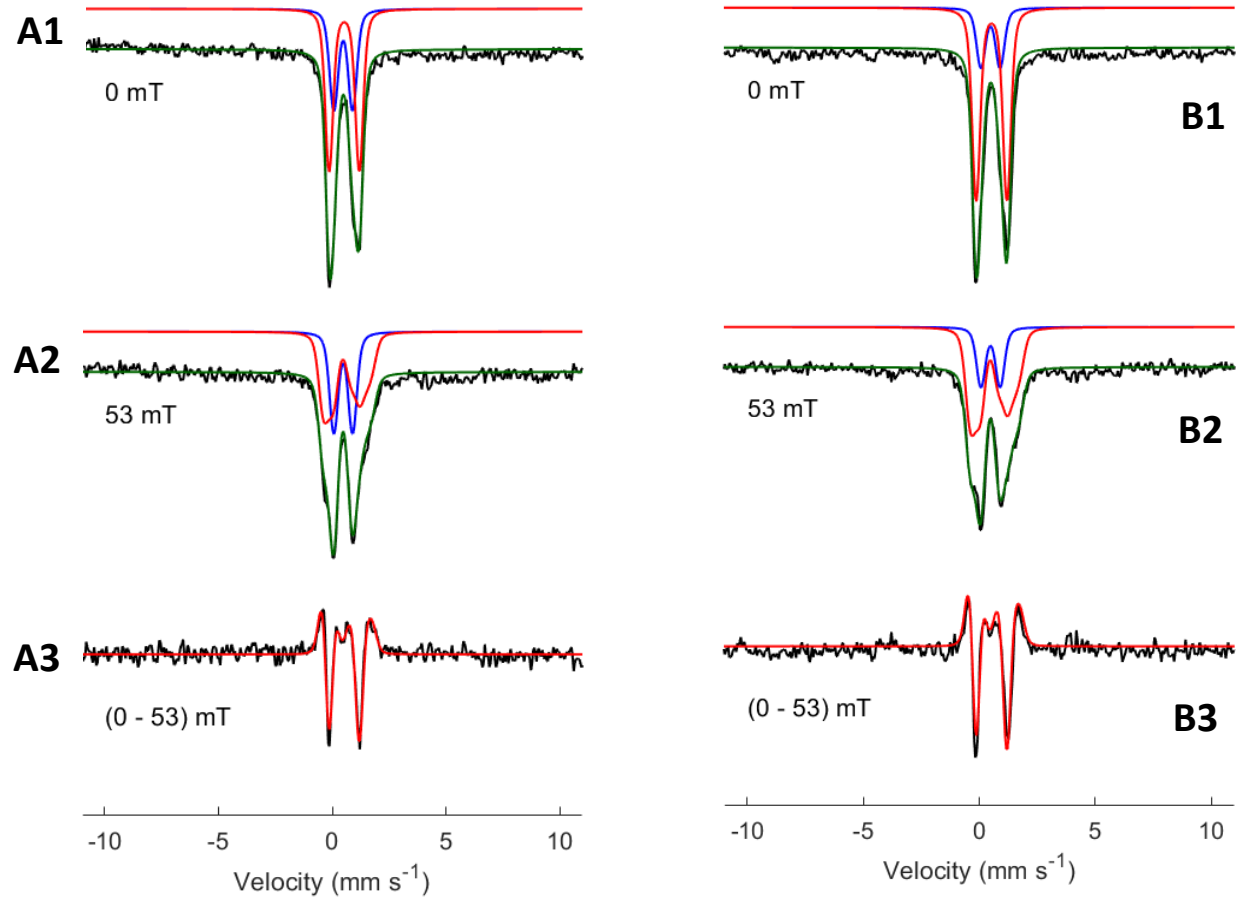


Figure 9. Mössbauer spectra of the activation product states of Mn/Fe reconstituted and oxygen activated *Gm* β wt (A) and Y234F variant (B). The top traces represent the 0 field spectra (1), the middle traces represent the 53 mT applied and oriented parallel to the γ -beam spectra (2), and the bottom represent the difference between (1) and (2) spectra. Raw data are in black, red and blue traces in (1) and (2) represent the simulated contributions from β -Mn^{IV}/Fe^{III}, and β -Fe^{III}/Fe^{III}, respectively. In green are the simulated sum of the blue and red. Red in (3) the simulated difference spectra between green from (1) and (2).

– O₂ reaction likely yields two products, the successor of β -Mn^{IV}/Fe^{IV}, the active β -Mn^{IV}/Fe^{III} RT cofactor and the successor of X_{Gm} , the β -Fe^{III}/Fe^{III} cofactor. Similarly, to *Ct* RNR, we observed no X-band EPR signals in the product of the reaction of *Gm* β with manganese and iron with dioxygen

because we expect both the *Gm* β -Fe^{III}/Fe^{III} and β -Mn^{IV}/Fe^{III} cofactors with $S_{total} = 0$ and $S_{total} = 1$, respectively, to be EPR silent. Like the previous studies in *Ct* RNR, the diferric and Mn/Fe products were analyzed via Mössbauer spectroscopy at 0 field and the 53 mT (**Figure 9**). The diferric cofactor with the total spin of $S_{Total} = 0$, is characterized by a quadrupole doublet with the following parameters $\delta = 0.49$ mm/s and $\Delta E_Q = 0.83$ mm/s at 4.2 K. The signal of this specie is unaffected upon the application of an external magnetic field and closely resembles the signals of other, high spin diferric, antiferromagnetically coupled ions.⁴⁹ On the other hand, the β -Mn^{IV}/Fe^{III} activation product is a spin coupled system with $S_{Total} = 1$ also characterized by a quadrupole doublet at 4.2 K which broadens upon the application of an external magnetic field. Mössbauer parameters used to simulate this state are of $\delta = 0.53$ mm/s, $\Delta E_Q = 1.33$ mm/s, and the observed $A_{57Fe} = [-40.9, -36.6, -34.2]$ MHz. These parameters closely resemble parameters obtained for the *Ct* RNR⁴⁰ β -Mn^{IV}/Fe^{III}. The relative amounts of β -Mn^{IV}/Fe^{III} and β -Fe^{III}/Fe^{III} were obtained by first establishing a difference spectrum by subtracting the zero-field spectrum from the spectrum obtained from the 53 mT applied and oriented parallel to the γ -beam. By adjusting and subtracting the relative amounts of the simulated β -Mn^{IV}/Fe^{III} and β -Fe^{III}/Fe^{III} spectra to match the difference spectrum obtained via the subtraction of the experimentally obtained data, we determined that in activated *Gm* β wild type 50% of the iron belonged to the β -Mn^{IV}/Fe^{III} state and 33% to diferric. The Mössbauer spectra of the *Gm* β Y234F variant very closely resemble the spectra of the wild type enzyme and can be simulated well using identical parameters. These results indicate that both the wild type and the Y234F variant can assemble the β -Mn^{IV}/Fe^{III} cofactor in *Gm* β . Activity assays and EPR spectroscopy were both used to assess whether this cofactor is active in *Gm* RNR.

CATALYSIS

Gm RNR activity assays

Activity assays performed on the *Gm* RNR system showed comparable rates to the other class I RNRs. The assays were performed by mixing *Gm* β and α , CDP, ATP, and DTT, and measuring activity using LC-MS methods. Initial studies involved the truncated *Gm* α constructs α - Δ (1-143) and α - Δ (1-218), where the former has ~ 1.5 and the latter both ATP cones removed.

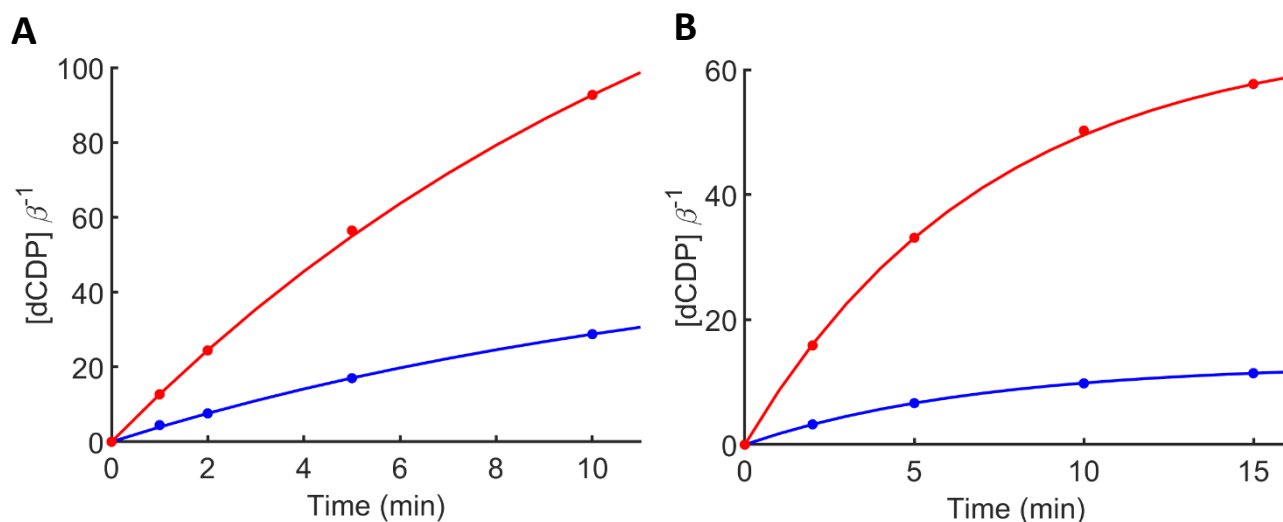


Figure 10. A) Reaction of the wt-*Gm* β (in blue) and *Gm* β Y234F variant (in red) with *Gm* α . The exponential fits produced $0.07 \text{ s}^{-1} \beta^{-1}$ rate of reduction for *Gm* β wt and $0.22 \text{ s}^{-1} \beta^{-1}$ rate of reaction for *Gm* Y234F variant. **B)** Effects of presence of 30 mM ascorbate in the reaction solution on ribonucleotide reduction. Under these conditions the exponential fits produced $0.03 \text{ s}^{-1} \beta^{-1}$ rate of reduction for *Gm* β wt and $0.15 \text{ s}^{-1} \beta^{-1}$ rate of reaction for *Gm* Y234F variant. Reaction conditions: $25 \mu\text{M}$ α_2 , $5 \mu\text{M}$ β_2 , 2 mM ATP, 1 mM CDP, 10 mM DTT, 10 mM Mg^{+2} . Reaction quenched with 2 M formic acid.

The α - Δ (1-143) construct showed barely detectable ribonucleotide reduction, while the α - Δ (1-218) was insoluble in buffer. However, upon the acquisition of the full-length *Gm* α , the reaction rates improved significantly. The results of the assays showed catalytic activity for both *Gm* β wild type ($0.07 \text{ s}^{-1} \beta^{-1}$) and *Gm* β Y234F variant ($0.22 \text{ s}^{-1} \beta^{-1}$). The variant, unlike in *Ct* RNR, was shown to be ~ 3.4 times more active than the wild type (**Figure 10**). In addition, we have also tested

ribonucleotide reduction in the presence of 30 mM sodium ascorbate which yielded the following rate constants, $0.03 \text{ s}^{-1} \beta^{-1}$ and $0.15 \text{ s}^{-1} \beta^{-1}$ for *Gm* β and *Gm* β Y234F variant respectively.

Spectroscopic evidence of radical translocation in *Gm* RNR

One reliable test of RT from the β into the α subunit was established in *Ct* RNR and it involves the association of the β and α subunits in the presence of the substrate, the effector, dithiol reductant, and hydroxyurea. It was shown that upon radical translocation into α , hydroxyurea reduces pathway radicals to trap the RT product, $\beta\text{-Mn}^{\text{III}}/\text{Fe}^{\text{III}}$ cofactor state.²⁹ Upon this reduction, the cofactor in β is in the EPR active, RT product state, $\beta\text{-Mn}^{\text{III}}/\text{Fe}^{\text{III}}$. In the absence of substrate, the univalent cofactor reduction is not favorable, and no $\beta\text{-Mn}^{\text{III}}/\text{Fe}^{\text{III}}$ state is observed. We have reproduced this result in *Gm* RNR by utilizing *Gm* β and *Gm* α . The signal of the RT product state, probed by X-band EPR, is very similar to the signal obtained from the $\beta\text{-Mn}^{\text{III}}/\text{Fe}^{\text{III}}$ state from *C. trachomatis*. Simulations yielded EPR parameters (**Figure 11-A** in red) $g = [2.026, 2.016, 2.013] \pm 0.01$ and $A_{55\text{Mn}} = [270, 400, 315] \pm 10 \text{ MHz}$, comparable to the parameters used to simulate the

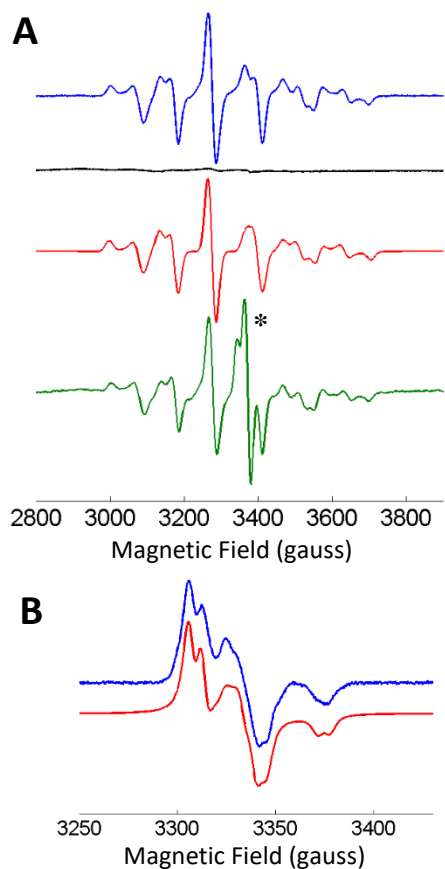


Figure 11. (A) Field swept CW-EPR spectrum of the *Gm* β RNR, β -Mn^{III}/Fe^{III} RT product state generated via the use of the reaction inhibitor and pathway radical scavenger hydroxyurea (blue). The EPR spectrum of the no substrate control reaction sample (black). Simulation of the hydroxyurea generated RT product state (red). The β -Mn^{III}/Fe^{III} EPR spectrum generated via the use of the N₃UDP reaction inhibitor (green). Asterisk indicates the location of the saturated signal of the N• in α (B) CW-EPR spectrum of the N• in *Gm* α - Δ (1-143) (blue) and the appropriate simulation (red) Spectrometer conditions were: Temperature 14K for (A) and 100K for (B), microwave frequency, 9.48 GHz; microwave power, 20 uW; modulation frequency, 100 kHz; modulation amplitude, 10 G; scantime, 180 s for (A), 30 s for (B); time constant, 180.

Ct RNR spectra ($g = [2.030, 2.020, 2.015]$ and $A_{55\text{Mn}} = [269, 392, 314]$ MHz). The parameters agree to a great extent with slightly larger manganese hyperfine values for the *Gm* β cofactor. In addition to performing the experiment that involved hydroxyurea with the appropriate control that lacks the substrate, we have also observed RT in *Gm* RNR via the use of the substrate analog N₃UDP. The reaction of the *Gm* β and α subunits in the presence of ATP, DTT, and N₃UDP resulted in the EPR tested appearance of the RT product state of the cofactor, β -Mn^{III}/Fe^{III}, as well as the appearance of N• in the larger subunit (**Figure 11**, green). The EPR spectrum at 100 K (**Figure 11-B**) shows the nitrogen centered radical in the larger subunit. The signal is typical of N• radicals generated in other RNR α subunits^{36, 50} characterized by a strong, axial ¹⁴N hyperfine coupling and strong isotropic ¹H coupling. The CW-EPR simulation yielded the following EPR parameters $g = [2.016, 2.006, 2.002] \pm 0.005$, ¹⁴N $A_{\text{HF}} = [5.6, 5.6, 89.6] \pm 2$ MHz, and ¹H $A_{\text{HF}} = [17.6, 17.6, 17.6] \pm 1$ MHz. These parameters are virtually identical to the parameters previously published by first van der Donk⁵¹ and later Fritscher.³⁶ The conditions of the N₃UPD

reaction were: 400 μ M *Gm* β , 800 μ M *Gm* α , 1 mM 2'-azido-UDP, 10 mM DTT, 2 mM ATP. However, we believe it is important to note that in order to successfully observe the RT into the larger subunit via EPR, it was crucial to remove any additional salt, glycerol and decrease the concentration of buffer in the reaction solution to 50 mM. With the instability of the *Gm* α construct in such a buffer in mind, the reaction was performed immediately after exchanging into the aforementioned buffer.

To further investigate the activation-catalysis branched electron relay in *Gm* RNR, we have obtained the *Gm* β Y350F variant (*Ct* β Y338F analogue). Since the Y234F variant was significantly more active than the wild type *Gm* β , we attempted to react the *Gm* β -Mn^{IV}/Fe^{III} Y350F variant with *Gm* α in the presence of ATP, DTT and CDP with the expectation of observing the Y234• via EPR since it was shown that the radical hole can translocate to either Y222 or Y338 in *Ct* RNR. However, during the protein purification step that involves metal removal from the *Gm* β Y350F variant, we have observed that this APO variant is not stable in buffer and therefore no further conclusions could be made about the activation-catalysis branched electron relays in *Gm* RNR.

OUTLOOK AND DISCUSSION

The O₂ activation reaction of *Gm* β showed very similar properties to the O₂ activation of *Ct* β , with three notable differences. First, the UV-vis stopped-flow observed activation of *Gm* β was characterized by a slow, broad (325 - 400 nm) formation phase of an absorbing species that was apparent in stopped-flow traces after 10 s with the growth phase lasting into several minutes,

especially in the presence of ascorbate. EPR spectroscopy performed on samples that were reconstituted with Mn/Fe and exposed to molecular oxygen in the presence of 15 mM ascorbate and quenched at 400 ms and 5 minutes showed no novel EPR signals. In addition, the sample of *Gm* β containing 15 mM sodium ascorbate and anoxically reconstituted with ^{57}Fe and ^{55}Mn , and subsequently reacted with oxygen showed no novel signals in its Mössbauer spectrum after a 15-minute incubation period. Therefore, the slow forming absorption signal likely originates from an analogous species previously observed in the activation reaction of *Ct* RNR. The cofactor product of activation, $\beta\text{-Mn}^{\text{IV}}/\text{Fe}^{\text{III}}$, with $S_{\text{Total}} = 1$, displays no X-band EPR signal and is characterized by a quadrupole doublet that broadens after exposure to a weak magnetic field. If the formation of the $\beta\text{-Mn}^{\text{IV}}/\text{Fe}^{\text{IV}}$ intermediate was somehow slowed down with the decay remaining the same the $\beta\text{-Mn}^{\text{IV}}/\text{Fe}^{\text{IV}}$ intermediate would never be observed and the product state, $\beta\text{-Mn}^{\text{IV}}/\text{Fe}^{\text{III}}$, would accumulate slowly over time. We have taken advantage of global kinetic simulations to attempt to support this hypothesis. Global simulations that involve a model that accounts for the slow formation due to half-of-sites reactivity simulate the experimental data reasonably well. Previous studies of *Ec* RNR⁵² and in delta-9-desaturase⁵³ show that metal binding and oxygen activation can play a complex role in dimeric proteins. We could speculate that a possible slow rearrangement step happens only after one monomer has reacted with dioxygen. This rearrangement might be required for the metals to bind to the second dimer, at which time the second *Gm* β dimer can undergo the activation process.

The global kinetic simulations show that rate constant of ascorbate reduction of the *Gm* $\beta\text{-Mn}^{\text{IV}}/\text{Fe}^{\text{IV}}$ is ~100 times greater compared to the decay rate of reduction by ascorbate of *Ct* $\beta\text{-Mn}^{\text{IV}}/\text{Fe}^{\text{IV}}$. These results are consistent with the presence of an activation electron relay presented for *Ct* RNR,³⁴ where the $\beta\text{-Mn}^{\text{IV}}/\text{Fe}^{\text{IV}}$ state is in a dynamic equilibrium that comprises 3 different

radical harboring states in β . These states in *Gm* β include β -Mn^{IV}/Fe^{IV}-W63-Y234, β -Mn^{IV}/Fe^{III}-W63⁺-Y234, and β -Mn^{IV}/Fe^{III}-W63-Y234[•], with the equilibrium shifted to the β -Mn^{IV}/Fe^{IV} state. We have observed in *Ct* RNR that ascorbate cannot reduce the cofactor directly but can reduce the solvent exposed, transient Y234[•].³⁴ As expected, the results show a ~ 2-fold diminished rate of reduction of the Y234F β variant compared to the wild type *Gm* β ascorbate mediated reduction.

The second notable difference in the activation process of *Gimesia Maris* β RNR compared to *Chlamydia trachomatis* β RNR lies in the analysis of the activation of the variant *Gm* β Y234F. In the activation of the *Gm* β Y234F variant, stopped-flow monitored UV-vis spectroscopy indicated a two-phase formation and about 1.5 times (**Figure 5**) more accumulation of the β -Mn^{IV}/Fe^{IV} intermediate compared to the activation of the wild type enzyme. EPR spectroscopy further supports this hypothesis by demonstrating that the ratio of the maxima in the stopped flow traces match the ratio of the EPR intensities of the β -Mn^{IV}/Fe^{IV} signal at the appropriate quench times. Global kinetic simulations for the *Gm* β Y234F variant did not require a slower reaction of the β -Mn^{II}/Fe^{II} with O₂ in the second monomer. Instead, the rate of decay of the β -Mn^{IV}/Fe^{IV} intermediate in the second monomer is slowed down by an order of magnitude. Since single amino acid replacements could have profound effects on the reactivity of an enzyme this change is not unlikely. However, Mössbauer analysis of both the wild type and Y234F variant *Gm* β cofactors show comparable amounts of β -Mn^{IV}/Fe^{III} active RT state, despite the apparent transient increase in formation of the β -Mn^{IV}/Fe^{IV} intermediate in the variant. It is possible that maybe the Y234F *Gm* β variant β -Mn^{IV}/Fe^{III} is more susceptible to dialysis mediated metal removal via EDTA since the small subunits are exposed to 10 mM EDTA prior to freezing. However, further studies are required to confirm this hypothesis. A simple Mössbauer study would suffice that would analyze

half of a *Gm* β -Mn^{IV}/Fe^{III} sample immediately after reconstitution and the other half after the treatment with EDTA.

The third notable difference between the activation processes of *Gm* and *Ct* small subunits lies in the magnitude of the second order rate constant of β -Mn^{IV}/Fe^{IV} intermediate reduction with respect to the concentration of ascorbate. This rate is 0.13 mM⁻¹ s⁻¹ in the *Ct* RNR³⁴ while in the *Gm* β RNR this rate is ~100x larger at 12 mM⁻¹ s⁻¹. It is likely that during activation, the Y234• in *Gm* β is more solvent exposed compared to Y222• in *Ct* β and is therefore more readily able to accept the electron from ascorbate, effectively increasing the rate of decay of β -Mn^{IV}/Fe^{IV}.

In addition to the differences between the activation processes in the *Ct* and *Gm* RNR β cofactors, there are differences in the catalytic activity between these two class Ic ribonucleotide reductases. *Gimesia maris* ribonucleotide reductase is a catalytically competent class I RNR with comparable reduction rates to other RNRs from this class. Typical class I RNR catalytic rates range from 0.15 - 5 s⁻¹ β ⁻¹.^{5, 11} Our initial studies involved only the *Gm* α - Δ (1-143) construct and due to the poor solubility and stability of this construct we obtained barely detectable conversion of CDP to dCDP. While the removal of the first two out of three N-terminal ATP cones improved the stability and activity of *Ct* RNR,⁵⁴ we likely observed the opposite effect when ~1.5 out of two N-terminal ATP cones were removed from *Gm* α . We attempted to overexpress and purify the construct of *Gm* α that lacks both ATP cones, *Gm* α - Δ (1-218). However, this variant was shown to be completely insoluble in buffer. Therefore, the presence of both ATP cones in *Gm* α may be crucial for both stability and effective ribonucleotide reduction. Fortunately, after obtaining the full-length *Gm* α gene and overexpressing the protein in *E. Coli*, the full-length *Gm* α and *Gm* β complex in the presence of ATP, DTT, Mg²⁺ and CDP, was able to produce respectable rates of reaction of 0.07 s⁻¹ β ⁻¹ for wild type *Gm* β and 0.22 s⁻¹ β ⁻¹ for the Y234F *Gm* β variant. In addition

to these rates we were also able to use EPR spectroscopic evidence to solidify *Gm* RNR as a definite second class Ic RNR that uses a $\beta\text{-Mn}^{\text{IV}}/\text{Fe}^{\text{III}}$ cofactor to initiate RT. The reaction of *Gm* β and α subunits in the presence of DTT, ATP and N_3UDP unambiguously demonstrated RT into α and identified the RT cofactor product state as the $\beta\text{-Mn}^{\text{III}}/\text{Fe}^{\text{III}}$. Additionally, by observing the $\text{Y234}\bullet$ in the diferrous reaction with O_2 in *Gm* β and by establishing ascorbate as an effective electron donor to $\text{Y234}\bullet$ during the activation process of *Gm* β with Mn/Fe, we have shown experimental evidence that *Gm* β possess the activation electron relay. Moreover, the fact that we observe the RT product state exclusively in the presence of the substrate in addition to ATP, DTT, HU and the two *Gm* RNR subunits, we supported the proposed gated mechanism in *Ct* RNR as a class Ic phenomenon. Therefore, by confirming that *Gm* RNR possessed both the activation and catalytic electron relays, we have also shown very strong evidence that the branched electron relay pathways are likely a class Ic RNR phenomenon.

Arguably, the most intriguing finding in the *Gm* RNR system is the fact that the Y234F *Gm* β variant is about 3.4x more active than the wild type enzyme. We therefore speculate that once catalytic conditions are established for *Gm* RNR, the electron hole resting on Mn^{IV} can transfer either to Y234 in β or to initiate ribonucleotide reduction in α . In *Ct* RNR, the catalytic RT pathway is likely thermodynamically favored since we did not observe an increase in the catalytic rate in the *Ct* β Y222 variant. However, the 3.4-fold rate increase observed with the *Gm* RNR variant compared to the wild type protein could possibly suggest that the $\text{Y234}\bullet$ could be more stable than $\text{Y222}\bullet$ in *Ct* and the catalytic RT electron relay is not strongly favored in *Gm* RNR. In attempt to further solidify this hypothesis, we have tested ribonucleotide reduction in the presence of 30 mM sodium ascorbate. Since this reductant can rapidly reduce the $\text{Y234}\bullet$ during the activation process, we hypothesized that it would rapidly inactivate catalysis as well. However,

we did not observe a higher inactivation rate for the variant compared to the experiment with no ascorbate added (**Figure 10-B**). Interestingly, under these conditions, we were still able to observe a ~5 greater reaction amplitude for the Y234F variant reaction compared to *Gm* β wt reaction.

In summary, after over a decade of search, we found a second representative of Class Ic RNR from *Gimesia maris* that can assemble the β -Mn^{IV}/Fe^{III} cofactor and perform ribonucleotide reduction. Not only did we support the branched electron relay hypothesis established in *Ct* RNR, but also introduced the possibility that the electron relays can be differently tuned depending on the specie from which the class Ic RNR belongs to. However, the *Gm* RNR β gene is very similar to the *Ct* RNR gene (65% identity). In in gene cluster presented in **Figure 1** there are ~100 tentative class Ic RNR genes that do not separate along with the *C. trachomatis* gene at alignment score values of 145 and higher. The natural question to ask is whether these RNRs use a Mn/Fe cofactor and belong to the class Ic subclass or function under a different *modus operandi*. Performing the experiments like the ones presented in the work on a tentative class Ic RNR β whose gene is not very similar to *Ct* RNR β would likely answer that question.

REFERENCES

1. Nordlund, P.; Reichard, P., Ribonucleotide reductases. *Annu Rev Biochem* **2006**, *75*, 681-706.
2. Licht, S.; Gerfen, G. J.; Stubbe, J. A., Thiyl radicals in ribonucleotide reductases. *Science* **1996**, *271* (5248), 477-481.
3. Gambarelli, S.; Luttringer, F.; Padovani, D.; Mulliez, E.; Fontecave, M., Activation of the anaerobic ribonucleotide reductase by S-adenosylmethionine. *Chembiochem* **2005**, *6* (11), 1960-1962.
4. Lawrence, C. C.; Stubbe, J., The function of adenosylcobalamin in the mechanism of ribonucleoside triphosphate reductase from *Lactobacillus leichmannii*. *Curr Opin Chem Biol* **1998**, *2* (5), 650-655.
5. Stubbe, J.; Nocera, D. G.; Yee, C. S.; Chang, M. C. Y., Radical initiation in the class I ribonucleotide reductase: Long-range proton-coupled electron transfer? *Chem Rev* **2003**, *103* (6), 2167-2201.
6. Cotruvo, J. A.; Stubbe, J., Class I ribonucleotide reductases: metallocofactor assembly and repair in vitro and in vivo. *Annu Rev Biochem* **2011**, *80*, 733-67.
7. Blaes, E. J.; Palowitch, G. M.; Hu, K.; Kim, A. J.; Rose, H. R.; Alapati, R.; Lougee, M. G.; Kim, H. J.; Taguchi, A. T.; Tan, K. O.; Laremore, T. N.; Griffin, R. G.; Krebs, C.; Matthews, M. L.; Silakov, A.; Bollinger, J. M., Jr.; Allen, B. D.; Boal, A. K., Metal-free class Ie ribonucleotide reductase from pathogens initiates catalysis with a tyrosine-derived dihydroxyphenylalanine radical. *Proc Natl Acad Sci U S A* **2018**, *115* (40), 10022-10027.

8. Vivek Srinivas, H. L., Daniel Lundin, Yuri Kutin, Margareta Sahlin, Michael Lerche, Jürgen Eirich, Rui Branca, Nicholas Cox, Britt-Marie Sjöberg, Martin Högbom, Metal-independent ribonucleotide reduction powered by a DOPA radical in Mycoplasma pathogens. *BiorXiv* **2018**, preprint.
9. Ravi, N.; Bollinger, J. M.; Huynh, B. H.; Edmondson, D. E.; Stubbe, J., Mechanism of Assembly of the Tyrosyl Radical-Diiron(III) Cofactor of Escherichia-Coli Ribonucleotide Reductase .1. Mossbauer Characterization of the Diferric Radical Precursor. *J Am Chem Soc* **1994**, *116* (18), 8007-8014.
10. Cotruvo, J. A.; Stubbe, J., NrdI, a flavodoxin involved in maintenance of the diferric-tyrosyl radical cofactor in Escherichia coli class Ib ribonucleotide reductase. *P Natl Acad Sci USA* **2008**, *105* (38), 14383-14388.
11. Jiang, W.; Yun, D.; Saleh, L.; Barr, E. W.; Xing, G.; Hoffart, L. M.; Maslak, M. A.; Krebs, C.; Bollinger, J. M., A manganese(IV)/iron(III) cofactor in Chlamydia trachomatis ribonucleotide reductase. *Science* **2007**, *316* (5828), 1188-1191.
12. Rose, H. R.; Ghosh, M. K.; Maggiolo, A. O.; Pollock, C. J.; Blaes, E. J.; Hajj, V.; Wei, Y.; Rajakovich, L. J.; Chang, W. C.; Han, Y.; Hajj, M.; Krebs, C.; Silakov, A.; Pandelia, M. E.; Bollinger, J. M., Jr.; Boal, A. K., Structural Basis for Superoxide Activation of Flavobacterium johnsoniae Class I Ribonucleotide Reductase and for Radical Initiation by Its Dimanganese Cofactor. *Biochemistry-US* **2018**.
13. Reichard, P.; Estborn, B., Utilization of desoxyribosides in the synthesis of polynucleotides. *J Biol Chem* **1951**, *188* (2), 839-46.
14. Reichard, P.; Ehrenberg, A., Ribonucleotide Reductase - a Radical Enzyme. *Science* **1983**, *221* (4610), 514-519.

15. Asturias, F.; Brignole, E.; Tsai, K. L.; Drennan, C.; Stubbe, J., Quaternary Structure and Activity Modulation in Human Ribonucleotide Reductase. *FASEB J* **2015**, *29*.
16. Strand, K. R.; Karlsen, S.; Kolberg, M.; Rohr, A. K.; Gorbitz, C. H.; Andersson, K. K., Crystal structural studies of changes in the native dinuclear iron center of ribonucleotide reductase protein R2 from mouse. *J Biol Chem* **2004**, *279* (45), 46794-46801.
17. Xu, H.; Faber, C.; Uchiki, T.; Racca, J.; Dealwis, C., Structures of eukaryotic ribonucleotide reductase I define gemcitabine diphosphate binding and subunit assembly. *P Natl Acad Sci USA* **2006**, *103* (11), 4028-4033.
18. Cotruvo, J. A.; Stubbe, J., An Active Dimanganese(III)-Tyrosyl Radical Cofactor in Escherichia coli Class Ib Ribonucleotide Reductase. *Biochemistry-US* **2010**, *49* (6), 1297-1309.
19. Zhang, Y.; Stubbe, J., Bacillus subtilis Class Ib Ribonucleotide Reductase Is a Dimanganese(III)-Tyrosyl Radical Enzyme. *Biochemistry-US* **2011**, *50* (25), 5615-5623.
20. Cox, N.; Ogata, H.; Stolle, P.; Reijerse, E.; Auling, G.; Lubitz, W., A Tyrosyl-Dimanganese Coupled Spin System is the Native Metalloradical Cofactor of the R2F Subunit of the Ribonucleotide Reductase of Corynebacterium ammoniagenes. *J Am Chem Soc* **2010**, *132* (32), 11197-11213.
21. Berggren, G.; Duraffourg, N.; Sahlin, M.; Sjöberg, B. M., Semiquinone-induced Maturation of Bacillus anthracis Ribonucleotide Reductase by a Superoxide Intermediate. *J Biol Chem* **2014**, *289* (46), 31940-31949.
22. Lofstad, M.; Gudim, I.; Hammerstad, M.; Rohr, A. K.; Hersleth, H. P., Activation of the Class Ib Ribonucleotide Reductase by a Flavodoxin Reductase in Bacillus cereus. *Biochemistry-US* **2016**, *55* (36), 4998-5001.

23. Makhlynets, O.; Boal, A. K.; Rhodes, D. V.; Kitten, T.; Rosenzweig, A. C.; Stubbe, J., Streptococcus sanguinis Class Ib Ribonucleotide Reductase HIGH ACTIVITY WITH BOTH IRON AND MANGANESE COFACTORS AND STRUCTURAL INSIGHTS. *J Biol Chem* **2014**, 289 (9), 6259-6272.
24. Rozman Grinberg, I.; Lundin, D.; Hasan, M.; Crona, M.; Jonna, V. R.; Loderer, C.; Sahlin, M.; Markova, N.; Borovok, I.; Berggren, G.; Hofer, A.; Logan, D. T.; Sjoberg, B. M., Novel ATP-cone-driven allosteric regulation of ribonucleotide reductase via the radical-generating subunit. *Elife* **2018**, 7.
25. Rose, H. R.; Maggiolo, A. O.; McBride, M. J.; Palowitch, G. M.; Pandelia, M. E.; Davis, K. M.; Yennawar, N. H.; Boal, A. K., Structures of Class Id Ribonucleotide Reductase Catalytic Subunits Reveal a Minimal Architecture for Deoxynucleotide Biosynthesis. *Biochemistry-US* **2019**, 58 (14), 1845-1860.
26. Hogbom, M.; Stenmark, P.; Voevodskaya, N.; McClarty, G.; Graslund, A.; Nordlund, P., The radical site in chlamydial ribonucleotide reductase defines a new R2 subclass. *Science* **2004**, 305 (5681), 245-248.
27. Bollinger, J. M.; Jiang, W.; Green, M. T.; Krebs, C., The manganese(IV)/iron(III) cofactor of Chlamydia trachomatis ribonucleotide reductase: structure, assembly, radical initiation, and evolution. *Curr Opin Struc Biol* **2008**, 18 (6), 650-657.
28. Griese, J. J.; Kositzki, R.; Schrapers, P.; Branca, R. M. M.; Nordstrom, A.; Lehtio, J.; Haumann, M.; Hogbom, M., Structural Basis for Oxygen Activation at a Heterodinuclear Manganese/Iron Cofactor. *J Biol Chem* **2015**, 290 (42), 25254-25272.
29. Jiang, W.; Xie, J. J.; Varano, P. T.; Krebs, C.; Bollinger, J. M., Two Distinct Mechanisms of Inactivation of the Class Ic Ribonucleotide Reductase from Chlamydia trachomatis by

Hydroxyurea: Implications for the Protein Gating of Intersubunit Electron Transfer. *Biochemistry-Us* **2010**, *49* (25), 5340-5349.

30. Scheuner, C.; Tindall, B. J.; Lu, M.; Nolan, M.; Lapidus, A.; Cheng, J. F.; Goodwin, L.; Pitluck, S.; Huntemann, M.; Liolios, K.; Pagani, I.; Mavromatis, K.; Ivanova, N.; Pati, A.; Chen, A.; Palaniappan, K.; Jeffries, C. D.; Hauser, L.; Land, M.; Mwirichia, R.; Rohde, M.; Abt, B.; Detter, J. C.; Woyke, T.; Eisen, J. A.; Markowitz, V.; Hugenholtz, P.; Goker, M.; Kyrpides, N. C.; Klenk, H. P., Complete genome sequence of *Planctomyces brasiliensis* type strain (DSM 5305(T)), phylogenomic analysis and reclassification of Planctomycetes including the descriptions of *Gimesia* gen. nov., *Planctopirus* gen. nov and *Rubinisphaera* gen. nov and emended descriptions of the order Planctomycetales and the family Planctomycetaceae. *Stand Genomic Sci* **2014**, *9* (1).

31. Bauld, J.; Staley, J. T., *Planctomyces-Maris* Sp-Nov - Marine Isolate of *Planctomyces-Blastocaulis* Group of Budding Bacteria. *J Gen Microbiol* **1976**, *97* (Nov), 45-55.

32. Dassama, L. M. K.; Krebs, C.; Bollinger, J. M.; Rosenzweig, A. C.; Boal, A. K., Structural Basis for Assembly of the Mn-IV/Fe-III Cofactor in the Class Ic Ribonucleotide Reductase from *Chlamydia trachomatis*. *Biochemistry-Us* **2013**, *52* (37), 6424-6436.

33. Jiang, W.; Hoffart, L. M.; Krebs, C.; Bollinger, J. M., A manganese(IV)/iron(IV) intermediate in assembly of the manganese(IV)/iron(III) cofactor of *Chlamydia trachomatis* ribonucleotide reductase. *Biochemistry-Us* **2007**, *46* (30), 8709-8716.

34. Jiang, W.; Saleh, L.; Barr, E. W.; Xie, J. J.; Gardner, M. M.; Krebs, C.; Bollinger, J. M., Branched activation- and catalysis-specific pathways for electron relay to the manganese/iron cofactor in ribonucleotide reductase from *Chlamydia trachomatis*. *Biochemistry-Us* **2008**, *47* (33), 8477-8484.

35. Jiang, W.; Bollinger, J. M.; Krebs, C., The active form of Chlamydia trachomatis ribonucleotide reductase R2 protein contains a heterodinuclear Mn(IV)/Fe(III) cluster with S=1 ground state. *J Am Chem Soc* **2007**, *129* (24), 7504-+.
36. Fritscher, J.; Artin, E.; Wnuk, S.; Bar, G.; Robblee, J. H.; Kacprzak, S.; Kaupp, M.; Griffin, R. G.; Bennati, M.; Stubbe, J., Structure of the nitrogen-centered radical formed during inactivation of E-coli ribonucleotide reductase by 2 '-azido-2 '-deoxyuridine-5 '-diphosphate: Trapping of the 3 '-ketonucleotide. *J Am Chem Soc* **2005**, *127* (21), 7729-7738.
37. Bollinger, J. M. On the chemical mechanism of assembly of the tyrosyl radical-dinuclear iron cluster cofactor of E. coli ribonucleotide reductase. Massachusetts Institute of Technology, Boston, MA, 1993.
38. <https://web.expasy.org/protparam/>, Accessed in years 2013-2017.
39. Gill, S. C.; von Hippel, P. H., Calculation of protein extinction coefficients from amino acid sequence data. *Anal Biochem* **1989**, *182* (2), 319-26.
40. Jiang, W. FORMATION AND FUNCTION OF A NOVEL HETEROBINUCLEAR MN/FE REDOX COFACTOR IN RIBONUCLEOTIDE REDUCTASE FROM CHLAMYDIA TRACHOMATIS. Penn State, University Park, 2007.
41. Price, J. C.; Barr, E. W.; Tirupati, B.; Bollinger, J. M., Jr.; Krebs, C., The first direct characterization of a high-valent iron intermediate in the reaction of an alpha-ketoglutarate-dependent dioxygenase: a high-spin FeIV complex in taurine/alpha-ketoglutarate dioxygenase (TauD) from Escherichia coli. *Biochemistry-Us* **2003**, *42* (24), 7497-508.
42. Stoll, S.; Schweiger, A., EasySpin, a comprehensive software package for spectral simulation and analysis in EPR. *J Magn Reson* **2006**, *178* (1), 42-55.
43. Kazan Viewer-Homepage Alexey Silakov: <https://sites.google>.

com/site/silakovalexey/kazan-viewer; accessed July 7, 2017.

44. <http://efi.igb.illinois.edu/efi-est>, Accessed May 10th 2017.
45. Tong, W. H.; Chen, S.; Lloyd, S. G.; Edmondson, D. E.; Huynh, B. H.; Stubbe, J., Mechanism of assembly of the diferric cluster-tyrosyl radical cofactor of Escherichia coli ribonucleotide reductase from the diferrous form of the R2 subunit. *J Am Chem Soc* **1996**, *118* (8), 2107-2108.
46. Saleh, L. OXYGEN ACTIVATION AND ELECTRON TRANSFER IN CLASS I RIBONUCLEOTIDE REDUCTASE. Penn State University, University Park, PA, 16802, 2005.
47. Bollinger, J. M.; Stubbe, J.; Huynh, B. H.; Edmondson, D. E., Novel Diferric Radical Intermediate Responsible for Tyrosyl Radical Formation in Assembly of the Cofactor of Ribonucleotide Reductase. *J Am Chem Soc* **1991**, *113* (16), 6289-6291.
48. Saleh, L.; Bollinger, J. M., Jr., Cation mediation of radical transfer between Trp48 and Tyr356 during O₂ activation by protein R2 of Escherichia coli ribonucleotide reductase: relevance to R1-R2 radical transfer in nucleotide reduction? *Biochemistry-Us* **2006**, *45* (29), 8823-30.
49. Atkin, C. L.; Thelander, L.; Reichard, P.; Lang, G., Iron and Free-Radical in Ribonucleotide Reductase - Exchange of Iron and Mossbauer-Spectroscopy of Protein-B2 Subunit of Escherichia-Coli Enzyme. *J Biol Chem* **1973**, *248* (21), 7464-7472.
50. Ator, M.; Salowe, S. P.; Stubbe, J.; Emptage, M. H.; Robins, M. J., 2'-Azido-2'-Deoxynucleotide Interaction with Escherichia-Coli Ribonucleotide Reductase - Generation of a New Radical Species. *J Am Chem Soc* **1984**, *106* (6), 1886-1887.
51. VANDERDONK, W. S., J; GERFEN, GJ; et al., EPR INVESTIGATIONS OF THE INACTIVATION OF ESCHERICHIA-COLI RIBONUCLEOTIDE REDUCTASE WITH 2'-

AZIDO-2'-DEOXYURIDINE 5'-DIPHOSPHATE - EVIDENCE FOR THE INVOLVEMENT OF THE THIYL RADICAL OF C225-R1. *J Am Chem Soc* **1995**, *117* (35), 8908-8916.

52. Pierce, B. S.; Hendrich, M. P., Local and global effects of metal binding within the small subunit of ribonucleotide reductase. *J Am Chem Soc* **2005**, *127* (10), 3613-23.

53. Lyle, K. S.; Haas, J. A.; Fox, B. G., Rapid-mix and chemical quench studies of ferredoxin-reduced stearyl-acyl carrier protein desaturase. *Biochemistry-Us* **2003**, *42* (19), 5857-66.

54. Roshick, C.; Iliffe-Lee, E. R.; McClarty, G., Cloning and characterization of ribonucleotide reductase from *Chlamydia trachomatis*. *J Biol Chem* **2000**, *275* (48), 38111-38119.

Chapter 3

Across Species and Subclasses Ribonucleotide

Reduction: Insight into the Multi-Step Radical

Translocation Mechanism in class I RNRs

Across Species and Subclasses Ribonucleotide Reduction: Insight into the Multi-Step Radical Translocation Mechanism in class I RNRs

Jovan Livada,^a Gordon Zrelak, Carsten Krebs,^{a,b} and J. Martin Bollinger, Jr.,^{a,b}

Departments of ^aChemistry and of ^bBiochemistry and Molecular Biology, Pennsylvania State University, University Park, PA USA 16802.

ABSTRACT

The life-essential catalytic reaction performed by ribonucleotide reductases (RNRs) is the sole known way of converting ribonucleotides to deoxyribonucleotides. All RNRs use a transient cysteine thiyl radical (Cys•) to abstract a hydrogen atom (H•) from the 3' position of the ribose ring of ribonucleotides and thus initiate ribonucleotide reduction. Based on the method of generating the Cys•, RNRs are divided into three major classes (I-III), while class I is further divided into five subclasses (a-e). Class I RNRs that are typically found in eukaryotic organisms and pathogenic bacteria contain an active oxidant generating smaller subunit β and a larger subunit α where the transient Cys• is formed during catalysis. The radical translocation (RT) process from the active oxidant in β to the catalytic Cys in α is a multi-step process which involves multiple proton transfers (PTs) and several redox active residues that span both the α and β subunits. Class I RNRs are divided into five subclasses based on the intrinsic properties of the β subunit, specifically the use of (i) a dimetal center (Mn₂, Fe₂, Mn/Fe, or none), (ii) the active oxidant (Y•, DOPA•, Mn^{IV}), (iii) oxygen species required for active oxidant generation (O₂ or O₂^{•-}), and (iv) the requirement of an activase protein NrdI. In this work, we have identified closely related

genome clusters that both encode for the RNR α and β subunits that belong to two different subclasses Ia and Ic. We have identified and characterized two RNRs that belong to these clusters, RNR from *Methylococcus capsulatus* (*Mc*) as a class Ia member that uses a $Y\bullet$ as the active oxidant and the class Ic RNR from *Salinisphaera hydrothermalis* (*Sh*) that uses Mn^{IV} as the active oxidant. We showed that the heterologous pairs of subunits α and β that belong to a different class I RNR subclass can competently perform bidirectional radical translocation. Therefore, we concluded there were no adaptations required for activity made to either subunit to accommodate a complementary subunit from a different subclass except for the evolution of the β subunit to host a distinct active cofactor. We have shown first experimental evidence that the multi-step, one electron, multiple proton transfer mechanism is likely conserved between the class Ia and Ic RNR subclasses, and we can speculate that this mechanism is conserved in all class I RNR subclasses (a-e).

INTRODUCTION

Ribonucleotide reductases (RNRs) are responsible for all *de novo* production of deoxyribonucleotides for all living organisms by catalyzing the essential reduction of ribonucleotides.¹ This family of enzymes is divided into three classes (I, II, and III) depending on the strategy used to generate an essential transient Cys• that initiates ribonucleotide reduction.¹⁻³ In addition to the essential cysteine residue that is transiently oxidized during catalysis, the active site harbors two reduced cysteine residues (in RNR classes I and II) that are oxidized during the catalytic cycle in order to provide the electron equivalents to the substrate.⁴ Alternatively, in class III RNRs, formate is responsible for substrate reduction. All class I RNRs structurally contain two subunits: the larger α subunit that harbors the substrate binding site and the smaller β subunit that uses an active oxidant to generate the Cys• in α .² In this work, we are exclusively concerned with class I RNRs that are further divided into five subclasses (a-e).⁵ The subclass defining differences that lay in the smaller β subunit can be divided into four categories. One, the nature of the active oxidant (Y•, DOPA•, Mn^{IV}), two, the presence of a dimetal center (Fe/Fe, Mn/Mn, Mn/Fe, or none), three, the oxygen derived oxidizing species required for the formation of the active oxidant (O₂ or O₂^{•-}), and four, the necessity of an activase protein NrdI. Once catalytic conditions are established, the “radical hole” (resting on the active oxidant) in β is translocated into the α subunit via a chain of conserved redox active tyrosine residues that span both α and β subunits, to initiate ribonucleotide reduction.⁶ After product formation, the radical hole is translocated back into β . However, this reaction is not reversible because after product formation, the two cysteine residues in the active site are oxidized while the radical hole is translocated back to β . Therefore, we classify the radical translocation as bidirectional. This process has been characterized as a multi-step

reaction, where the electron transfer (ET) is long range (~35 Å) while there are multiple proton transfers believed to be local.⁷⁻⁹ While there has been significant progress made in the understanding of the mechanism of this reaction, some details still remain unclear, specifically, the communication between the two subunits.

Current literature suggests that a conformation change in both α and β subunits is required for ribonucleotide reduction.¹⁰ One of the noteworthy properties of the class I RNR β subunits is the remarkable stability of the active oxidant that forms the transient Cys• in the α subunit. In the hallmark class Ia RNR from *Escherichia coli* (*Ec*), the active cofactor and oxidant are the β -Fe^{III}/Fe^{III}-Y₁₂₂• complex. This complex is stable for days at 4 °C.¹¹ In the class Ic RNR β from *Chlamydia trachomatis* (*Ct*), the β -Mn^{IV}/Fe^{III} active cofactor is stable for hours at 4 °C. However, both cofactors are reduced *in vitro* on a millisecond time scale in the presence of the α subunit, the disulfide reductant dithiothreitol (DTT), the effector adenosine triphosphate (ATP) and the substrate cytidine diphosphate (CDP).^{12, 13} It has previously been shown that substrate binding in the holoenzyme complex triggers a conformational change in the α subunit that communicates a conformational change to the β subunit¹⁰ through either the PCET involved chain of residues or some other pathway. Studies of *Ec*¹² and *Ct*¹³ RNRs suggest that upon conformation change in β , a local proton transfer to the vicinity of the active oxidant is probable. Our group has shown in *Ct* RNR that the redox active residues involved in catalysis are not essential for the conformational change of the subunits nor the radical migration from the active oxidant in β . Therefore, it is likely that the α subunit communicates the conformational change to the β subunit via a mechanism that does not involve the redox active residues.

The complex one electron multiple proton RT process of hole transfer from the localized active oxidant in β to the catalytic Cys in α involves at a minimum four distinct ET steps that

involve one tyrosine residue in β and two tyrosine residues in the α subunit. Also, this process is likely gated by a proton transfer that is only possible upon substrate binding in the α subunit. Each of these individual ET steps may or may not be accompanied with a local PT step. This possible PT step can be either orthogonal to the ET step, or parallel – in the form of an effective H^\bullet transfer. Previous Mössbauer and density functional theory studies in *Ec* RNR⁷ suggest that the initial ET step is accompanied by an orthogonal PT step. In the same enzyme system, the probable second ET step involves the reduction of Y_{356}^\bullet and likely is not accompanied by local PT.¹⁴ The third and fourth ET steps located in the α subunit in *Ec* RNR involve the reduction of Y_{731}^\bullet and Y_{730}^\bullet sequentially to generate the catalytic Cys_{439}^\bullet . These two final ET steps are very likely accompanied by two consecutive and parallel H^+ transfer steps. However, we do not know if each individual ET step is directly coupled to the PT step (as H^\bullet transfer), or whether the two transfer steps are sequential.¹⁵ All the aforementioned details of this complex, one electron, multiple proton transfer mechanism have only been elucidated in class Ia RNRs. Most of the mechanistic details in other class Ib-e RNRs remain unknown.

The fact that class I RNR β subunits have evolved into five subclasses raises the question whether there were any other evolutionary modifications made to the subunit except for the oxidized active cofactor. Up until recently, the only member of the class Ic RNRs was the original RNR from *Chlamydia trachomatis*¹⁶. This RNR has been thoroughly studied and compared to the hallmark class Ia RNR from *Escherichia coli* (*Ec*). The comparison of these two enzymes^{13, 16} indicates that the redox active pathway residues involved in radical translocation between the α and β subunits are conserved between subclasses Ia and Ic RNRs. This finding presented a question of whether the key differences that pertain to the multi-step electron transfer (ET) mechanism between subclasses Ia and Ic RNRs are limited to the nature of the cofactor in the small subunit or

if the larger subunit coevolved as well. To answer this question the obvious idea would be to test for ribonucleotide reduction using an α subunit from *Ct* RNR and a β subunit from *Ec* RNR and vice versa. However, the modest sequence identity of both β (24%) and α (32%) indicates that this particular cross species α and β subunit binding is likely unfeasible. This is apparent in the comparison of the C-terminal tails that have been shown to be involved in subunit association,¹⁷ of *Ct* and *Ec* RNR β subunits. The *Ec* β RNR subunit C-terminal tail has 19 amino acid residues that succeed Y356, the residue involved in the radical translocation pathway, while the *Ct* β RNR has only 8 residues that succeed the final redox active residue involved in RT in *Ct* β , Y338. This significant difference in tail length would likely not allow the different RNR subunits between the two species to create favorable interactions, to associate and to potentially initiate ribonucleotide reduction.

To remedy the issues subunit association, we identified putative class Ia and class Ic pairs that exhibit both higher overall sequence identity and similarity of the C-terminal tails involved in subunit association. In this work, we have chosen to pair a class Ia and a class Ic RNRs that contain significant sequence identity (~65%). The InterPro's Ribonucleotide reductase small subunit family (IPR000358) contains ~10,000 viable class I RNR members. We have previously^{18, 19} identified a sub-cluster of genes that is generated when minimal alignment score is set to 100 in the sequence similarity network. This sub-cluster contains genes that encode for both tentative class Ia and class Ic RNRs. This finding was based on the defining characteristics of each subclass, the D/Y residue dyad for class Ia RNRs and E/F dyad for class Ic RNRs.¹⁶ In May, 2017, the total sub-cluster contained 1110 ribonucleotide reductase encoding genes of which 931 contain the D/Y dyad and are tentative class Ia RNR enzymes and 179 contain the E/F dyad and are tentative class Ic RNRs. Interestingly, within this cluster, we have identified pairs of similar (~65% identical) β

RNR genes that encode for putative class Ia and class Ic β s. In a previous study, we identified a catalytically active class Ia RNR from *Methylococcus capsulatus* (*Mc*) and paired it with a very similar (67% identical β , and 69% identical α) tentative class Ic RNR from *Saccharopolyspora erythraea* (*Se*).¹⁸ Even though *Se* β can assemble a β -Mn^{IV}/Fe^{III} cofactor, current *in vitro* activity assay studies do not show that this cofactor is a competent radical translocation initiator.¹⁸ However, the reaction of *Mc* β and *Se* α RNRs yielded ribonucleotide reduction at a rate of 0.08 s⁻¹ β ⁻¹.¹⁸ The catalytic competency may suggest that the α subunits that belong to different subclasses may not have coevolved in any major way as it pertains to their catalytic mechanism along with the small subunit that has evolved to harbor a different metal cofactor. However, this result where the only cross subclass catalytic activity observed was with a class Ia β and a class Ic α and not vice versa, by its nature is not conclusive. In this work, we attempted to achieve across subclass and across species activity between RNR subunits where ribonucleotide reduction is possible both when class Ia β and class Ic α are combined and when class Ic β and class Ia α are combined. We have picked a new tentative class Ic ribonucleotide reductase to be paired with a catalytically active class Ia RNR from *M. capsulatus*. Similarly to the RNR from *G. maris* we chose a candidate whose genome possessed only a single, tentative class Ic RNR, in order to avoid the potential that the RNR of interest has lost its *in vivo* functionality through evolution. We picked the RNR from *Salinisphaera hydrothermalis* (*Sh*), because its β subunit is very similar to the β subunit from *Mc* with an amino acid residue identity of 65%. *Salinisphaera hydrothermalis* is a Gram-negative, aerobic, mesophilic facultatively chemolithoautotrophic, bacterium found in deep sea hydrothermal vents in the East Pacific Rise.²⁰

Using two catalytically competent RNRs that belong to different class I subclasses, we were able to show ribonucleotide reduction by using the α subunit of one subclass and the β subunit

from another and vice versa. In this work, we show that the RNR from *Mc* is a typical class Ia RNR that uses a Y^\bullet as the active oxidant while the RNR from *Sh* is a typical class Ic RNR that self assembles the $\beta\text{-Mn}^{\text{IV}}/\text{Fe}^{\text{III}}$ cofactor and uses the Mn^{IV} as the active oxidant. We have paired the subunits in such a way that the complement subunit belonged to a different subclass we were able to observe bidirectional radical translocation. By achieving ribonucleotide reduction with the α subunit from one RNR subclass and organism and the β subunit from another RNR subclass and organism we present strong evidence that the α subunits have not coevolved to accommodate a β that uses a different active cofactor. With this, we present the first experimental evidence that suggests that the complex, one electron, multiple proton RT mechanism that was elucidated in class Ia RNRs is very likely conserved in class Ic RNRs. Based on this finding, we could speculate that the RT mechanism studied in *Ec* RNR could be conserved in all class I RNRs.

EXPERIMENTAL DETAILS

Overexpression and purification of the α and β RNR proteins

The vectors that contained the *Sh* and *Mc* gene sequences were inserted into the competent BL21(DE3) *E. coli* expression strain cells by heat shock for 45 seconds at 42 °C. The conditions used for the growth of *E. coli* cell strains were 37 °C in LB (Lysogeny broth) medium that contains 35 g/L tryptone, 20 g/L yeast extract, and 5g/L sodium chloride. The growth solution was after an autoclave procedure supplemented with 0.05 g/L kanamycin and grown to an OD₆₀₀ of 0.7-1.0. The cells were cooled rapidly to 4 °C by incubation on ice for 1 hour upon induced by addition of

Isopropyl β -D-1-thiogalactopyranoside (IPTG) in the 50 μ M concentration for the α subunits and 200 μ M for the β subunits. The overexpression was incubated for 16-24 h at 18 °C. The cells were harvested by centrifugation and the cell pellet was frozen in liquid N₂ and stored at -80 ° C or immediately used for purification. A typical yield was ~ 6.5g of wet cell paste per liter of culture. If necessary, the frozen cell paste was allowed to thaw in Tris-HCl buffer (pH 7.6, 50 mM) containing 10 mM imidazole, 10% (v/v) glycerol and 0.25 mM PMSF. The cell paste that contained the vectors encoding the α subunits were additionally supplemented with 10 mM β -mercaptoethanol. The cells were lysed via the use of a microfluidizer where the dissolved cell paste was exposed to 15000 kPA pressure 4 times. After lysis, the paste was centrifuged at 10000x g for 20 minutes. The supernatant was poured into a column containing Ni-NTA agarose (Qiagen or Biolabs). 300ml of wash buffer (20 mM imidazole) was applied to the column followed by ~50ml of elution buffer (250 mM imidazole) in order to elute the protein. The protein solution was further concentrated with the use of an ultrafiltration cell with a YM30 membrane (Amicon) to a concentration of ~1mM. All protein solutions were exchanged into 100mM HEPES buffer (pH 7.6, 10% glycerol) via dialysis. All protein solutions used to purify the α subunit contained additional 10 mM β -mercaptoethanol to preserve the thiols in their reduced state. The final buffer of all α subunits contained 10mM DTT. If further metal removal was necessary, the purified protein solution was further exposed to 10 mM EDTA for 4 hours and then dialyzed back in to the HEPES buffer that lacked EDTA.

Ferrozine chelating procedure for β subunits.

Typically, the β subunits were found to contain 0.7 and 0.05 equivalents of Fe and Mn respectively by ICP-AES analysis. While the manganese was removed via the EDTA chelation procedure described above the iron bound in the subunits was removed in the following way:²¹ Fe was first reduced in an anoxic environment to ferrous by a ~1 hour incubation @ 25 °C in the presence of sodium hydrosulfite (60 mM) and methyl viologen (20 μ M). Methyl viologen turned a bright blue color upon reduction by sodium hydrosulfite. Ferrozine was added in about 300-fold stoichiometrical excess. After the addition of ferrozine, the solution turned bright purple. Following a two-hour period of aerobic incubation, the protein solution was poured into a column packed with Sephadex G-50 resin in order to separate the protein from both the “free ferrozine” and the $\text{Fe}^{\text{II}}\text{-(ferrozine)}_3$ complex. This procedure sometimes needed to be applied twice. ICP-AES analysis indicated that there was 0.1 equivalent of iron per β . The protein was frozen at -80 °C for storage.

Protein concentration determination

Absorbance @ 280 nm was monitored by a UV-visible spectrometer (Agilent). Molar absorptivities of all protein solutions were calculated via the Expasy protparam²² software and the method of Gill and von Hippel.²³

Activity assay details of β subunits in the presence of excess α

Substrate CDP with the m/z of 402 and the product of ribonucleotide reduction dCDP with the m/z of 386 were both eluted with a mobile phase of a gradient of pure acetonitrile (**1**) and 25 mM ammonium formate (pH 9) (**2**). The elution gradient was the following:

10% **1** for 3 minutes followed by 10-50% **1** over 3 minutes, followed by 50% **1** for another 3 minutes and finally 50-10% **1** over 7 minutes. Both the substrate and the product were detected and quantified by mass spectrometry via the electrospray ionization in the (-) ion mode. The peak ratio of $[dCDP]/([CDP]+[dCDP]) \times [InitialCDP]$ was used to measure ribonucleotide reduction at each time point. Validation of these assays is presented in detail by Jiang.²⁴

EPR Spectroscopy

Field swept CW-EPR spectra were recorded on an ESP300 spectrometer (Bruker, Billerica, MA) equipped with an ER 041 MR Microwave Bridge and a 4102ST X-band resonator as described previously.²⁵ The cryostat responsible for liquid He storage was from Oxford Instruments.

Mössbauer Spectroscopy

We recorded Mössbauer spectra on the WEB research (Edina, MN) spectrometers operating in the constant acceleration mode in a transmission geometry. Temperature was held constant at 4.2K. For spectra where the low field of 53 mT was applied, the sample was kept inside a SVT-400 dewar (Janis, Wilmington, MA). Digital Tesla meter (model 132D) was used to record the magnitudes of the static magnetic fields. The probe used in these experiments was a Hall probe LPT 130-20S (Group3 Technologies Inc., Auckland, NZ).

Mössbauer Spectra simulations

WMOSS (Web Research, Edina, MN) was used on Windows 10 with the Windows 95 compatibility mode setting. The fluctuation rate of the electron spin was considered slow in comparison to the ^{57}Fe Larmor frequency in all our simulations.

Sequence Similarity Networks (SSN)

InterPro Databases (IPR000358 and IPR039718) were used to construct the SSNs that belonged to the β and α RNR subunits, respectively. The networks were generated via the Enzyme Similarity Tool (EFI-EST) web site.²⁶ The aforementioned family was used as input. All figures that concern SSN were generated via the Cytoscape software (v3.3.0 and v3.7.1).

RESULTS AND DISCUSSION

The RNR from *Methylococcus capsulatus* (*Mc*) is a class Ia RNR representative

The gene sequence that encodes for the β RNR subunit from *Methylococcus capsulatus* suggests that the RNR from *Mc* contains a key tyrosine, Y₁₈₂, that aligns with the Y₁₂₂ from *Ec* RNR β . Therefore, *Mc* RNR β likely belongs to class Ia RNRs and therefore uses O₂ to oxidize a β -Fe^{II}/Fe^{II} cofactor and generate the β -Fe^{III}/Fe^{III}-Y[•] active oxidant which initiates ribonucleotide reduction by generating the transient Cys[•] in the α subunit. To verify this hypothesis, we obtained the *Mc* β RNR gene and produced the His-tagged apoprotein via *E. coli* overexpression and purification. We added 2 equivalents per β of Fe^{II} to the enzyme in aerobic conditions, incubated the solution for 60 minutes and froze the protein solution in an EPR sample tube. EPR analysis of the sample (**Figure 1**)

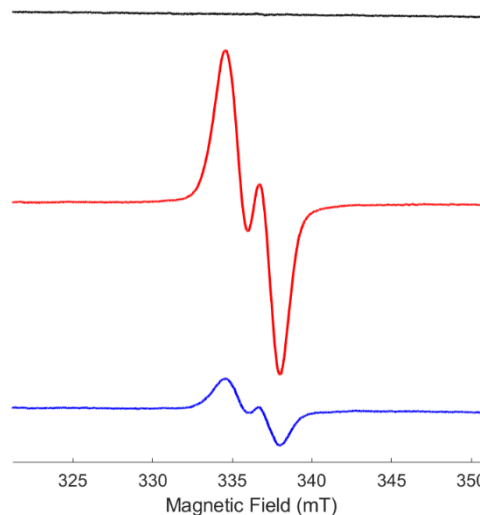


Figure 1. EPR spectra of the *Mc* β Y₁₈₂[•]. In black, the EPR spectrum of 160 μ M *Mc* β APO. In red, 160 μ M *Mc* β , reconstituted with 320 μ M Fe^{II} and incubated for 60 minutes with O₂. This trace corresponds to 64 μ M Y₁₈₂[•]. To obtain the blue trace, the same sample preparation was used as red except for the additional 20-minute incubation of the solution with 25 mM hydroxyurea. The blue trace corresponds to 13 μ M Y₁₈₂[•]. Experimental conditions: MW frequency 9.5 GHz, Temperature 70 K, MW power 31 dB, scan time 60 seconds, modulation amplitude 10 gauss, npoints 1024.

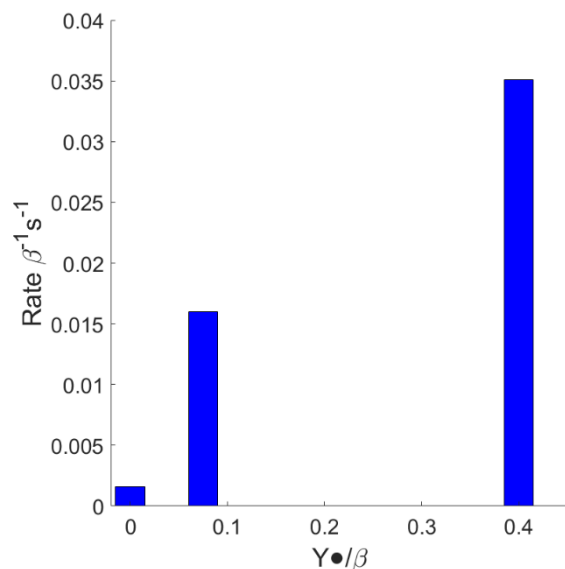


Figure 2. Bar graph that correlates the presence of the $Y_{182}\bullet$ in $Mc\ \beta$ and the rate of activity of the Mc RNR $\alpha\beta$ complex.

the RNR from Mc is indeed a class Ia RNR, we correlated the activity of the $Mc\ \alpha\beta$ complex with the presence of the $Y\bullet$ radical in $Mc\ \beta$ (**Figure 2**). The graph shows a clear positive correlation between the amount of $Y\bullet/\beta$ and the rate of ribonucleotide reduction of the $Mc\ \alpha\beta$ holoenzyme complex. Therefore, we can conclude that $Y_{182}\bullet$ is indeed the active oxidant in $Mc\ \beta$ responsible for the transient generation of the $Cys\bullet$ in $Mc\ \alpha$. These results suggest that the RNR from *Methylococcus capsulatus* belongs to the Ia RNR subclass. We have also optimized the *in vitro* reaction conditions and attempted to find the maximum rate of reduction possible per active oxidant, $Y\bullet$. The activity assay results in **Figure 3** indicate that doubling the

shows the generation of a radical signal at 70 K similar to the signal of $Y_{122}\bullet$ from *Ec* β .²⁷ The signal is ~10 mT wide and shows a doublet likely arising from the strong hyperfine interaction between the electron spin and the β -methylene protons.²⁸ In previous studies, hydroxyurea was shown to reduce the $Y_{122}\bullet$ to the met state of the cofactor $\beta\text{-Fe}^{\text{III}}/\text{Fe}^{\text{III}}\text{-YH}$.¹²

The EPR analysis of the apoprotein did not show any tyrosine radical signal. To verify that

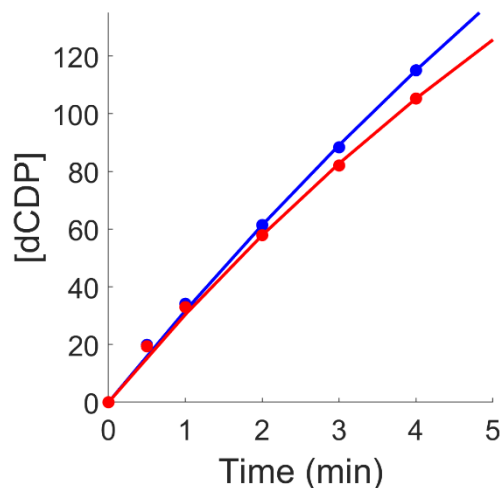


Figure 3. Reaction of the wt $Mc\ \beta$ with wt $Mc\ \alpha$. The exponential fits produced $0.14\ \text{s}^{-1}Y\bullet^{-1}$ rate of reaction when $5\ \mu\text{M}\ \beta_2$ (red) was used and the reaction rate of $0.28\ \text{s}^{-1}Y\bullet^{-1}$ when $2.5\ \mu\text{M}\ \beta_2$ (blue) was used. General reaction conditions: $25\ \mu\text{M}\ \alpha_2$, $2\ \text{mM}\ \text{ATP}$, $1\ \text{mM}\ \text{CDP}$, $10\ \text{mM}\ \text{DTT}$, and $10\ \text{mM}\ \text{MgCl}_2$. Reaction quenched with $2\ \text{M}$ formic acid.

amount of *Mc* β in the enzymatic reaction did not increase the total rate per $Y\bullet$. This led us to believe that even though the reaction mixture contained five times more *Mc* α than *Mc* β , the rate of reaction was limited by the poor activity of the *Mc* α subunit. Therefore, we set the lower limit for the rate of ribonucleotide reduction of the *Mc* $\alpha\beta$ complex to $0.28\text{ s}^{-1}Y\bullet^{-1}$.

The RNR from *Salinisphaera hydrothermalis* (*Sh*) is a bona fide class Ic RNR

Previously established methods of class Ic RNR β reconstitution and activation used for *Ct* and *Gm* β s did not yield any success in teasing out the cofactor assembly details of *Sh* RNR β and yielded very poor activation of *Sh* β *in vitro*. Therefore, we decided to explore other ways of activating the small subunit of *S. hydrothermalis*. To achieve a more favorable metal reconstitution of the small subunit of *Sh* RNR, we supplemented the *E. coli* growth medium with both manganese and iron to try to obtain the desired *Sh* β active $\beta\text{-Mn}^{\text{IV}}/\text{Fe}^{\text{III}}$ cofactor state *in vivo*. We have tested our yeast extract using the ferrozine assay for its iron content and determined that we have ~20

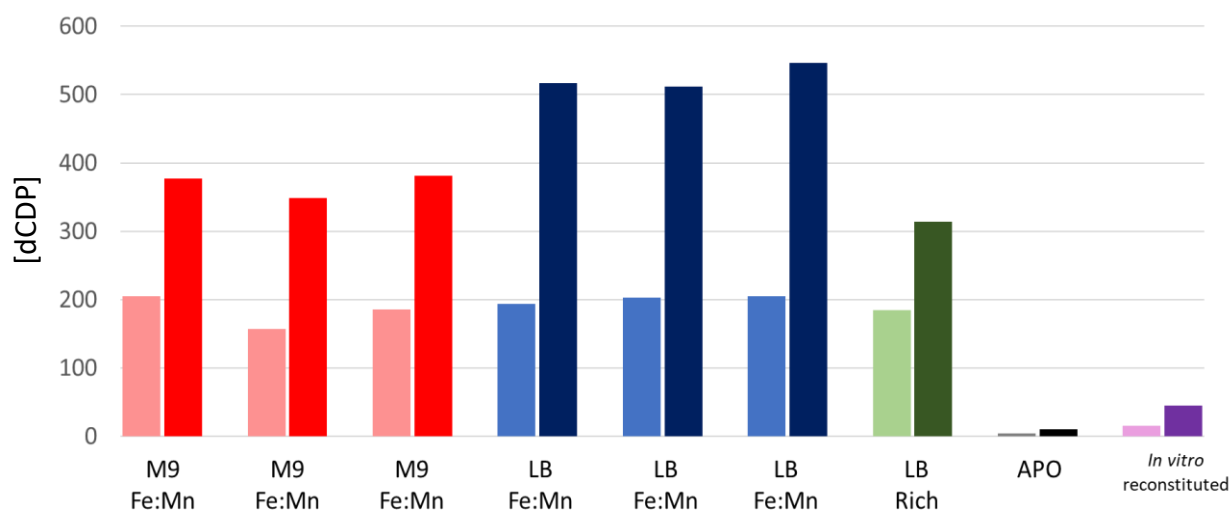


Figure 4 Obtained dCDP production dependent on the method used to activate *Sh* β . CDP reduced by utilizing *Sh* β overexpressed in M9 minimal medium (red), LB rich medium (blue) supplemented with different ratios of Mn and Fe to a total metal concentration of $250\text{ }\mu\text{M}$ in growth medium. Activity of *Sh* β overexpressed in non-metal supplemented LB rich medium (in green), *Sh* β APO (in black), and *in vitro* reconstituted and O_2 activated *Sh* β (in purple). Lighter shade colored bars represent the 3-minute reaction quench time-point while the darker colored bars represent the 10-minute reaction quench time-point dCDP production. Reaction was initiated by adding $10\text{ }\mu\text{M}$ of β_2 into a solution containing $50\text{ }\mu\text{M}$ *Sh* α_2 , 10 mM DTT, 1 mM CDP and 2 mM ATP. Reaction was quenched via the addition of 2 mM formic acid.

μM iron in LB rich medium. Literature suggested that manganese content compared to iron content in yeast extract was negligible.²⁹ Keeping the iron content of LB rich medium in mind, we have

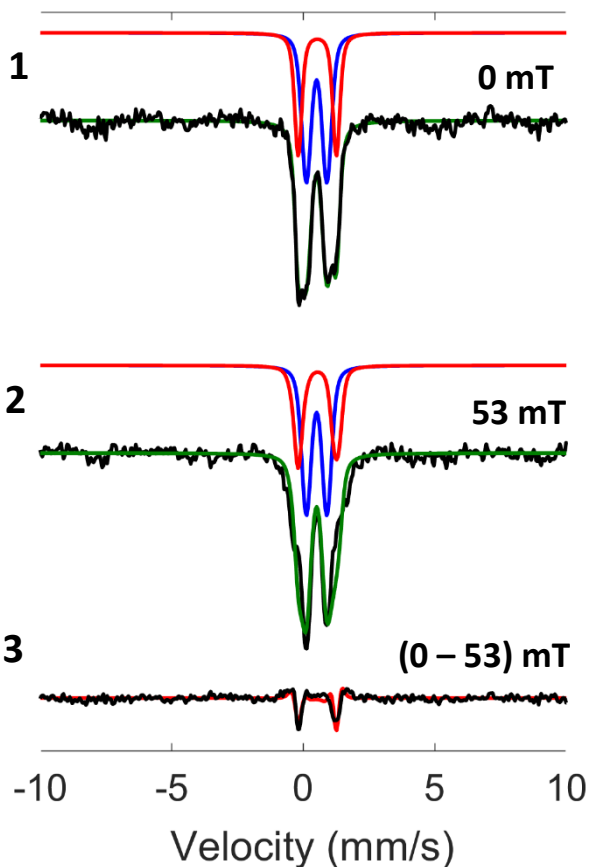


Figure 5. Mössbauer spectra of the activation product state of $^{55}\text{Mn}/^{57}\text{Fe}$ reconstituted and oxygen activated *Sh* β wt and subsequently treated with EDTA. The top traces represent the 0 field spectra (1), the middle traces represent the 53 mT applied and oriented parallel to the γ -beam spectra (2), and the bottom represent the difference between (1) and (2) spectra. Raw data are in black, red and blue traces in (1) and (2) represent the simulated contributions from $\beta\text{-Mn}^{\text{IV}}/\text{Fe}^{\text{III}}$, and $\beta\text{-Fe}^{\text{III}}/\text{Fe}^{\text{III}}$, respectively. In green are the simulated sum of the blue and red. Red in (3) the simulated difference spectra between green from (1) and (2).

applied the same Mössbauer data analysis on *Gm* β RNR. The raw data was simulated as a sum of the high spin ferric state with the ground state of the $S_{\text{total}} = 1$ for the $\beta\text{-Mn}^{\text{IV}}/\text{Fe}^{\text{III}}$ state and $S_{\text{total}} = 0$ for the unavoidable formation of the $\beta\text{-Fe}^{\text{III}}/\text{Fe}^{\text{III}}$ state. The exact parameters used for *Gm* β

proceeded to overexpress the *Sh* β subunit in both LB rich and M9 mediums supplemented with Mn and Fe in ratios 1:3, 1:1:, 3:1, Fe:Mn to a total metal concentration of 250 μM . To assess the activity of *Sh* β reconstituted *in vivo*, we have tested the six *Sh* β s that were overexpressed under different conditions, for CDP reduction (**Figure 4**). For comparison, we have also included comparable activity assessments of *Sh* β APO and our best *in vitro* reconstituted *Sh* β sample. Although poor, our best attempt of forming the $\beta\text{-Mn}^{\text{IV}}/\text{Fe}^{\text{III}}$ cofactor *in vitro* was done using the ^{57}Fe isotope in order to assess the cofactor in *Sh* β via Mössbauer spectroscopy (**Figure 5**).

Since the 0 mT and 53 mT Mössbauer spectra of the *Sh* β RNR resembled the spectra observed in both *Ct* and *Gm* RNR β s, we

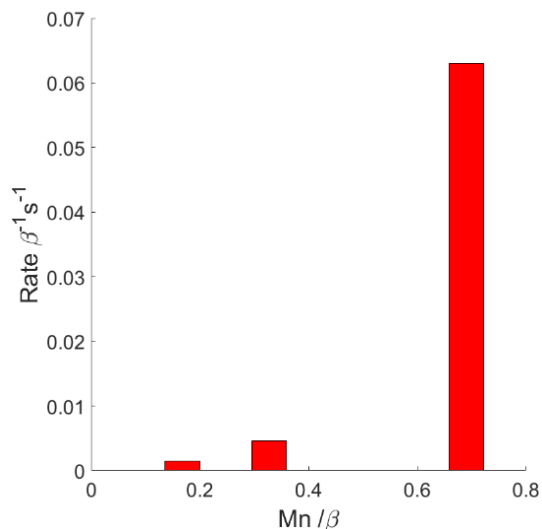


Figure 6. Bar graph that correlates the presence of total Mn in *Sh* β and the rate of activity of the *Sh* RNR $\alpha\beta$ complex. The lowest rate of reaction sample contained *Sh* β APO. The slightly more active reaction contained *Sh* β reconstituted *in vitro* (Mössbauer sample), while the most active reaction contained the *in vivo* reconstituted *Sh* β overexpressed in the *E. coli* host organism grown and in LB rich medium supplemented with 125 μM of both Mn and Fe.

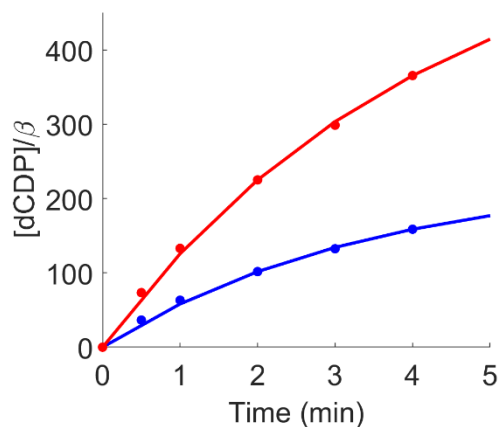


Figure 7. Reaction of the wt *Sh* β with wt *Sh* α . The exponential fits produced $0.34 \text{ s}^{-1}\text{Mn}^{-1}$ rate of reaction when $5 \mu\text{M}$ β_2 (red) was used and the reaction rate of $0.32 \text{ s}^{-1}\text{Mn}^{-1}$ when $2.5 \mu\text{M}$ β_2 (blue) was used. General reaction conditions: $25 \mu\text{M}$ α_2 , 2 mM ATP, 1 mM CDP, 10 mM DTT, and 10 mM MgCl_2 . Reaction quenched with 2 M formic acid.

$0.34 \text{ s}^{-1} \text{Mn}^{-1}$.

Mössbauer simulations were used here and while the diferric cofactor was simulated with parameters $\delta = 0.49 \text{ mm/s}$ and $\Delta E_Q = 0.83 \text{ mm/s}$ at 4.2 K , the Fe^{III} bound to Mn^{IV} was simulated with $\delta = 0.53 \text{ mm/s}$, $\Delta E_Q = 0.33 \text{ mm/s}$, and ^{57}Fe $A_{\text{HF}} = [-40.9, -36.6, -34.2] \text{ MHz}$ parameters. The relative amounts of iron in $\beta\text{-Mn}^{\text{IV}}/\text{Fe}^{\text{III}}$ and $\beta\text{-Fe}^{\text{III}}/\text{Fe}^{\text{III}}$ were determined to be 32% and 33% respectively. To present evidence that the *Sh* RNR β uses Mn^{IV} as the active oxidant and therefore is a member of class Ic RNRs, we attempted to correlate the activity of the *Sh* $\alpha\beta$ complex to the total amount of Mn in *Sh* β measured via ICP-MS methods. The bar graph in **Figure 6** shows positive correlation between the amount of Mn in *Sh* β and the reaction rate. Like for *Mc* RNR, we have also optimized the *in vitro* reaction conditions to attempted to find the maximum rate of reduction of the *Sh* $\alpha\beta$ complex. Upon doubling the amount of β in the reaction assay, we have observed the approximate doubling of the rate of ribonucleotide reduction. Therefore, we have determined that the maximum rate of reduction for the *Sh* $\alpha\beta$ complex is

Another way to test for RT and to test for the nature of the active cofactor in class Ic RNRs is via using the pathway radical scavenger, hydroxyurea (HU) and EPR spectroscopy. Previous studies on *Ct* RNR¹³ have indicated that the binding of the substrate was essential to opening the conformational gate that enabled the reduction of the active cofactor $\beta\text{-Mn}^{\text{IV}}/\text{Fe}^{\text{III}}$ in β to the EPR active, RT-product state $\beta\text{-Mn}^{\text{III}}/\text{Fe}^{\text{III}}$. To provide further evidence that the active oxidant in *Sh* RNR is Mn^{IV} , we attempted to reproduce this result in *Sh* RNR. The reaction of *Sh* α , *Sh* β , ATP,

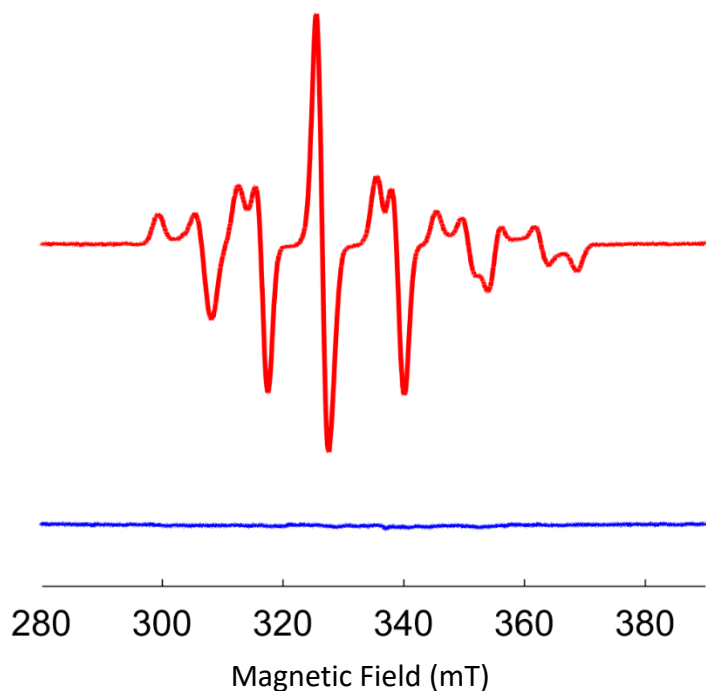


Figure 8. Field swept, CW-EPR spectra of the samples containing (in blue) 100 μM *Sh* β , 100 μM *Sh* α , 2mM ATP, 10 mM DTT, 10 mM HU, 10 mM MgCl_2 , and (in red) the sample contained all the ingredients as the sample in blue except for the additional 2mM CDP. Both samples were incubated for 10 minutes at 25°C prior to freezing. Experimental conditions: MW frequency 9.5 GHz, Temperature 15 K, MW power 20 dB, scan time 120 seconds, modulation amplitude 10 gauss, npoints 4096.

CDP, DTT, and HU confirmed that the presence of the substrate in the reaction mixture was essential in the formation of the RT-product $\beta\text{-Mn}^{\text{III}}/\text{Fe}^{\text{III}}$ cofactor state (**Figure 8**). This result provides evidence for the two following claims. One, the gated radical translocation mechanism in *Ct* RNR is likely present in *Sh* RNR, and two, that the active cofactor of *Sh* RNR is likely the $\beta\text{-Mn}^{\text{IV}}/\text{Fe}^{\text{III}}$, with the Mn^{IV} ion being the active oxidant.

In summary, three distinct experimental pieces of evidence together strongly suggest that *Sh* RNR uses Mn^{IV} as the active oxidant. One, Mössbauer spectroscopy has confirmed that *Sh* β can assemble a $\beta\text{-Mn}^{\text{IV}}/\text{Fe}^{\text{III}}$ cofactor. Two, reaction activity rates positively correlate with the total amount of manganese in

Sh β . And three, substrate binding in *Sh* α initiates radical translocation and generates the EPR detected RT-product $\beta\text{-Mn}^{\text{III}}/\text{Fe}^{\text{III}}$ cofactor state. This combined evidence indicates that *Sh* RNR is indeed a bona fide member of the class Ic RNR subclass that uses a Mn^{IV} in β as the active oxidant.

Heterologous catalytic activity of *Methylococcus capsulatus* and *Salinisphaera hydrothermalis* Ribonucleotide Reductases

To test if bidirectional radical translocation is feasible between heterologous pairs of α and β subunits that belong to different class I RNR subclasses, we have performed the appropriate activity assays (**Figure 9**). The data suggest that both heterologous $\alpha\beta$ complexes can perform

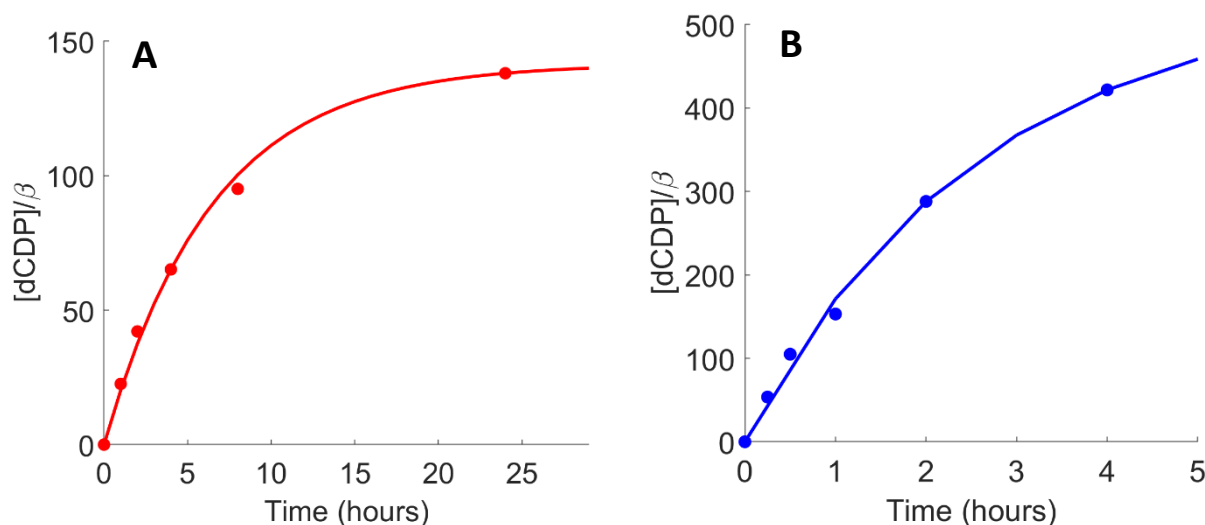


Figure 9. Reaction of the **A)** wt *Sh* β and wt *Mc* α complex and **B)** wt *Mc* β with wt *Sh* α complex. The exponential fits produced $0.53 \text{ min}^{-1}\text{Mn}^{-1}$ rate for **A)** and $0.14 \text{ s}^{-1}\text{Y}\cdot^{-1}$ for **B)** General reaction conditions: $5 \mu\text{M } \beta_2$, $25 \mu\text{M } \alpha_2$, 2 mM ATP , 2 mM CDP for **A)**, and 20 mM CDP for **B)**, 10 mM DTT , and 10 mM MgCl_2 . Reactions quenched with 2 M formic acid .

multiple turn-over ribonucleotide reduction, with the *Sh* β and *Mc* α complex performing with the $0.53 \text{ min}^{-1}\text{Mn}^{-1}$ rate of reaction and the *Mc* β and *Sh* α complex performing with the $0.14 \text{ s}^{-1}\text{Y}\cdot^{-1}$ rate of ribonucleotide reduction. We attribute the significantly poorer performance of the *Sh* β and *Mc* α complex to the inadequacy of the *Mc* α subunit as observed in the homologous reaction of *Mc* β and *Mc* α . To ensure that the rates shown indeed rise from the heterologous $\alpha\beta$ complexes

we have performed two control experiments. The first control experiment was concerned with the *Sh* β *Mc* α complex and it involved three reaction mixtures incubated for 7 hours that all possessed 2 mM ATP, 2 mM CDP, 10 mM DTT, and 10 mM MgCl₂. The reaction mixture that also contained 5 μ M *Sh* β ₂ has shown no conversion of CDP into dCDP via LCMS methods. The reaction mixture that contained 25 μ M *Mc* α ₂ in addition to the nucleotides only showed 16 μ M of dCDP when analyzed. We attribute this low amount of dCDP to reproducibly observed dCDP bound to both *Sh* α and *Mc* α subunits likely arising from cellular dCDP binding during overexpression in *E. coli*. The LCMS analysis of the reaction mixture that contained both 5 μ M *Sh* β and 25 μ M *Mc* α showed 600 μ M conversion of CDP to dCDP. The analogous control experiment was performed for the *Mc* β *Sh* α pair; the three reaction mixtures were incubated for 4 hours, no or minimal dCDP was observed in the reaction mixtures where only one RNR subunit was present and only in the mixture that contained both *Mc* β and *Sh* α did we observe significant ribonucleotide reduction (~2.5 mM dCDP in 4 hours). The combined results of these control experiments indicate that the reaction rates observed in **Figure 9** are indeed due to ribonucleotide reduction coming exclusively from two different heterologous pairs of α and β subunits.

To test whether the active cofactor in the reaction that involves the *Sh* β and *Mc* α was indeed the *Sh* β -Mn^{IV}/Fe^{III} cofactor we performed several experiments. Previous work on *Ct* RNR has shown that dithionite (DT) can univalently reduce the active cofactor of *Ct* RNR, β -Mn^{IV}/Fe^{III} to the catalytically inactive but EPR detectable β -Mn^{III}/Fe^{III} that is distinct from the RT-product β -Mn^{III}/Fe^{III} cofactor.¹³ Incubation of the active, *in vivo* reconstituted *Sh* β RNR for 5 minutes with 280 mM DT both significantly deactivated the *Sh* β cofactor in the *Sh* β *Mc* α reaction but also generated the inactive *Sh* β -Mn^{III}/Fe^{III} cofactor (**Figure 10**).

A different study of *Ct* RNR suggested that the inactive *Ct* β -Mn^{III}/Fe^{III} cofactor can be oxidized and reactivated to *Ct* β -Mn^{IV}/Fe^{III} via hydrogen peroxide (HOOH).³⁰ We have tested this property by using the heterologous pair of α and β subunits, the *Sh* β and *Mc* α complex. We show (**Figure 11**) that, although slightly, we were able to reactivate the inactivated *Sh* β -Mn^{III}/Fe^{III} complex via a 10-minute incubation of partially inactivated *Sh* β with 8 mM HOOH. By observing a partial increase in the rate of reaction (40% increase) we have likely achieved the oxidation of the *Sh* β -Mn^{III}/Fe^{III} state to the active *Sh* β -Mn^{IV}/Fe^{III} cofactor. By observing this result in the heterologous reaction of *Sh* β and *Mc* α we provide evidence that the active cofactor in this reaction is very likely the *Sh* β -Mn^{IV}/Fe^{III}.

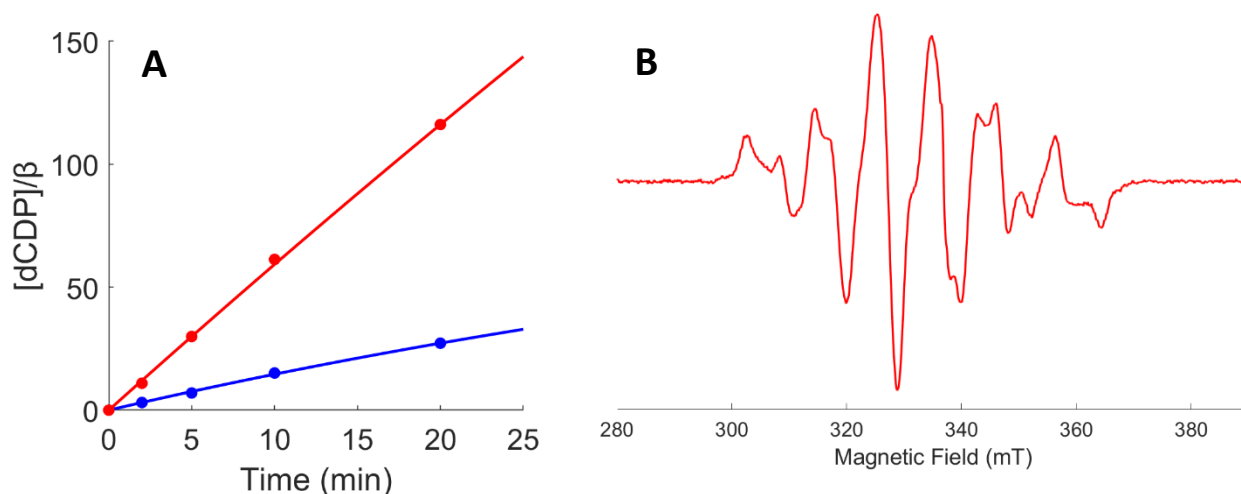


Figure 10. A) Reaction of the wt *Sh* β and wt *Mc* α complex (in red) yielded linear fits that produced $0.05 \text{ s}^{-1}\beta^{-1}$ rate or ribonucleotide reduction. The reaction of *Sh* β incubated with 280 mM DT for 5 minutes (in blue) with *Mc* α yielded the $0.014 \text{ s}^{-1}\beta^{-1}$ rate of reaction. Reaction conditions $2 \mu\text{M } \beta_2$, $25 \mu\text{M } \alpha_2$, 2 mM ATP, 0.5 mM CDP, 10 mM DTT, and 10 mM MgCl_2 . Reactions quenched with 2 M formic acid. **B)** Field swept CW-EPR spectrum of the sample containing the active *Sh* β RNR incubated with 280 mM DT for 5 minutes. Experimental conditions: MW frequency 9.5 GHz, Temperature 15 K, MW power 20 dB, scan time 120 seconds, modulation amplitude 10 gauss, npoints 4096.

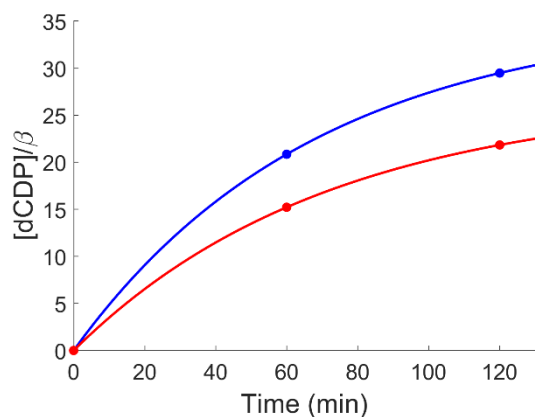


Figure 11. Reaction of the DT inactivated *Sh* β and *Mc* α complex (in red), and the reaction of the inactivated and subsequently reactivated *Sh* β via a 10-minute incubation of the smaller subunit with 8 mM HOOH, with *Mc* α . The reactivation process increased the rate of reaction from $0.37 \text{ min}^{-1} \beta^{-1}$ to $0.52 \text{ min}^{-1} \beta^{-1}$. Reaction conditions $2 \mu\text{M } \beta_2$, $25 \mu\text{M } \alpha_2$, 2 mM ATP, 0.5 mM CDP, 10 mM DTT, and 10 mM MgCl_2 . Reactions quenched with 2 M formic acid.

that involved the substrate analog N_3UDP . In the reaction of *Sh* β and *Mc* α in the presence of DTT, ATP, and N_3UDP , an active complex should yield the increase of the RT product cofactor state in *Sh* β as well as the formation of the N^\bullet radical in the *Mc* α subunit. We have performed the desired EPR experiment on a sample that contained both the *Sh* β and *Mc* α subunits, ATP, DTT, and the substrate analog, N_3UDP . We have detected the EPR signals typical for the RT product $\beta\text{-Mn}^{\text{III}}/\text{Fe}^{\text{III}}$ state and the N^\bullet (**Figure 12-A**). Like with the *Gm* and *Ct* RNRs, at 14 K we observed the $S_{\text{Total}} =$

We used yet another way to confirm that the complex of *Sh* β and *Mc* α RNR subunits is indeed capable of reducing ribonucleotides via the Mn^{IV} active oxidant. We have performed an experiment

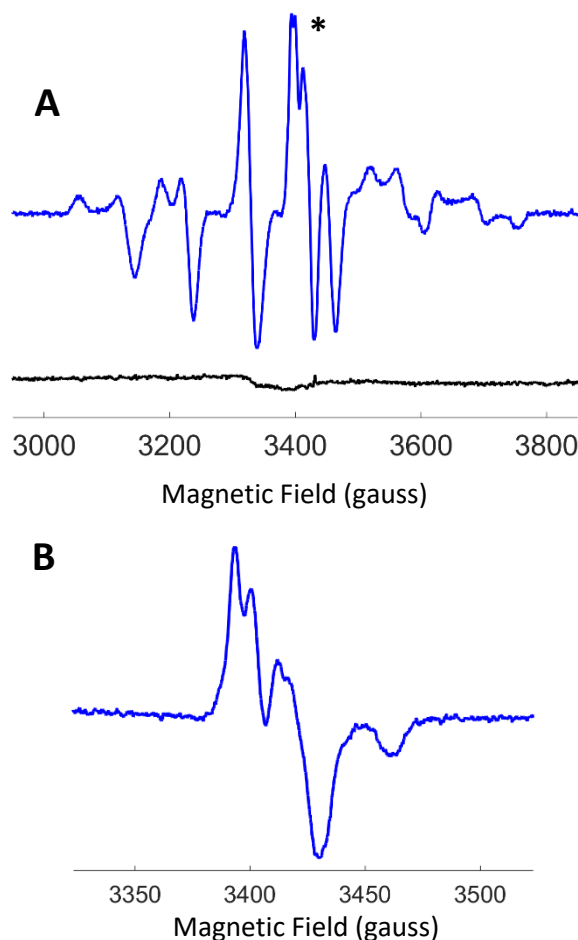


Figure 12. (A) Field swept X-band CW-EPR spectra of the *Sh* β RNR, $\beta\text{-Mn}^{\text{III}}/\text{Fe}^{\text{III}}$ RT product state (blue) (B) and the nitrogen centered radical. Both were generated via the reaction of $200 \mu\text{M } Sh \beta_2$, $300 \mu\text{M } Mc \alpha_2$, 10 mM DTT, 2 mM ATP and 1 mM N_3UDP . The black spectrum in (A) was obtained from the control reaction that did not contain the substrate analog. Asterisk indicates the location of the saturated signal of the N^\bullet in *Mc* α . Spectrometer conditions: Temperature 14 K for (A) and 100 K for (B), microwave frequency, 9.48 GHz; microwave power, 20 μW ; modulation frequency, 100 kHz; modulation amplitude, 10 G; scantime, 180 s for (A), 60 s for (B); npoints 1024.

$\frac{1}{2}$ antiferromagnetically spin coupled system between Mn^{III} and Fe^{III} where the EPR signal is characterized by the strong hyperfine interaction between the electron spin and the ^{55}Mn nucleus. The nitrogen centered radical is saturated at 14 K but is well resolved at 100 K (**Figure 12-B**). The control reaction sample that did not contain 2'-azido-UDP, showed no X-band EPR signals and therefore, confirms that the EPR signals that we observe in the N_3UDP reaction do indeed result exclusively from inter-subunit radical translocation.

Discussion and Outlook

The activation process of *Sh* β remains a puzzle. However, Mössbauer spectroscopy confirmed that the presence of both the $\beta\text{-Mn}^{\text{IV}}/\text{Fe}^{\text{III}}$ and the $\beta\text{-Fe}^{\text{III}}/\text{Fe}^{\text{III}}$ cofactors in *Sh* β upon the anoxic addition of Mn^{II} and Fe^{II} to *Sh* β APO and subsequent exposure to O_2 . Most likely, the *in vitro* metal loading process of *Sh* β is distinct from the metal loading processes of *Ct* and *Gm* β RNRs. To understand the complexities of the reconstitution and oxygen activation of *Sh* β further experimentation is required. At the moment, the most effective way known to us of assembling the $\beta\text{-Mn}^{\text{IV}}/\text{Fe}^{\text{III}}$ active cofactor in *Sh* β is reconstitution and activation *in vivo* with *Sh* β overexpressed in *E. coli* that are grown in LB rich medium. We can speculate that according to our activity assays, supplementation of the LB rich medium with Mn and Fe does not seem to significantly affect the amount of the active cofactor produced. To solidify this hypothesis that *E. coli* can *in vivo* reconstitute and activate *Sh* β to a significant degree, we could grow the *E. coli* in minimal medium and supplement the growth solution with ^{57}Fe so that we can analyze the active cofactor of *Sh* β reconstituted *in vivo* by Mössbauer spectroscopy.

Using an array of methods which include, activity assays, Mössbauer and EPR spectroscopies, we were able to characterize *Mc* and *Sh* RNRs as class Ia and class Ic RNRs, respectively. Also using activity assays, we were able to show that the *Sh* β *Mc* α and *Mc* β *Sh* α

complexes are characterized by turnover numbers of ~140 and ~400, respectively. With the turnover numbers in the hundreds, we can conclude that the heterologous class Ia and Ic $\alpha\beta$ complexes can perform bidirectional radical translocation. Therefore, we concluded there were no adaptations made required for activity, to either subunit to accommodate a complementary subunit from a different subclass except for the change of the β subunit to host a distinct active cofactor. Thus, the RT mechanism for classes Ia and Ic is likely the same.

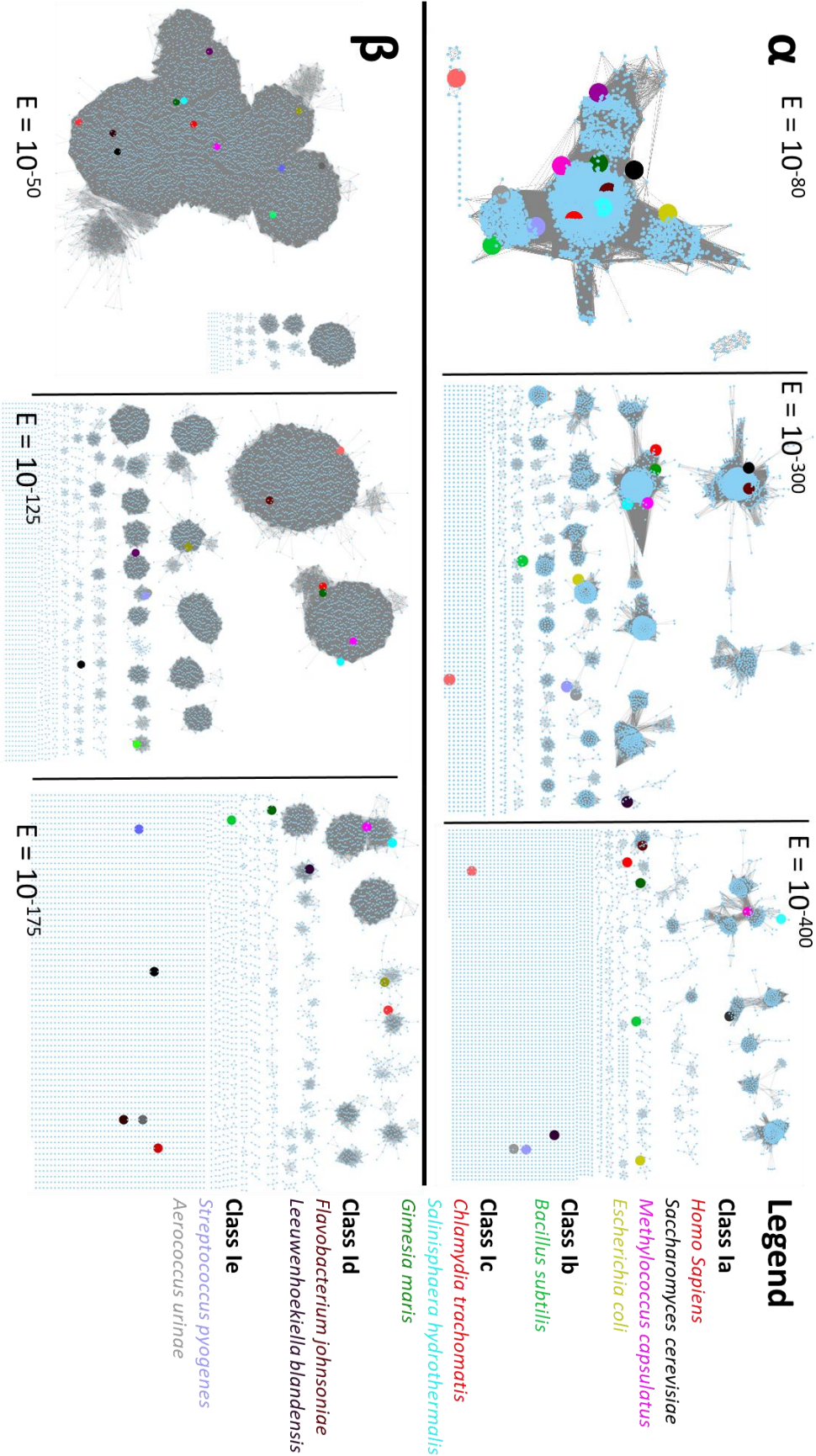


Figure 13. Sequence similarity networks of InterPro IPR000358 and IPR039718 super-families that represent all RNR β and α subunit genes, respectively. The nodes that represent class I RNR notable representatives are color coded in the legend. All gene sequences that are 80% identical are combined into distinct nodes. The network was generated in June 2019 and visualized via the Cytoscape software package.

The sequence similarity network (SSN) analysis of both the α and β RNR gene encoding sequences indicate that, compared to most other *in vitro* characterized class I RNRs, the sub-cluster that contains both class Ia and Ic RNRs has, by far, least diverged (**Figure 13**). While all other gene sequences that encode for other well established RNRs have diverged, at low expect value stringencies ($E = 10^{-400}$ for α and $E = 10^{-175}$ for β), the class Ia RNR from *Mc* (magenta) and the class Ic RNR from *Sh* (teal) still share the same gene cluster. By observing bidirectional radical translocation in heterologous pairs of class Ia and Ic RNR subunits, we can draw four important conclusions. One, previous studies have shown that both the class Ia and class Ic RNRs are characterized by a gated mechanism that involves substrate binding in the α subunit. In this work, using EPR spectroscopy, we have shown in the heterologous pair that included a class Ic β and a class Ia α , that substrate binding in the larger subunit was essential for RT. Therefore, we present the first piece of experimental evidence that the gated mechanism is likely the same in classes Ia and Ic RNRs. Two, the α subunits were able to use substantially different active cofactors and active oxidants when paired with heterologous β subunits. In the case of class Ia RNRs, the active cofactor is $\beta\text{-Fe}^{\text{III}}/\text{Fe}^{\text{III}}$ paired with the active oxidant Y^\bullet , which is an organic radical. In class Ic RNRs, the active cofactor is $\beta\text{-Mn}^{\text{IV}}/\text{Fe}^{\text{III}}$, with the active oxidant being an oxidized metal, Mn^{IV} . Three, sequence similarity network analysis of both subunits individually suggests that of all class I RNRs, the cluster in which *Mc* and *Sh* RNR gene sequences belong to seems to have diverged the least. It gives us the impression that the only significant evolutionary difference in this sub-cluster is the change of the β subunit to host a different active cofactor and use a different active oxidant. Therefore, there may have been evolutionary pressure, a possible lack of manganese (since its ~ 2 orders of magnitude less abundant than iron)³¹ in an organism's environment, in the distant past. Such pressure could have been responsible for the evolution of its RNR β subunit to

use a different, more abundant metal (possibly iron). And four, we present the first experimental evidence that the complex multi-step, one electron, multiple proton transfer mechanism that has been virtually exclusively elucidated in *Ec* class Ia RNR, is conserved between the class Ia and Ic RNR subclasses and we can postulate that this mechanism is conserved in all class I RNR subclasses (a-e).

By contrasting the sequences of C-terminal tails of *Sh* β and *Mc* β , we can observe a striking similarity between the residues that succeed the RT involved, redox active cognates of Y356 from *Ec* β ; Y393 in *Sh* β and Y394 in *Mc* β . Both the class Ic and class Ia representatives have nine residues in this region that are strikingly similar except for a threonine in position 399 in *Mc* β that is replaced by an alanine in the equivalent 398 position in *Sh* β . It was previously shown in *Ec*

Ec β : YLVGQIDSEVDTDDL SNFQL
Mc β : YQTGGTLSWD
Sh β : YQTGGALSWD

Figure 14. Gene sequence alignment focused on the region that succeeds the final tyrosine of the sequence in *Ec*, *Ct*, and *Sh* β subunits. This Y residue is the last redox active residue involved in PCET during ribonucleotide reduction. Sequence alignment performed by the EMBL-EBI Omega tool.

RNR that the residues that succeed the final RT redox active residue (Y356) in the small subunit are essential for subunit association and therefore activity.¹⁷ By choosing the representatives with nearly identical C-

terminal tails we could have essentially removed the issue of subunit binding, narrowing down the differences between the subclasses Ia and Ic representatives to the nature of the oxidizing agent in the small subunit and the multi-step radical translocation pathway. By observing multiple turnovers in reactions that involved β and α subunits from different species and subclasses, we can conclude that the RT process is achieved in both the forward and back directions. The RT details are most likely conserved in the larger subunit between class Ia and class Ic RNRs. Additionally, it seems like that only difference that pertains to the mechanism of ribonucleotide reduction between *Sh* and *Mc* RNRs lies in the small subunit, specifically in the cofactor. Even though the

two classes utilize a different strategy to generate the resting radical translocation state in β , class Ia a $\beta\text{-Fe}^{\text{III}}/\text{Fe}^{\text{III}}\text{-Y}\bullet$ cofactor and class Ic a $\beta\text{-Mn}^{\text{IV}}/\text{Fe}^{\text{III}}$ cofactor, the rest of the RT details likely remain the same. Therefore, all of the relevant differences are narrowed down to the two subclass defining residues: where in class Ia RNR β s an aspartate ligates to site 1 and the active oxidant lays on a nearby tyrosine, while in class Ic, instead of an aspartate, a glutamate ligates site 1 and the nearby tyrosine is replaced by the redox inert phenylalanine. In addition to the two key residues above there might be other amino acid residues involved in the active cofactor generation or stabilization. For future studies, it would be interesting to probe which of the residues in β are responsible for forming which cofactor. We have previously shown¹⁸ that *Se* β variant that possesses the D/Y dyad can assemble the $\beta\text{-Fe}^{\text{III}}/\text{Fe}^{\text{III}}\text{-Y}\bullet$ cofactor. However, the tyrosyl radical was not stable enough to show that this variant is catalytically competent. Perhaps there are other amino acid features of the active site of class Ia β s that are required for stabilizing the active oxidant that are not present in class Ic β s. Therefore, the conversion of a class Ic β into a class Ia β may not be as simple as exchanging the subclass defining D and Y residues into E and F, and vice versa. In this work, we have laid solid groundwork for studies that would include the inter-conversion of β subunits to a different RNR subclass.

While we had success observing bidirectional radical translocation in RNRs with high sequence similarity, it could be possible to intelligently engineer a chimeric protein which combines residues from two β subunits that belong to different class I subclasses. This chimeric protein could possibly be able to achieve RT when paired with an α subunit that uses a non-native active cofactor. A significant evolutionary conclusion that can be drawn from this study is that there are no co-adaptations in the α subunit of either class Ia or class Ic RNR that were required for the larger subunit to accommodate a β subunit from a different subclass and organism.

Therefore, while the smaller subunits have evolved to harbor a different active cofactor, the larger subunits have not co-evolved. Bearing this in mind, we could postulate that the thoroughly studied,¹¹ intrinsic multi-step radical translocation mechanism details that pertain to *E. coli* RNR and most likely pertain to all class Ia RNRs, also pertain to the all class Ic RNRs. To test this hypothesis further one could, for example, make a β construct that includes two parts: an N-

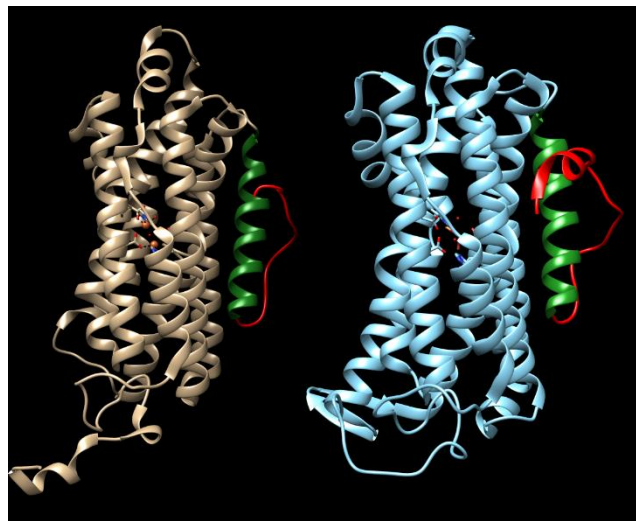


Figure 15. X-Ray crystal structures of β RNRs from *C. trachomatis* (PDB: 1SYY) in beige and from *E. coli* (PDB: 1RIB) in cyan. In green is the final ordered α helical region in the C-terminus of both subunits and in red the flexible loop most likely responsible for subunit association. Due to the highly disordered and flexible C-terminal regions, β s are missing the final 28 and 36 C-terminal amino acid residues from *Ct* and *Ec* β s, respectively.

terminal cofactor hosting part that would include the first ~300 residues that mimic the residues of one class I RNR β , and a subunit binding part that would include the final ~50 residues that are likely responsible for subunit association to mimic the sequence belonging to a member of another class I

RNR β . In **Figure 15** we show the two crystal structures of quite different (only 24% identical) class Ia *E. coli* (cyan) and class Ic *C. trachomatis* (in beige) β s. We speculate

that the first six α -helical bundles that correspond to β - Δ (300-350) are likely responsible for the cofactor formation and stabilization. This larger chunk of the protein contains all the amino acids that directly ligate the metals and its helices are in proximity of the cofactor. The seventh α -helix, being on the β - α subunit interface (in green in **Figure 15**) may, perhaps, be either a structural stabilizing component of the other six α -helices or be involved in subunit association, or both. Interestingly this α -helical region is bookmarked by cognate glycyl residues in both *Ct* and *Ec* β s. The final 43 residues in *Ec* β have been shown to both be non-essential for active cofactor generation

and essential to holoenzyme formation.¹⁷ We propose that if the residues shown in red in **Figure 15** as well as residues that follow are the ones solely responsible for subunit association. Should this hold true, a fusion construct that involves *Ct* β Δ (304-346) and *Ec* β Δ (1-320) and is activated by Mn/Fe could show catalytic competence when paired with *Ec* α . If these subunits would associate and show activity, this experiment would show compelling evidence that the multi-step, radical transfer mechanism is indeed the same between in all class Ia and class Ic RNRs excluding the mechanism involved at the active oxidant. This hypothetical result would open the door for studies that test the RT process differences between pairs of all five class I RNRs.

REFERENCES:

1. Nordlund, P.; Reichard, P., Ribonucleotide reductases. *Annu Rev Biochem* **2006**, *75*, 681-706.
2. Cotruvo, J. A.; Stubbe, J., Class I ribonucleotide reductases: metallocofactor assembly and repair in vitro and in vivo. *Annu Rev Biochem* **2011**, *80*, 733-67.
3. Rose, H. R.; Ghosh, M. K.; Maggiolo, A. O.; Pollock, C. J.; Blaes, E. J.; Hajj, V.; Wei, Y.; Rajakovich, L. J.; Chang, W. C.; Han, Y.; Hajj, M.; Krebs, C.; Silakov, A.; Pandelia, M. E.; Bollinger, J. M., Jr.; Boal, A. K., Structural Basis for Superoxide Activation of *Flavobacterium johnsoniae* Class I Ribonucleotide Reductase and for Radical Initiation by Its Dimanganese Cofactor. *Biochemistry-US* **2018**.
4. Mao, S. S.; Holler, T. P.; Yu, G. X.; Bollinger, J. M.; Booker, S.; Johnston, M. I.; Stubbe, J., A Model for the Role of Multiple Cysteine Residues Involved in Ribonucleotide Reduction - Amazing and Still Confusing. *Biochemistry-US* **1992**, *31* (40), 9733-9743.
5. Blaes, E. J.; Palowitch, G. M.; Hu, K.; Kim, A. J.; Rose, H. R.; Alapati, R.; Lougee, M. G.; Kim, H. J.; Taguchi, A. T.; Tan, K. O.; Laremore, T. N.; Griffin, R. G.; Krebs, C.; Matthews, M. L.; Silakov, A.; Bollinger, J. M., Jr.; Allen, B. D.; Boal, A. K., Metal-free class Ie ribonucleotide reductase from pathogens initiates catalysis with a tyrosine-derived dihydroxyphenylalanine radical. *Proc Natl Acad Sci U S A* **2018**, *115* (40), 10022-10027.
6. Stubbe, J.; Nocera, D. G.; Yee, C. S.; Chang, M. C. Y., Radical initiation in the class I ribonucleotide reductase: Long-range proton-coupled electron transfer? *Chem Rev* **2003**, *103* (6), 2167-2201.

7. Worsdorfer, B.; Conner, D. A.; Yokoyama, K.; Livada, J.; Seyedsayamdost, M.; Jiang, W.; Silakov, A.; Stubbe, J.; Bollinger, J. M., Jr.; Krebs, C., Function of the diiron cluster of Escherichia coli class Ia ribonucleotide reductase in proton-coupled electron transfer. *J Am Chem Soc* **2013**, *135* (23), 8585-93.
8. Seyedsayamdost, M. R.; Yee, C. S.; Reece, S. Y.; Nocera, D. G.; Stubbe, J., pH rate profiles of FnY356-R2s (n=2, 3, 4) in Escherichia coli ribonucleotide reductase: Evidence that Y-356 is a redox-active amino acid along the radical propagation pathway. *J Am Chem Soc* **2006**, *128* (5), 1562-1568.
9. Seyedsayamdost, M. R.; Xie, J.; Chan, C. T. Y.; Schultz, P. G.; Stubbe, J., Site-specific insertion of 3-aminotyrosine into subunit alpha 2 of E-coli ribonucleotide reductase: Direct evidence for involvement of Y-730 and Y-731 in radical propagation. *J Am Chem Soc* **2007**, *129* (48), 15060-15071.
10. Zlateva, T.; Quaroni, L.; Que, L.; Stankovich, M. T., Redox studies of subunit interactivity in aerobic ribonucleotide reductase from Escherichia coli. *J Biol Chem* **2004**, *279* (18), 18742-7.
11. Minnihan, E. C.; Nocera, D. G.; Stubbe, J., Reversible, Long-Range Radical Transfer in E-coli Class Ia Ribonucleotide Reductase. *Accounts Chem Res* **2013**, *46* (11), 2524-2535.
12. Karlsson, M.; Sahlin, M.; Sjoberg, B. M., Escherichia-Coli Ribonucleotide Reductase - Radical Susceptibility to Hydroxyurea Is Dependent on the Regulatory State of the Enzyme. *J Biol Chem* **1992**, *267* (18), 12622-12626.
13. Jiang, W.; Xie, J. J.; Varano, P. T.; Krebs, C.; Bollinger, J. M., Two Distinct Mechanisms of Inactivation of the Class Ic Ribonucleotide Reductase from Chlamydia trachomatis by

Hydroxyurea: Implications for the Protein Gating of Intersubunit Electron Transfer. *Biochemistry-Us* **2010**, *49* (25), 5340-5349.

14. Nick, T. U.; Ravichandran, K. R.; Stubbe, J.; Kasanmascheff, M.; Bennati, M., Spectroscopic Evidence for a H Bond Network at Y356 Located at the Subunit Interface of Active E. coli Ribonucleotide Reductase. *Biochemistry-Us* **2017**, *56* (28), 3647-3656.

15. Argirevic, T.; Riplinger, C.; Stubbe, J.; Neese, F.; Bennati, M., ENDOR spectroscopy and DFT calculations: evidence for the hydrogen-bond network within alpha2 in the PCET of E. coli ribonucleotide reductase. *J Am Chem Soc* **2012**, *134* (42), 17661-70.

16. Jiang, W.; Yun, D.; Saleh, L.; Barr, E. W.; Xing, G.; Hoffart, L. M.; Maslak, M. A.; Krebs, C.; Bollinger, J. M., A manganese(IV)/iron(III) cofactor in Chlamydia trachomatis ribonucleotide reductase. *Science* **2007**, *316* (5828), 1188-1191.

17. Sjoberg, B. M.; Karlsson, M.; Jornvall, H., Half-Site Reactivity of the Tyrosyl Radical of Ribonucleotide Reductase from Escherichia-Coli. *J Biol Chem* **1987**, *262* (20), 9736-9743.

18. Zrelak, G. EXPANSION OF THE CLASS IC RIBONUCLEOTIDE REDUCTASE, CONVERSION OF A CLASS IC TO A CLASS IA, AND SUBUNIT SWAPPING BETWEEN THE CLASSES. Penn State Univeristy, University Park, PA, 16802, 2013.

19. Bollinger, J. M.; Jiang, W.; Green, M. T.; Krebs, C., The manganese(IV)/iron(III) cofactor of Chlamydia trachomatis ribonucleotide reductase: structure, assembly, radical initiation, and evolution. *Curr Opin Struc Biol* **2008**, *18* (6), 650-657.

20. Crespo-Medina, M.; Chatziefthimiou, A.; Cruz-Matos, R.; Perez-Rodriguez, I.; Barkay, T.; Lutz, R. A.; Starovoytov, V.; Vetriani, C., Salinisphaera hydrothermalis sp nov., a mesophilic,

halotolerant, facultatively autotrophic, thiosulfate-oxidizing gammaproteobacterium from deep-sea hydrothermal vents, and emended description of the genus *Salinisphaera*. *Int J Syst Evol Micr* **2009**, *59*, 1497-1503.

21. Bollinger, J. M. On the chemical mechanism of assembly of the tyrosyl radical-dinuclear iron cluster cofactor of *E. coli* ribonucleotide reductase. Massachusetts Institute of Technology, Boston, MA, 1993.

22. <https://web.expasy.org/protparam/>, Accessed in years 2013-2017.

23. Gill, S. C.; von Hippel, P. H., Calculation of protein extinction coefficients from amino acid sequence data. *Anal Biochem* **1989**, *182* (2), 319-26.

24. Jiang, W. FORMATION AND FUNCTION OF A NOVEL HETEROBINUCLEAR MN/FE REDOX COFACTOR IN RIBONUCLEOTIDE REDUCTASE FROM *CHLAMYDIA TRACHOMATIS*. Penn State, University Park, 2007.

25. Price, J. C.; Barr, E. W.; Tirupati, B.; Bollinger, J. M., Jr.; Krebs, C., The first direct characterization of a high-valent iron intermediate in the reaction of an α -ketoglutarate-dependent dioxygenase: a high-spin FeIV complex in taurine/ α -ketoglutarate dioxygenase (TauD) from *Escherichia coli*. *Biochemistry-US* **2003**, *42* (24), 7497-508.

26. <http://efi.igb.illinois.edu/efi-est>, Accessed May 10th 2017.

27. Reichard, P.; Ehrenberg, A., Ribonucleotide Reductase - a Radical Enzyme. *Science* **1983**, *221* (4610), 514-519.

28. Bender, C. J.; Sahlin, M.; Babcock, G. T.; Barry, B. A.; Chandrashekar, T. K.; Salowe, S. P.; Stubbe, J.; Lindstrom, B.; Petersson, L.; Ehrenberg, A.; Sjöberg, B. M., An EPR Study

of the Tyrosyl Free-Radical in Ribonucleotide Reductase from Escherichia-Coli. *J Am Chem Soc* **1989**, *111* (21), 8076-8083.

29. Grant, C. L.; Pramer, D., Minor Element Composition of Yeast Extract. *Journal of Bacteriology* **1962**, *84* (4), 869-&.

30. Jiang, W.; Xie, J. J.; Norgaard, H.; Bollinger, J. M.; Krebs, C., Rapid and quantitative activation of Chlamydia trachomatis ribonucleotide reductase by hydrogen peroxide. *Biochemistry-Us* **2008**, *47* (15), 4477-4483.

31. Anderson, D. L., Chemical Composition of the Mantle in *Theory of the Earth*. pp. 147-175.

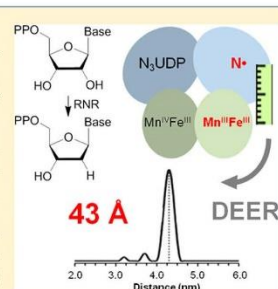
Chapter 4

Direct Measurement of the Radical Translocation Distance in the Class I Ribonucleotide Reductase from *Chlamydia trachomatis*

Direct Measurement of the Radical Translocation Distance in the
Class I Ribonucleotide Reductase from *Chlamydia trachomatis*Jovan Livada,^{†,‡} Ryan J. Martinie,^{†,‡} Laura M. K. Dassama,^{‡,§} Carsten Krebs,^{†,‡} J. Martin Bollinger, Jr.,^{†,‡}
and Alexey Silakov^{*,†}Departments of [†]Chemistry and [‡]Biochemistry and Molecular Biology, The Pennsylvania State University, University Park,
Pennsylvania 16802, United States

S Supporting Information

ABSTRACT: Ribonucleotide reductases (RNRs) catalyze conversion of ribonucleotides to deoxyribonucleotides in all organisms via a free-radical mechanism that is essentially conserved. In class I RNRs, the reaction is initiated and terminated by radical translocation (RT) between the α and β subunits. In the class Ic RNR from *Chlamydia trachomatis* (Ct RNR), the initiating event converts the active $S = 1$ Mn(IV)/Fe(III) cofactor to the $S = 1/2$ Mn(III)/Fe(III) "RT-product" form in the β subunit and generates a cysteinyl radical in the α active site. The radical can be trapped via the well-described decomposition reaction of the mechanism-based inactivator, 2'-azido-2'-deoxyuridine-5'-diphosphate, resulting in the generation of a long-lived, nitrogen-centered radical (N^{\bullet}) in α . In this work, we have determined the distance between the Mn(III)/Fe(III) cofactor in β and N^{\bullet} in α to be 43 ± 1 Å by using double electron–electron resonance experiments. This study provides the first structural data on the Ct RNR holoenzyme complex and the first direct experimental measurement of the inter-subunit RT distance in any class I RNR.



■ INTRODUCTION

Ribonucleotide reductases (RNRs) catalyze the reduction of ribonucleotides to deoxyribonucleotides; these enzymes occur in nearly all organisms across all three domains of life and provide the essential precursors for DNA replication and repair.^{1,2} To effect this transformation, RNRs employ a largely conserved free-radical mechanism, initiated by a transient cysteine thiyl radical (Figure 1A),^{3,4} and are classified by the differing mechanisms used to generate this cysteinyl radical.¹ Class I RNRs use an oxidized cofactor generated in an oxygen-dependent manner at a dinuclear metal site.⁵ Class II enzymes harbor an adenosylcobalamin cofactor, of which the Co–C bond is homolytically cleaved during catalysis, for radical generation.^{3,6,7} Finally, class III RNRs depend on a glycol radical, installed by an activating enzyme in the radical S-adenosylmethionine superfamily.^{8–11}

Class I RNRs, present in eukaryotes and model organisms such as *Escherichia coli* (*Ec*), have been intensively studied over the past several decades and comprise two subunits, α and β . The α component harbors the site of nucleotide reduction and the initiating cysteine residue, as well as binding sites for allosteric effectors,¹² whereas β harbors the dimetal site and a stable one-electron oxidant. The nature of this oxidant further subdivides class I.¹ In subclass Ia (which includes the enzymes from humans and aerobically free-living *Ec*), a carboxylate-bridged non-heme diiron cluster installs the radical equivalent, activating O_2 to oxidize a nearby tyrosine residue to a stable tyrosyl radical (Figure 1A, top).^{13–17} The Ib enzymes employ a structurally similar dimanganese cluster along with a superoxide-generating activator protein (designated NrdI) to install

the analogous tyrosyl radical.^{18,19} The class Ic RNRs, exemplified by the RNR from *Chlamydia trachomatis* (Ct) utilized in this work, are characterized by a redox-incompetent phenylalanine residue at the sequence position of the tyrosyl radicals in the class Ia/b enzymes, and the radical equivalent is instead harbored directly on a heterodinuclear Mn(IV)/Fe(III) cofactor (Figure 1A, bottom).^{20–23} Regardless of subclass, binding of the substrate and allosteric effector permits the radical equivalent to migrate from the dinuclear site in β to the key cysteine in α (C439 in the *Ec* enzyme; C672 in the Ct enzyme), and the thiyl radical then initiates substrate reduction by abstraction of a hydrogen atom from the 3' position.^{24,25} Among the first evidence that this radical translocation (RT) initiates turnover was the outcome of the interaction of *Ec* RNR with the mechanism-based inhibitor, 2'-azido-2'-deoxyuridine-5'-diphosphate (N_3 UDP): processing of this analogue leads to permanent loss of the stable radical equivalent in β and accumulation of a relatively stable, nitrogen-centered radical (N^{\bullet}) in α (Figure 1B).^{26–30} The equivalent outcome was later demonstrated for the Ct enzyme and provided the most definitive evidence that the initiating hole in the class Ic enzyme is the Mn(IV)/Fe(III) cluster.²⁰ RT in the *Ec* class Ia enzyme has been the subject of intense study and serves as a model of long-range biological electron transfer.²⁴

Special Issue: Wolfgang Lubitz Festschrift

Received: April 28, 2015

Revised: June 11, 2015

Published: June 18, 2015

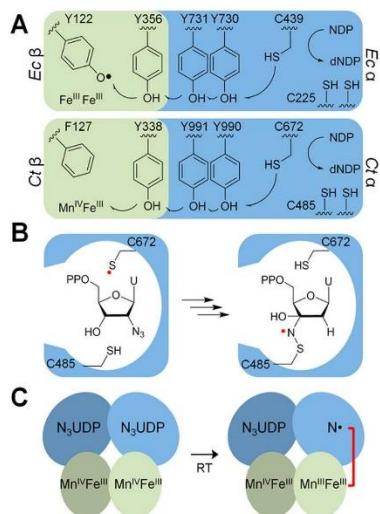


Figure 1. Structure and function of the class I ribonucleotide reductases (RNRs). (A) Key residues in the RT pathway that generates the catalytically essential thiyl radical in *Escherichia coli* (*Ec*) (top) and *Chlamydia trachomatis* (*Ct*) (bottom) RNRs. The resting states, prior to forward RT, are depicted, and the black arrows schematically depict the direction of electron transfer. (B) Conversion of the mechanism-based inhibitor N_3UDP to a long-lived radical (N^*). Amino acid position labels use *Ct* RNR numbering. (C) Location of paramagnetic species in the presumptive *Ct* RNR $\alpha_2\beta_2$ complex before (left) and after (right) RT in the presence of N_3UDP . Gray shading indicates the α/β pair that is inactive as a result of the "half-of-sites" reactivity demonstrated for both the *Ec* and *Ct* enzymes.

Paramount to a complete understanding of this protein-gated RT process is the elucidation of its structural determinants. Current consensus is that the active complex of the *Ec* enzyme is a dimer of homodimers, designated α_2 and β_2 (Figure 1C),^{12,25,31} although more complex, differentially (in)active oligomeric forms have been reported.^{25,32,33} In the absence of evidence to the contrary, the simplest assumption is that this $\alpha_2\beta_2$ arrangement of the active complex is conserved in *Ct* RNR (Figure 1C), though determination of the oligomeric states and structures of active complexes in RNRs from various organisms remains an area of active research.^{34–37} Despite intense scrutiny, the active $\alpha_2\beta_2$ complex has evaded characterization at atomic resolution. Such characterization has been limited by the fact that α and β associate rather weakly (K_d in the 0.1–1 μM range) and the $\alpha_2\beta_2$ complex is in equilibrium with other oligomeric forms.²⁵ To date, analysis of the RT pathway and gating mechanism has been dependent on a docking model for the *Ec* enzyme, formulated from high-resolution crystal structures of the isolated α_2 and β_2 subunits (Figure 1C).^{12,38} According to this model, RT occurs over a distance of ~ 35 Å from the tyrosyl radical in β to the initiating cysteine C439 in α (Figure 1A), too long for a direct electron transfer process.^{12,24} Multiple studies have indicated that a chain of aromatic residues, predominantly tyrosines, spanning the α and β subunits mediates the overall RT process in discrete, radical-hopping steps (Figure 1A, top).^{12,24,39–44}

Despite the inherent uncertainty associated with the type of structural modeling employed for the $\alpha_2\beta_2$ complex of *Ec* RNR,¹² the model has been shown to be fully consistent with the available structural data. The electron-density envelope deduced from small-angle X-ray scattering (SAXS) experiments²⁵ is largely consistent with the predicted arrangement of the subunits. Furthermore, SAXS and cryo-electron microscopy (cryoEM) characterization of the active complex,³¹ trapped by incorporation of 3-aminotyrosine at position 730 in α ,⁴¹ is also indicative of an $\alpha_2\beta_2$ arrangement. These experiments constitute the most direct characterization of the active complex to date, but are limited by low resolution. Additional structural information has been obtained by using double electron–electron resonance (DEER or PELDOR) to measure precise distances between two paramagnetic species, each having $S = 1/2$.⁴⁵ The class Ia β_2 component contains two tyrosyl radicals, one in each β monomer (Supporting Information, Figure S1A). The distance between these two tyrosine residues was determined to be 33.1 ± 0.2 and 32.5 ± 0.5 Å in the *Ec* and *Mus musculus* (mouse) RNRs, respectively,^{46,47} consistent with the crystal structures.^{38,48,49} More recent DEER studies have exploited the "half-of-sites" reactivity characteristic of class I RNRs for intersubunit distance measurements. Engagement in RT of a single $\alpha\beta$ pair in the $\alpha_2\beta_2$ complex results in a radical in α on that side of the complex and leaves the tyrosyl radical in β on the unengaged side (Figure S1B).^{40,50} By using N_3UDP to trap the radical in α of the engaged $\alpha\beta$ in *Ec* RNR, the "diagonal" distance between the N^* on the engaged side and the resting tyrosyl radical on the other side was determined to be 48 ± 1 Å (Figure S1B).⁵¹ In a follow-up study by Seyedsayamdost et al., the translocating radical was instead trapped along the RT pathway by incorporation of the tyrosine analogues 3-hydroxytyrosine (at Y356 in β) and 3-aminotyrosine (at Y730 and Y731 in α). The diagonal distances between these stabilized pathway radicals and the resting tyrosyl radical were determined to be 30.6 ± 0.5 , 38.7 ± 1.8 , and 38.1 ± 1.2 Å, respectively (Figure S1C,D).⁴² Each of these metrics is fully consistent with the proposed model of the *Ec* RNR complex.^{42,46,47,51}

Despite this extensive work, direct measurement of the RT distance within the active $\alpha\beta$ pair of a class I RNR has not been achieved, largely because RT in the best-studied class Ia and Ib enzymes moves a radical equivalent between β and α , leaving the other subunit without a "spin" to interrogate (Figure S1). The class Ic RNRs afford the opportunity to measure this distance. As noted, the prototypical *Ct* enzyme has a heterodinuclear, EPR-silent ($S = 1$) Mn(IV)/Fe(III) cofactor;²¹ the radical-harboring tyrosine found in the other two subclasses is replaced by phenylalanine. The cofactor spontaneously self-assembles in a reaction among the apo protein, Mn(II), Fe(II), and O_2 . First, the protein directs formation of the Mn(II)/Fe(II) complex with manganese in site 1 and iron in site 2.^{22,23,52,53} The Mn(II)/Fe(II) complex then reacts with O_2 to generate a Mn(IV)/Fe(IV) intermediate,^{54,55} and the protein mediates one-electron reduction of the Fe(IV) site to yield the active Mn(IV)/Fe(III) cofactor.^{20,21} In the initiating RT step, the cluster is reduced by one electron to the EPR-active Mn(III)/Fe(III) form (Figure 1C), which has an $S = 1/2$ ground state as a consequence of antiferromagnetic coupling between the high-spin Mn(III) ($S = 2$) and Fe(III) ($S = 5/2$) ions.^{22,23,43} Thus, when the enzyme processes the substrate analogue N_3UDP , two EPR-active species directly associated with a single RT pathway are formed: one in the α subunit [N^* ,

$S = 1/2$],^{28,30} and the other in β [Mn(III)/Fe(III), $S = 1/2$] (Figure 1C). In contrast to the DEER studies on the class Ia enzymes, these two species lie *along the same RT pathway* (Figure 1C, red bar). Furthermore, half-of-sites reactivity precludes formation of half-integer-spin species in the second $\alpha\beta$ pair, reducing ambiguity in spectral interpretation (Figure 1C, gray shading). Finally, the DEER method is selective for the Ct RNR active complex, as only complexes that undergo successful RT contain the two requisite EPR-active species.

Herein, we report the formation of the Mn(III)/Fe(III):N[•] form of Ct RNR and its characterization by DEER spectroscopy. These data yield the first direct measurement of the RT distance in a class I RNR, 43 ± 1 Å, and constitute the first structural data on the active Ct RNR complex.

RESULTS AND DISCUSSION

To prepare samples for determination of the RT distance by DEER spectroscopy, Ct α , the allosteric effector, ATP, and the substrate analogue, N₃UDP, were mixed. RT was initiated at ambient temperature (~ 21 °C) by addition of Mn(IV)/Fe(III) Ct β_2 , and the sample was frozen in liquid nitrogen after the reaction had been allowed to proceed for ~ 3 min. The resulting electron paramagnetic resonance (EPR) spectrum (Figure 2)

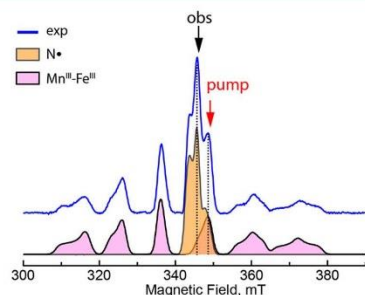


Figure 2. Pulse electron spin-echo-detected EPR spectrum of Ct RNR in the presence of N₃UDP. Experimental spectrum (blue) and simulations (Mn(III)/Fe(III), shaded purple; N[•], shaded orange). Simulation parameters are presented in the Supporting Information. Arrows and dotted lines indicate the portion of the spectrum probed by the detection (obs) and ELDOR (pump) pulses in DEER experiments. Experimental conditions: microwave frequency, 9.767 GHz; $t(\pi/2) = 12$ ns; $\tau = 336$ ns; temperature, 14 K; shot repetition time, 1.5 ms.

comprises two components with different temperature dependencies. One of the components is readily detected at 100 K; it is centered around $g = 2.006$ and has a line shape characteristic of the N[•] (Figure 2, shaded orange). This line shape arises from strong hyperfine (HF) couplings with a nitrogen ($A(^{14}\text{N}) = [6, 6, 90]$ MHz) and a proton ($A(^1\text{H}) = 18$ MHz) (Supporting Information, Figure S2).²⁸ At diminished temperatures (14 K), a broad six-packet signal is also detected, attributed to the Mn(III)/Fe(III) form of the cofactor (Figure 2, shaded purple).²⁰ Simulation of the spectrum yields spin Hamiltonian parameters similar to those previously published ($A(^{55}\text{Mn}) = [314, 396, 269]$ MHz and $g = [2.009, 2.014, 2.024]$) (Figure S2). Notably, the Mn(III)/Fe(III) spectrum obtained is identical to the spectrum generated when the pathway-radical equivalent, induced to form by the native substrate, CDP, is

reductively trapped by the RNR inhibitor, hydroxyurea (Figure S2).⁴³

Preliminary experiments performed on samples in ¹H₂O buffer at 14 K indicated that the transverse relaxation, T_2 , of the Mn(III)/Fe(III) cluster is too short to obtain DEER data of acceptable quality with a span beyond ~ 1.5 μ s. However, preparation of the sample under identical conditions but in ²H₂O buffer was found to enhance the DEER signal significantly, consistent with previous reports.⁴⁷ Data acquisition at diminished temperature (4 K) was found to afford further improvement in the signal-to-noise ratio. Figure 3A shows the four-pulse DEER trace obtained from this sample at 4 K. In the DEER measurements, “probe” pulses were applied with a frequency corresponding to the signal of the N[•] (Figure 2, black arrow), and the ELDOR “pump” pulse was applied on the packet of the Mn(III)/Fe(III) spectrum at a field position 28 G (79 MHz) greater than that of the radical (Figure 2, red arrow). The data in Figure 3A show clear periodical oscillations, indicative of a small distance distribution between paramagnetic species. To exclude the possibility that the observed modulations arise from electron spin echo envelope modulation (ESEEM) effects, we performed an additional measurement in which the ELDOR pump pulse was applied to the most isotropic Mn(III)/Fe(III) packet, at a field position 77 G (214 MHz) less than that of the center of the N[•] signal (Supporting Information, Figure S3). However, as the 214-MHz separation between the pump and detection frequencies dictated the use of considerably longer pulses (owing to the resonator bandwidth), the diminished signal intensity limited the length of the pulse sequence to 2 μ s. Nevertheless, the trace obtained (Figure S3) is strikingly similar to the one described above, strongly suggesting that the observed traces arise from the interaction between the Mn(III)/Fe(III) cluster and the N[•].

The data were analyzed by Tikhonov regularization fitting, as implemented in the DeerAnalysis software package (Figure 3B).⁵⁶ The raw DEER trace was subjected to background subtraction with a second order polynomial fit (inset Figure 3A, red) to the last two-thirds of the data (inset Figure 3A, shaded region). Figure 3B (inset) shows the calculated L-curve with the optimal regularization parameter indicated (red arrow).⁴⁵ The resulting fit (Figure 3B) shows a distinct peak with a narrow distribution centered at 43 Å. To illustrate the validity of the obtained distance, we analyzed the data by a second method. The trace was directly fit to a simple model corresponding to a Gaussian distribution of distances centered at 43 Å with full width at half-height of 2 Å. Equivalent simulations with centroids ranging from 41 to 45 Å were also generated for comparison (Supporting Information, Figure S4). When centered at 43 Å, this simple model provided a good fit to the experimental data, but the distance perturbations resulted in a significant decrease in fit quality (Figure S4), suggesting a margin of error of approximately ± 1 Å.

These data provide, to our knowledge, the first structural information obtained for the active complex in Ct RNR. All previous characterization of the active complex (using DEER, SAXS, and cryoEM) has been performed with members of class Ia;^{25,31,33,42,51} therefore, our results provide new insight into the less well-understood class Ic RNRs. Moreover, this is the first direct measurement of the RT distance in *any* class I RNR. To date, all estimates of RT distance (~ 35 Å) have been based exclusively on the hypothetical, albeit experimentally supported, docking model for the Ec enzyme.¹² This distance has been widely cited in discussions of the RNR mechanism and long-

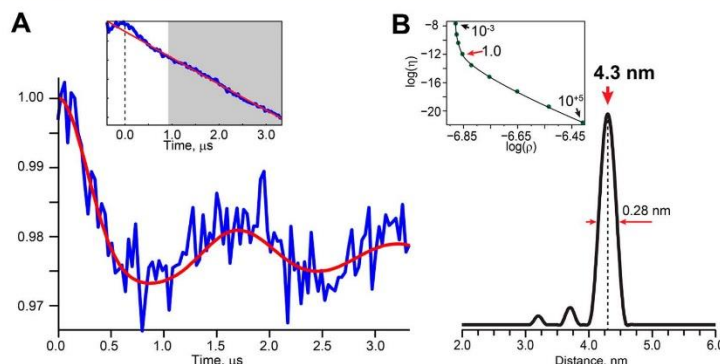


Figure 3. Double electron–electron resonance (DEER) analysis of the Mn(III)/Fe(III):N* state of *Ct* RNR. (A) DEER spectrum obtained for *Ct* RNR in $^2\text{H}_2\text{O}$ buffer at 4 K (blue) and simulation (red). The inset shows the background subtraction (red line) and the region of the data that was fit (gray shading). (B) Tikhonov regularization analysis of the data in panel A. The inset shows the choice of regularization parameter (red arrow) based on the calculated L-curve. Experimental conditions: microwave frequency, 9.767 GHz; ELDOR frequency, 9.688 GHz; temperature, 4 K; τ , 400 ns; $t_{1,\text{start}}$, 200 ns; $t_{2,\text{start}}$, 3.2 μs ; shot repetition time, 50 ms.

range biological electron transfer.^{1,22,24} The present study provides this RT distance, as measured between two EPR-active species produced by RT through a single pathway in the active complex (Figure 1C, red bar). Although the distance measured here is significantly longer than 35 Å, these two distances cannot be directly compared. Specifically, the commonly cited distance corresponds to that between the tyrosyl radical in β (residing on Y122 in the *Ec* enzyme) and the sulfur of the initiating cysteine in α (C439 in *Ec* RNR and C672 in the *Ct* enzyme; Figure 1A), whereas the distance measured in this work is essentially that between the Mn(III)/Fe(III) cluster and the N*. Published work implies that, in *Ec* RNR, this N* is bonded to C225, which corresponds to C485 of the *Ct* enzyme (Figure 1B).^{28,30}

To enable deeper interpretation of the distance obtained and provide more direct comparison with the aforementioned *Ec* RNR docking model, we generated a structural model for the *Ct* RNR active complex using a simple molecular dynamics approach (for details, see Materials and Methods). Given the lack of available data concerning the subunit arrangement in *Ct* RNR, we constructed our model under the simplest assumption that, like the *Ec* RNR, the active *Ct* RNR forms an $\alpha_2\beta_2$ complex. During the course of the simulation, subtle rearrangements occurred in the structure, particularly the α/β binding region. Despite the fact that no distance restraints were imposed in this model, the distance between the dinuclear metal center and the nitrogen atom of N* (presumably covalently linked to C485, Figure 1B), approaches the experimentally observed value quite closely (~ 43 Å, Figure 4A). The arrangement of the two $\alpha\beta$ pairs is slightly asymmetric as a result of a tilting of the β_2 dimer toward one side of the α_2 dimer, resulting in slightly different average distances of 42 and 44 Å. Obviously, this predicted deviation is potentially relevant to the half-of-sites reactivity observed for class I RNRs, but this possibility requires further inquiry.

In our model, the average distance between the dinuclear metal center and C485 agrees well with the experimentally determined value, within experimental error (Figure 3). Given that our model is predicated on the assumption of an $\alpha_2\beta_2$ subunit arrangement similar to that predicted for the *Ec*

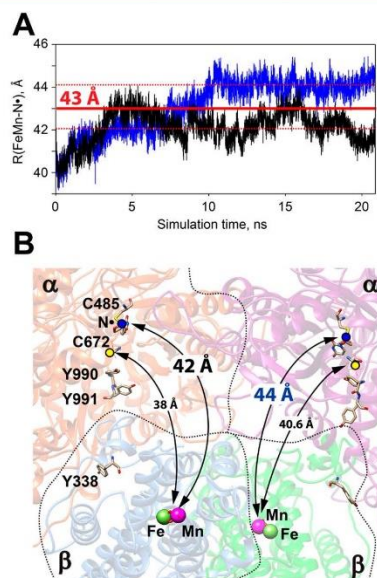


Figure 4. Structural modeling of the presumptive *Ct* RNR $\alpha_2\beta_2$ complex. (A) Variation of the distance between the dinuclear metal center and N* during the course of the molecular dynamics simulation. The distance was calculated for both electron transfer pathways, which are shown separately in black and blue. The experimental value for this distance is indicated by the red bar, with uncertainty indicated by dotted lines. (B) Ribbon representation of the resulting model, with key residues and distances highlighted.

enzyme, this level of consistency between the experimental observation and model provides the first evidence that the class Ic and Ia enzymes share a similar active complex topology. Furthermore, the comparable distance in the *Ec* RNR docking model, that between the diiron center and N*-C225, is 41–42

Å. Although slightly less than the value for Ct RNR, this small difference could readily be attributed to (i) minor inaccuracies in one or both models (e.g., the position of the C-terminal region of β) or (ii) small structural differences between the orthologues. Furthermore, because the Mn(III)/Fe(III) cofactor does not constitute a point dipole, the spectroscopically observed distance may not, *a priori*, represent the actual distance between the geometric center of the cofactor and the N^{*}. Rather, both the $S = 2$ Mn(III) and $S = 5/2$ Fe(III) centers contribute to the observed dipolar coupling, according to the spin-projection factors, $-4/3$ and $+7/3$, respectively.^{57–60} Our calculations show (see Supporting Information) that in the extreme cases in which the Mn–Fe vector is colinear with the dipolar vector, the deviation can be up to 9 Å, whereas in the perpendicular case there is no deviation (Figure S5), consistent with published work.^{59,60} In this case, both the Ec RNR model and our Ct RNR model indicate that the angle between the metal–metal vector and the dipolar vector is within 8° of the perpendicular case, and the resulting deviation (~ 0.6 Å) is within the experimental error.

It is also noteworthy that the overall distribution of the distance observed in our DEER measurements is rather narrow, especially considering that the formation of the active complex is most likely transient. These data suggest, in agreement with previous reports,^{42,51} that the association between α and β is relatively rigid and well defined in states of the catalytic cycle having the radical equivalent away from its resting position in β . Such tight association is likely important for efficient coupling of RT and nucleotide reduction.

This study has provided new insight into the structural arrangement of the active complex in class Ic RNRs, supporting the conclusion that Ct RNR shares a subunit arrangement similar to that proposed for class Ia RNRs. Furthermore, these data furnish the first direct measurement of the intersubunit RT distance in any class I RNR, enhancing the quantitative understanding of this canonical long-range electron transfer event.

MATERIALS AND METHODS

Cloning and Preparation of α and β Proteins. Wild-type Ct β and Ct $\Delta(1-248)\alpha$ were overexpressed in pET28a vectors and purified via nickel affinity chromatography according to established procedures.²⁰ In this study, as in prior work, the first 248 residues of the α subunit are absent because the truncation improves protein overexpression and solubility. Our previous mechanistic studies of $\Delta(1-248)\alpha$ ^{20,23} and observation of RT products in the current experiments imply that the activity of Ct RNR is not affected by this modification. Proteins were rendered metal-free by dialysis of $\Delta(1-248)\alpha$ against buffer containing EDTA and by ferrozine chelation of β , which was subsequently removed using a Sephadex G-50 column.⁵⁵ Reconstitution to generate the active Mn(IV)/Fe(III) cofactor was also performed according to previously reported methods.⁵⁵ The extent of active cofactor formation and specific activity were found to be consistent with previous reports.⁵⁵

EPR Sample Preparation. Exchange of the protein into ²H₂O buffer (100 mM sodium HEPES, pH 8.0) was performed by 10-fold dilution of ~ 2 mL of concentrated protein (~ 1 mM) with ²H₂O buffer and subsequent concentration to the original volume in an Amicon ultrafiltration cell with a YM30 membrane. This procedure was repeated twice. Removal of O₂ from preparations of the α and β proteins was performed as

previously described.⁶¹ Following deoxygenation, all sample manipulations were carried out in an anaerobic chamber (Coy Laboratories, Grass Lake, MI). Dithiothreitol (DTT) (Sigma-Aldrich), present in the purification buffer, was removed from the α sample by passing it through a PD-10 desalting column (GE Healthcare, Little Chalfont, UK). The α protein, the allosteric effector ATP (Sigma-Aldrich), and the substrate analogue N₃UDP were mixed to a final volume of 0.20 mL with final concentrations of 2.4 mM, 2 mM, and 2 mM, respectively. RT was initiated by adding 0.075 mL of 3 mM β_2 to the mixture. Addition of glycerol (0–40% final v/v) was evaluated and found not to have a significant effect on signal quality. The mixture was then transferred to a 3.8 mm o.d./2.8 mm i.d. quartz EPR tube (QSIL Corp.), incubated for 3 min, and subsequently frozen in liquid N₂. Spin quantitation indicated final spin concentrations of 250 and 370 μ M for N^{*} and Mn(III)/Fe(III), respectively. Incubation time was varied in a separate experiment at lower protein concentration (1 mM β), and no increase in the signal intensity of the radical was observed at time points after 1 min.

EPR Measurements. All EPR measurements were performed on a Bruker Elexsys E580 X-band spectrometer equipped with a SuperX-FT microwave bridge. CW EPR measurements were performed using an ER 4122 SHQE SuperX high-sensitivity cavity in combination with an ER 4112-HV Oxford Instruments variable-temperature liquid helium flow cryostat. For pulse EPR/DEER measurements, a Bruker EN 4118X-MD4 dielectric ENDOR resonator was used in concert with an Oxford CF935 helium flow cryostat. Microwave pulses generated by the microwave bridge were amplified by a 1 kW traveling wave tube amplifier (Applied Systems Engineering, model 117x). The field-swept EPR spectra were obtained using a two-pulse Hahn echo sequence with a π -pulse of 24 ns and τ of 212 ns. The following four-pulse sequence⁴⁵ was used to perform DEER measurements: $[\pi/2] - \tau - [\pi] - t_1 - [\text{ELDOR}] - t_2 - [\pi]$, where $t(\pi/2) = 12$ ns, $t(\pi) = 24$ ns, $t = 400$ ns, $t_{1,\text{start}} = 200$ ns, $t(\text{ELDOR}) = 32$ ns, $t_{2,\text{start}} = 3.5$ μ s, and $t(\text{step}) = 28$ ns. The shot repetition rate was 50 ms with 20 shots per point, averaged for ~ 600 scans. DEER results were obtained by applying the pump pulse to the Mn(III)/Fe(III) signal and observing on the N^{*} signal. The inverse was also attempted, and found not to significantly alter data quality.

Molecular Dynamics Simulations. Initial coordinates for the presumptive $\alpha_2\beta_2$ complex were generated by the following approach. First, crystallographic data on Ct β_2 (PDB 4D8F⁵²) were complemented with *ab initio* modeling (as implemented in I-TASSER modeling^{62–64}) of the unstructured portions of the protein not included in the crystallographic data set. Second, a structural homology model of the presumptive Ct α_2 subunit was generated, starting from the crystallographically determined yeast α_2 structure, using the I-TASSER structure prediction server.^{62–64} Third, these structures for α_2 and β_2 were arranged on the basis of the Ec RNR docking model and the available experimental data (*vide supra*). The resulting $\alpha_2\beta_2$ complex was subjected to molecular dynamics simulations in which the initial model was allowed to evolve for >20 ns (Figure 4). After 10 ns, the conformation of the complex remained relatively stable, with small perturbations (Figure 4A).

All calculations were performed using the NAMD simulation package.⁶⁵ The CHARMM27 force field was employed for all protein interactions.⁶⁶ CHARMM parameters for the Cys-N-UDP construct and the dinuclear cofactor (including amino

acid ligands) were generated using the paratool plugin of the VMD visualization package.⁶⁷ Partial charges and Hessian matrices were calculated using UB3LYP/6-311G density functional theory and the Gaussian 03 software package.⁶⁸ The structure was encapsulated in a water sphere of 72 Å radius, and simulation was performed using spherical boundary conditions. The time step was set to 2 fs throughout the simulation. Aside from the initial equilibration for 1000 steps, all simulations were performed at constant volume and temperature (310 K). Temperature was regulated using Langevin dynamics with damping constants of 5 ps⁻¹ as implemented in the NAMD package.⁶⁵

■ ASSOCIATED CONTENT

■ Supporting Information

Continuous wave EPR spectra and simulations, comparison of DEER spectra with differing pump/probe frequencies, DEER analyses using Gaussian distribution modeling, dipolar coupling calculation, and descriptive diagrams. The Supporting Information is available free of charge on the ACS Publications website at DOI: 10.1021/acs.jpcb.5b04067.

■ AUTHOR INFORMATION

Corresponding Author

*E-mail: alexey.silakov@gmail.com.

Present Address

§L.M.K.D.: Department of Chemistry, Northwestern University, Evanston, IL 60208, USA

Author Contributions

[†]J.L. and R.J.M. contributed equally to this work.

Notes

The authors declare no competing financial interest.

■ ACKNOWLEDGMENTS

We gratefully acknowledge JoAnne Stubbe and Lisa Olshansky for providing the N₅UDP used in this study. This work was supported by a grant from the National Institutes of Health (GM55365 to J.M.B. and C.K.).

■ REFERENCES

- (1) Stubbe, J.; van der Donk, W. A. Protein Radicals in Enzyme Catalysis. *Chem. Rev.* **1998**, *98*, 705–762.
- (2) Nordlund, P.; Reichard, P. Ribonucleotide Reductases. *Annu. Rev. Biochem.* **2006**, *75*, 681–706.
- (3) Licht, S.; Gerfen, G. J.; Stubbe, J. Thiol Radicals in Ribonucleotide Reductases. *Science* **1996**, *271*, 477–481.
- (4) Mao, S. S.; Yu, G. X.; Chalfoun, D.; Stubbe, J. Characterization of C439SR1, a Mutant of *Escherichia coli* Ribonucleotide Diphosphate Reductase: Evidence That C439 Is a Residue Essential for Nucleotide Reduction and C439SR1 Is a Protein Possessing Novel Thioredoxin-like Activity. *Biochemistry* **1992**, *31*, 9752–9759.
- (5) Bollinger, J. M., Jr.; Edmondson, D. E.; Huynh, B. H.; Filley, J.; Norton, J. R.; Stubbe, J. Mechanism of Assembly of the Tyrosyl Radical-Dinuclear Iron Cluster Cofactor of Ribonucleotide Reductase. *Science* **1991**, *253*, 292–298.
- (6) Tamao, Y.; Blakley, R. L. Direct Spectrophotometric Observation of an Intermediate Formed from Deoxyadenosylcobalamin in Ribonucleotide Reduction. *Biochemistry* **1973**, *12*, 24–34.
- (7) Sintchak, M. D.; Arjara, G.; Kellogg, B. A.; Stubbe, J.; Drennan, C. L. The Crystal Structure of Class II Ribonucleotide Reductase Reveals How an Allosterically Regulated Monomer Mimics a Dimer. *Nat. Struct. Biol.* **2002**, *9*, 293–300.
- (8) Sun, X.; Ollagnier, S.; Schmidt, P. P.; Atta, M.; Mulliez, E.; Lepape, L.; Eliasson, R.; Gräslund, A.; Fontecave, M.; Reichard, P.; Sjöberg, B.-M. The Free Radical of the Anaerobic Ribonucleotide Reductase from *Escherichia coli* Is at Glycine 681. *J. Biol. Chem.* **1996**, *271*, 6827–6831.
- (9) Young, P.; Andersson, J.; Sahlin, M.; Sjöberg, B.-M. Bacteriophage T4 Anaerobic Ribonucleotide Reductase Contains a Stable Glycyl Radical at Position 580. *J. Biol. Chem.* **1996**, *271*, 20770–20775.
- (10) Ollagnier, S.; Mulliez, E.; Schmidt, P. P.; Eliasson, R.; Gaillard, J.; Deronzier, C.; Bergman, T.; Gräslund, A.; Reichard, P.; Fontecave, M. Activation of the Anaerobic Ribonucleotide Reductase from *Escherichia coli*. The Essential Role of the Iron-Sulfur Center for S-Adenosylmethionine Reduction. *J. Biol. Chem.* **1997**, *272*, 24216–24223.
- (11) Logan, D. T.; Andersson, J.; Sjöberg, B.-M.; Nordlund, P. A Glycyl Radical Site in the Crystal Structure of a Class III Ribonucleotide Reductase. *Science* **1999**, *283*, 1499–1504.
- (12) Uhlin, U.; Eklund, H. Structure of Ribonucleotide Reductase Protein R1. *Nature* **1994**, *370*, 533–539.
- (13) Ehrenberg, A.; Reichard, P. Electron Spin Resonance of the Iron-Containing Protein B2 from Ribonucleotide Reductase. *J. Biol. Chem.* **1972**, *247*, 3485–3488.
- (14) Atkin, C. L.; Thelander, L.; Reichard, P.; Lang, G. Iron and Free Radical in Ribonucleotide Reductase: Exchange of Iron and Mössbauer Spectroscopy of the Protein B2 Subunit of the *Escherichia coli* Enzyme. *J. Biol. Chem.* **1973**, *248*, 7464–7472.
- (15) Sjöberg, B.-M.; Reichard, P. Nature of the Free Radical in Ribonucleotide Reductase from *Escherichia coli*. *J. Biol. Chem.* **1977**, *252*, 536–541.
- (16) Sjöberg, B.-M.; Reichard, P.; Gräslund, A.; Ehrenberg, A. The Tyrosine Free Radical in Ribonucleotide Reductase from *Escherichia coli*. *J. Biol. Chem.* **1978**, *253*, 6863–6865.
- (17) Larsson, A.; Sjöberg, B.-M. Identification of the Stable Free Radical Tyrosine Residue in Ribonucleotide Reductase. *EMBO J.* **1986**, *5*, 2037–2040.
- (18) Cotruvo, J. A., Jr.; Stubbe, J. *Escherichia coli* Class Ib Ribonucleotide Reductase Contains a Dimanganese(III)-Tyrosyl Radical Cofactor in Vivo. *Biochemistry* **2011**, *50*, 1672–1681.
- (19) Cotruvo, J. A., Jr.; Stüch, T. A.; Britt, R. D.; Stubbe, J. Mechanism of Assembly of the Dimanganese-Tyrosyl Radical Cofactor of Class Ib Ribonucleotide Reductase: Enzymatic Generation of Superoxide Is Required for Tyrosine Oxidation via a Mn(III)Mn(IV) Intermediate. *J. Am. Chem. Soc.* **2013**, *135*, 4027–4039.
- (20) Jiang, W.; Yun, D.; Saleh, L.; Barr, E. W.; Xing, G.; Hoffart, L. M.; Maslak, M. A.; Krebs, C.; Bollinger, J. M., Jr. A Manganese(IV)/Iron(III) Cofactor in *Chlamydia trachomatis* Ribonucleotide Reductase. *Science* **2007**, *316*, 1188–1191.
- (21) Jiang, W.; Bollinger, J. M., Jr.; Krebs, C. The Active Form of *Chlamydia trachomatis* Ribonucleotide Reductase R2 Protein Contains a Heterodinuclear Mn(IV)/Fe(III) Cluster with S = 1 Ground State. *J. Am. Chem. Soc.* **2007**, *129*, 7504–7505.
- (22) Bollinger, J. M., Jr.; Jiang, W.; Green, M. T.; Krebs, C. The Manganese(IV)/Iron(III) Cofactor of *Chlamydia trachomatis* Ribonucleotide Reductase: Structure, Assembly, Radical Initiation, and Evolution. *Curr. Opin. Struct. Biol.* **2008**, *18*, 650–657.
- (23) Jiang, W.; Yun, D.; Saleh, L.; Bollinger, J. M., Jr.; Krebs, C. Formation and Function of the Manganese(IV)/Iron(III) Cofactor in *Chlamydia trachomatis* Ribonucleotide Reductase. *Biochemistry* **2008**, *47*, 13736–13744.
- (24) Stubbe, J.; Nocera, D. G.; Yee, C. S.; Chang, M. C. Y. Radical Initiation in the Class I Ribonucleotide Reductase: Long-Range Proton-Coupled Electron Transfer? *Chem. Rev.* **2003**, *103*, 2167–2202.
- (25) Ando, N.; Brignole, E. J.; Zimanyi, C. M.; Funk, M. A.; Yokoyama, K.; Asturias, F. J.; Stubbe, J.; Drennan, C. L. Structural Interconversions Modulate Activity of *Escherichia coli* Ribonucleotide Reductase. *Proc. Natl. Acad. Sci. U.S.A.* **2011**, *108*, 21046–21051.
- (26) Thelander, L.; Larsson, B. Active Site of Ribonucleoside Diphosphate Reductase from *Escherichia coli*: Inactivation of the

- Enzyme by 2'-Substituted Ribonucleoside Diphosphates. *J. Biol. Chem.* **1976**, *251*, 1398–1405.
- (27) Behravan, G.; Sen, S.; Rova, U.; Thelander, L.; Eckstein, F.; Gräslund, A. Formation of a Free Radical of the Sulfenylimine Type in the Mouse Ribonucleotide Reductase Reaction with 2'-Azido-2'-Deoxycytidine 5'-Diphosphate. *Biochim. Biophys. Acta* **1995**, *1264*, 323–329.
- (28) van der Donk, W. A.; Stubbe, J.; Gerfen, G. J.; Bellew, B. F.; Griffin, R. G. EPR Investigations of the Inactivation of *E. coli* Ribonucleotide Reductase with 2'-Azido-2'-Deoxyuridine 5'-Diphosphate: Evidence for the Involvement of the Thiyl Radical of C225-R1. *J. Am. Chem. Soc.* **1995**, *117*, 8908–8916.
- (29) Eriksson, L. A. Sulfenylimine Radical in Azido-CDP- and Azido-UDP-Inhibited Ribonucleotide Reductase. *J. Am. Chem. Soc.* **1998**, *120*, 8051–8054.
- (30) Fritscher, J.; Artin, E.; Wnuk, S.; Bar, G.; Robblee, J. H.; Kacprzak, S.; Kaupp, M.; Griffin, R. G.; Bennati, M.; Stubbe, J. Structure of the Nitrogen-Centered Radical Formed during Inactivation of *E. coli* Ribonucleotide Reductase by 2'-Azido-2'-Deoxyuridine-5'-Diphosphate: Trapping of the 3'-Ketonucleotide. *J. Am. Chem. Soc.* **2005**, *127*, 7729–7738.
- (31) Minnihan, E. C.; Ando, N.; Brignole, E. J.; Olshansky, L.; Chittuluru, J.; Asturias, F. J.; Drennan, C. L.; Nocera, D. G.; Stubbe, J. Generation of a Stable, Amino-tyrosyl Radical-Induced $\alpha\beta\gamma$ Complex of *Escherichia coli* Class Ia Ribonucleotide Reductase. *Proc. Natl. Acad. Sci. U.S.A.* **2013**, *110*, 3835–3840.
- (32) Rofougaran, R.; Crona, M.; Vodnala, M.; Sjöberg, B.-M.; Hofer, A. Oligomerization Status Directs Overall Activity Regulation of the *Escherichia coli* Class Ia Ribonucleotide Reductase. *J. Biol. Chem.* **2008**, *283*, 35310–35318.
- (33) Zimanyi, C. M.; Ando, N.; Brignole, E. J.; Asturias, F. J.; Stubbe, J.; Drennan, C. L. Tangled up in Knots: Structures of Inactivated Forms of *E. coli* Class Ia Ribonucleotide Reductase. *Structure* **2012**, *20*, 1374–1383.
- (34) Ahmad, M. F.; Dealwis, C. G. The Structural Basis for the Allosteric Regulation of Ribonucleotide Reductase. *Prog. Mol. Biol. Transl.* **2013**, *117*, 389–410.
- (35) Fairman, J. W.; Wijerathna, S. R.; Ahmad, M. F.; Xu, H.; Nakano, R.; Jha, S.; Prendergast, J.; Welin, R. M.; Flodin, S.; Roos, A.; Nordlund, P.; Li, Z.; Walz, T.; Dealwis, C. G. Structural Basis for Allosteric Regulation of Human Ribonucleotide Reductase by Nucleotide-Induced Oligomerization. *Nat. Struct. Mol. Biol.* **2011**, *18*, 316–322.
- (36) Fu, Y.; Long, M. J. C.; Rigney, M.; Parvez, S.; Blessing, W. A.; Aye, Y. Uncoupling of Allosteric and Oligomeric Regulation in a Functional Hybrid Enzyme Constructed from *Escherichia coli* and Human Ribonucleotide Reductase. *Biochemistry* **2013**, *52*, 7050–7059.
- (37) Jonna, V. R.; Crona, M.; Rofougaran, R.; Lundin, D.; Johansson, S.; Brännström, K.; Sjöberg, B.-M.; Hofer, A. Diversity in Overall Activity Regulation of Ribonucleotide Reductase. *J. Biol. Chem.* **2015**, DOI: 10.1074/jbc.M115.649624.
- (38) Högbom, M.; Galander, M.; Andersson, M.; Kolberg, M.; Hofbauer, W.; Lassmann, G.; Nordlund, P.; Lendzian, F. Displacement of the Tyrosyl Radical Cofactor in Ribonucleotide Reductase Obtained by Single-Crystal High-Field EPR and 1.4-Å X-ray Data. *Proc. Natl. Acad. Sci. U.S.A.* **2003**, *100*, 3209–3214.
- (39) Seyedsayamdost, M. R.; Yee, C. S.; Reece, S. Y.; Nocera, D. G.; Stubbe, J. pH Rate Profiles of $F_nY_{356}R2s$ ($n = 2, 3, 4$) in *Escherichia coli* Ribonucleotide Reductase: Evidence That Y_{356} Is a Redox-Active Amino Acid along the Radical Propagation Pathway. *J. Am. Chem. Soc.* **2006**, *128*, 1562–1568.
- (40) Seyedsayamdost, M. R.; Stubbe, J. Site-Specific Replacement of Y_{356} with 3,4-Dihydroxyphenylalanine in the $\beta 2$ Subunit of *E. coli* Ribonucleotide Reductase. *J. Am. Chem. Soc.* **2006**, *128*, 2522–2523.
- (41) Seyedsayamdost, M. R.; Xie, J.; Chan, C. T. Y.; Schultz, P. G.; Stubbe, J. Site-Specific Insertion of 3-Aminotyrosine into Subunit $\alpha 2$ of *E. coli* Ribonucleotide Reductase: Direct Evidence for Involvement of Y_{730} and Y_{731} in Radical Propagation. *J. Am. Chem. Soc.* **2007**, *129*, 15060–15071.
- (42) Seyedsayamdost, M. R.; Chan, C. T. Y.; Mugnaini, V.; Stubbe, J.; Bennati, M. PELDOR Spectroscopy with DOPA- $\beta 2$ and $NH_2Y_{\alpha 2s}$: Distance Measurements between Residues Involved in the Radical Propagation Pathway of *E. coli* Ribonucleotide Reductase. *J. Am. Chem. Soc.* **2007**, *129*, 15748–15749.
- (43) Jiang, W.; Xie, J.; Varano, P. T.; Krebs, C.; Bollinger, J. M., Jr. Two Distinct Mechanisms of Inactivation of the Class Ic Ribonucleotide Reductase from *Chlamydia trachomatis* by Hydroxyurea: Implications for the Protein Gating of Intersubunit Electron Transfer. *Biochemistry* **2010**, *49*, 5340–5349.
- (44) Dassama, L. M. K.; Jiang, W.; Varano, P. T.; Pandelia, M.-E.; Conner, D. A.; Xie, J.; Bollinger, J. M., Jr.; Krebs, C. Radical-Translocation Intermediates and Hurdling of Pathway Defects in “Super-oxidized” (Mn(IV)/Fe(IV)) *Chlamydia trachomatis* Ribonucleotide Reductase. *J. Am. Chem. Soc.* **2012**, *134*, 20498–20506.
- (45) Jeschke, G. DEER Distance Measurements on Proteins. *Annu. Rev. Phys. Chem.* **2012**, *63*, 419–446.
- (46) Bennati, M.; Weber, A.; Antonic, J.; Perlstein, D. L.; Robblee, J.; Stubbe, J. Pulsed ELDOR Spectroscopy Measures the Distance between the Two Tyrosyl Radicals in the R2 Subunit of the *E. coli* Ribonucleotide Reductase. *J. Am. Chem. Soc.* **2003**, *125*, 14988–14989.
- (47) Biglino, D.; Schmidt, P. P.; Reijerse, E. J.; Lubitz, W. PELDOR Study on the Tyrosyl Radicals in the R2 Protein of Mouse Ribonucleotide Reductase. *Phys. Chem. Chem. Phys.* **2006**, *8*, 58–62.
- (48) Kauppi, B.; Nielsen, B. B.; Ramaswamy, S.; Larsen, I. K.; Thelander, M.; Thelander, L.; Eklund, H. The Three-Dimensional Structure of Mammalian Ribonucleotide Reductase Protein R2 Reveals a More-Accessible Iron-Radical Site than *Escherichia coli* R2. *J. Mol. Biol.* **1996**, *262*, 706–720.
- (49) Strand, K. R.; Karlsen, S.; Kolberg, M.; Röhr, Å. K.; Görbitz, C. H.; Andersson, K. K. Crystal Structural Studies of Changes in the Native Dinuclear Iron Center of Ribonucleotide Reductase Protein R2 from Mouse. *J. Biol. Chem.* **2004**, *279*, 46794–46801.
- (50) Ge, J.; Yu, G.; Ator, M. A.; Stubbe, J. Pre-Steady-State and Steady-State Kinetic Analysis of *E. coli* Class I Ribonucleotide Reductase. *Biochemistry* **2003**, *42*, 10071–10083.
- (51) Bennati, M.; Robblee, J. H.; Mugnaini, V.; Stubbe, J.; Freed, J. H.; Borbat, P. EPR Distance Measurements Support a Model for Long-Range Radical Initiation in *E. coli* Ribonucleotide Reductase. *J. Am. Chem. Soc.* **2005**, *127*, 15014–15015.
- (52) Dassama, L. M. K.; Boal, A. K.; Krebs, C.; Rosenzweig, A. C.; Bollinger, J. M., Jr. Evidence That the β Subunit of *Chlamydia trachomatis* Ribonucleotide Reductase Is Active with the Manganese Ion of Its Manganese(IV)/Iron(III) Cofactor in Site 1. *J. Am. Chem. Soc.* **2012**, *134*, 2520–2523.
- (53) Dassama, L. M. K.; Krebs, C.; Bollinger, J. M., Jr.; Rosenzweig, A. C.; Boal, A. K. Structural Basis for Assembly of the Mn(IV)/Fe(III) Cofactor in the Class Ic Ribonucleotide Reductase from *Chlamydia trachomatis*. *Biochemistry* **2013**, *52*, 6424–6436.
- (54) Jiang, W.; Hoffart, L. M.; Krebs, C.; Bollinger, J. M., Jr. A Manganese(IV)/Iron(IV) Intermediate in Assembly of the Manganese(IV)/Iron(III) Cofactor of *Chlamydia trachomatis* Ribonucleotide Reductase. *Biochemistry* **2007**, *46*, 8709–8716.
- (55) Jiang, W.; Saleh, L.; Barr, E. W.; Xie, J.; Gardner, M. M.; Krebs, C.; Bollinger, J. M., Jr. Branched Activation- and Catalysis-Specific Pathways for Electron Relay to the Manganese/Iron Cofactor in Ribonucleotide Reductase from *Chlamydia trachomatis*. *Biochemistry* **2008**, *47*, 8477–8484.
- (56) Jeschke, G. *DeerAnalysis*; ETH Zurich, 2013; <http://www.epr.ethz.ch/software/index>.
- (57) Bencini, A.; Gatteschi, D. *EPR of Exchange Coupled Systems*; Springer-Verlag: Berlin, 1990.
- (58) Bertrand, P.; More, C.; Guigliarelli, B.; Fournel, A.; Bennett, B.; Howes, B. Biological Polynuclear Clusters Coupled by Magnetic Interactions: From the Point Dipole Approximation to a Local Spin Model. *J. Am. Chem. Soc.* **1994**, *116*, 3078–3086.
- (59) Elsässer, C.; Brecht, M.; Bittl, R. Pulsed Electron–Electron Double Resonance on Multinuclear Metal Clusters: Assignment of

Spin Projection Factors Based on the Dipolar Interaction. *J. Am. Chem. Soc.* **2002**, *124*, 12606–12611.

(60) Elsaesser, C.; Brecht, M.; Bittl, R. Treatment of Spin-Coupled Metal-Centres in Pulsed Electron–electron Double-Resonance Experiments. *Biochem. Soc. Trans.* **2005**, *33*, 15–19.

(61) Price, J. C.; Barr, E. W.; Tirupati, B.; Bollinger, J. M., Jr.; Krebs, C. The First Direct Characterization of a High-Valent Iron Intermediate in the Reaction of an α -Ketoglutarate-Dependent Dioxygenase: A High-Spin Fe(IV) Complex in Taurine/ α -Ketoglutarate Dioxygenase (TauD) from *Escherichia coli*. *Biochemistry* **2003**, *42*, 7497–7508.

(62) Yang, J.; Yan, R.; Roy, A.; Xu, D.; Poisson, J.; Zhang, Y. The I-TASSER Suite: Protein Structure and Function Prediction. *Nat. Methods* **2015**, *12*, 7–8.

(63) Roy, A.; Kucukural, A.; Zhang, Y. I-TASSER: A Unified Platform for Automated Protein Structure and Function Prediction. *Nat. Protoc.* **2010**, *5*, 725–738.

(64) Zhang, Y. I-TASSER Server for Protein 3D Structure Prediction. *BMC Bioinformatics* **2008**, *9*, 40.

(65) Phillips, J. C.; Braun, R.; Wang, W.; Gumbart, J.; Tajkhorshid, E.; Villa, E.; Chipot, C.; Skeel, R. D.; Kalé, L.; Schulten, K. Scalable Molecular Dynamics with NAMD. *J. Comput. Chem.* **2005**, *26*, 1781–1802.

(66) Mackerell, A. D.; Feig, M.; Brooks, C. L. Extending the Treatment of Backbone Energetics in Protein Force Fields: Limitations of Gas-Phase Quantum Mechanics in Reproducing Protein Conformational Distributions in Molecular Dynamics Simulations. *J. Comput. Chem.* **2004**, *25*, 1400–1415.

(67) Humphrey, W.; Dalke, A.; Schulten, K. VMD: Visual Molecular Dynamics. *J. Mol. Graphics* **1996**, *14*, 33–38.

(68) Frisch, M. J.; Trucks, G. W.; Schlegel, H. B.; Scuseria, G. E.; Robb, M. A.; Cheeseman, J. R.; Montgomery, J. A., Jr.; Vreven, T.; Kudin, K. N.; Burant, J. C.; Millam, J. M.; Iyengar, S. S.; Tomasi, J.; Barone, V.; Mennucci, B.; Cossi, M.; Scalmani, G.; Rega, N.; Petersson, G. A.; Nakatsuji, H.; Hada, M.; Ehara, M.; Toyota, K.; Fukuda, R.; Hasegawa, J.; Ishida, M.; Nakajima, T.; Honda, Y.; Kitao, O.; Nakai, H.; Klene, M.; Li, X.; Knox, J. E.; Hratchian, H. P.; Cross, J. B.; Bakken, V.; Adamo, C.; Jaramillo, J.; Gomperts, R.; Stratmann, R. E.; Yazyev, O.; Austin, A. J.; Cammi, R.; Pomelli, C.; Ochterski, J. W.; Ayala, P. Y.; Morokuma, K.; Voth, G. A.; Salvador, P.; Dannenberg, J. J.; Zakrzewski, V. G.; Dapprich, S.; Daniels, A. D.; Strain, M. C.; Farkas, O.; Malick, D. K.; Rabuck, A. D.; Raghavachari, K.; Foresman, J. B.; Ortiz, J. V.; Cui, Q.; Baboul, A. G.; Clifford, S.; Cioslowski, J.; Stefanov, B. B.; Liu, G.; Liashenko, A.; Piskorz, P.; Komaromi, I.; Martin, R. L.; Fox, D. J.; Keith, T.; Al-Laham, M. A.; Peng, C. Y.; Nanayakkara, A.; Challacombe, M.; Gill, P. M. W.; Johnson, B.; Chen, W.; Wong, M. W.; Gonzalez, C.; and Pople, J. A. *Gaussian 03*, Revision C.02; Gaussian, Inc.: Wallingford, CT, 2004.

Supporting Information for:

**Direct Measurement of the Radical Translocation Distance in the Class I Ribonucleotide
Reductase from *Chlamydia trachomatis***

Jovan Livada,^{a†} Ryan J. Martinie,^{a†} Laura M. K. Dassama,^{b,§} Carsten Krebs,^{a,b} J. Martin
Bollinger, Jr.,^{a,b} and Alexey Silakov^{a*}

Departments of ^aChemistry and of ^bBiochemistry and Molecular Biology, Pennsylvania State
University, University Park, PA USA 16802. [§]Present address: Department of Chemistry,
Northwestern University, Evanston, IL USA 60208.

[†]These authors contributed equally to this work.

SI Figures

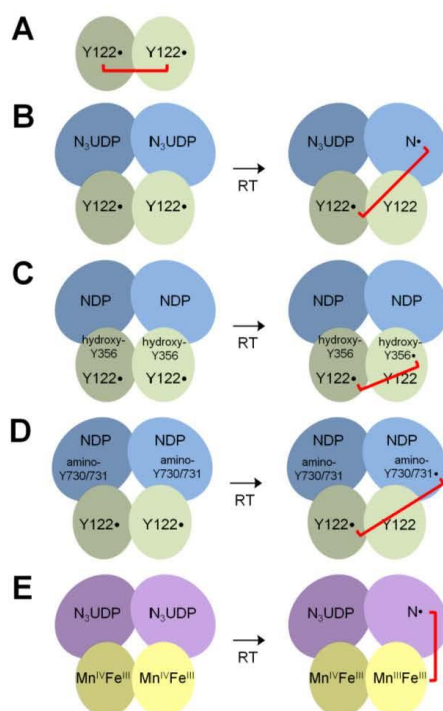


Figure S1. Schematic representation of distances probed by DEER experiments in *Ec* (A-D) and *Ct* (E) RNR. Experiments were performed on the β_2 complex (A) and on the putative $\alpha_2\beta_2$ complex (B-E), depicted before (left) and after (right) radical translocation in the presence of N_3UDP (B and E) or substrate (C and D). Grey shading indicates the $\alpha\beta$ pair that is inactive as a result of the "half-of-sites" reactivity demonstrated for both the *Ec* and *Ct* enzymes. Red bars indicate distance measurements performed using DEER in previous studies (A-D) and herein (E).

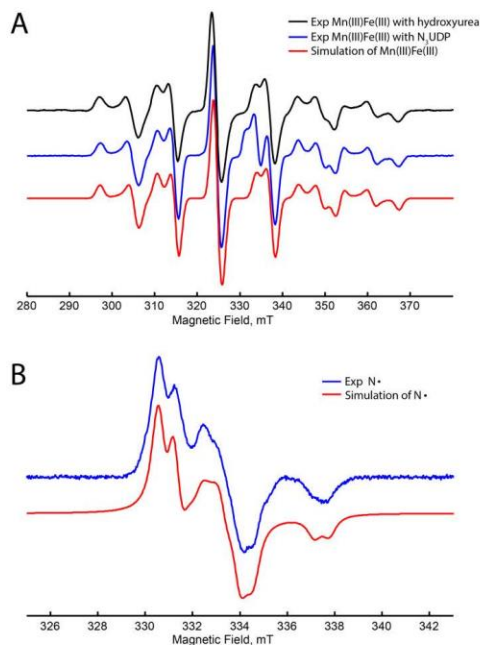


Figure S2. Continuous-wave electron paramagnetic resonance spectra of *Ct* RNR. A) Spectra measured at 14 K of the *Ct* RNR Mn(III)/Fe(III) state produced by hydroxyurea reduction in the presence of α (black), radical trapping with N_3 UDP (blue), and simulation (red). B) Experimental (blue) and simulated (red) spectra of the $N\bullet$ radical collected at 77 K. Spectrometer conditions: Microwave frequency, 9.3832 GHz; microwave power, 20 μ W; modulation amplitude, 10 G; modulation frequency, 100 kHz; scan time, 167 s; time constant, 167 ms. Simulations were performed using ‘pepper’ program (Easyspin)¹ and yielded the following parameters for the Mn(III)/Fe(III) state: $\mathbf{g} = [2.009, 2.014, 2.024]$ and $\mathbf{A}(^{55}\text{Mn}) = [314, 396, 269]$ MHz, and the following for $N\bullet$: $\mathbf{g} = [2.01557, 2.00625, 2.00209]$, $\mathbf{A}(^{14}\text{N}) = [5.6, 5.6, 89.6]$ MHz, and $\mathbf{A}(^1\text{H}) = [17.64, 17.64, 17.64]$ MHz.

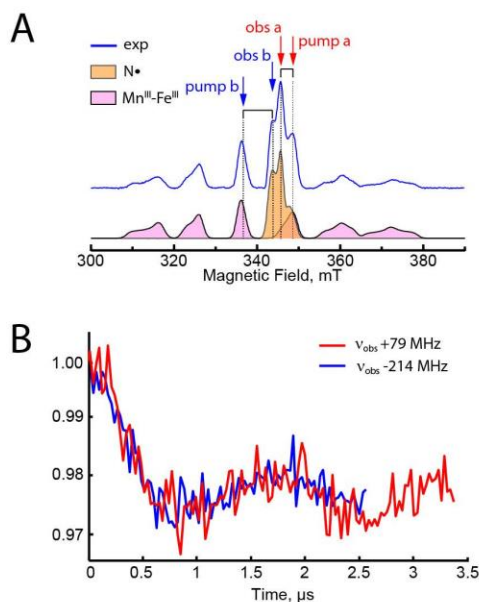


Figure S3. Pulse EPR spectrum of *Ct* RNR in the presence of N_3 UDP (A) and a comparison of DEER traces collected using differing pump/observe frequency combinations $\nu_{\text{pump}} = \nu_{\text{obs}} + 79$ MHz (red) and $\nu_{\text{pump}} = \nu_{\text{obs}} - 214$ MHz (blue) (B).

A) Experimental spectrum is in blue, the simulation for $Mn(III)/Fe(III)$ is shaded purple, and the simulation for N^\bullet is shaded orange. Arrows indicate the portion of the spectrum probed by the detection (obs) and ELDOR (pump) pulses for both DEER traces with color coding the same as in panel B. Experimental conditions: 2-pulse electron-spin-echo detection, MW frequency, 9.767 GHz; temperature, 14 K; τ , 400 ns.

B) Experimental conditions for the red trace: MW frequency, 9.767 GHz; ELDOR frequency, 9.688 GHz; temperature, 4 K; τ , 400 ns; $t_{1,\text{start}}$, 200ns; $t_{2,\text{start}}$, 3.2 μs ; shot repetition time, 50 ms. For the blue trace: microwave frequency, 9.616 GHz; ELDOR frequency, 9.830 GHz; temperature, 4 K; τ , 400 ns; $t_{1,\text{start}}$, 200ns; $t_{2,\text{start}}$, 2.4 μs ; $t(\text{step}) = 28$ ns. The shot repetition rate was 50 ms with 5 shots per point, averaged for 994 scans.

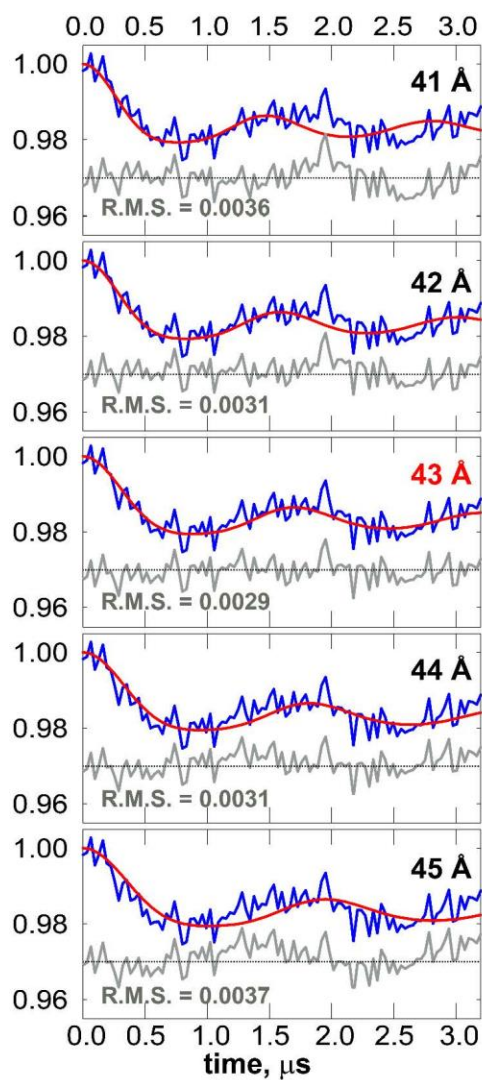


Figure S4. Simulation of the DEER trace using a Gaussian distance distribution model with fixed full-width at half-height set to 2 Å. Experimental traces are in blue, simulations are red, and residuals are in gray (plotted below).

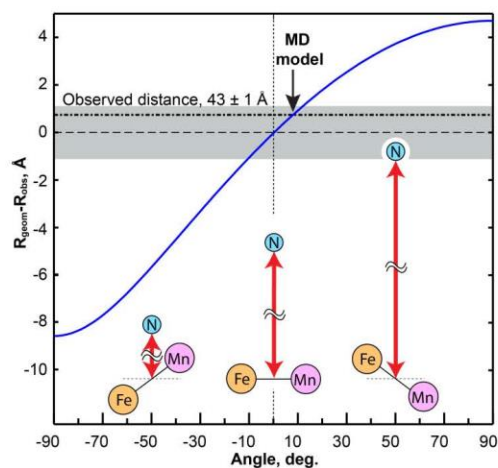


Figure S5. Deviation of the actual geometric distance between the center of the Mn(III)/Fe(III) cofactor and the N• radical (R_{geom}) and the observed dipolar distance ($R_{\text{obs}} = 43 \text{ \AA}$) as a function of the angle between the Mn-Fe vector and the vector connecting the radical-harboring nitrogen (N•) and the geometric center of the Mn-Fe cluster (red double arrow). The black arrow indicates the average value of this angle observed in the *Ct* RNR molecular dynamics simulation, and the gray area indicates the experimental uncertainty. Calculations are based on the following equations:

$$R_{\text{obs}}^{-3} = c_1 * R_{\text{FeN}}^{-3} + c_2 * R_{\text{MnN}}^{-3} \quad (1)$$

$$R_{\text{geom}} = (R_{\text{FeN}} + R_{\text{MnN}})/2 \quad (2)$$

where $c_1 = 7/3$ and $c_2 = -4/3$ are the spin projection factors; distances R_{FeN} and R_{MnN} are calculated using $R_{\text{obs}} = 43 \text{ \AA}$ and $r_{\text{MnFe}} = 3.1 \text{ \AA}$. The value of $r_{\text{MnFe}} = 3.1 \text{ \AA}$ was based on the crystallographic structure of β_2 obtained by Dassama et al. (PDB: 4D8F).²

Literature Cited

- (1) Stoll, S.; Schweiger, A. EasySpin, a Comprehensive Software Package for Spectral Simulation and Analysis in EPR. *Journal of Magnetic Resonance* **2006**, *178*, 42–55.
- (2) Dassama, L. M. K.; Boal, A. K.; Krebs, C.; Rosenzweig, A. C.; Bollinger, J. M. Jr. Evidence That the β Subunit of *Chlamydia trachomatis* Ribonucleotide Reductase Is Active with the Manganese Ion of Its Manganese(IV)/Iron(III) Cofactor in Site 1. *J. Am. Chem. Soc.* **2012**, *134*, 2520–2523.

Chapter 5

Spectroscopic and Computational Analysis of Proton

Transfer in the Turnover-initiating Transient

Reduction of the β -Mn^{IV}/Fe^{III} Cofactor of a Class Ic

Ribonucleotide Reductase

Spectroscopic and Computational Analysis of Proton Transfer in the Turnover-initiating Transient Reduction of the β -Mn^{IV}/Fe^{III} Cofactor of a Class Ic Ribonucleotide Reductase

Jovan Livada,^a Carsten Krebs,^{a,b} J. Martin Bollinger, Jr.,^{a,b} and Alexey Silakov^a

Departments of ^aChemistry and of ^bBiochemistry and Molecular Biology, Pennsylvania State University, University Park, PA USA 16802.

ABSTRACT

In a class I ribonucleotide reductase (RNR), a stable dimetal(III/IV) cluster or tyrosine-derived free radical in the β subunit reversibly oxidizes a cysteine (Cys) residue more than 30 Å away in the α subunit to generate a thiyl radical (Cys•), which initiates substrate reduction. This radical-translocation (RT) step is mediated by a chain of strictly conserved Tyr residues (two in α and one in β) via discrete hole-hopping and proton-coupled-electron-transfer (PCET) steps and is conformationally gated to occur only with the substrate bound in α . Opening of the gate is likely to involve the connection of a proton-transfer (PT) pathway in β ; PT enables local charge compensation for the electron arriving to the buried oxidant and makes migration of the hole toward α thermodynamically feasible. In the class Ia RNR from *Escherichia coli*, the proton is transferred from a water ligand of the β -Fe^{III}/Fe^{III} cluster to the radical Tyr as the radical undergoes reduction. The presumptive PT step in the class Ic RNR from *Chlamydia trachomatis*, in which reduction of a β -Mn^{IV}/Fe^{III} cluster to an EPR-active ($S = 1/2$) β -Mn^{III}/Fe^{III} state drives Cys oxidation in α , is not understood. In this study, we have applied advanced electron paramagnetic

resonance spectroscopies and density-functional theory (DFT) calculations to the β -Mn^{III}/Fe^{III} RT product to determine the number and location of its protons. Together with previous structural characterization of the β -Mn^{IV}/Fe^{III} RT-reactant state, these new results imply that the acceptor for the RT-gating PT step is a hydroxide ligand on the Mn^{IV}.

INTRODUCTION

All cells and organisms obtain the 2'-deoxyribonucleotide precursors for DNA replication from the corresponding ribonucleotides through the action of a ribonucleotide reductase (RNR).¹ Although evolution has diversified this important group of enzymes to a remarkable extent, a single mechanistic solution to the chemically challenging nucleotide 2'-dehydroxylation reaction appears to have been strictly conserved.² The mechanism begins with formation of a carbon-centered radical on the 3' position of the nucleoside di- or tri-phosphate substrate by hydrogen atom (H•) transfer (HAT) to a cysteine thiyl radical (Cys•). The Cys• is not present in the resting enzyme; rather, it is generated by univalent oxidation of a conserved, substrate-proximal Cys residue at the start of each turnover and reduced again at the end. The different means by which RNRs from different organisms generate this common Cys• underpin their surprising diversity. Modern class III RNRs, which are functional only in microbes living in anaerobic niches and are thought to be most similar to the primordial RNR, use a stable glycyl radical, installed by the action of an iron-sulfur/radical-S-adenosyl-L-methionine activase, to generate the Cys•.³ Class II enzymes, present in both aerobic and anaerobic microbes, use the classic, reversible Co-C-bond homolysis of 5'-deoxyadenosylcob(III)alamin to generate the Cys•.⁴ Class I RNRs, the main topic of this study, are found in all eukaryotes (including humans) and many pathogenic bacteria and are unique in deploying separate “cofactor” subunits, β , for Cys• generation in their catalytic subunits, α .⁵

The α subunits of class I RNRs are structurally and functionally homologous to the self-contained, single-subunit enzymes of classes II and III. The β subunits are α -helical proteins of the “ferritin-like” structural superfamily. They bind redox-active divalent transition metal ions (most often, two) that react with dioxygen, or a reduced form thereof, to generate one of several

types of one-electron oxidants, as elaborated below.⁶ Although other oligomeric structures have been observed, and their formation appears to be important in cellular regulation of RNR activity, a 1:1 complex of the homodimeric α and β subunits ($\alpha_2\beta_2$) is the active state in the most extensively studied class I enzyme from *Escherichia coli* (*Ec*) and, it is thought, in other orthologs.⁷ Evidence implies that only one $\alpha\beta$ pair of this potentially two-fold symmetrical heterotetramer engages in catalysis at a given time (“half-of-sites activity”), suggesting both that the C_2 axes of the subunits might not be collinear in the complex and that stringent structural requirements for Cys• generation might be achievable only on one side of the complex at a time.⁸ The oxidant site in β and HAT-mediating Cys in α are both buried in the subunit interiors, implying that the bidirectional translocation of the oxidant (hereafter, radical translocation or RT) from one site to the other must proceed over a considerable distance (estimated from models of the complex and EPR experiments to be ~ 35 Å).⁹⁻¹¹ This long-distance, intersubunit RT is mediated by a chain of three tyrosine residues, two in α and one in β , with possible participation by a cofactor-proximal tryptophan in β .¹² Along with the radical Cys, these four aromatic residues are conserved in all known, functional class I RNRs. RT is thought to proceed by multiple steps involving discrete pathway radicals, but these radicals do not accumulate in the wild-type enzymes under turnover conditions. Only by substitution of the Tyr residues in the pathway with more easily oxidized (unnatural) analogs, or by use of more oxidizing cofactor forms, have accumulation and detection of pathway radicals been achieved.^{9, 13-16} In fact, the entire sequence of steps – (i) migration of the electron hole in β to the Cys in α , (ii) reduction of the substrate, and (iii) RT in the opposite direction to regenerate the reduced Cys and oxidized β cofactor – is obscured by a rate-limiting conformational change required for the forward RT to proceed.^{17, 18} This conformational change reflects “gating” of hole migration so that it occurs only when the enzyme is poised for turnover.

Evidence indicates that binding of the substrate in α triggers opening of the gate, but the gating mechanism itself is not generally well understood (*vide infra*).

The location of the potent oxidant of the Cys•-generating cofactor in the core of the ferritin-like four-helix bundle of β is essential for its gated reactivity, and, in turn, for the efficient function of a class I enzyme. The four core helices generally provide as many as six metal ligands (two His and four Glu/Asp residues), which most often bind two redox-active transition metal ions (iron, manganese, or one of each) in a coupled dimetal cluster. The cluster can generate and/or store the oxidant, and it can also play a role in the RT process and the gating thereof. Remarkably, five different oxidant/cofactor types have been identified within class I, resulting in the further subdivision of the enzymes into subclasses a-e. Four characteristics of the β subunit determine its subclass (Table 1): (i) the identity of the α -Cys oxidant – tyrosyl radical (Tyr•) in subclasses a and

	Oxidant	Metals	Dioxygen species	NrdI Activase
Ia	Y•	Fe/Fe	O ₂	-
Ib	Y•	Mn/Mn	O ₂ ^{-•}	Yes
Ic	Mn ^{IV}	Mn/Fe	O ₂	-
Id	Mn ^{IV}	Mn/Mn	O ₂ ^{-•}	-
Ie	DOPA•	?	O ₂ ^{-•} (?)	Yes

Table 1. Diversity of class I ribonucleotide reductases. The five known classes differ in the oxidant used to transiently generate the Cys•, the metals they employ, the dioxygen species required for activation and the necessity of an activase protein NrdI.

b, dimetal cluster in c and d, and dihydroxyphenylalanyl (DOPA) radical (DOPA•) in e; (ii) the identities of the metal ions – Fe₂ in subclass a, Mn₂ in b and d, Mn/Fe in c, and none in e (although a transition metal could be required for activation); (iii) the dioxygen species that serves to install the α -Cys oxidant in β – O₂ in subclasses a and c, and O₂⁻ (superoxide) in b, d, and (most likely)

e; and (iv) whether a flavoprotein activase, NrdI, is (in subclasses b and e) or is not (in a, c, and d) required to generate the dioxygen species that activates β .

The activation of β and the conformationally gated, intersubunit RT step have been studied most extensively for the *Ec* Ia enzyme and the Ic ortholog from *Chlamydia trachomatis* (*Ct*). In activation of *Ec* β , the protein self-assembles a $\text{Fe}^{\text{II}}/\text{Fe}^{\text{II}}$ cluster, which reacts with O_2 via μ -(peroxo)- $\text{Fe}^{\text{III}}/\text{Fe}^{\text{III}}$ and $\text{Fe}^{\text{III}}/\text{Fe}^{\text{IV}}$ intermediates.¹⁹⁻²² The latter complex formally abstracts $\text{H}\cdot$ from the nearby ($\sim 5 \text{ \AA}$ from Fe1) Tyr residue (Y122) to produce the stable, neutral Tyr radical (Y122 \cdot). The resultant $\text{Fe}^{\text{III}}/\text{Fe}^{\text{III}}$ cluster of the active subunit has a bridging μ -oxo derived from O_2 and one terminal OH_x ($x = 1$ or 2) ligand to each Fe^{III} .

Ct β self-assembles a β - $\text{Mn}^{\text{II}}/\text{Fe}^{\text{II}}$ cluster by binding Mn^{II} in site 1 and Fe^{II} in site 2.^{23, 24} The intrinsic specificities of the sites help direct the proper locations of the two metal ions. O_2 adds to the reduced cluster, producing an $S_{\text{Total}} = 1/2$, EPR-active β - $\text{Mn}^{\text{IV}}/\text{Fe}^{\text{IV}}$ intermediate assigned based on spectroscopic and computational results as having two bridging oxo ligands and a hydroxo ligand to the Mn^{IV} ion.²⁵ A Tyr residue (Y222) that is not on the RT pathway shuttles an electron to the iron site to generate the functional β - $\text{Mn}^{\text{IV}}/\text{Fe}^{\text{III}}$ cofactor.²⁶ Results of spectroscopic and computational studies of this cluster – the RT reactant state – imply that it has bridging oxo and hydroxo ligands and a terminal hydroxo on the Mn^{IV} ion.^{27, 28} Thus, reduction of the activation intermediate to the functional cofactor is coupled to proton transfer to a bridging oxo.

Because one merely generates the Tyr \cdot , which then serves as Cys oxidant, whereas the other is, itself, the functional oxidant, the dimetal clusters in the Ia and Ic RNRs necessarily have different roles in catalytic nucleotide reduction. For the *Ec* Ia enzyme, use of either a radical-trapping substrate analog, 2'-azido-2'-deoxyuridine 5'-diphosphate (N_3UDP), or a variant α

subunit with a radical-stabilizing unnatural amino acid in the RT pathway enabled demonstration of a perturbation to the Mössbauer spectrum of Fe1, the Fe^{III} ion closer to the Tyr•, in formation of the Tyr•-reduced RT product state. Density functional theory (DFT) calculations implied that the observed decrease in ΔE_Q results from deprotonation of a water ligand, thus identifying this ligand as the proton donor for the RT-initiating PCET step to the Tyr• in the buried β cofactor site.²⁹ The coupled proton-transfer (PT) step presumably obviates formation of the tyrosinate anion in the hydrophobic site, which would strongly thermodynamically disfavor Tyr• reduction and likely make the oxidant insufficiently potent for α -Cys oxidation. Thus, a simple working hypothesis for the mechanism of gating of the RT step would invoke propagation of a conformational change associated with binding of the substrate in α into the β active site to change the Fe1–O–H \leftrightarrow •O–Tyr distance or disposition of an intervening PT-mediating functional group, thereby connecting the PT pathway and permitting the electron hole to migrate toward α in the initial PCET step of the multi-step RT process.

In the *Ct* class Ic RNR, the RT process directly reduces the Mn^{IV} ion of the cluster to yield the β -Mn^{III}/Fe^{III} state, which has an electron-spin ground state with $S_{\text{Total}} = 1/2$ and is EPR active. It is reasonable to expect that a local PT might be associated with cofactor reduction, serving (as in the *Ec* system) to tune its potential to enable RT in both directions. However, neither the donor nor the acceptor for this presumptive PT step had been identified prior to this work.

Multiple manifestations of the gated nature of the RT process and of substrate binding as the gate-opening signal have been reported for the *Ec* Ia and the *Ct* Ic RNRs. The demonstration that cytidine diphosphate (CDP) binding to the *Ec* holoenzyme can accelerate (by a factor of 10) reductive quenching of the Tyr• by the RNR-targeting drug, hydroxyurea (HU), provided the initial hint of gating by the substrate.³⁰ It suggested that the drug has limited access to the electron hole

in its resting location on Y122 within the hydrophobic β active site but increased access during turnover. Later experiments with *Ec* β bearing the more easily oxidized DOPA in place of the subunit-interfacial, RT-mediating Tyr residue (Y356) revealed rapid DOPA• accumulation upon substrate (CDP) addition,³¹ and subsequent studies with other unnatural amino acids (e.g., 3-aminotyrosine) in the RT pathway yielded similar observations.³² Together, the results imply localization of the electron hole on the buried Tyr of the resting subunit and migration toward α after a conformational change driven by substrate binding opens the gate.

The *Ct* system afforded even richer physical evidence for conformational gating by substrate binding. Treatment of the functional holoenzyme with HU led to rapid (maximum rate constant of 0.7 s^{-1} at $22\text{ }^{\circ}\text{C}$) reduction of the $\beta\text{-Mn}^{\text{IV}}/\text{Fe}^{\text{III}}$ cofactor to the EPR-active, $S_{\text{Total}} = 1/2$, $\beta\text{-Mn}^{\text{III}}/\text{Fe}^{\text{III}}$ form, and this reaction exhibited absolute requirements for both the substrate and a functional pathway for migration of the electron hole away from its buried site in β .¹⁸ HU treatment of (i) the wild-type β in the absence of α , (ii) the holoenzyme in the absence of substrate, or (iii) variant β subunits lacking a functional RT pathway in the presence of α and substrate led to a much slower (~ 1000 -fold) conversion of the $\beta\text{-Mn}^{\text{IV}}/\text{Fe}^{\text{III}}$ cofactor to a different and diamagnetic [formally $\beta\text{-Mn}^{\text{II}}/\text{Fe}^{\text{III}}$] cluster form. The conclusion drawn – that HU rapidly intercepts a radical along the RT pathway to trap the $\beta\text{-Mn}^{\text{III}}/\text{Fe}^{\text{III}}$ product of functional RT but can only sluggishly reduce the buried $\beta\text{-Mn}^{\text{IV}}/\text{Fe}^{\text{III}}$ oxidant when it must react directly – concurred with interpretation in the earlier work of substrate-potentiated reduction of the cofactor Tyr• in the *Ec* Ia system. Intriguingly, the data on *Ct* RNR also suggested that the amino acid radical trapped by HU need not be a Tyr• in the functional RT pathway. So long as Y222, the Tyr which shuttles an electron to the cofactor during its assembly but has no role in catalytic nucleotide reduction, was not also substituted, α - and CDP-dependent univalent reduction of the cofactor by HU was still observed

with the enzymatically inactive variant β protein lacking its subunit-interfacial, RT-mediating Tyr (Y338). This observation suggested that gating events needed to enable the initial hole migration are proximal to the β cofactor and allow either the catalytically functional Y338 or the activation-specific Y222 to serve as the immediate cluster reductant.¹⁸ Univalent reduction of the β -Mn^{IV}/Fe^{III} cofactor by the stronger reductant, dithionite, did not require turnover conditions, but the nature of the resultant β -Mn^{III}/Fe^{III} product of this reduction, as reflected by its EPR signature, *did* depend on whether α and the substrate were present. Only in their presence did the spectrum of the product match that afforded by treatment under turnover conditions with either HU or a mechanism-based inactivator capable of trapping the electron hole in α following Cys• generation. Dithionite reduction of the cofactor in the absence of α and CDP yielded a broader, more

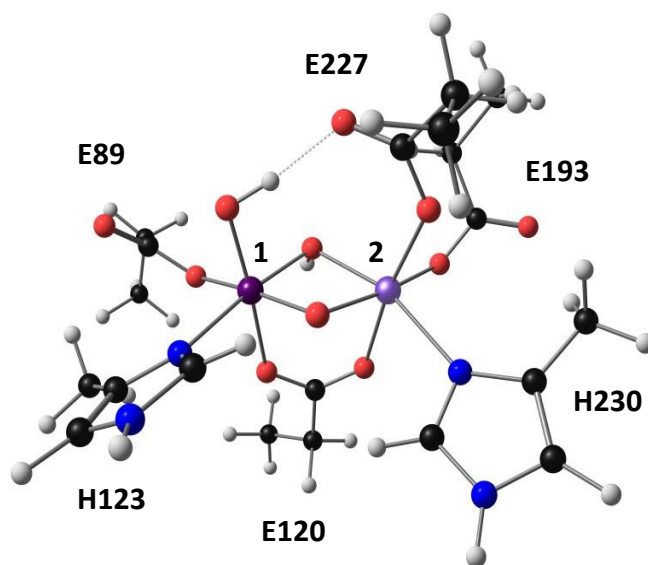


Figure 1. Computationally derived model of the β -Mn^{IV}/Fe^{III} RT reactant state of *Ctr* β . Arabic numerals 1 and 2 indicate the conventional metal site designations. Adapted from ref (28).

complex, less reproducible spectrum reflecting structural heterogeneity of the cluster. One attractive possibility for the source of this heterogeneity is the number or location of protons delivered to the cofactor as it undergoes one-electron reduction. In later experiments, accumulation of pathway radicals by assembly of the holoenzyme complex from β harboring the “superoxidized” β -Mn^{IV}/Fe^{IV} cofactor (the activation intermediate) was also shown to depend on the presence of substrate.¹⁶

Given the importance of conformational gating of RT to efficient function of a class I RNR, the precedent from the *Ec* Ia system for the role of local PT in controlling the RT process, and the indirect evidence summarized above that local events gate RT also in the Ic *Ct* system, we sought to address whether and how a local PT step might be coupled to ET to the $\beta\text{-Mn}^{\text{IV}}/\text{Fe}^{\text{III}}$ cofactor to control its effective potential and enable conformational gating. In this study, we employed ^2H hyperfine sublevel correlation (HYSCORE) and electron-nuclear double resonance (ENDOR) spectroscopies to detect the hydrons that are coupled to the $S_{\text{Total}} = 1/2$ $\beta\text{-Mn}^{\text{III}}/\text{Fe}^{\text{III}}$ RT-product state in order to determine whether, and to what functional group, PT to the cofactor is coupled to the ET step that initiates RT. By also determining ^{14}N couplings by ENDOR (**Figure S1**) experiments and the exchange coupling constant, J , governing interaction of the Mn^{III} and Fe^{III} ions by relaxation measurements, we obtained further experimental calibration for density-functional-theory (DFT) calculations to interpret the experimental results in terms of cofactor structure and the number and locations of the hydrogens. Comparison to the prior structural description of the $\beta\text{-Mn}^{\text{IV}}/\text{Fe}^{\text{III}}$ RT reactant state (**Figure 1**) revealed that the functional RT process involves PT to the terminal hydroxo ligand to the Mn ion of the cofactor. This conclusion suggests that control of the coupled PT step could be generally important in the conformational gating of RT across all subclasses of class I, including the two (c and d) for which the dimetal cluster itself, rather than a nearby amino acid radical, is the functional oxidant.

Experimental Results, and Discussion

CW EPR Spectrum of the β -Mn^{III}/Fe^{III} state

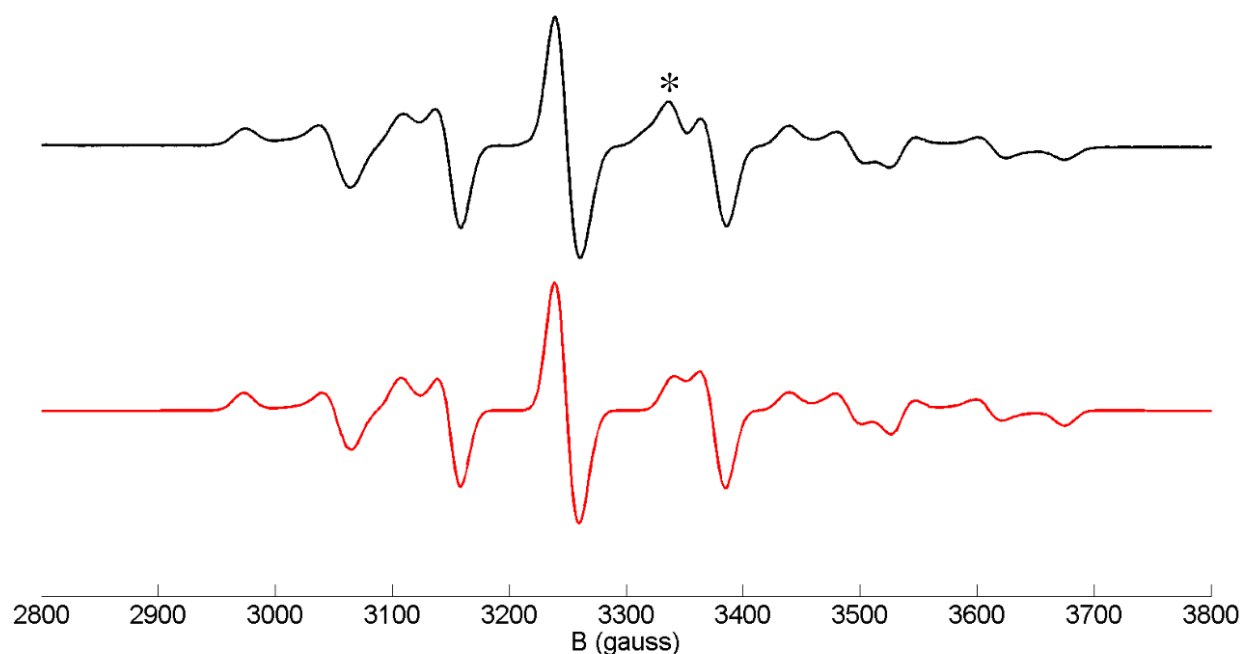


Figure 2. Field swept CW EPR spectrum of the β -Mn^{III}/Fe^{III} RT product state generated via N₃UDP in black and the simulation in red. The asterisk indicates the location of the saturated N•. Experimental condition: MW frequency 9.4 GHz, Temperature 14 K, MW power 15 dB, scan time 120 sec, modulation amplitude 10 gauss, npoints 1024.

Previous studies^{18, 33} prescribed three ways that the functional cofactor RT product state could be generated, all requiring the presence of α , CDP, dithiothreitol (DTT), and adenosine triphosphate (ATP) with β . The three published methods used to generate the RT product state include direct cofactor reduction by dithionite (DT), reduction via the scavenging ability of hydroxyurea (HU) to reduce pathway radicals during radical translocation, and the use of the substrate analog, N₃UDP. The third way is only way to trap the RT product β -Mn^{III}/Fe^{III} cofactor state while ensuring that the radical has been translocated into the α subunit. For this reason, we chose the third method for this study which upon radical translocation generates two radical

species, the sought β -Mn^{III}/Fe^{III} cofactor state as well as the previously well characterized N• in the α subunit.³⁴ One difficulty in generating a substantial quantity of the desired RT product state arises from the fact that class I RNRs exhibit half-sites reactivity⁸ where only one monomer pair in the holoenzyme dimer is able to perform its catalytic function at a time. The RT reactant state, β -Mn^{IV}/Fe^{III} cofactor has an electron spin $S_{\text{Total}} = 1$ making it undetectable using perpendicular mode EPR methods. Therefore, the only EPR signal observed after radical translocation is the sought-out RT product state β -Mn^{III}/Fe^{III}. In our case, spin quantification indicated that 370 μ M concentration of spin was generated in the reaction mixture of *Ct* α and β -Mn^{IV}/Fe^{III}, ATP, DTT and N₃UDP. The β -Mn^{III}/Fe^{III} RT product state of the *Ct* RNR β cofactor is comprised of antiferromagnetically coupled $S = 2$ Mn^{III} and $S = 5/2$ Fe^{III} ions with a ground state having total electron-spin quantum number, S_{Total} , of 1/2. The EPR resonance of the coupled system (**Figure 2**) is split into six well-resolved packets by the strong hyperfine (HF) coupling between the delocalized unpaired electron and the spin of the ⁵⁵Mn nucleus ($I = 5/2$). Previous studies showed that the optimal simulation of this spectrum was achieved by assuming $g = [2.024, 2.014, 2.009]$ for the electron spin system and a ⁵⁵Mn hyperfine tensor $A_{55\text{Mn}} = [269, 396, 314]$ MHz (**Figure 2**).

Analysis of hyperfine parameters of solvent exchangeable hydrons in dinuclear systems

The solvent exchangeable hydrons in the vicinity of a dinuclear metal center are generally bonded to bridging or terminal oxygen ligands. Previous ENDOR and HYSCORE experiments on antiferromagnetically coupled dimetal clusters with $S_{\text{Total}} = 1/2$ ($\text{Fe}_2^{\text{II/III}}$,³⁵⁻³⁸ $\text{Fe}_2^{\text{III/IV}}$,³⁹ $\text{Mn}_2^{\text{III/IV}}$,⁴⁰⁻⁴³ and $\text{Mn}^{\text{III}}/\text{Fe}^{\text{III/IV}}$) have shown that hydrons bonded to bridging oxygen ligands exhibit stronger maximum HF coupling ($|T| > 20$ MHz for protium, corresponding to $|T| > 3$ MHz for deuterium) than those bonded to terminal oxygens ($|T| < 20$ MHz for protium, corresponding to $|T| < 3$ MHz for deuterium). The former coupling generally exhibits more rhombic symmetry ($\eta > 0.8$, where the principal components of the hyperfine tensor are rank-ordered as $|A_{zz}| > |A_{xx}| > |A_{yy}|$ and $\eta = |(A_{xx} - A_{yy})/A_{zz}|$), whereas the latter is generally more axially symmetric ($\eta < 0.3$). A bridging hydron is usually nearly equidistant from the two metal ions, resulting in its strong interaction with the spin associated with each metal and the characteristic rhombic hyperfine tensor. A terminal hydron interacts much more strongly with one of the two metal ions (the one that coordinates the oxygen to which the hydron is bonded), resulting in the axial hyperfine tensor (**Figure 3**). To define the positions of solvent exchangeable hydrons, we used advanced EPR methods ENDOR

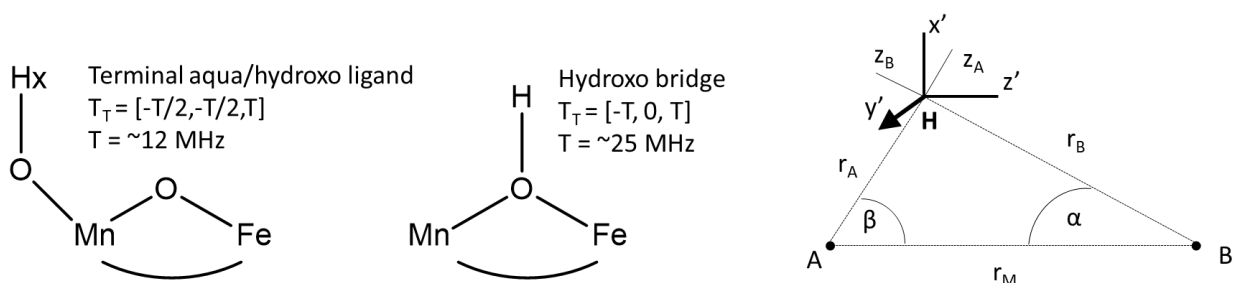


Figure 3. Two simple models of the Mn-Fe cofactor and the typical corresponding hyperfine coupling of the proton located on the terminal oxygen ligand (left) and bridging oxygen ligand (middle). The geometry of the dipolar interaction tensor T (right) of the proton of interest calculated as a sum of the contributions of the two metal sites A and B. Adapted from ref (36).

and HYSCORE to elucidate the hyperfine interaction between those hydrons and the electron spin associated with the Mn^{III} and Fe^{III} ions.

Observation of a bridging hydron via HYSCORE

In acquiring Q-band ^2H HYSCORE data on the $\beta\text{-Mn}^{\text{III}}/\text{Fe}^{\text{III}}$ cofactor, we interrogated five field positions in the range of 11720 – 11800 G of the two-pulse echo detected field swept EPR spectrum to ensure unique fits of the hyperfine and quadrupolar parameters to the experimental data. A sample prepared in D_2O revealed a “double-eyebrow” shaped signal in the first quadrant, indicating high hyperfine rhombicity and the presence of a significant nuclear quadrupolar interaction. The observed HYSCORE signal is characterized by both the cross-correlation ridges that span ~ 4.0 MHz as a result of the strong hyperfine interaction and by the splitting of the signal into two parallel lines as a result of the deuterium quadrupolar coupling. This signal is significantly upshifted from the anti-diagonal and is therefore anisotropic in nature. Simulation of the experimental data with a single strongly coupled deuteron yielded the hyperfine tensor $A_{2\text{H}} = [-4.15, 4.00, 0.00] \pm 0.1$ MHz with Euler rotation angles of $[-10, -35, 5] \pm 10^\circ$, and the quadrupolar-coupling tensor $Q_{2\text{H}} = [0.075, 0.045, -0.12] \pm 0.01$ MHz with Euler angles of $[60, 0, 90] \pm 15^\circ$. The estimated uncertainties were derived from visual evaluation of the agreement between the simulated and experimental spectra. Both the maximum hyperfine coupling parameter ($|T| = \sim 27$ MHz protium equivalent) and the hyperfine tensor rhombicity ($\eta = 0.95$) strongly suggest that the observed hydron is bonded to a bridging oxygen ligand. However, despite being able to simulate the HYSCORE spectra well with the assumption of a single ^2H nucleus, we could not rule out the possibility that two indistinguishable ^2H nuclei coupled to the electron spin give rise to the observed signals. We also observed a signal that likely corresponds to an exchangeable weakly coupled deuteron, as indicated by the black arrows in **Figure 4-C**, top. ESEEM methods, including HYSCORE, are not able to reproduce the true shape of the hyperfine ridges because the signals

lack intensity on the edges of the Fourier transformed signal. This lack of intensity is especially inconvenient and make simulations difficult when the signals are weak and overlap with signals arising from matrix deuterons. The ENDOR method, by contrast, does not suffer from this disadvantage and can reproduce true ridges.

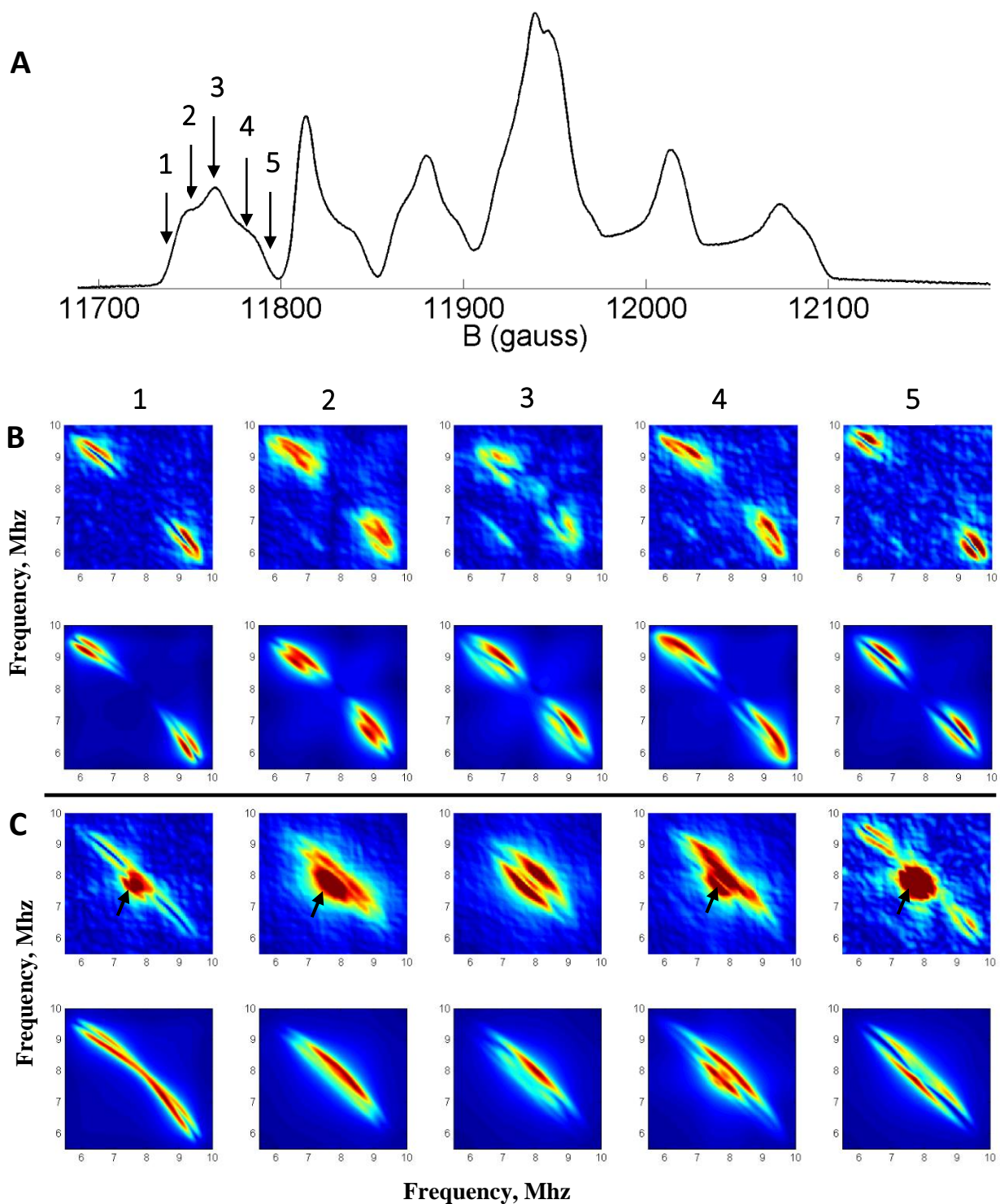


Figure 4 (A) Q-band two-pulse spin echo detected EPR spectrum of the β -Mn^{III}/Fe^{III} state. (B) experimental HYSCORE spectra (top) and simulations (bottom) for two τ values, τ =256 ns and (C) τ =188 ns. Experimental conditions: MW frequency 34.2 GHz, Temperature 15 K, $\pi/2$ of 12 ns, step size 36 ns, npoints 200, exact field values: 11775 G, 11808 G, 11825 G, 11850 G, and 11880 G.

Observation of a terminal hydron via ENDOR

We tested for weakly coupled hydrons by X-band ^2H ENDOR spectroscopy and discovered signals in the region of the deuterium Larmor frequency. The signals used to determine the hyperfine interaction were obtained by the difference of spectra of samples prepared in D_2O and H_2O . The five spectra were obtained across the rhombic Mn hyperfine spin packet between 3500-3700 G of the X-band EPR spectrum (**Figure 5B**). Simulation as a single deuteron yielded the hyperfine tensor $A_{2\text{H}} = [1.10, 0.60, -1.71] \pm 0.05$ MHz with Euler rotation angles of $[0, -20, 0] \pm 10^\circ$ and a quadrupolar tensor of $Q_{2\text{H}} = [0.01, 0.07, -0.08] \pm 0.01$ MHz with Euler angles of $[0, 55, 0] \pm 15^\circ$. These parameters fall near the high end of the range of magnitude (11.1 MHz protium

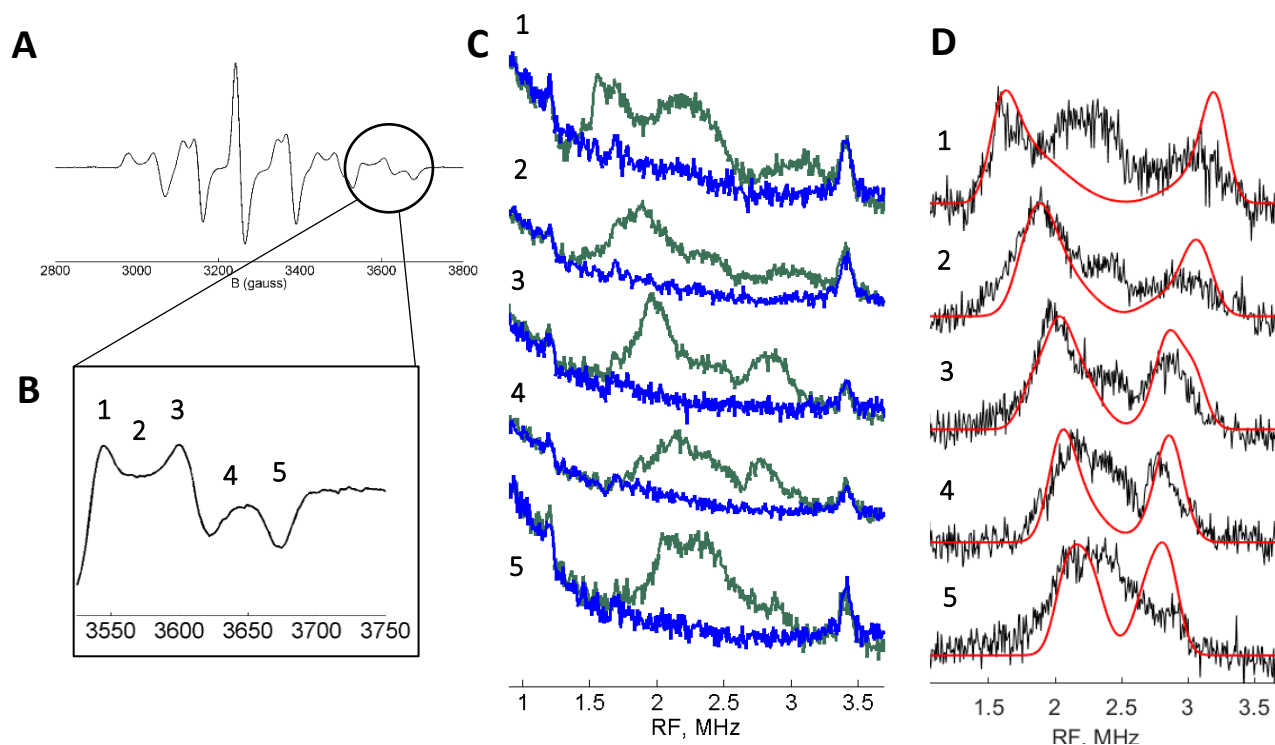


Figure 5. (A) CW EPR spectrum of the $\beta\text{-Mn}^{\text{III}}/\text{Fe}^{\text{III}}$ state and (B) the region used for obtaining the ENDOR spectra to the right. (C) The spectra were obtained via a subtraction of D_2O (in green) and H_2O (in blue) prepared samples and (D) the resulting subtracted spectra in black and the simulations in red. Experimental conditions: MW frequency 9.70 GHz, Temperature 14 K, $\pi/2$ of 8 ns, tau 312 ns, RF pulse 12 μs , exact field values: 3664 G, 3692 G, 3720 G, 3748 G, and 3776 G.

equivalent) and rhombicity ($\eta = 0.29$) for hydrons bonded to terminal oxygen ligands. As for the case of the bridging hydron(s), these data alone did not reveal whether a single or multiple ^2H nuclei give rise to the detected ENDOR signals.

Structural assignment of the observed hydrons

Examination of the published x-ray crystal structures and computationally derived models of *Ct* β and its cofactor forms^{24,45,46} identified only two chemically reasonable locations for the detected solvent-exchangeable ^2H nuclei that would position them $< 5 \text{ \AA}$ from one of the metal ions, as required to give hyperfine couplings greater than 0.1 MHz: bonded to the terminal oxygen ligand of the Mn site (site 1) or to one of the bridging oxygen ligands. The presence of a single hydron on the pair of bridging oxygens would result in a μ -oxo/ μ -hydroxo core structure, whereas the presence of two hydrons could, in principle, yield either a di- μ -hydroxo or a μ -oxo/ μ -aqua core. However, we dismissed the latter possibility on the basis of two considerations. First, bridging water ligands are relatively uncommon. Second, the water hydrons would not be expected to be as strongly coupled ($A_{\text{max}} = 27 \text{ MHz}$) as those detected in the HYSCORE experiments because of the anticipated weaker bonding and greater separation between the metal ions and the oxygen of the neutral bridge. The signal associated with the more weakly coupled, solvent-exchangeable ^2H nucleus detected by ENDOR is characteristic of hydrons bonded to terminal oxygen ligands in other dimetal systems⁴⁷ and could thus imply the presence of either a water or hydroxo ligand, which, from the published structural models would be expected to be coordinated to the Mn ion. The HYSCORE and ENDOR data thus converge on two possible models for the cluster core: $\text{H}_x\text{O-Mn-(}\mu\text{-O}^{2-}\text{)(}\mu\text{-HO}^-\text{)-Fe}$ and $\text{H}_x\text{O-Mn-(}\mu\text{-HO}^-\text{)}_2\text{-Fe}$, where $x = 1$ or 2 .

Determination of the Heisenberg Exchange Coupling Constant, J , by Spin-lattice-Relaxation/Power-Saturation Measurements

Previous studies have shown that the magnitude of the Heisenberg exchange coupling constant, J , depends primarily on the nature of the bridging ligands. The presence of a bridging oxo dianion, with its short strong bond to both metals, often leads to the largest values of J . Conversely, protonation of the μ -oxo, leading to a monoanionic hydroxo bridge, typically leads to a marked decrease in the magnitude of J .^{48, 49} Therefore, to determine whether the β -Mn^{III}/Fe^{III} RT-product cluster in *Ct* β contains an oxo bridge, we used spin-lattice relaxation measurements to determine J . We recorded CW-EPR spectra with varying microwave power (P) and temperature. The doubly-integrated intensities ($\iint S$) of the spectra were analyzed according to equations 1 and 2 to obtain $P_{1/2}$, the power required for 50% saturation, at each temperature,⁵⁰⁻⁵³

$$\iint S/\sqrt{P} = \frac{A}{\left[1 + \left(\frac{P}{P_{1/2}}\right)\right]^{b/2}} \quad (1)$$

$$\iint S = \frac{\sqrt{P}A}{\left[1 + \left(\frac{P}{P_{1/2}}\right)\right]^{b/2}} \quad (2)$$

where A is a constant proportional to the spin concentration, and b is the inhomogeneous line broadening parameter that ranges from a value of 1 for fully homogeneous broadening to 3 for fully inhomogeneous line broadening.⁵⁰⁻⁵² We analyzed only the two lowest-field “spin packets,” because the nitrogen-centered radical produced from N₃UDP contributes to the spectral intensity in the region of the third and fourth packets and another unassigned broad signal contributes in the

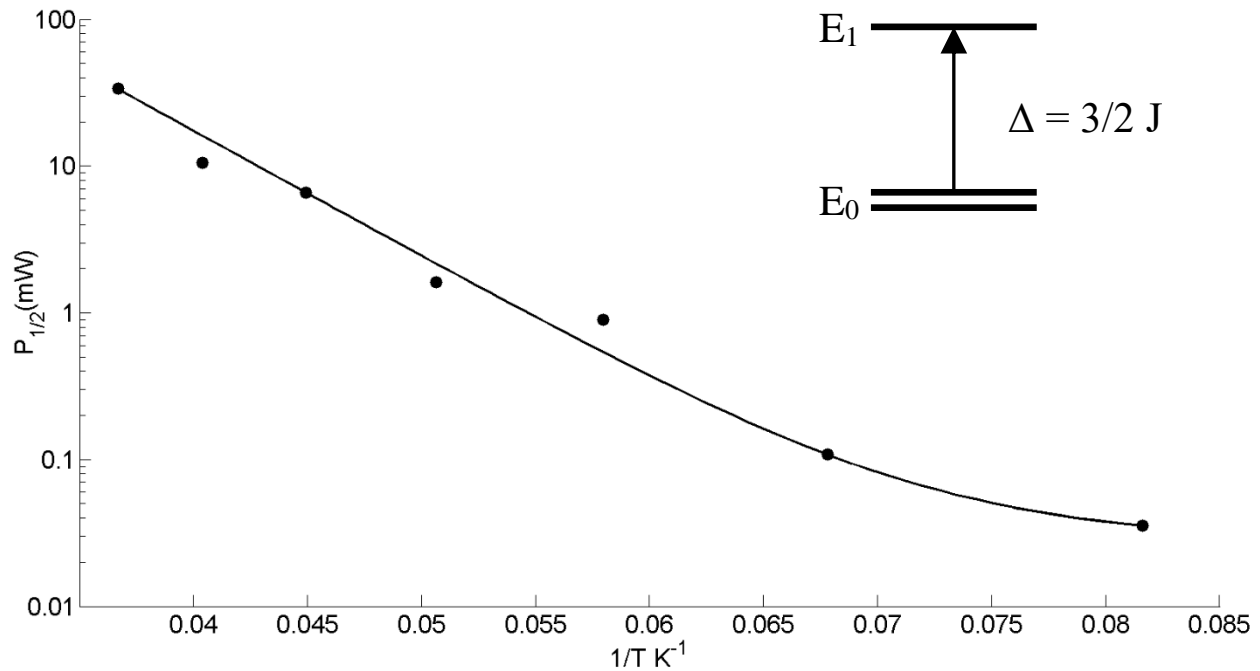


Figure 6. Half-saturation power ($P_{1/2}$) as a function of temperature. The data were fitted with equation 3 that yielded an energy difference between ground and first excited state of $\Delta = 138 \pm 5 \text{ cm}^{-1}$.

region of the fifth and sixth packets. At each temperature, EPR spectra and their doubly integrated intensities were obtained at a minimum of five different values of P . We obtained the $P_{1/2}$ values at each temperature by a least-squares fit to the data of the equally weighted linear combination of functions in equations 1 and 2. Fitting the data only to equation 1 would risk biasing the fits to match the low power signal intensities, whereas fitting to equation 2 alone would risk over-emphasizing the intensities of the spectra at higher values of P . By fitting the data to the equally weighted linear combination of the two equations, we avoided these biases. The homogeneity broadening parameter b was set to 1 in all fits. The fits yielded the A amplitude parameter values and the desired values of $P_{1/2}$. The $P_{1/2}$ values obtained at seven different temperatures were then plotted versus reciprocal temperature (**Figure 6**) and fit to the equation (**Eq 3**) accounting for both direct and Orbach mechanisms of spin relaxation:⁵⁴

$$P_{1/2} = AT + \frac{B}{e^{-\frac{\Delta}{T}}} - 1 \quad (3)$$

The fit shown in **Figure 6** yielded a Δ energy of $138 \pm 5 \text{ cm}^{-1}$. According to previous reports,^{55, 56} zero-field splitting terms from Mn^{III} and Fe^{III} ions can be neglected, allowing Δ to be equated to $3/2 J$ and yielding $92 \pm 5 \text{ cm}^{-1}$ for J . In previously studied diferric complexes,⁴⁸ the hydroxo- and acetoxo-bridged complexes were characterized by much weaker exchange coupling ($J < 20 \text{ cm}^{-1}$). By contrast, known oxo-bridged complexes of which we are aware have values of J ($87 \text{ cm}^{-1} < J < 131 \text{ cm}^{-1}$) comparable to that measured for the *Ct* $\beta\text{-Mn}^{\text{III}}/\text{Fe}^{\text{III}}$ cluster. In one study that examined a series of dimanganese ($\text{Mn}^{\text{III}}/\text{Mn}^{\text{III}}$ and $\text{Mn}^{\text{IV}}/\text{Mn}^{\text{III}}$) clusters,⁴⁹ only complexes with an oxo bridge exhibited such large values of J . The comparison to these precedents implies that the $\beta\text{-Mn}^{\text{III}}/\text{Fe}^{\text{III}}$ cluster must also have at least one oxo-bridge. Given the detection in the HYSCORE experiments of a hydron bonded to a bridging oxygen, the possible core structures can be further narrowed to $\text{H}_x\text{O-Mn-(}\mu\text{-O}^{2-}\text{)(}\mu\text{-HO}^-\text{)-Fe}$, where $x = 1$ or 2. Which of the two bridging oxygen ligands – the one that is *trans* to the two His ligands or the one that is *cis* – is more likely to bear the hydron and whether the terminal oxygen bears one or two hydrons cannot be discerned from the HYSCORE and ENDOR data alone and were therefore probed by computational methods.

Computational Results, and Discussion

Prior structural studies have shown that the terminal oxygen ligand to the Mn ion in site 1 can donate a hydrogen bond to either E89 or E227. This variable, combined with the aforementioned uncertainty in the number of hydrons associated with this ligand (1 or 2) and the disposition of the μ -hydroxo ligand (*cis* or *trans* to H123 and H230) resulted in six possible core structures, differing in the number, locations and/or interactions of the hydrons, to consider (**Figure 7**). To identify the most likely structure(s) from among these 6 candidates, we compared the parameters obtained as described above to those that we could calculate from the DFT-derived

models with the aid of semi-empirical correlations developed by Neese,⁵⁷ Noodleman⁵⁸ and others. A previous study assessed how well broken symmetry (BS) DFT can reproduce EPR parameters in high spin manganese systems.⁵⁵ The authors compared experimentally obtained hyperfine parameters of four mononuclear manganese complexes and one dimanganese complex, $[\text{Mn}^{\text{III}}/\text{Mn}^{\text{IV}}(\mu\text{-O})_2(\mu\text{-OAc})\text{DTNE}]^{2+}$, to the same parameters calculated by DFT. They showed that, after applying a scaling factor of 1.5 that is now standard practice in these types of calculations,^{59, 60} the isotropic part of the ^{55}Mn hyperfine could be calculated to an accuracy of $\sim 15\%$ by DFT methods. The magnitude of the anisotropic hyperfine interaction was not able to be calculated with useful accuracy. Therefore, in our comparison, we made use only of the isotropic part of the manganese hyperfine tensor, 326 ± 5 MHz, obtained via the simulation of the X-band EPR spectrum. Similarly, in the same study, as well as in two related studies,^{61, 62} the authors reported that the calculation overestimated the dipolar part of the ^{14}N hyperfine tensor, whereas the calculated Fermi contact parameter correlated well with experiment.⁵⁵ We therefore considered only the isotropic part of the ^{14}N hyperfine interaction to distinguish among the models.

Calculating EPR parameters via broken symmetry DFT can be quite challenging for nuclei that lie between two metal centers,⁵⁵ especially when one or both of the metal centers is iron. In the aforementioned dimanganese system, the spin density is mostly localized on the metal ions, whereas, in similar complexes involving iron, the spin density tends to be delocalized onto the ligands.^{55, 63, 64} In previous work that involved DFT calculations of diiron, dimanganese, and manganese-iron systems,^{46, 55, 65, 66} the authors assigned each nucleus of interest to a single metal center. The point-dipole model is a 3-point model that can predict the dipolar HF interaction of a

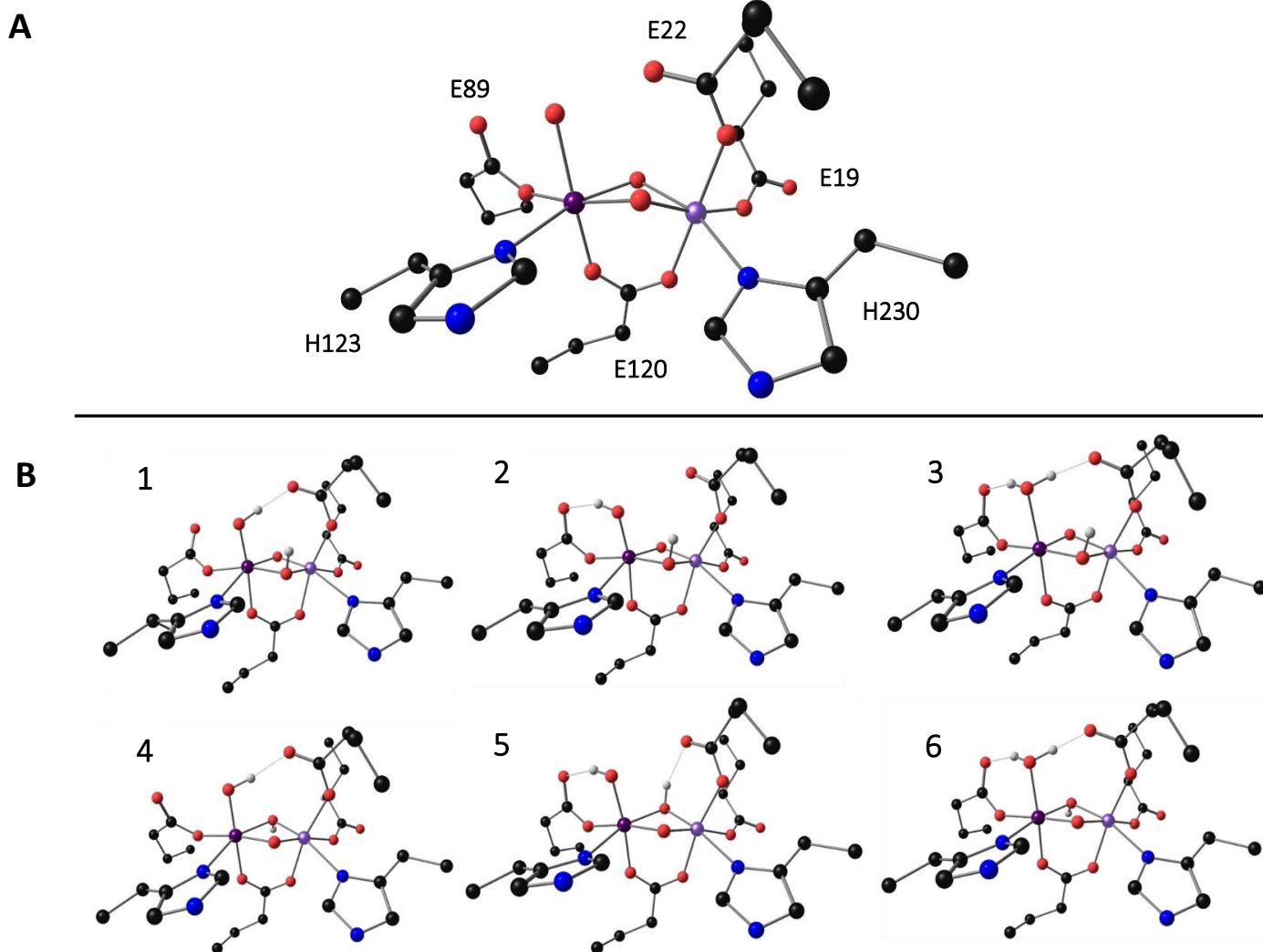


Figure 7 (A) The metallocofactor in $\beta\text{-Mn}^{\text{III}}/\text{Fe}^{\text{III}}$ state and all first shell ligands of *Ct* β taken from the crystal structure (PDB 4D8F). (B) DFT optimized structures of six possible candidates that differ in oxygenic proton count and position of $\beta\text{-Mn}^{\text{III}}/\text{Fe}^{\text{III}}$ state in *Ct* β . Non-oxygenic protons were omitted for visibility.

nucleus in relation to two metal centers. It is a sum of the two-individual point-dipolar interactions between a nucleus and each of the two metals. The formula used to calculate hyperfine tensor of each proton is given by:

$$\mathbf{A}_{dip} = R_1(a_1)c_1\mathbf{A}_T * \frac{78.97}{r_1^3} + R_2(a_2)c_2\mathbf{A}_T * \frac{78.97}{r_2^3} \quad (4)$$

where \mathbf{A}_{dip} is the total hyperfine coupling obtained from the dipolar model, R_1 and R_2 are the pair of matrices that rotate the individual metal site electron-proton dipolar contributions via second Euler angles a_1 and a_2 respectively to a common coordinate system. The c_1 and c_2 terms are the spin projection coupling coefficients of each metal site, \mathbf{A}_T is the traceless axial unit tensor with principal values of [1, 1, -2], and the 78.97 constant is the electron- ^1H dipolar contribution in $\text{MHz}\cdot\text{\AA}^3$. The point-dipole approximation model is fairly accurate when it comes to terminal ligands, but not when bridging nuclei are considered.⁵⁵ The BS-DFT calculations in Orca and Gaussian09 both calculate a spin-expectation value that is based on the total spin (in our case $S_T = |S_{\text{Fe}} - S_{\text{Mn}}| = 1/2$). To obtain the intrinsic hyperfine tensors \mathbf{a}_i for each nucleus, the values obtained from the calculation were multiplied by S_T/S_i (1/4 for Mn^{III} and 1/5 for Fe^{III}), where S_i represents the spin of the individual metal site. These values were then further rescaled by their spin projection coupling coefficients c_i , 7/3 for Fe and -4/3 for Mn, to obtain the experimentally obtained parameter as $\mathbf{A}_i = |c_i\mathbf{a}_i|$.^{55, 67} In the aforementioned study of the Mn_2 model system, the point-dipole approximation was applied to the DFT optimized geometries. The point-dipole model yielded ^1H hyperfine parameters that matched measured values more accurately than the those obtained directly from BS-DFT wavefunctions.⁵⁵ In addition, the point-dipole model has been used for predicting EPR/ENDOR parameters of dimetal systems similar to the $\beta\text{-Mn}^{\text{III}}/\text{Fe}^{\text{III}}$ RT-product in *Ct* β .^{25, 43, 55, 68, 69} In summary, the DFT calculated isotropic ^{55}Mn , ^{57}Fe , and ^{14}N hyperfine parameters, both DFT calculated and approximated with the dipolar model (using the DFT

calculated 3-point geometry) proton hyperfine couplings, and the J exchange parameters were compared to experiment (**Table 2**).

Analysis of the data that pertain to a proton residing on a terminal oxygen ligand indicate that both the DFT and the dipolar model calculated hyperfine parameters of the two models where water is coordinated to the manganese in site **1 (3,6)** agree better with experimental parameters than with the terminal hydroxo containing models (**1,2,4,5**). This conclusion can also be derived from basic chemical principles. The observed hyperfine parameters did not have a significant isotropic component indicating a weak overlap between the oxygen and metal orbitals. Such weak overlap is indicative of a greater distance between the oxygen and the metal center. This greater distance is more typical

Model Number	Hyperfine (MHz)											J cm ⁻¹	
	Terminal (DFT)			Terminal (Dipolar Model)		Bridging ¹ H (DFT)	Bridging ¹ H (DFT) (A _{iso})	Bridging ¹ H Dipolar model [Ax,Ay,Az]	Mn	Fe	N _{Fe}		N _{Mn}
	H ₁	H ₁	H ₂	H ₁	H ₂								
1	—	—	[3.9,11.8,-15.7]	—	[4.0,14.3,-18.3]	[0.5,18.6,-19.2]	-3.3	[-3.0,26.7,-23.7]	227	40	7.0	3.9	38
2	[6.2,7.0,-13.2]	-7.9	—	[6.6,8.3,-14.9]	—	[0.6,18.9,-19.5]	-5.6	[-3.0,27.4,-24.5]	221	39	7.1	4.6	39
3	[3.7,7.1,-10.9]	+1.9	[4.1,7.6,-11.8]	[4.4,6.4,-10.8]	[2.18,9.7,-11.9]	[-0.2,19.6,-19.4]	-5.5	[-4.7,28.6,-23.9]	250	45	12.0	1.8	48
4	—	—	[6.3,7.2,-13.5]	—	[6.5,8.2,-14.8]	[-4.8,24.3,-19.5]	+1.2	[-8.4,30.8,-22.5]	144	40	12.5	8.9	35
5	[3.6,12.6,-16.1]	-4.6	—	[3.4,15.5,-18.8]	—	[-2.4,29.2,-26.8]	+3.5	[-7.9,25.1,-17.3]	136	42	12.6	9.15	35
6	[4.7,6.6,-11.3]	-0.6	[3.6,9.0,-12.6]	[4.7,7.0,-11.7]	[2.2,11.5,-13.7]	[-0.2,24.6,-24.4]	+1.5	[-5.6,24.6,-19.0]	307	43	15.6	6.32	42
EXP	[3.9,7.2,-11.1]	0	[3.9,7.2,-11.1]	[3.9,7.2,-11.1]	[3.9,7.2,-11.1]	[-26.0,27.0,1.0]	-1.0	[-26.0,27.0,1.0]	326	70	14.6	14.6	92

Table 2 DFT, dipolar model and experimentally obtained hyperfine parameters of one bridging, two terminal protons, isotropic hyperfine of ⁵⁵Mn ⁵⁷Fe, and ¹⁴N nuclei as well as the Heisenberg exchange coupling constant J. The Ax, Ay, and Az are the principal components of the dipolar hyperfine tensor. All hydron hyperfine couplings presented in the ¹H hyperfine regime. H₁ and H₂ are protons hydrogen bonded to E89 and E227, respectively.

for water ligands than for hydroxo ligands. The terminal hydroxo models had significantly higher isotropic hyperfine values that do not match the experimentally obtained ENDOR parameters. With these results in mind and considering that the experimental ENDOR data could be simulated with hydrons with very similar magnetic parameters, we can rule out models **1,2,4**, and **5**. While the DFT generated hyperfine parameters of the bridging hydron are underestimated, the values calculated according to the point-dipole model agreed with the measured parameters to within 15% for all models. Even though theory and experiment match reasonably well in this case, no insight into the working model for the $\beta\text{-Mn}^{\text{III}}/\text{Fe}^{\text{III}}$ can be gained from these data. Similarly, the DFT calculated ^{14}N , ^{55}Mn , and ^{57}Fe isotropic hyperfine parameters in all models did not deviate significantly enough from one another and thus could not help us eliminate any of the calculated structures as candidates for the $\beta\text{-Mn}^{\text{III}}/\text{Fe}^{\text{III}}$ cofactor. Therefore, solely based on terminal hydron hyperfine analysis, models that contain a terminal water ligand (**3** and **6**) best match the experimental results. The two models differ in the position of the hydroxo bridge: model **3** has the hydroxo bridge *cis* to the histidines H123 and H230, while model **6** has the oxo bridge in this position. In summary, the experimental data is a bit more consistent with a water rather than a hydroxo terminal ligand. Thus, we suggest a $\text{H}_2\text{O-Mn(III)(}\mu\text{-oxo)(}\mu\text{-hydroxo)Fe(III)}$ core structure (models **3** and **6**) for the $\beta\text{-Mn}^{\text{III}}/\text{Fe}^{\text{III}}$ radical translocation product state of *Ct* β .

Comparison of the structures of the RT reactant state, derived from prior spectroscopic and computational studies,^{28, 70} and product state clarified in this study reveals important details regarding the mechanism of the initial PCET step that initiated RT and ribonucleotide reduction. The preferred models differ by a single electron and a single proton, analogously to the PCET step in *Ec* RNR that converts the $\text{Fe}^{\text{III}}/\text{Fe}^{\text{III}}\text{-Y}\cdot$ to the $\text{Fe}^{\text{III}}/\text{Fe}^{\text{III}}\text{-YH}$ form at the outset of radical translocation. The proposed structure of the $\beta\text{-Mn}^{\text{IV}}/\text{Fe}^{\text{III}}$ structure possesses a single hydroxo

bridge *trans* to the histidines. By analogy to the initial step of radical translocation in *Ec* RNR, it is likely that the first step of RT in *Ct* RNR β is a single proton and single electron transfer, and not a proton transfer to the terminal hydroxide ligand bound to manganese, a proton relocation from the hydroxo to the oxo bridging ligand, and the electron transfer. Additionally, the *trans* effect dictates that the oxo ligand that is *trans* to the histidines is more basic compared to the oxo that is *cis* to the histidines favoring model **6** over model **3**. Therefore, in this work, we propose model **6** as the β -Mn^{III}/Fe^{III} radical translocation product state. In this study we have elucidated the proton acceptor of the initial RT step – the hydroxide group terminally bonded to the manganese in site **1**. However, the proton donor still remains unknown. Upon the analysis of the crystal structure and upon the sequence comparison of tentative class Ic orthologs, we were able to identify a few conserved amino acid residues within 10 Å of the proton acceptor site on the hydroxide ligated to Mn^{IV} that could potentially facilitate proton donation. However, since we do not know the nature of the gated conformational change in β that occurs after forward RT, the proposition of any single, nearby amino acid residue as the proton donation facilitator would be highly speculative. Therefore, at this time, the proton donor remains unknown.

One recent and relevant example of how advanced EPR methods have been used to provide structural information of a related paramagnetic metallocofactor state is the study of oxygen activation of *Ct* β , the electronic and geometric characterization of the β -Mn^{IV}/Fe^{IV} intermediate.²⁵ Application of ENDOR revealed a relatively weak, $|T| = 0.7$ MHz, hyperfine coupling of the electron spin to a solvent exchangeable deuterium. Additionally, no stronger couplings were present as probed by either ENDOR or HYSCORE methods, indicating very low probability of bridging deuterons. In addition, EXAFS via both the Mn- and Fe- edge scattering results yielded a relatively short Mn-Fe distance of 2.75 Å. From these results the β -Mn^{IV}/Fe^{IV} activation

intermediate of *Ct* β was deducted to have $\text{HO-Mn(IV)}-(\mu\text{-O})_2\text{-Fe(IV)}$ core structure with the proton of the terminal hydroxide ligand on the manganese hydrogen bonded to E89.

The elucidation of the structure of the $\beta\text{-Mn}^{\text{III}}/\text{Fe}^{\text{III}}$ RT product state of the *Ct* β cofactor is the final piece of the structural puzzle that consists of the most relevant cofactor states in *Ct* β activation and catalysis processes. The graphical representation of the known states is shown in **Figure 8**. One question that arises from the comparison of the published $\beta\text{-Mn}^{\text{IV}}/\text{Fe}^{\text{IV}}$ state and the $\beta\text{-Mn}^{\text{IV}}/\text{Fe}^{\text{III}}$ state is the location of the proton on the terminal hydroxide ligand. The authors of the $\beta\text{-Mn}^{\text{IV}}/\text{Fe}^{\text{IV}}$ study address this question in detail and present experimental evidence that supports their rationale that in the $\beta\text{-Mn}^{\text{IV}}/\text{Fe}^{\text{IV}}$ state of *Ct* β , the proton of the terminal hydroxo ligand to site **1** is hydrogen bonded to E89 and not to E227. Even though a structural change is possible between the two states of interest that could affect the hydrogen bonding of the aforementioned proton, the authors of the $\beta\text{-Mn}^{\text{IV}}/\text{Fe}^{\text{III}}$ study never address this question in their work. To attempt to answer this query, one could perform a

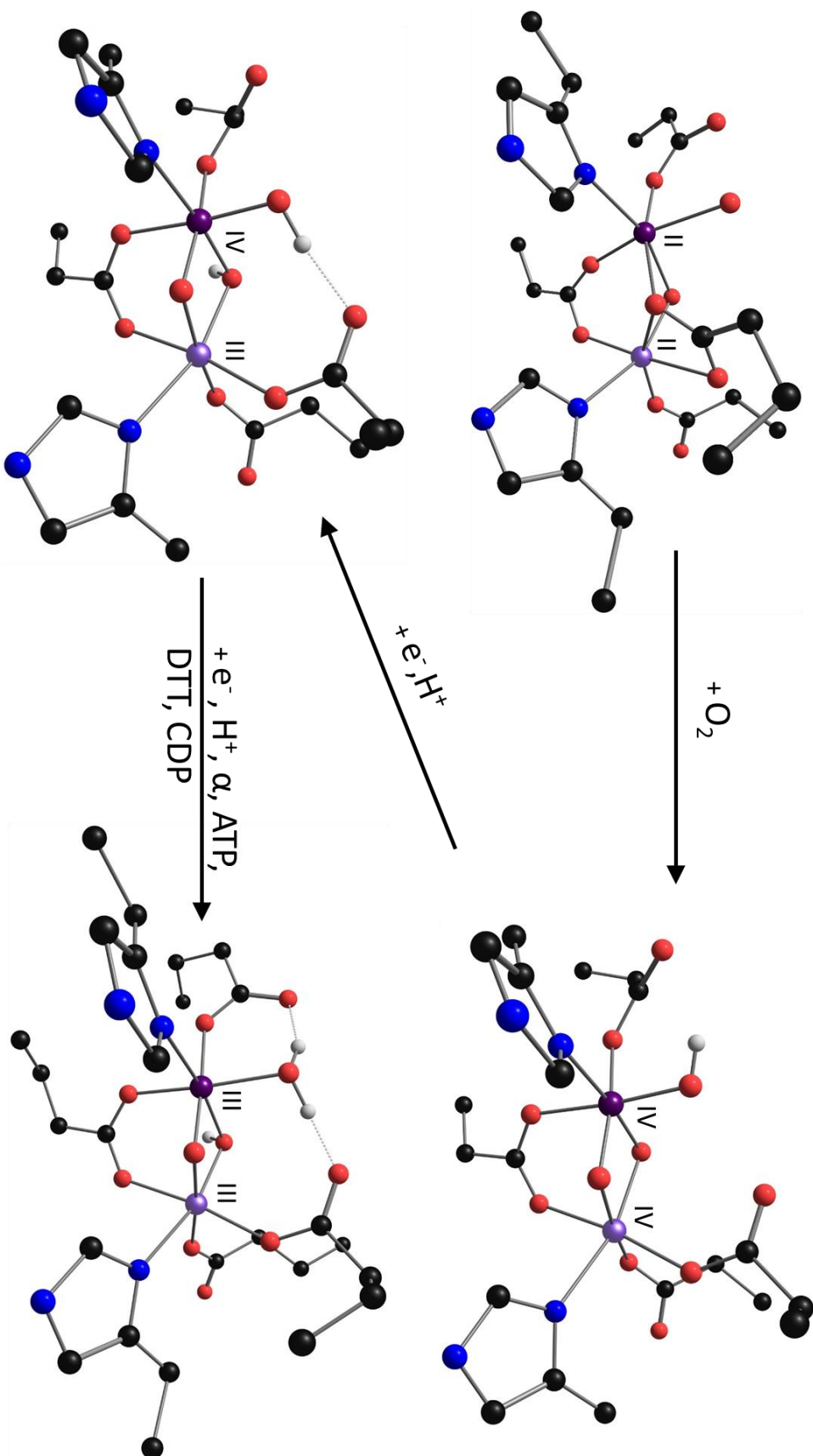


Figure 8 Structures of the Mn/Fe C β cofactor in the most relevant activation and catalytic states. The coordinates for the β -Mn^{II}Fe^{II}, β -Mn^{IV}Fe^{IV} and β -Mn^{IV}Fe^{III} states have been taken from references (24), (25) and (28), respectively. Model 6 of this work represents the β -Mn^{III}Fe^{III}. Non-oxegenic protons were omitted for visibility.

cryoreduction experiment on the $\beta\text{-Mn}^{\text{IV}}/\text{Fe}^{\text{III}}$ state to reduce the active cofactor to an EPR active state, $\beta\text{-Mn}^{\text{III}}/\text{Fe}^{\text{III}}$, and perform ENDOR to attempt to obtain the hyperfine couplings of the terminal hydron of interest. If the hydron is hydrogen bonded to E227, it would due to its greater proximity to the Fe metal center exhibit a stronger hyperfine interaction when compared to a hydron that is hydrogen bonded to E89 and is more distal to the Fe. This way we could construct a more accurate model of the $\beta\text{-Mn}^{\text{IV}}/\text{Fe}^{\text{III}}$ reactant RT state of *Ct* β . An important assumption of this experiment is that the proton transfer that follows the reduction of the cofactor during catalysis does not happen at cryogenic conditions.

Materials and methods

EPR sample preparation of the $\beta\text{-Mn}^{\text{III}}/\text{Fe}^{\text{III}}$ RT product cofactor state of *Ct* β_2 . The procedure described in our previous work⁷¹ was used to generate the desired $\beta\text{-Mn}^{\text{III}}/\text{Fe}^{\text{III}}$ *Ct* β_2 cofactor state with no modifications.

EPR spectrometer details. All continuous wave measurements were performed on an X-band Bruker ESP 300 spectrometer equipped with an ER 041 MR microwave bridge and the ER 4116DM resonator. Pulsed measurements including ENDOR and HYSCORE experiments were performed on the Bruker's X-band pulsed spectrometer Eleksys E580 equipped with a home-built frequency extension to access Q-band frequencies. This spectrometer contained: a SuperX-FT microwave bridge with a Militech 5 W pulse power amplifier, an EN 4118X-MD4 resonator and an Oxford CF935 cryostat.

EPR data simulations and data analysis. Kazan viewer⁷², a MATLAB suit of utilities was used for data processing while all spectral simulations were performed via the Easyspin⁷³ software package. The pepper function was used to simulate CW spectra while all pulsed experiments were simulated via the saffron function. In all simulations it was assumed that the ⁵⁵Mn hyperfine tensor was colinear with the g tensor.

Computational details. GAUSSIAN 09⁷⁴ revision C.01 software package was used to obtain all geometry optimizations. The starting structure for all calculations was based on the crystal structure of *Ct* RNR β_2 , high Mn procedure, PDB 4D8F.²³ In addition to Mn and Fe metals and the oxygenic ligands bound to them, the models contained the following amino acid residues: E89, E227, E193, H230, E120, H123, all cut at the α carbon. To attempt to simulate the semi rigid protein environment, in addition to the α carbon, two more adjacent hydrogen atoms were frozen in all calculations similarly to the procedure was introduced by Roos and Siegbahn.⁷⁵ COSMO⁷⁶, a conductor-like screening model in the polarizable continuum model, PCM⁷⁷, framework was implemented in all calculations with $\epsilon = 4$. The unrestricted DFT formalism with the three-parameter Becke–Lee–Yang–Parr (B3LYP)^{78,79} hybrid functional was used in all calculations. The broken symmetry method of Noodleman *et al*⁵⁸ was used to achieve the antiferromagnetic coupling between the Mn^{III} and Fe^{III} ions in all geometry optimization calculations. The DZP⁸⁰ basis set was used to treat all the H, C, N and O atoms in our models while the TZVPP⁸¹ basis set was used to treat the Mn and Fe metals. To obtain the sought magnetic parameters, single point calculations were performed on the optimized geometries using the ORCA-3⁵⁷ package. The CP(PPP)⁸² basis set was used for the metal atoms while the EPR-II⁸³ basis set was used to treat all non-metal atoms.

REFERENCES:

1. Nordlund, P.; Reichard, P., Ribonucleotide reductases. *Annu Rev Biochem* **2006**, *75*, 681-706.
2. Licht, S.; Gerfen, G. J.; Stubbe, J. A., Thiyl radicals in ribonucleotide reductases. *Science* **1996**, *271* (5248), 477-481.
3. Gambarelli, S.; Luttringer, F.; Padovani, D.; Mulliez, E.; Fontecave, M., Activation of the anaerobic ribonucleotide reductase by S-adenosylmethionine. *Chembiochem* **2005**, *6* (11), 1960-1962.
4. Lawrence, C. C.; Stubbe, J., The function of adenosylcobalamin in the mechanism of ribonucleoside triphosphate reductase from *Lactobacillus leichmannii*. *Curr Opin Chem Biol* **1998**, *2* (5), 650-655.
5. Cotruvo, J. A.; Stubbe, J., Class I ribonucleotide reductases: metallocofactor assembly and repair in vitro and in vivo. *Annu Rev Biochem* **2011**, *80*, 733-67.
6. Blaesi, E. J.; Palowitch, G. M.; Hu, K.; Kim, A. J.; Rose, H. R.; Alapati, R.; Lougee, M. G.; Kim, H. J.; Taguchi, A. T.; Tan, K. O.; Laremore, T. N.; Griffin, R. G.; Krebs, C.; Matthews, M. L.; Silakov, A.; Bollinger, J. M., Jr.; Allen, B. D.; Boal, A. K., Metal-free class Ie ribonucleotide reductase from pathogens initiates catalysis with a tyrosine-derived dihydroxyphenylalanine radical. *Proc Natl Acad Sci U S A* **2018**, *115* (40), 10022-10027.
7. Stubbe, J., Ribonucleotide reductases. *Adv Enzymol Relat Areas Mol Biol* **1990**, *63*, 349-419.

8. Sjoberg, B. M.; Karlsson, M.; Jornvall, H., Half-Site Reactivity of the Tyrosyl Radical of Ribonucleotide Reductase from Escherichia-Coli. *J Biol Chem* **1987**, 262 (20), 9736-9743.
9. Seyedsayamdost, M. R.; Chan, C. T. Y.; Mugnaini, V.; Stubbe, J.; Bennati, M., PELDOR spectroscopy with DOPA-beta 2 and NH₂Y-alpha 2s: Distance measurements between residues involved in the radical propagation pathway of E-coli ribonucleotide reductase. *J Am Chem Soc* **2007**, 129 (51), 15748-+.
10. Livada, J.; Martinie, R. J.; Dassama, L. M.; Krebs, C.; Bollinger, J. M., Jr.; Silakov, A., Direct Measurement of the Radical Translocation Distance in the Class I Ribonucleotide Reductase from Chlamydia trachomatis. *J Phys Chem B* **2015**, 119 (43), 13777-84.
11. Uhlin, U.; Eklund, H., Structure of ribonucleotide reductase protein R1. *Nature* **1994**, 370 (6490), 533-9.
12. Stubbe, J.; Nocera, D. G.; Yee, C. S.; Chang, M. C. Y., Radical initiation in the class I ribonucleotide reductase: Long-range proton-coupled electron transfer? *Chem Rev* **2003**, 103 (6), 2167-2201.
13. Seyedsayamdost, M. R.; Stubbe, J., Forward and reverse electron transfer with the Y(356)DOPA-beta 2 heterodimer of E-coli ribonucleotide reductase. *J Am Chem Soc* **2007**, 129 (8), 2226-+.
14. Seyedsayamdost, M. R.; Yee, C. S.; Reece, S. Y.; Nocera, D. G.; Stubbe, J., pH rate profiles of FnY356-R2s (n=2, 3, 4) in Escherichia coli ribonucleotide reductase: Evidence that Y-356 is a redox-active amino acid along the radical propagation pathway. *J Am Chem Soc* **2006**, 128 (5), 1562-1568.

15. Yokoyama, K.; Uhlin, U.; Stubbe, J., Site-Specific Incorporation of 3-Nitrotyrosine as a Probe of pK(a) Perturbation of Redox-Active Tyrosines in Ribonucleotide Reductase. *J Am Chem Soc* **2010**, *132* (24), 8385-8397.
16. Dassama, L. M. K.; Jiang, W.; Varano, P. T.; Pandelia, M. E.; Conner, D. A.; Xie, J. J.; Bollinger, J. M.; Krebs, C., Radical-Translocation Intermediates and Hurdling of Pathway Defects in "Super-oxidized" (Mn-IV/Fe-IV) Chlamydia trachomatis Ribonucleotide Reductase. *J Am Chem Soc* **2012**, *134* (50), 20498-20506.
17. Zlateva, T.; Quaroni, L.; Que, L.; Stankovich, M. T., Redox studies of subunit interactivity in aerobic ribonucleotide reductase from Escherichia coli. *J Biol Chem* **2004**, *279* (18), 18742-7.
18. Jiang, W.; Xie, J. J.; Varano, P. T.; Krebs, C.; Bollinger, J. M., Two Distinct Mechanisms of Inactivation of the Class Ic Ribonucleotide Reductase from Chlamydia trachomatis by Hydroxyurea: Implications for the Protein Gating of Intersubunit Electron Transfer. *Biochemistry-U S* **2010**, *49* (25), 5340-5349.
19. Tong, W. H.; Chen, S.; Lloyd, S. G.; Edmondson, D. E.; Huynh, B. H.; Stubbe, J., Mechanism of assembly of the diferric cluster-tyrosyl radical cofactor of Escherichia coli ribonucleotide reductase from the diferrous form of the R2 subunit. *J Am Chem Soc* **1996**, *118* (8), 2107-2108.
20. Atkin, C. L.; Thelande, L.; Reichard, P.; Lang, G., Iron and Free-Radical in Ribonucleotide Reductase - Exchange of Iron and Mossbauer-Spectroscopy of Protein-B2 Subunit of Escherichia-Coli Enzyme. *J Biol Chem* **1973**, *248* (21), 7464-7472.

21. Doan, P. E.; Shanmugam, M.; Stubbe, J.; Hoffman, B. M., Composition and Structure of the Inorganic Core of Relaxed Intermediate X(Y122F) of Escherichia coli Ribonucleotide Reductase. *J Am Chem Soc* **2015**, *137* (49), 15558-15566.
22. Burdi, D.; Sturgeon, B. E.; Tong, W. H.; Stubbe, J. A.; Hoffman, B. M., Rapid freeze-quench ENDOR of the radical X intermediate of Escherichia coli ribonucleotide reductase using O-17(2), (H2O)-O-17, and (H2O)-H-2. *J Am Chem Soc* **1996**, *118* (1), 281-282.
23. Dassama, L. M. K.; Boal, A. K.; Krebs, C.; Rosenzweig, A. C.; Bollinger, J. M., Evidence That the beta Subunit of Chlamydia trachomatis Ribonucleotide Reductase Is Active with the Manganese Ion of Its Manganese(IV)/Iron(III) Cofactor in Site 1. *J Am Chem Soc* **2012**, *134* (5), 2520-2523.
24. Dassama, L. M. K.; Krebs, C.; Bollinger, J. M.; Rosenzweig, A. C.; Boal, A. K., Structural Basis for Assembly of the Mn-IV/Fe-III Cofactor in the Class Ic Ribonucleotide Reductase from Chlamydia trachomatis. *Biochemistry-Us* **2013**, *52* (37), 6424-6436.
25. Martinie, R. J.; Blaes, E. J.; Krebs, C.; Bollinger, J. M.; Silakov, A.; Pollock, C. J., Evidence for a Di-μ-oxo Diamond Core in the Mn(IV)/Fe(IV) Activation Intermediate of Ribonucleotide Reductase from Chlamydia trachomatis. *J Am Chem Soc* **2017**, *139* (5), 1950-1957.
26. Jiang, W.; Saleh, L.; Barr, E. W.; Xie, J. J.; Gardner, M. M.; Krebs, C.; Bollinger, J. M., Branched activation- and catalysis-specific pathways for electron relay to the manganese/iron cofactor in ribonucleotide reductase from Chlamydia trachomatis. *Biochemistry-Us* **2008**, *47* (33), 8477-8484.

27. Younker, J. M.; Krest, C. M.; Jiang, W.; Krebs, C.; Bollinger, J. M.; Green, M. T., Structural Analysis of the Mn(IV)/Fe(III) Cofactor of Chlamydia trachomatis Ribonucleotide Reductase by Extended X-ray Absorption Fine Structure Spectroscopy and Density Functional Theory Calculations. *J Am Chem Soc* **2008**, *130* (45), 15022-15027.
28. Kwak, Y.; Jiang, W.; Dassama, L. M. K.; Park, K.; Bell, C. B.; Liu, L. V.; Wong, S. D.; Saito, M.; Kobayashi, Y.; Kitao, S.; Seto, M.; Yoda, Y.; Alp, E. E.; Zhao, J. Y.; Bollinger, J. M.; Krebs, C.; Solomon, E. I., Geometric and Electronic Structure of the Mn(IV)Fe(III) Cofactor in Class Ic Ribonucleotide Reductase: Correlation to the Class Ia Binuclear Non-Heme Iron Enzyme. *J Am Chem Soc* **2013**, *135* (46), 17573-17584.
29. Worsdorfer, B.; Conner, D. A.; Yokoyama, K.; Livada, J.; Seyedsayamdost, M.; Jiang, W.; Silakov, A.; Stubbe, J.; Bollinger, J. M., Jr.; Krebs, C., Function of the diiron cluster of Escherichia coli class Ia ribonucleotide reductase in proton-coupled electron transfer. *J Am Chem Soc* **2013**, *135* (23), 8585-93.
30. Karlsson, M.; Sahlin, M.; Sjoberg, B. M., Escherichia-Coli Ribonucleotide Reductase - Radical Susceptibility to Hydroxyurea Is Dependent on the Regulatory State of the Enzyme. *J Biol Chem* **1992**, *267* (18), 12622-12626.
31. Seyedsayamdost, M. R.; Stubbe, J., Site-specific replacement of Y-356 with 3,4-dihydroxyphenylalanine in the beta 2 subunit of E. coli ribonucleotide reductase. *J Am Chem Soc* **2006**, *128* (8), 2522-2523.
32. Minnihan, E. C.; Seyedsayamdost, M. R.; Stubbe, J., Use of 3-Aminotyrosine To Examine the Pathway Dependence of Radical Propagation in Escherichia coli Ribonucleotide Reductase. *Biochemistry-US* **2009**, *48* (51), 12125-12132.

33. Jiang, W.; Yun, D.; Saleh, L.; Barr, E. W.; Xing, G.; Hoffart, L. M.; Maslak, M. A.; Krebs, C.; Bollinger, J. M., A manganese(IV)/iron(III) cofactor in *Chlamydia trachomatis* ribonucleotide reductase. *Science* **2007**, *316* (5828), 1188-1191.
34. Fritscher, J.; Artin, E.; Wnuk, S.; Bar, G.; Robblee, J. H.; Kacprzak, S.; Kaupp, M.; Griffin, R. G.; Bennati, M.; Stubbe, J., Structure of the nitrogen-centered radical formed during inactivation of E-coli ribonucleotide reductase by 2'-azido-2'-deoxyuridine-5'-diphosphate: Trapping of the 3'-ketonucleotide. *J Am Chem Soc* **2005**, *127* (21), 7729-7738.
35. Derose, V. J.; Liu, K. E.; Kurtz, D. M.; Hoffman, B. M.; Lippard, S. J., Proton Endor Identification of Bridging Hydroxide Ligands in Mixed-Valent Diiron Centers of Proteins - Methane Monooxygenase and Semimet Azidohemerythrin. *J Am Chem Soc* **1993**, *115* (14), 6440-6441.
36. DeRose, V. J.; Liu, K. E.; Lippard, S. J.; Hoffman, B. M., Investigation of the dinuclear Fe center of methane monooxygenase by advanced paramagnetic resonance techniques: On the geometry of DMSO binding. *J Am Chem Soc* **1996**, *118* (1), 121-134.
37. Smoukov, S. K.; Davydov, R. M.; Doan, P. E.; Sturgeon, B.; Kung, I. Y.; Hoffman, B. M.; Kurtz, D. M., EPR and ENDOR evidence for a 1-His, hydroxo-bridged mixed-valent diiron site in *Desulfovibrio vulgaris* rubrerythrin. *Biochemistry-Us* **2003**, *42* (20), 6201-6208.
38. Smoukov, S. K.; Quaroni, L.; Wang, X. D.; Doan, P. E.; Hoffman, B. M.; Que, L., Electron-nuclear double resonance spectroscopic evidence for a hydroxo-bridge nucleophile involved in catalysis by a dinuclear hydrolase. *J Am Chem Soc* **2002**, *124* (11), 2595-2603.

39. Sturgeon, B. E.; Burdi, D.; Chen, S. X.; Huynh, B. H.; Edmondson, D. E.; Stubbe, J.; Hoffman, B. M., Reconsideration of X, the diiron intermediate formed during cofactor assembly in E-coli ribonucleotide reductase. *J Am Chem Soc* **1996**, *118* (32), 7551-7557.
40. Khangulov, S.; Dismukes, G. C., Determination of the Positions of Magnetic Ligand Atoms in Spin Coupled Multi-Spin Systems from Endor Hyperfine Constants. *Biophys J* **1993**, *64* (2), A51-A51.
41. Fiege, R.; Zwegart, W.; Bittl, R.; Adir, N.; Renger, G.; Lubitz, W., EPR and ENDOR studies of the water oxidizing complex of Photosystem II. *Photosynth Res* **1996**, *48* (1-2), 227-237.
42. Milikisiyants, S.; Chatterjee, R.; Lakshmi, K. V., Two-Dimensional H-1 HYSCORE Spectroscopy of Dimanganese Di-mu-oxo Mimics of the Oxygen-Evolving Complex of Photosystem II. *J Phys Chem B* **2011**, *115* (42), 12220-12229.
43. Randall, D. W.; Gelasco, A.; Caudle, M. T.; Pecoraro, V. L.; Britt, R. D., ESE-ENDOR and ESEEM characterization of water and methanol ligation to a dinuclear Mn(III)Mn(IV) complex. *J Am Chem Soc* **1997**, *119* (19), 4481-4491.
44. Shafaat, H. S.; Griese, J. J.; Pantazis, D. A.; Roos, K.; Andersson, C. S.; Popovic-Bijelic, A.; Graslund, A.; Siegbahn, P. E. M.; Neese, F.; Lubitz, W.; Hogbom, M.; Cox, N., Electronic Structural Flexibility of Heterobimetallic Mn/Fe Cofactors: R2lox and R2c Proteins. *J Am Chem Soc* **2014**, *136* (38), 13399-13409.
45. Andersson, C. S.; Ohrstrom, M.; Popovic-Bijelic, A.; Graslund, A.; Stenmark, P.; Hogbom, M., The Manganese Ion of the Heterodinuclear Mn/Fe Cofactor in Chlamydia

trachomatis Ribonucleotide Reductase R2c Is Located at Metal Position 1. *J Am Chem Soc* **2012**, *134* (1), 123-125.

46. Han, W. G.; Giammona, D. A.; Bashford, D.; Noodleman, L., Density Functional Theory Analysis of Structure, Energetics, and Spectroscopy for the Mn-Fe Active Site of Chlamydia trachomatis Ribonucleotide Reductase in Four Oxidation States. *Inorg Chem* **2010**, *49* (16), 7266-7281.

47. McConnell, I. L.; Grigoryants, V. M.; Scholes, C. P.; Myers, W. K.; Chen, P. Y.; Whittaker, J. W.; Brudvig, G. W., EPR-ENDOR Characterization of (O-17, H-1, H-2) Water in Manganese Catalase and Its Relevance to the Oxygen-Evolving Complex of Photosystem II. *J Am Chem Soc* **2012**, *134* (3), 1504-1512.

48. Gorun, S. M.; Lippard, S. J., Magnetostructural Correlations in Magnetically Coupled (μ-Oxo)Diiron(III) Complexes. *Inorg Chem* **1991**, *30* (7), 1625-1630.

49. Mukhopadhyay, S.; Mandal, S. K.; Bhaduri, S.; Armstrong, W. H., Manganese clusters with relevance to photosystem II. *Chem Rev* **2004**, *104* (9), 3981-4026.

50. Tomter, A. B.; Zoppellaro, G.; Bell, C. B.; Barra, A. L.; Andersen, N. H.; Solomon, E. I.; Andersson, K. K., Spectroscopic Studies of the Iron and Manganese Reconstituted Tyrosyl Radical in Bacillus Cereus Ribonucleotide Reductase R2 Protein. *Plos One* **2012**, *7* (3).

51. Zoppellaro, G.; Harbitz, E.; Kaur, R.; Ensign, A. A.; Bren, K. L.; Andersson, K. K., Modulation of the Ligand-Field Anisotropy in a Series of Ferric Low-Spin Cytochrome c Mutants derived from Pseudomonas aeruginosa Cytochrome c-551 and Nitrosomonas europaea Cytochrome c-552: A Nuclear Magnetic Resonance and Electron Paramagnetic Resonance Study. *J Am Chem Soc* **2008**, *130* (46), 15348-15360.

52. Portis, A. M., Electronic Structure of F-Centers - Saturation of the Electron Spin Resonance. *Phys Rev* **1953**, *91* (5), 1071-1078.
53. Castner, T. G., Saturation of the Paramagnetic Resonance of a V-Center. *Phys Rev* **1959**, *115* (6), 1506-1515.
54. Pearce, L. L.; Kurtz, D. M.; Xia, Y. M.; Debrunner, P. G., Reduction of the Binuclear Iron Site in Octameric Methemerythrins - Characterizations of Intermediates and a Unifying Reaction Scheme. *J Am Chem Soc* **1987**, *109* (24), 7286-7293.
55. Sinnecker, S.; Neese, F.; Noodleman, L.; Lubitz, W., Calculating the electron paramagnetic resonance parameters of exchange coupled transition metal complexes using broken symmetry density functional theory: Application to a Mn-III/Mn-IV model compound. *J Am Chem Soc* **2004**, *126* (8), 2613-2622.
56. Que, L., *Physical Methods in Bioinorganic Chemistry*. University Science Books: 2000.
57. Neese, F., The ORCA program system. *Wires Comput Mol Sci* **2012**, *2* (1), 73-78.
58. Noodleman, L., Valence Bond Description of Anti-Ferromagnetic Coupling in Transition-Metal Dimers. *J Chem Phys* **1981**, *74* (10), 5737-5743.
59. Lohmiller, T.; Krewald, V.; Navarro, M. P.; Retegan, M.; Rapatskiy, L.; Nowaczyk, M. M.; Boussac, A.; Neese, F.; Lubitz, W.; Pantazis, D. A.; Cox, N., Structure, ligands and substrate coordination of the oxygen-evolving complex of photosystem II in the S-2 state: a combined EPR and DFT study. *Phys Chem Chem Phys* **2014**, *16* (24), 11877-11892.
60. Orio, M.; Pantazis, D. A.; Neese, F., Density functional theory. *Photosynth Res* **2009**, *102* (2-3), 443-453.

61. Jaszewski, A. R.; Jezierska, J., Hybrid density functional approach to the isotropic and anisotropic hyperfine couplings with N-14 and H-1 nuclei in the blue copper proteins. *Chem Phys Lett* **2001**, 343 (5-6), 571-580.
62. Neese, F., Theoretical study of ligand superhyperfine structure. Application to Cu(II) complexes. *J Phys Chem A* **2001**, 105 (17), 4290-4299.
63. Rodriguez, J. H.; McCusker, J. K., Density functional theory of spin-coupled models for diiron-oxo proteins: Effects of oxo and hydroxo bridging on geometry, electronic structure, and magnetism. *J Chem Phys* **2002**, 116 (14), 6253-6270.
64. Binning, R. C.; Bacelo, D. E., A DFT Study of Two Diiron (II) Synthetic Model Compounds and Their Diiron(III) Peroxide Oxygenation Products. *Int J Quantum Chem* **2009**, 109 (15), 3533-3540.
65. Roos, K.; Siegbahn, P. E. M., Density Functional Theory Study of the Manganese-Containing Ribonucleotide Reductase from *Chlamydia trachomatis*: Why Manganese Is Needed in the Active Complex. *Biochemistry-Us* **2009**, 48 (9), 1878-1887.
66. Han, W. G.; Noodleman, L., DFT calculations of comparative energetics and ENDOR/Mossbauer properties for two protonation states of the iron dimer cluster of ribonucleotide reductase intermediate X. *Dalton T* **2009**, (30), 6045-6057.
67. Bencini, A. G., D., *EPR of Exchange Coupled Systems*. Springer-Verlag: Berlin, 1990.
68. Zwegart, W. ESR und ENDOR Untersuchungen an mehrkernigen gemischtaalenten Mangankomplexen als Modelle für das wasserstoffoxidierende Enzymsystem im Photosystem II. Technische Universität, Berlin, 1995.

69. Schafer, K. O.; Bittl, R.; Zwegart, W.; Lendzian, F.; Haselhorst, G.; Weyhermuller, T.; Wieghardt, K.; Lubitz, W., Electronic structure of antiferromagnetically coupled dinuclear manganese ((MnMnIV)-Mn-III) complexes studied by magnetic resonance techniques. *J Am Chem Soc* **1998**, *120* (50), 13104-13120.
70. Sproviero, E. M., Geometrical properties of the manganese(IV)/iron(III) cofactor of Chlamydia trachomatis ribonucleotide reductase unveiled by simulations of XAS spectra. *Dalton T* **2017**, *46* (14), 4724-4736.
71. Livada, J.; Martinie, R. J.; Dassama, L. M. K.; Krebs, C.; Bollinger, J. M.; Silakov, A., Direct Measurement of the Radical Translocation Distance in the Class I Ribonucleotide Reductase from Chlamydia trachomatis. *J Phys Chem B* **2015**, *119* (43), 13777-13784.
72. Kazan Viewer-Homepage Alexey Silakov: <https://sites.google.com/site/silakovalexey/kazan-viewer>; accessed July 7, 2017.
73. Stoll, S.; Schweiger, A., EasySpin, a comprehensive software package for spectral simulation and analysis in EPR. *J Magn Reson* **2006**, *178* (1), 42-55.
74. Frisch, MJ.; T, GW.; Schlegel, HB.; Scuseria, GE.; Robb, MA.; Cheeseman, JR.; Scalmani, G.;

Barone, V.; Mennucci, B.; Petersson, GA.; Nakatsuji, H.; Caricato, M.; Li, X.; Hratchian, HP.;

Izmaylov, AF.; Bloino, J.; Zheng, G.; Sonnenberg, JL.; Hada, M.; Ehara, M.; Toyota, K.; Fukuda, R.; Hasegawa, J.; Ishida, M.; Nakajima, T.; Honda, Y.; Kitao, O.; Nakai, H.; Vreven, T.;

Montgomery, JA., Jr; Peralta, JE.; Ogliaro, F.; Bearpark, M.; Heyd, JJ.; Brothers, E.; Kudin, KN.;

- Staroverov, VN.; Kobayashi, R.; Normand, J.; Raghavachari, K.; Rendell, A.; Burant, JC.; Iyengar, SS.; Tomasi, J.; Cossi, M.; Rega, N.; Millam, JM.; Klene, M.; Knox, JE.; Cross, JB.; Bakken, V.; Adamo, C.; Jaramillo, J.; Gomperts, R.; Stratmann, RE.; Yazyev, O.; Austin, AJ.; Cammi, R.; Pomelli, C.; Ochterski, JW.; Martin, RL.; Morokuma, K.; Zakrzewski, VG.; Voth, GA.; Salvador, P.; Dannenberg, JJ.; Dapprich, S.; Daniels, AD.; Farkas, Ö.; Foresman, JB.; Ortiz, JV.; Cioslowski, J.; Fox, DJ. Gaussian 09, Revision C 01. Gaussian, Inc.; Wallingford CT: 2009.
75. Roos, K.; Siegbahn, P. E. M., Oxygen cleavage with manganese and iron in ribonucleotide reductase from *Chlamydia trachomatis*. *J Biol Inorg Chem* **2011**, *16* (4), 553-565.
76. Klamt, A.; Schuurmann, G., Cosmo - a New Approach to Dielectric Screening in Solvents with Explicit Expressions for the Screening Energy and Its Gradient. *J Chem Soc Perk T 2* **1993**, (5), 799-805.
77. Cossi, M.; Rega, N.; Scalmani, G.; Barone, V., Energies, structures, and electronic properties of molecules in solution with the C-PCM solvation model. *J Comput Chem* **2003**, *24* (6), 669-681.
78. Becke, A. D., Density-Functional Thermochemistry .3. The Role of Exact Exchange. *J Chem Phys* **1993**, *98* (7), 5648-5652.
79. Lee, I. H. Electron Spin Echo Envelope Modulation Studies of Some Transition Metal Model Complexes. Michigan State University, 1994.
80. Schafer, A.; Horn, H.; Ahlrichs, R., Fully Optimized Contracted Gaussian-Basis Sets for Atoms Li to Kr. *J Chem Phys* **1992**, *97* (4), 2571-2577.

81. Schafer, A.; Huber, C.; Ahlrichs, R., Fully Optimized Contracted Gaussian-Basis Sets of Triple Zeta Valence Quality for Atoms Li to Kr. *J Chem Phys* **1994**, *100* (8), 5829-5835.
82. Neese, F., Prediction and interpretation of the Fe-57 isomer shift in Mossbauer spectra by density functional theory. *Inorg Chim Acta* **2002**, *337*, 181-192.
83. V. Barone, in Recent Advances in Density Functional Methods, Part I, Ed. D. P. Chong (World Scientific Publ. Co., Singapore, 1996).

Appendix 5-A

Observation of a strongly coupled ^{14}N signal probed via Davies ENDOR

Using Davies ENDOR, we have observed an isotropic signal and assigned to a strongly coupled ^{14}N nucleus likely ligated to either Mn or Fe. In order to propose the best model for the $\text{Mn}^{\text{III}}/\text{Fe}^{\text{III}}$ RT state in *Ct* β we attempted to obtain the hyperfine tensors of any nearby nuclei that we can observe in order to compare the experimentally observed tensors to the DFT calculated ones. In addition to the two hydron signals discussed, we also observed one ^{14}N signal revealed via Davies ENDOR. Unlike Mims that suffers from periodic blind spots, Davies ENDOR has proven to be a great tool for discerning strong HF couplings ($A_{\text{HF}} > 2\omega_{\text{I}}$) in biological systems

because it only suffers from a single blind spot centered at ω_{I} and dependent on the mw inversion pulse and the HF coupling. Signals observed in these ENDOR experiments (figure 6C) are characteristic of the hyperfine coupling in the strongly coupled regime where the ENDOR doublet spectrum is centered at $\frac{1}{2}A_{\text{HF}}$ and split by twice the larmor frequency. These

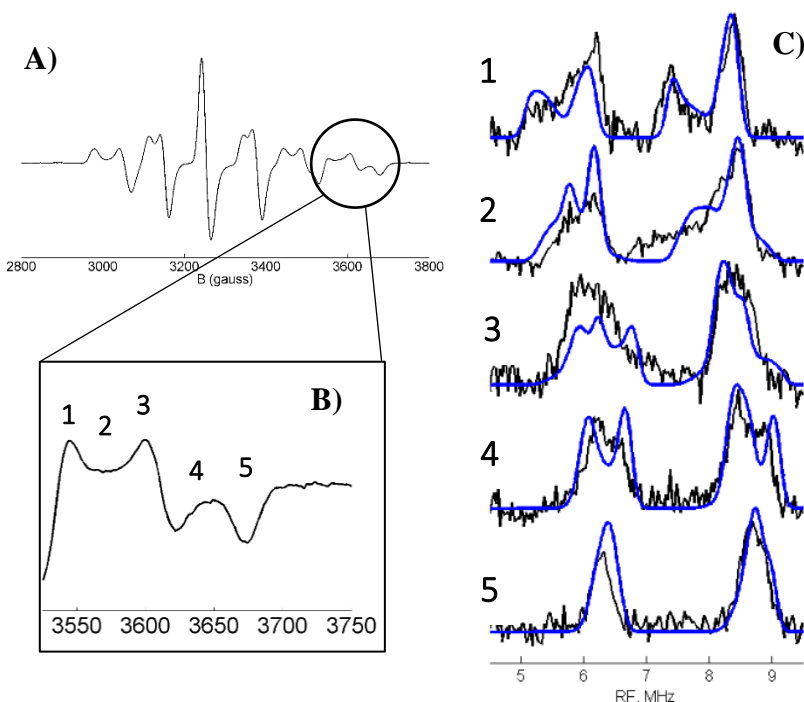


Figure S1. (A) CW EPR spectrum of the $\beta\text{-Mn}^{\text{III}}/\text{Fe}^{\text{III}}$ state and (B) the region used for obtaining the (C) Davies ENDOR spectra in black and in blue the simulation. Experimental conditions: MW frequency 9.70 GHz, Temperature 13.5 K, $\pi/2$ of 56 ns, RF pulse 7 μs , tau 420 ns, exact field values: 3670 G, 3700 G, 3726 G, 3750 G, and 3770 G.

signals were simulated via the following parameters $\mathbf{A}_{\text{HF}} = [13.5, 15, 15.2] \pm 0.5$ MHz, with the Euler angles $[45, 25, -60] \pm 10^\circ$, and the quadrupolar tensor of $[0.25, 0.15, -0.4] \pm 0.05$ MHz with the following Euler angles $[0, 110, 45] \pm 10^\circ$. The parameters were obtained by a best fit of the spectra at all field positions simultaneously. The isotropic hyperfine coupling we observed correlates well with other nitrogen ligated paramagnetic metals ($a_{\text{iso}} \sim 10$ MHz), however, the quadrupolar interaction in our study was much weaker than the ones previously reported ($Q \sim 2.2$ MHz). The hyperfine interaction is dominated by the isotropic component indicating a significant amount of spin density on the ^{14}N . Therefore, the nuclei that give rise to the signal definitely belong to at least one nitrogen atom directly ligated to Mn or Fe and that belongs to a histidine residue (H123 and H230). Similarly to the case of the hydron observed, we cannot determine if the observed signal belongs to a single nitrogen or two nearly identical ones.

Appendix 5-B EPR Theory

Description of the Spin Hamiltonian, EPR Methods and Spin Relaxation Theory

Continuous wave (CW) EPR is a very useful tool for obtaining fingerprint EPR spectra as well as determining very strong hyperfine interactions of the first ligation shell nuclei bound to the paramagnetic metal. In the case of the $\text{Mn}^{\text{III}}/\text{Fe}^{\text{III}}$, *Ct* RNR β cofactor product state, the naturally abundant ^{55}Mn nucleus exhibits strong hyperfine coupling (HF) to the electron spin. This strong HF coupling can be readily obtained by simulating the CW EPR spectrum. However, nuclear Zeeman, quadrupole, and weaker hyperfine interactions are not resolved in CW EPR signals. Moreover, in the majority of cases, the HF splitting is hidden well within the EPR line-shape. Therefore, higher resolution spectroscopy is needed to discern these weaker interactions. This is one of the primary reasons for the development of pulsed EPR methods. These methods are capable of resolving weak hyperfine interactions ($\sim < 10$ MHz) of nuclei in both first and second ligation shells of bioinorganic systems.¹ To delve into the theory of advanced EPR methods we will first introduce the Hamiltonian for our spin system.

In chapter 2 we are dealing with the *Ct* RNR β $\text{Mn}^{\text{III}}/\text{Fe}^{\text{III}}$ cofactor. The two metal ions are antiferromagnetically coupled to a ground state of $S=1/2$. The total spin Hamiltonian of this system can be described as a sum of the electron Zeeman term, the Heisenberg exchange coupling, the zero-field interactions, the hyperfine interaction, nuclear Zeeman, and nuclear quadrupole interactions:²

$$\begin{aligned} \mathbf{H}_S = & \beta_e S_1 \mathbf{g}_1 \mathbf{B} + \beta_e S_2 \mathbf{g}_2 \mathbf{B} + JS_1 S_2 + S_1 \mathbf{d}_1 S_1 + S_2 \mathbf{d}_2 S_2 + \sum_j S_1 \mathbf{a}_{1j} I_j + \sum_j S_2 \mathbf{a}_{2j} I_j + \\ & \beta_n B \sum_j g_{n_j} I_j + \sum_j I_j \mathbf{P}_j I_j \end{aligned} \quad (1)$$

with β_e and β_n as the electron and nuclear Bohr magnetons, $\mathbf{g}_{1,2}$ the intrinsic g-tensors of isolated ions, g_n the nuclear g value, \mathbf{B} the applied magnetic field vector, J the Heisenberg exchange coupling constant, $\mathbf{d}_{1,2}$ the zero-field splitting tensors, \mathbf{a}_{ij} hyperfine interaction tensor between an electron spin S_i and a nuclear spin I_j , $S_{1,2}$ and I_j the electron and nuclear spin operators respectively, while \mathbf{P}_j is the quadrupolar tensor. In this work, we took advantage of the strong exchange coupling approximation ($D/J \ll 1$) to construct the effective spin Hamiltonian that corresponds only to the antiferromagnetic ground state ($S=1/2$). In this manner, the observed \mathbf{g}_{eff} , \mathbf{A}_j , and \mathbf{P}_{eff} values are comparable to the experimentally determined ones. The $S=1/2$ effective spin Hamiltonian can be described as:

$$\mathbf{H}_{\text{eff}} = \beta_e \mathbf{g}_{\text{eff}} \mathbf{B}_0 S_{\text{eff}} + \sum_j S_{\text{eff}} \mathbf{A}_j I_j + \sum_j I_j \mathbf{P}_{\text{eff}_j} I_j \quad (2)$$

where \mathbf{g}_{eff} , S_{eff} , \mathbf{P}_{eff} , are the \mathbf{g} tensor, the spin operator, and the quadrupolar tensor, respectively, they all correspond to the simplified effective spin Hamiltonian where $S=1/2$. The isolation of the individual Mn and Fe ion contributions to observed effective spin Hamiltonian parameters can be achieved via a vector spin projection model³⁻⁶ with the following equations that describe effective \mathbf{g}_{eff} and $\mathbf{A}_{\text{Mn,Fe}}$ tensors of the exchange coupled system:

$$\mathbf{g}_{eff} = c_1 \mathbf{g}_1 + c_2 \mathbf{g}_2 + \frac{c_1 c_2}{5J} (\mathbf{g}_1 - \mathbf{g}_2) [(3c_1 + 1) \cdot \mathbf{d}_1 - (3c_2 + 1) \cdot \mathbf{d}_2] \quad (3)$$

$$\mathbf{A}_{Mn} = c_1 \mathbf{a}_1 - \frac{\mathbf{a}_1 c_1 c_2}{5J} [(3c_1 + 1) \cdot \mathbf{d}_1 - (3c_2 + 1) \cdot \mathbf{d}_2] \quad (4)$$

$$\mathbf{A}_{Fe} = c_2 \mathbf{a}_2 - \frac{\mathbf{a}_2 c_1 c_2}{5J} [(3c_1 + 1) \cdot \mathbf{d}_1 - (3c_2 + 1) \cdot \mathbf{d}_2] \quad (5)$$

where $c_{1,2}$ represent the spin projection factors, that are assigned to either spin site 1 or 2. For the $\text{Mn}^{\text{III}}/\text{Fe}^{\text{III}}$ spin system, $c_1=7/3$ for the Fe ion and $c_2=-4/3$ for the Mn ion, derived via the following equations:⁴

$$c_1 = \frac{S(S+1) + S_1(S_1+1) - S_2(S_2+1)}{2S(S+1)} \quad (6)$$

$$c_2 = \frac{S(S+1) - S_1(S_1+1) + S_2(S_2+1)}{2S(S+1)} \quad (7)$$

This is a zero-order approximation that is only valid in the strong exchange limit.⁷ When zero-field interaction of a spin coupled system is non-zero, a mixing of higher spin states (e.g. $\pm 5/2$, $\pm 3/2$) into the ground state doublet ($\pm 1/2$) occurs. This mixing can be treating as a first-order perturbation on the total spin functions shown in equations 3-10. Zero-field contribution for both Mn^{III} ^{2, 7}, and Fe^{III} ⁸ ions in a strongly coupled regime are very small (D_{Mn} , $D_{\text{Fe}} \sim 5 \text{ cm}^{-1}$) compared to the J coupling ($J_{\text{Mn,Mn}} \sim 100 \text{ cm}^{-1}$) and therefore may be neglected. As a result of this approximation the following expressions for the \mathbf{g}_{eff} and \mathbf{A} tensors for the combined spin system can be derived:

$$\mathbf{g}_{eff} = c_1 \mathbf{g}_1 + c_2 \mathbf{g}_2 \quad (8)$$

$$\mathbf{A}_{Mn} = c_1 \mathbf{a}_{Mn} \quad (9)$$

$$\mathbf{A}_{Fe} = c_2 \mathbf{a}_{Fe} \quad (10)$$

where \mathbf{A}_{Mn} is the observed hyperfine interaction of the Mn while \mathbf{A}_{Fe} is analogously the observed hyperfine interaction of the Fe. The hyperfine interaction of the first- and second-shell nuclei provides information that can be used to create models of paramagnetic enzyme cofactors and therefore elucidate the atomic structure of the cofactor. The HF Hamiltonian (\mathbf{H}_{HF}) can be defined as a sum of isotropic or Fermi contact interaction \mathbf{H}_F and the electron-nuclear dipole-dipole interaction \mathbf{H}_{DD} :

$$\mathbf{H}_{HF} = \mathbf{H}_F + \mathbf{H}_{DD} = \alpha_{iso} \tilde{\mathbf{S}}\mathbf{I} + \tilde{\mathbf{S}}\mathbf{T}\mathbf{I} \quad (11)$$

where α_{iso} is the isotropic hyperfine coupling constant and matrix \mathbf{T} represents the anisotropic dipole-dipole coupling.⁹ In more detail α_{iso} is directly related to the spin density at the nucleus:

$$\alpha_{iso} = \frac{2\mu_0}{3\hbar} g\beta_e g_n \beta_n |\Psi_0(0)|^2 \quad (12)$$

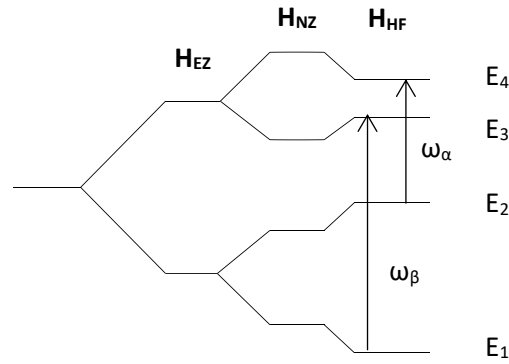
where $\Psi_0(0)$ is the value of the electron wavefunction at the nucleus. The anisotropic part of the hyperfine is a through-space interaction often used to calculate the electron-nuclear distance and orientation of the anisotropic hyperfine tensor with respect to the magnetic field:

$$\mathbf{T} = \frac{\mu_0}{4\pi\hbar} g\beta_e g_n \beta_n \sum_{k \neq N} \frac{\rho_k (3\tilde{\mathbf{n}}_k \mathbf{n}_k - 1)}{r_k^3} \quad (13)$$

where the sum is calculated with all nuclei of spin population ρ_k at distance r_k from the nucleus

with the electron–nucleus unit vector \mathbf{n}_k . In order to obtain both components of hyperfine interactions in the study, especially the hyperfine tensors of the nearby protons we utilized pulsed EPR methods ESEEM and ENDOR.

The Electron Spin Echo Envelope Modulation (ESEEM) effect can be understood by examining a simple two-spin model that consists of one electron spin ($S = \frac{1}{2}$) and one nuclear



Appendix 5-B Figure 1 Energy level diagram of a model containing isotropic $g=2$ tensor, the electron (EZ) and nuclear (NZ) Zeeman as well as the hyperfine interaction (HF). The allowed EPR transitions are illustrated with an arrow.

spin ($I = \frac{1}{2}$) in the case of an axially symmetric hyperfine interaction. The basic energy level diagram of such system is presented in Figure Ax 1. In this four energy level diagram there are two allowed EPR transitions, $E_4 - E_2$, and $E_3 - E_1$, where $\Delta m_S = \pm 1$ and $\Delta m_I = 0$, two forbidden EPR transitions, $E_4 - E_1$, and $E_3 - E_2$, where $\Delta m_S = \pm 1$ and $\Delta m_I = \pm 1$, and two NMR transitions $E_4 - E_3$, and $E_2 - E_1$, ω_α and ω_β , where $\Delta m_S = 0$ and $\Delta m_I = \pm 1$. The frequencies of EPR transitions can be defined by the following set of equations:⁹

$$\omega_{13} = \omega_S + \frac{\omega_-}{2}$$

$$\omega_{24} = \omega_S - \frac{\omega_-}{2}$$

$$\omega_{14} = \omega_S + \frac{\omega_+}{2}$$

$$\omega_{23} = \omega_S - \frac{\omega_+}{2} \quad (14)$$

with $\omega_+ = \omega_\alpha + \omega_\beta$, and $\omega_- = \omega_\alpha - \omega_\beta$ and ω_S the electron Larmor frequency. Additionally, the nuclear frequencies are given by the following equations:

$$\omega_\alpha = \left[\left(\omega_I + \frac{A}{2} \right)^2 + \left(\frac{B}{2} \right)^2 \right]^{\frac{1}{2}}; \quad \omega_\beta = \left[\left(\omega_I - \frac{A}{2} \right)^2 + \left(\frac{B}{2} \right)^2 \right]^{\frac{1}{2}}; \quad (15)$$

where

$$A = a_{iso} + T(3 \cos^2 \theta - 1); \quad B = 3T \sin \theta \cos \theta; \quad (16)$$

Theta (θ) is defined as the angle between the dipolar hyperfine vector and the external magnetic field. The allowed (I_a) and forbidden (I_f) transition probabilities in this model system are defined by:⁹

$$I_a = \cos^2 \eta = \frac{\left| \omega_I^2 - \frac{1}{4} \omega_-^2 \right|}{\omega_\alpha \omega_\beta}$$

$$I_f = \sin^2 \eta = \frac{\left| \omega_I^2 - \frac{1}{4} \omega_+^2 \right|}{\omega_\alpha \omega_\beta} \quad (17)$$

in which 2η represents the angle between the nuclear quantization axes in the two m_s manifolds with respect to the static magnetic field vector \mathbf{B} . In the case of a purely isotropic hyperfine coupling where $T = 0$, the B term vanishes, and as a result $I_a = 1$ and $I_f = 0$ and $\omega = a_{iso}$. The

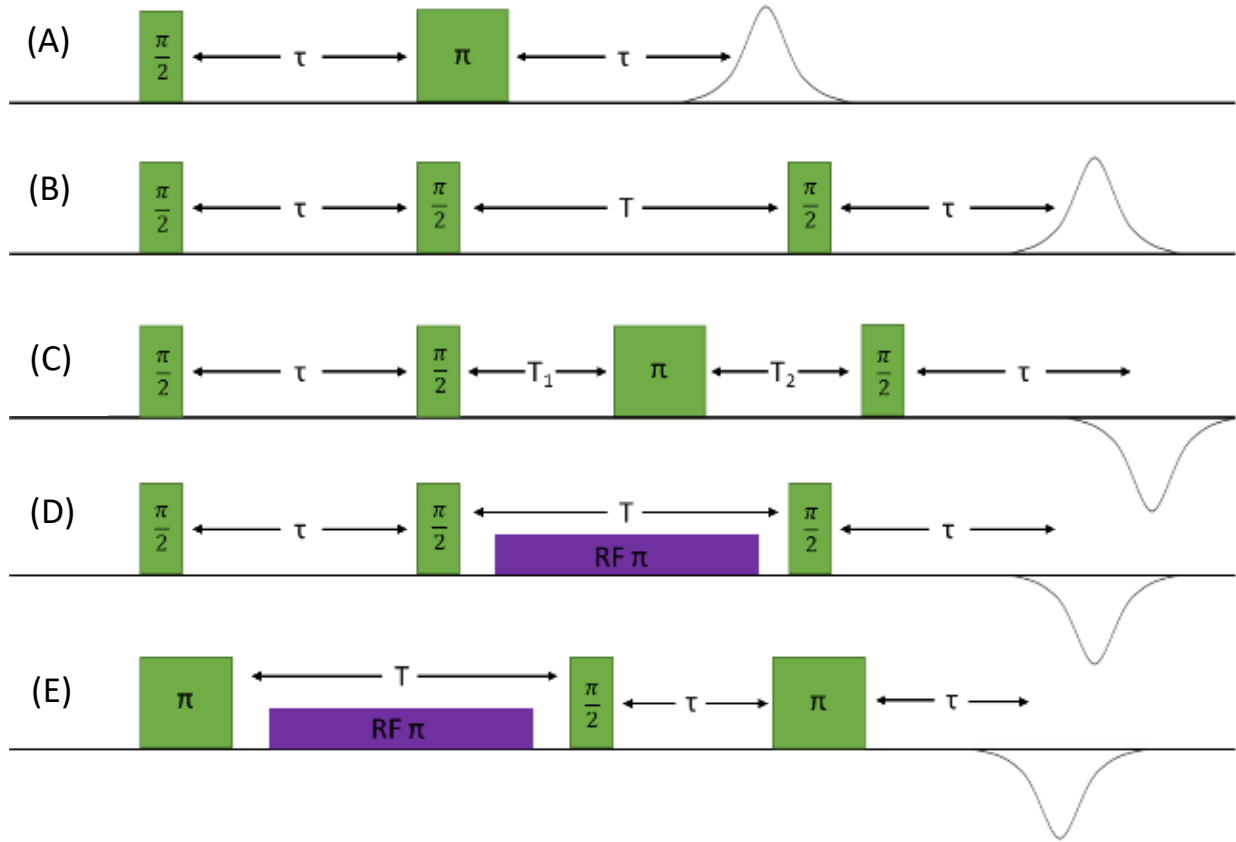


Figure 2 (A) Pulse sequences for two-pulse and (B) three-pulse ESEEM, (C) HYSCORE, (D) Mims ENDOR and (E) Davies ENDOR

anisotropic part is, therefore, responsible for the mixing of the energy levels so that they no longer correspond to pure α and β with respect to the nuclear spin. The resulting non-zero probability of “forbidden” EPR transition provides the basis of the ESEEM effect.

In this work, we have used a four pulse, HYSCORE sequence (figure Ax 2C) where an additional π pulse is added between the second and third $\pi/2$ pulses of the three-pulse ESEEM sequence. The general modulation formula for a HYSCORE experiment for the case of $S=1/2$, $I>1/2$ is given as:¹⁰

$$V'_{4p}(\tau, t_1, t_2) = \exp\left(\frac{-2\tau}{T_m}\right) \exp\left(-\left(\frac{t_1+t_2}{T_m^{(n)}}\right)\right) V_{4p}(\tau, t_1, t_2) \text{ , where}$$

$$V_{4p}(\tau, t_1, t_2) = \frac{1}{4(2I+1)} \sum_{i,k,l,n} \left[\chi_{ikln}^{\alpha\beta}(\tau) \exp(-i\omega_{ik}^\alpha t_1) \exp(-i\omega_{ln}^\beta t_2) + \right. \\ \left. \chi_{ikln}^{\beta\alpha}(\tau) \exp(-i\omega_{ln}^\alpha t_1) \exp(-i\omega_{ik}^\beta t_2) \right]$$

and:

$$\chi_{ikln}^{\alpha\beta} = \sum_{jm} (M_{il} M_{lj}^* M_{jn} M_{nk}^* M_{km} M_{mi}^*)^* \left[\exp\left(-i(\omega_{ij}^\alpha + \omega_{lm}^\beta)\tau\right) + \exp\left(i(\omega_{kj}^\alpha + \omega_{nm}^\beta)\tau\right) \right], \\ \chi_{ikln}^{\beta\alpha} = \sum_{jm} (M_{il} M_{lj}^* M_{jn} M_{nk}^* M_{km} M_{mi}^*)^* \left[\exp\left(-i(\omega_{ij}^\alpha + \omega_{lm}^\beta)\tau\right) + \exp\left(i(\omega_{kj}^\alpha + \omega_{nm}^\beta)\tau\right) \right] \quad (18)$$

where indices l and n designate the nuclear spin states in the electron spin α manifold. The indices m and p designate the nuclear spin states in the β manifold. Similarly to the three-pulse ESEEM, the resulting powder HYSCORE spectra also suffer from blind spots where the signal intensity drops to zero at frequencies that are multiples of $1/\tau$. In the strongly coupled case where $|A| > 2\omega_I$, the correlation ridges appear in the second quadrant and are oriented parallel to the diagonal and separated by $|2\omega_I|$. In the weakly coupled case where $|A| < 2\omega_I$, the two correlation arcs are present in the first quadrant, separated by $|A|$ and displaced from the anti-diagonal at ω_I by a maximum frequency shift that is directly proportional to the anisotropy of the hyperfine:¹¹

$$\Delta\omega_{max} = \frac{9T^2}{32|\omega_I|} \quad (19)$$

The resulting HYSCORE peaks are eyebrow shaped (figure Ax 3) and very different in the predominantly isotropic case where $\Delta\omega_{\max}$ is relatively small and in the highly anisotropic case where $\Delta\omega_{\max}$ is relatively large. Of the three ESEEM techniques, HYSCORE is the technique with the highest resolution and is often used in bioinorganic systems to assess the structures of metallocofactors.¹²⁻¹⁴ A complementary method to the ESEEM techniques is Electron Nuclear Double Resonance (ENDOR) spectroscopy first developed

by Feher.¹⁵ In this study we have exclusively used pulsed ENDOR methods in which the NMR transitions are detected via the changes in the electron spin echo.¹⁶ There are two main pulse sequences that are commonly used in pulsed EPR experiments,

Davies¹⁷ and Mims¹⁸ ENDOR. Davies ENDOR sequence (figure Ax 2E) consists of three microwave pulses with an addition of a radio frequency pulse between the first and the second MW pulses. All the pulses in Davies ENDOR sequence are stationary while the signal is recorded

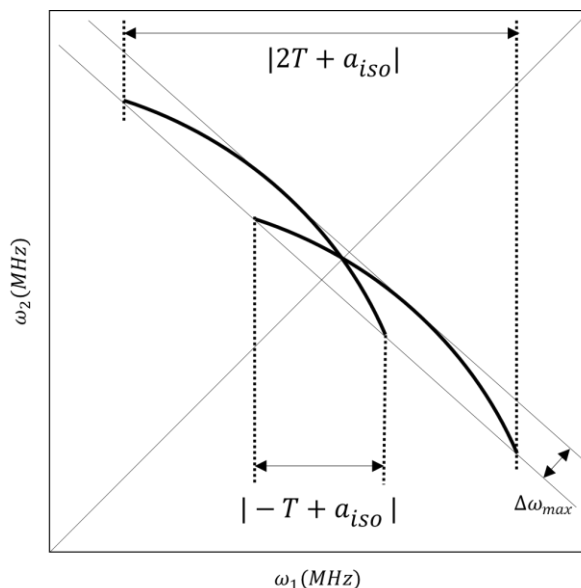


Figure 3. Theoretical HYSCORE spectrum of an $S=1/2$ electron spin coupled to an $I=1/2$ nucleus. Figure adopted from ref (21).

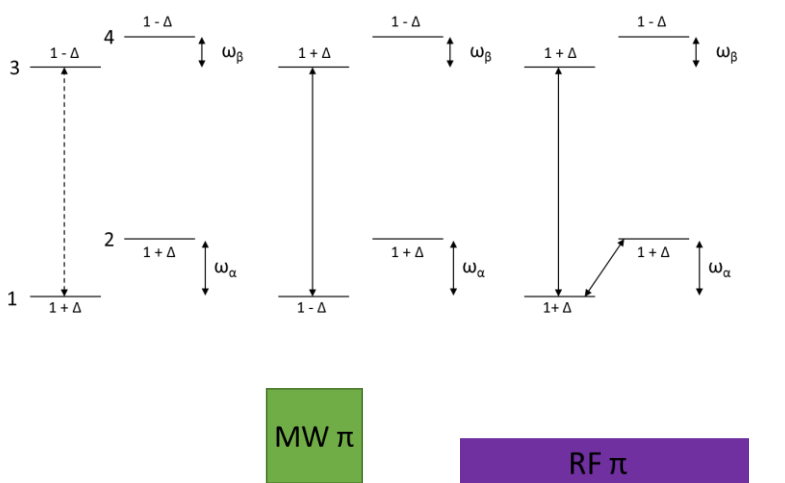


Figure 4. Basic principles of Davies ENDOR population inversion. Adapted from reference (16).

as a function of RF frequency. The intensity of Davies ENDOR signals as a function of the selectivity parameter η_s is represented by:¹⁹

$$V(\eta_s) = V_{max} \frac{\sqrt{2}\eta_s}{\eta_s^2 + 1/2} \quad (20)$$

where $\eta_s = a_{iso}t_{mw}/2\pi$, in which V_{max} is the maximum ENDOR intensity obtained with $\eta_s = \sqrt{2}/2$ and t_{mw} is the length of time of the first microwave π pulse. The resulting spectrum has a “hole” when the product of $a_{iso}t_{mw}$ approaches 0. Luckily, often times the optimization of pulse parameters can minimize this effect, especially for nuclei with relatively larger hyperfine couplings.²⁰

On the other hand, Mims ENDOR is a technique more suitable for determining the hyperfine interaction of weakly coupled nuclei.²⁰ This technique is based on the stimulated echo pulse sequence (fig. Ax-2D) of three $\pi/2$ microwave pulses and a radio frequency pulse placed between the second and third mw pulses. The Mims ENDOR efficiency is given by:¹⁸

$$V_{END}(\tau, A) = \frac{1}{4} (1 - \cos(A\tau)) \quad (21)$$

The efficiency is maximum when $\tau = (2n+1)\pi/A$ with n being a non-negative integer. Therefore, similarly to ESEEM techniques, Mims ENDOR suffers from the “blind-spot” effects, with the blind spot appearing when the $A\tau$ term is equal to zero. Often times for weaker hyperfine couplings, a τ can be chosen in such a way that it positions the blind spots at frequencies slightly above and slightly below the HF coupling of interest therefore enabling detection with minimal loss of signal.

Both ENDOR and ESEEM experiments are performed at distinct magnetic fields. The EPR signals of most powder spectra of metallocofactors have width greater than 50mT,⁹ and the microwave pulses cannot excite the entire EPR spectrum at once. Therefore, the pulsed

experiments are repeated at different field values to ensure that the hyperfine tensor of interest is probed at all g tensor values. Additionally, by obtaining ENDOR or ESEEM spectra at single crystal positions, typically located at the highest and lowest g values of a rhombic EPR spectrum, we can ensure that our simulations will produce more unique fits to the experimental data. A typical way of rotating the \mathbf{g} tensor, the \mathbf{A} tensor or the quadrupolar tensor is via the use of Euler angles. These angles correspond to three successive axis rotations (ZYZ) that rotate the hyperfine or quadrupolar matrix into the g matrix reference frame. In this work the three Euler angles used correspond to the zyz convention.²¹

Another useful EPR method that can be used to aid us in resolving metallocofactor structures is the determination of the Heisenberg exchange coupling constant (J) via spin-lattice relaxation methods. One of the most significant constants in EPR relaxation theory is the spin-lattice relaxation rate (T_1^{-1}). This rate, as it pertains to the lowest Kramers doublet, can be expressed as a sum of the direct, Orbach and Raman processes:²²

$$T_1^{-1} = A_{dir}T + A_{orb} \frac{\Delta^3}{e^{\frac{\Delta}{T}} - 1} + A_{ram}T^9 \quad (22)$$

in which T_1 represents the spin lattice relaxation time, T the absolute temperature, Δ the energy separation between the lowest Kramers doublet and the lowest lying excited state and parameters A_{dir} , A_{orb} , A_{ram} are quantities discussed in detail by Orbach.^{23, 24} The direct spin-lattice relaxation process is a single phonon direct transfer of energy from the spin system to the lattice. In this case the energy of the emitted phonon matches the energy of the absorbed phonon. Orbach relaxation is a two-phonon process in which the energy transferred to the spin lattice corresponds to the energy difference between the energy absorbed and emitted by a specific low-lying excited state. Raman contribution to spin-lattice relaxation is also a two phonon process where the energy

transferred to the lattice matches the difference between the energies absorbed and emitted by a virtual excited state at any energy less than the Debye temperature.²⁵ As equation 22 demonstrates, the direct relaxation process is linearly dependent on temperature, the Orbach process has an exponential reliance, while the Raman process is characterized by a power of 9 dependency on temperature. Even though all three processes are present at all temperature ranges to some degree, typically the Raman process dominates at relatively high temperatures $T > 30$ K, Orbach at intermediate $30 \text{ K} > T > 5$ K, and Direct at low $T < 5$ K temperature. In this study, the EPR signal of the $\text{Mn}^{\text{III}}/\text{Fe}^{\text{III}}$ state is best resolved between 10 and 30 K and is mostly affected by the Orbach and direct processes. By expanding the A_{orb} term from equation 22 this process can be described in more detail by:²⁵

$$T_{1\text{orb}}^{-1} = \frac{3}{2\pi\hbar^4\rho v^5} |V^{(1)}|^2 \frac{\Delta^3}{e^{-\Delta/kT} - 1} \quad (23)$$

where ρ represent the lattice density, v the photon velocity through a medium, k the Boltzmann constant, T the absolute temperature and $V^{(1)}$ a product of matrix elements that describe the two Kramers doublet states and the lowest lying excited state. In the limit that is applicable to our working conditions, $\Delta \gg kT$, and by grouping temperature-independent terms together we can simplify eq. 23 to:

$$T_1^{-1} = A_{\text{orb}2} e^{-\Delta/T} \quad (24)$$

To measure the spin-lattice relaxation rate in $\text{Mn}^{\text{III}}/\text{Fe}^{\text{III}}$ state we used the temperature dependent power saturation methods.^{26, 27}

In this work we utilized both CW-EPR, and the advanced EPR methods, ^2H -HYSCORE, and Davies and Mims ENDOR spectroscopies along with DFT methods to determine the core structure of the $\beta\text{-Mn}^{\text{III}}/\text{Fe}^{\text{III}}$ RT product state of *Ct* β and in turn, propose a model for this state.

REFERENCES

1. Deligiannakis, Y.; Louloudi, M.; Hadjiliadis, N., Electron spin echo envelope modulation (ESEEM) spectroscopy as a tool to investigate the coordination environment of metal centers. *Coordin Chem Rev* **2000**, *204*, 1-112.
2. Schafer, K. O.; Bittl, R.; Zwegart, W.; Lendzian, F.; Haselhorst, G.; Weyhermuller, T.; Wieghardt, K.; Lubitz, W., Electronic structure of antiferromagnetically coupled dinuclear manganese ((MnMnIV)-Mn-III) complexes studied by magnetic resonance techniques. *J Am Chem Soc* **1998**, *120* (50), 13104-13120.
3. Bertrand, P.; Guigliarelli, B.; More, C., The Mixed-Valence [Fe(III), Fe(II)] Binuclear Centers of Biological Molecules Viewed through Epr Spectroscopy. *New J Chem* **1991**, *15* (6), 445-454.
4. Bencini, A. G., D., *EPR of Exchange Coupled Systems*. Springer-Verlag: Berlin, 1990.
5. Blondin, G.; Girerd, J. J., Interplay of Electron Exchange and Electron-Transfer in Metal Polynuclear Complexes in Proteins or Chemical-Models. *Chem Rev* **1990**, *90* (8), 1359-1376.
6. Sands, R. H.; Dunham, W. R., Spectroscopic Studies on 2-Iron Ferredoxins. *Q Rev Biophys* **1974**, *7* (4), 443-504.

7. Zheng, M.; Khangulov, S. V.; Dismukes, G. C.; Barynin, V. V., Electronic-Structure of Dimanganese(Ii,Iii) and Dimanganese(Iii,Iv) Complexes and Dimanganese Catalase Enzyme - a General Epr Spectral Simulation Approach. *Inorg Chem* **1994**, 33 (2), 382-387.
8. Que, L., *Physical Methods in Bioinorganic Chemistry*. University Science Books: 2000.
9. Berliner, L., *Biological Magnetic Resonance*. Springer: New York, 2009; Vol. 28.
10. Tyryshkin, A. M.; Dikanov, S. A.; Goldfarb, D., Sum Combination Harmonics in 4-Pulse Esem Spectra - Study of the Ligand Geometry in Aqua Vanadyl Complexes in Polycrystalline and Glass Matrices. *J Magn Reson Ser A* **1993**, 105 (3), 271-283.
11. Poppl, A.; Kevan, L., A practical strategy for determination of proton hyperfine interaction parameters in paramagnetic transition metal ion complexes by two-dimensional HYSCORE electron spin resonance spectroscopy in disordered systems. *J Phys Chem-Us* **1996**, 100 (9), 3387-3394.
12. Ioanitescu, A. I.; Dewilde, S.; Kiger, L.; Marden, M. C.; Moens, L.; Van Doorslaer, S., Characterization of nonsymbiotic tomato hemoglobin. *Biophys J* **2005**, 89 (4), 2628-2639.
13. Garcia-Rubio, I.; Martinez, J. I.; Picorel, R.; Yruela, I. L.; Alonso, P. J., HYSCORE spectroscopy in the cytochrome b(559) of the photosystem II reaction center. *J Am Chem Soc* **2003**, 125 (51), 15846-15854.
14. Foerster, S.; van Gastel, M.; Brecht, M.; Lubitz, W., An orientation-selected ENDOR and HYSCORE study of the Ni-C active state of Desulfovibrio vulgaris Miyazaki F hydrogenase. *J Biol Inorg Chem* **2005**, 10 (1), 51-62.
15. Feher, G., Electron Nuclear Double Resonance (Endor) Experiments. *Physica* **1958**, 24, S80-S87.
16. Weber, R., Bruker EPR Manual, Pulsed Operations. **2001**.

17. Davies, E. R., New Pulse Endor Technique. *Phys Lett A* **1974**, A 47 (1), 1-2.
18. Mims, W. B., Pulsed Endor Experiments. *Proc R Soc Lon Ser-A* **1965**, 283 (1395), 452-&.
19. Fan, C. L.; Doan, P. E.; Davoust, C. E.; Hoffman, B. M., Quantitative Studies of Davies Pulsed Endor. *J Magn Reson* **1992**, 98 (1), 62-72.
20. Doan, P. E.; Lees, N. S.; Shanmugam, M.; Hoffman, B. M., Simulating Suppression Effects in Pulsed ENDOR, and the 'Hole in the Middle' of Mims and Davies ENDOR Spectra. *Appl Magn Reson* **2010**, 37 (1-4), 763-779.
21. Stoll, S.; Schweiger, A., EasySpin, a comprehensive software package for spectral simulation and analysis in EPR. *J Magn Reson* **2006**, 178 (1), 42-55.
22. Brya, W. J.; Wagner, P. E., Direct Orbach and Raman Relaxation in Dilute Cerous Magnesium Nitrate. *Phys Rev* **1966**, 147 (1), 239-&.
23. Orbach, R., On Theory of Spin-Lattice Relaxation in Paramagnetic Salts. *P Phys Soc Lond* **1961**, 77 (496), 821-&.
24. Orbach, R., Spin-Lattice Relaxation in Rare-Earth Salts. *Proc R Soc Lon Ser-A* **1961**, 264 (1318), 458-+.
25. Abragam, A.; Bleaney, B., *Electron Paramagnetic Resonance of Transition Ions*. Clarendon Press: Oxford, 1970.
26. Alger, R., *Electron Paramagnetic resonance*. John Wiley and Sons: New York, 1968.
27. Tomter, A. B.; Zoppellaro, G.; Bell, C. B.; Barra, A. L.; Andersen, N. H.; Solomon, E. I.; Andersson, K. K., Spectroscopic Studies of the Iron and Manganese Reconstituted Tyrosyl Radical in Bacillus Cereus Ribonucleotide Reductase R2 Protein. *Plos One* **2012**, 7 (3).

Appendix 5-C Cartesian coordinates of the 6 DFT generated models of the β -Mn^{III}/Fe^{III}

cofactor

Model 1

6	-3.511151000	2.466446000	0.581822000
8	-3.009754000	1.336314000	0.186887000
8	-2.918263000	3.368196000	1.192841000
6	-0.887452000	-0.474599000	-2.417459000
8	-1.657464000	-0.425211000	-1.396717000
8	0.333909000	-0.185110000	-2.425958000
6	-3.942106000	-1.907682000	1.333582000
7	-2.611681000	-1.534928000	1.197763000
6	3.661378000	1.963743000	-2.078228000
8	4.624018000	2.046624000	-2.878594000
8	2.970329000	0.893093000	-1.903858000
6	2.407218000	1.212454000	2.332170000
8	1.390166000	1.834765000	2.742801000
8	2.595190000	0.753703000	1.154534000
6	3.520463000	-2.518356000	-0.936678000
7	2.282294000	-1.900638000	-0.933487000
26	1.445966000	0.321700000	-0.624624000
25	-1.304244000	0.389189000	0.460522000
8	-1.194922000	0.831130000	2.225332000
8	-0.190917000	1.516569000	-0.179376000
8	0.124432000	-0.859544000	0.699274000
6	-4.993747000	2.651062000	0.201625000
6	-5.277047000	2.427547000	-1.292581000
6	-4.466786000	3.385851000	-2.165113000
6	4.787605000	-1.746128000	-0.731619000
6	6.038176000	-2.621651000	-0.775011000
6	-1.469647000	-0.973420000	-3.745501000
6	-2.991940000	-1.075033000	-3.863436000
6	-3.625294000	-2.048512000	-2.871562000
6	3.309586000	3.192772000	-1.232491000
6	4.363845000	3.426421000	-0.138212000
6	4.055803000	4.655347000	0.721019000
6	-5.086370000	-1.009528000	0.969927000
6	-6.445320000	-1.699320000	1.079062000
6	3.477483000	0.875013000	3.377564000
6	3.177085000	-0.493616000	4.025914000
6	3.534318000	-1.696349000	3.136790000
7	-2.692285000	-3.598975000	1.993353000
7	1.987100000	-4.068644000	-1.272714000
6	-4.004837000	-3.195528000	1.833999000
6	-1.894640000	-2.578084000	1.593920000

6	1.389485000	-2.857129000	-1.142551000
6	3.352129000	-3.874860000	-1.147451000
1	-5.288416000	3.673054000	0.498760000
1	-5.589863000	1.943227000	0.806436000
1	-5.027745000	1.384287000	-1.558475000
1	-6.360314000	2.559631000	-1.482160000
1	-3.386772000	3.272808000	-1.954238000
1	4.724522000	-1.205839000	0.230487000
1	4.845300000	-0.959048000	-1.505609000
1	6.932264000	-1.993507000	-0.715024000
1	6.064181000	-3.355167000	0.051671000
1	6.083680000	-3.171395000	-1.722940000
1	-1.012422000	-1.969129000	-3.919381000
1	-1.059828000	-0.316519000	-4.533170000
1	-3.440041000	-0.072648000	-3.721012000
1	-3.234538000	-1.381135000	-4.899984000
1	-3.513628000	-1.669137000	-1.845877000
1	2.313662000	3.073425000	-0.772718000
1	3.277035000	4.075387000	-1.899329000
1	5.353100000	3.549496000	-0.619738000
1	4.423032000	2.525996000	0.499672000
1	3.101961000	4.542793000	1.267747000
1	4.857892000	4.836636000	1.446742000
1	3.982254000	5.539435000	0.074615000
1	-4.928416000	-0.627011000	-0.052991000
1	-5.061768000	-0.116779000	1.620686000
1	-7.256285000	-1.029636000	0.775639000
1	-6.652615000	-2.016660000	2.118477000
1	4.480809000	0.854336000	2.913543000
1	3.461171000	1.659671000	4.152859000
1	3.755500000	-0.574636000	4.967339000
1	2.108367000	-0.523198000	4.315480000
1	2.982446000	-1.706684000	2.184359000
1	3.347093000	-2.626303000	3.689234000
1	4.611652000	-1.644869000	2.935081000
1	-6.500891000	-2.595151000	0.448736000
1	-4.698102000	-2.189554000	-3.053329000
1	-4.587597000	3.219608000	-3.241905000
1	-3.161590000	-3.046036000	-2.883628000
1	-4.719371000	4.433929000	-1.958391000
1	0.514488000	-0.600636000	1.551363000
1	-0.371470000	1.364232000	2.342256000
1	-2.372165000	-4.497248000	2.343084000
1	1.513630000	-4.945658000	-1.467800000
1	-4.843538000	-3.843451000	2.077867000
1	-0.807342000	-2.613742000	1.578397000

1	0.311390000	-2.722228000	-1.177781000
1	4.058334000	-4.699794000	-1.205979000

Model 2

6	-3.790682000	2.394871000	0.804848000
8	-3.021436000	1.643337000	0.090185000
8	-3.522680000	2.831374000	1.944064000
6	-0.891543000	-0.492522000	-2.310146000
8	-1.725016000	-0.154840000	-1.409269000
8	0.364691000	-0.465066000	-2.190955000
6	-3.987102000	-1.986067000	1.479556000
7	-2.660299000	-1.672073000	1.273717000
6	3.587453000	1.946470000	-2.047926000
8	4.501014000	1.962404000	-2.901213000
8	2.889173000	0.889327000	-1.782756000
6	2.627091000	1.361217000	2.209327000
8	2.009543000	2.434185000	2.341816000
8	2.604452000	0.587389000	1.170489000
6	3.514354000	-2.553113000	-0.752946000
7	2.271708000	-1.953543000	-0.644003000
26	1.389122000	0.430231000	-0.501507000
25	-1.348507000	0.653155000	0.447440000
8	-1.332496000	1.107585000	2.232969000
8	0.161244000	1.726714000	-0.401377000
8	0.046596000	-0.660751000	0.764741000
6	-5.162590000	2.719627000	0.193014000
6	-5.325513000	2.453218000	-1.308071000
6	-4.466808000	3.385857000	-2.165129000
6	4.782690000	-1.756397000	-0.704833000
6	6.038156000	-2.621647000	-0.775022000
6	-1.430346000	-0.983735000	-3.659849000
6	-2.952221000	-1.068343000	-3.833184000
6	-3.625286000	-2.048565000	-2.871594000
6	3.298957000	3.212562000	-1.238051000
6	4.362289000	3.429344000	-0.145462000
6	4.055815000	4.655353000	0.721023000
6	-5.070613000	-1.056675000	1.019060000
6	-6.445318000	-1.699318000	1.079034000
6	3.523296000	0.882050000	3.364121000
6	3.120649000	-0.477286000	3.970973000
6	3.534369000	-1.696368000	3.136853000
7	-2.774074000	-3.603861000	2.350852000
7	1.987255000	-4.138012000	-0.866291000
6	-4.081198000	-3.194398000	2.149971000
6	-1.958695000	-2.657500000	1.808567000

6	1.382380000	-2.931074000	-0.713981000
6	3.354575000	-3.920544000	-0.893363000
1	-5.385947000	3.775862000	0.433498000
1	-5.892122000	2.117054000	0.768224000
1	-5.065350000	1.401461000	-1.522763000
1	-6.393433000	2.581106000	-1.573350000
1	-3.396488000	3.251025000	-1.930279000
1	4.783308000	-1.152160000	0.220647000
1	4.774914000	-1.023672000	-1.532416000
1	6.932273000	-1.993505000	-0.715021000
1	6.078718000	-3.356076000	0.050650000
1	6.083687000	-3.171400000	-1.722937000
1	-0.968063000	-1.974381000	-3.836888000
1	-0.994446000	-0.312795000	-4.423392000
1	-3.393647000	-0.063333000	-3.694761000
1	-3.157912000	-1.361404000	-4.881212000
1	-3.522384000	-1.682912000	-1.837091000
1	2.299246000	3.147456000	-0.778229000
1	3.312055000	4.075565000	-1.929725000
1	5.352609000	3.546687000	-0.627126000
1	4.420391000	2.527002000	0.489016000
1	3.105658000	4.528531000	1.266638000
1	4.857885000	4.836631000	1.446741000
1	3.982250000	5.539434000	0.074613000
1	-4.837952000	-0.720902000	-0.006602000
1	-5.048750000	-0.144959000	1.645767000
1	-7.256285000	-1.029634000	0.775654000
1	-6.681149000	-2.023013000	2.111420000
1	4.565707000	0.817771000	2.993617000
1	3.491841000	1.660564000	4.144443000
1	3.594871000	-0.556490000	4.969243000
1	2.027137000	-0.488463000	4.150093000
1	3.007659000	-1.732204000	2.171461000
1	3.347060000	-2.626298000	3.689212000
1	4.611638000	-1.644853000	2.935053000
1	-6.500889000	-2.595154000	0.448744000
1	-4.698113000	-2.189528000	-3.053313000
1	-4.587586000	3.219600000	-3.241897000
1	-3.161586000	-3.046014000	-2.883617000
1	-4.719363000	4.433931000	-1.958381000
1	0.349565000	-0.510420000	1.676696000
1	-2.004223000	1.819747000	2.342396000
1	-2.474137000	-4.453748000	2.820591000
1	1.515714000	-5.034071000	-0.949760000
1	-4.928064000	-3.784034000	2.495512000
1	-0.871642000	-2.719234000	1.819725000

1	0.303749000	-2.806655000	-0.653574000
1	4.066690000	-4.735220000	-1.005966000

Model 3

6	3.614930000	2.319496000	-0.706506000
8	3.013435000	1.362976000	-0.090451000
8	3.182268000	2.892114000	-1.736646000
6	0.832344000	-0.690967000	2.391124000
8	1.644270000	-0.667437000	1.424809000
8	-0.424177000	-0.525531000	2.275098000
6	3.912409000	-1.754141000	-1.461364000
7	2.577470000	-1.342680000	-1.437016000
6	-3.434595000	1.998341000	1.979164000
8	-4.356443000	1.998433000	2.813639000
8	-2.681018000	0.961030000	1.766128000
6	-2.383232000	1.192768000	-2.238379000
8	-1.390721000	1.857621000	-2.620656000
8	-2.543372000	0.677084000	-1.068921000
6	-3.584817000	-2.472785000	0.885467000
7	-2.317575000	-1.935101000	0.707481000
26	-1.336076000	0.216366000	0.539605000
25	1.365763000	0.286070000	-0.501317000
8	1.228628000	1.267810000	-2.519423000
8	0.139322000	1.363266000	0.261687000
8	-0.175313000	-0.879771000	-0.854911000
6	4.995607000	2.721913000	-0.168476000
6	5.255016000	2.481086000	1.326245000
6	4.452947000	3.443784000	2.202544000
6	-4.836064000	-1.647713000	0.842440000
6	-6.105784000	-2.496601000	0.937246000
6	1.347690000	-0.964391000	3.804226000
6	2.872215000	-0.969223000	3.970704000
6	3.559108000	-1.963860000	3.037789000
6	-3.172852000	3.246269000	1.138470000
6	-4.314866000	3.491834000	0.136978000
6	-4.052412000	4.723405000	-0.729466000
6	5.048069000	-0.996756000	-0.837878000
6	6.388926000	-1.736264000	-0.914686000
6	-3.473345000	0.878891000	-3.259708000
6	-3.210197000	-0.505862000	-3.896234000
6	-3.586679000	-1.689140000	-2.990838000
7	2.718578000	-3.217521000	-2.601320000
7	-2.118525000	-4.114729000	1.017747000
6	4.001469000	-2.926859000	-2.183513000

6	1.900291000	-2.252342000	-2.136660000
6	-1.466966000	-2.950593000	0.792041000
6	-3.471908000	-3.836881000	1.079347000
1	5.156160000	3.782907000	-0.430708000
1	5.721801000	2.144476000	-0.773354000
1	5.004046000	1.435721000	1.578889000
1	6.337298000	2.608861000	1.520085000
1	3.371677000	3.336616000	1.991998000
1	-4.838908000	-1.057831000	-0.092117000
1	-4.810428000	-0.905209000	1.661563000
1	-6.993820000	-1.861707000	0.860483000
1	-6.154060000	-3.249244000	0.129163000
1	-6.158065000	-3.022921000	1.898025000
1	0.928796000	-1.946077000	4.103297000
1	0.875438000	-0.220987000	4.471010000
1	3.267139000	0.047420000	3.781915000
1	3.101965000	-1.205347000	5.027316000
1	3.469793000	-1.626199000	1.998082000
1	-2.214520000	3.151332000	0.601397000
1	-3.100019000	4.110633000	1.824672000
1	-5.263103000	3.612862000	0.693755000
1	-4.430024000	2.599133000	-0.504603000
1	-3.104124000	4.618011000	-1.289190000
1	-4.851560000	4.894716000	-1.460851000
1	-3.971640000	5.622058000	-0.104353000
1	4.799501000	-0.749450000	0.208134000
1	5.141358000	-0.026938000	-1.358362000
1	7.205670000	-1.067099000	-0.625923000
1	6.605276000	-2.067626000	-1.946906000
1	-4.466753000	0.884411000	-2.776841000
1	-3.449259000	1.657560000	-4.039328000
1	-3.799226000	-0.575305000	-4.830561000
1	-2.146000000	-0.563999000	-4.198448000
1	-3.040889000	-1.690954000	-2.035516000
1	-3.407442000	-2.633847000	-3.520486000
1	-4.663936000	-1.622759000	-2.792552000
1	6.435003000	-2.617144000	-0.262934000
1	4.630255000	-2.110562000	3.224955000
1	4.570418000	3.302390000	3.283265000
1	3.086026000	-2.956416000	3.072954000
1	4.715776000	4.484191000	1.971195000
1	1.863981000	2.020715000	-2.332876000
1	0.304674000	1.637888000	-2.513291000
1	-0.591243000	-0.650146000	-1.703685000
1	2.427054000	-4.017931000	-3.156150000
1	-1.682617000	-5.026685000	1.124250000

1	4.847058000	-3.563514000	-2.429990000
1	0.826986000	-2.249819000	-2.297101000
1	-0.386710000	-2.880391000	0.693213000
1	-4.213384000	-4.614071000	1.248167000

Model 4

6	4.059129000	2.180556000	-1.136551000
8	3.119723000	1.674478000	-0.406594000
8	4.082821000	2.264240000	-2.378177000
6	0.908991000	-0.227639000	2.239735000
8	1.744052000	0.097082000	1.338572000
8	-0.353092000	-0.191342000	2.135721000
6	3.880319000	-1.840261000	-1.494565000
7	2.581518000	-1.369941000	-1.389584000
6	-3.674548000	2.000122000	1.816035000
8	-4.665865000	1.990542000	2.582899000
8	-2.888358000	0.988643000	1.661701000
6	-2.575207000	1.167401000	-2.401233000
8	-1.615858000	1.874407000	-2.783012000
8	-2.758102000	0.718924000	-1.208009000
6	-3.540556000	-2.406302000	0.771046000
7	-2.302568000	-1.796096000	0.605055000
26	-1.404299000	0.393799000	0.331070000
25	1.385787000	0.674507000	-0.665638000
8	1.093231000	1.415451000	-2.323203000
8	-0.318927000	2.051141000	0.345941000
8	-0.099446000	-0.379985000	-0.726475000
6	5.308265000	2.691243000	-0.386910000
6	5.347007000	2.542465000	1.134452000
6	4.437657000	3.523763000	1.878453000
6	-4.834149000	-1.645389000	0.726748000
6	-6.083661000	-2.527408000	0.848164000
6	1.431821000	-0.705463000	3.602616000
6	2.947645000	-0.832057000	3.783772000
6	3.591915000	-1.866762000	2.861453000
6	-3.386327000	3.267299000	1.000620000
6	-4.429520000	3.472857000	-0.110763000
6	-4.098596000	4.661782000	-1.022113000
6	5.045873000	-1.007661000	-1.050766000
6	6.390905000	-1.721398000	-1.116792000
6	-3.608650000	0.746520000	-3.449422000
6	-3.247030000	-0.631952000	-4.045382000

6	-3.599687000	-1.804139000	-3.118519000
7	2.531207000	-3.372293000	-2.326769000
7	-1.982475000	-3.965606000	0.887495000
6	3.865333000	-3.094196000	-2.077132000
6	1.800294000	-2.310729000	-1.898665000
6	-1.397359000	-2.761255000	0.677364000
6	-3.350847000	-3.763843000	0.949808000
1	5.442068000	3.752679000	-0.675021000
1	6.160385000	2.152695000	-0.842849000
1	5.073433000	1.506812000	1.407716000
1	6.390994000	2.695191000	1.474339000
1	3.376669000	3.355054000	1.628289000
1	-4.866965000	-1.073702000	-0.218626000
1	-4.826617000	-0.882538000	1.526742000
1	-6.977124000	-1.901484000	0.761480000
1	-6.123258000	-3.299033000	0.057495000
1	-6.124828000	-3.028764000	1.822724000
1	0.939136000	-1.677435000	3.799842000
1	1.014242000	-0.006056000	4.350996000
1	3.421895000	0.151875000	3.607500000
1	3.144588000	-1.091916000	4.842257000
1	3.483852000	-1.547120000	1.811766000
1	-2.378506000	3.207498000	0.560308000
1	-3.418002000	4.132637000	1.690546000
1	-5.425058000	3.623437000	0.350220000
1	-4.492418000	2.551448000	-0.716298000
1	-3.147453000	4.510255000	-1.562797000
1	-4.904331000	4.807791000	-1.751711000
1	-4.020186000	5.577067000	-0.421331000
1	4.854171000	-0.643314000	-0.026098000
1	5.079370000	-0.105479000	-1.686976000
1	7.204543000	-1.038756000	-0.851714000
1	6.598627000	-2.088878000	-2.139891000
1	-4.618349000	0.702428000	-3.001658000
1	-3.607698000	1.506547000	-4.248480000
1	-3.797613000	-0.757001000	-4.998217000
1	-2.170381000	-0.642388000	-4.303348000
1	-3.047089000	-1.774341000	-2.167209000
1	-3.416948000	-2.760999000	-3.624588000
1	-4.675904000	-1.740708000	-2.913922000
1	6.448596000	-2.584541000	-0.442543000
1	4.665488000	-2.000396000	3.044332000
1	4.564106000	3.411601000	2.961543000
1	3.126795000	-2.861607000	2.926098000
1	4.690705000	4.559693000	1.617973000
1	-0.233259000	2.428010000	1.237664000

1	0.120677000	1.497340000	-2.453889000
1	2.159827000	-4.213149000	-2.759744000
1	-1.496614000	-4.852863000	0.982704000
1	4.659029000	-3.793109000	-2.332877000
1	0.715025000	-2.241253000	-1.959287000
1	-0.323840000	-2.618819000	0.573553000
1	-4.048757000	-4.582844000	1.108568000

Model 5

6	3.755992000	2.291143000	-1.055559000
8	3.018755000	1.532075000	-0.323480000
8	3.485616000	2.668268000	-2.217638000
6	0.873915000	-0.225469000	2.321197000
8	1.701773000	0.047735000	1.400322000
8	-0.384836000	-0.120160000	2.230706000
6	3.905701000	-2.004330000	-1.385776000
7	2.588989000	-1.665954000	-1.141583000
6	-3.696676000	1.954752000	1.788259000
8	-4.699623000	1.952958000	2.541605000
8	-2.924111000	0.934478000	1.636606000
6	-2.607248000	1.202497000	-2.260589000
8	-1.871042000	2.207994000	-2.374028000
8	-2.713881000	0.474447000	-1.201530000
6	-3.554992000	-2.460490000	0.895739000
7	-2.296670000	-1.889279000	0.768862000
26	-1.407960000	0.256485000	0.374323000
25	1.357454000	0.424159000	-0.610517000
8	1.290704000	0.847565000	-2.430083000
8	-0.355584000	1.904898000	0.090142000
8	-0.091889000	-0.657886000	-0.602704000
6	5.108557000	2.712255000	-0.450382000
6	5.283455000	2.540898000	1.064284000
6	4.437671000	3.523767000	1.878427000
6	-4.820946000	-1.669623000	0.742877000
6	-6.083656000	-2.527404000	0.848153000
6	1.418823000	-0.733504000	3.661697000
6	2.943054000	-0.849015000	3.805177000
6	3.591922000	-1.866790000	2.861476000
6	-3.384945000	3.227483000	0.987776000
6	-4.424389000	3.460924000	-0.123246000
6	-4.098604000	4.661784000	-1.022105000

6	5.022203000	-1.061631000	-1.047327000
6	6.390930000	-1.721397000	-1.116742000
6	-3.483091000	0.772510000	-3.444606000
6	-3.153408000	-0.629747000	-4.000839000
6	-3.599725000	-1.804143000	-3.118534000
7	2.636318000	-3.662357000	-2.088932000
7	-2.045271000	-4.041826000	1.199974000
6	3.955089000	-3.255287000	-1.975532000
6	1.853145000	-2.676351000	-1.577752000
6	-1.419621000	-2.865007000	0.954208000
6	-3.409749000	-3.809016000	1.165406000
1	5.291395000	3.760566000	-0.752112000
1	5.866871000	2.108008000	-0.985914000
1	5.023318000	1.504851000	1.345655000
1	6.354137000	2.681978000	1.312006000
1	3.364033000	3.383127000	1.658528000
1	-4.790784000	-1.141498000	-0.226873000
1	-4.833087000	-0.872177000	1.508058000
1	-6.977127000	-1.901485000	0.761485000
1	-6.124190000	-3.302123000	0.060285000
1	-6.124830000	-3.028767000	1.822730000
1	0.940239000	-1.717348000	3.836756000
1	1.009979000	-0.063251000	4.440297000
1	3.400186000	0.143990000	3.634464000
1	3.163065000	-1.119644000	4.856411000
1	3.475982000	-1.539327000	1.816065000
1	-2.373831000	3.159394000	0.557377000
1	-3.408622000	4.084404000	1.688222000
1	-5.419117000	3.603411000	0.341825000
1	-4.496632000	2.550503000	-0.745888000
1	-3.149995000	4.512762000	-1.566091000
1	-4.904326000	4.807790000	-1.751719000
1	-4.020185000	5.577067000	-0.421331000
1	4.841396000	-0.646368000	-0.041107000
1	4.980706000	-0.198616000	-1.737952000
1	7.204533000	-1.038752000	-0.851738000
1	6.603577000	-2.092915000	-2.137444000
1	-4.541200000	0.794160000	-3.117214000
1	-3.359940000	1.524702000	-4.241562000
1	-3.643230000	-0.720953000	-4.990464000
1	-2.063891000	-0.695547000	-4.188782000
1	-3.071360000	-1.805592000	-2.153115000
1	-3.416928000	-2.760999000	-3.624583000
1	-4.675890000	-1.740703000	-2.913913000
1	6.448582000	-2.584546000	-0.442567000
1	4.665488000	-2.000382000	3.044320000

1	4.564099000	3.411599000	2.961557000
1	3.126789000	-2.861596000	2.926089000
1	4.690702000	4.559692000	1.617982000
1	-0.693207000	2.222860000	-0.778558000
1	1.969297000	1.546627000	-2.559002000
1	2.306888000	-4.535973000	-2.489950000
1	-1.587204000	-4.932027000	1.373140000
1	4.781109000	-3.874938000	-2.318336000
1	0.764956000	-2.705819000	-1.545957000
1	-0.338933000	-2.752061000	0.903322000
1	-4.134575000	-4.603189000	1.328764000

Model 6

6	3.608812000	2.385456000	-0.962095000
8	3.025881000	1.452730000	-0.292084000
8	3.132146000	2.939203000	-1.981811000
6	0.860581000	-0.415122000	2.341487000
8	1.705694000	-0.137926000	1.434587000
8	-0.397593000	-0.365578000	2.205698000
6	3.884464000	-1.842620000	-1.500714000
7	2.561977000	-1.431464000	-1.376530000
6	-3.583731000	1.952928000	1.751357000
8	-4.566465000	1.949118000	2.518027000
8	-2.792901000	0.933655000	1.614569000
6	-2.388320000	1.078574000	-2.424460000
8	-1.363244000	1.675652000	-2.837545000
8	-2.595597000	0.670501000	-1.224060000
6	-3.552455000	-2.457940000	0.762506000
7	-2.292941000	-1.894490000	0.585126000
26	-1.401892000	0.198829000	0.365692000
25	1.373236000	0.379586000	-0.539555000
8	1.174292000	1.216452000	-2.435766000
8	-0.118977000	1.751310000	0.249361000
8	-0.066106000	-0.625686000	-0.703077000
6	5.007906000	2.778221000	-0.474508000
6	5.271735000	2.567272000	1.024245000
6	4.437690000	3.523786000	1.878433000
6	-4.824162000	-1.662176000	0.721581000
6	-6.083663000	-2.527412000	0.848147000
6	1.402425000	-0.839684000	3.706490000
6	2.931023000	-0.883365000	3.831386000

6	3.591915000	-1.866782000	2.861474000
6	-3.289762000	3.203277000	0.916412000
6	-4.389525000	3.450528000	-0.130494000
6	-4.098586000	4.661784000	-1.022110000
6	5.041341000	-1.007955000	-1.034792000
6	6.390931000	-1.721397000	-1.116754000
6	-3.475213000	0.753570000	-3.445370000
6	-3.226668000	-0.644656000	-4.054462000
6	-3.599741000	-1.804154000	-3.118550000
7	2.593161000	-3.394874000	-2.388407000
7	-2.047142000	-4.068514000	0.881528000
6	3.912972000	-3.072373000	-2.129169000
6	1.819036000	-2.387762000	-1.923213000
6	-1.419327000	-2.892084000	0.660330000
6	-3.406169000	-3.818838000	0.948964000
1	5.181668000	3.829787000	-0.764843000
1	5.713872000	2.170437000	-1.073384000
1	5.049459000	1.519604000	1.291983000
1	6.348679000	2.730708000	1.220241000
1	3.360494000	3.389089000	1.668598000
1	-4.849606000	-1.091472000	-0.224657000
1	-4.799265000	-0.901404000	1.523131000
1	-6.977121000	-1.901485000	0.761489000
1	-6.130343000	-3.300198000	0.059235000
1	-6.124831000	-3.028760000	1.822732000
1	0.965523000	-1.833401000	3.926161000
1	0.966027000	-0.150122000	4.452529000
1	3.341300000	0.130499000	3.665437000
1	3.180209000	-1.158147000	4.874265000
1	3.473467000	-1.526417000	1.823220000
1	-2.309908000	3.106407000	0.421961000
1	-3.246296000	4.067507000	1.606456000
1	-5.356039000	3.590984000	0.389365000
1	-4.493298000	2.547561000	-0.759493000
1	-3.150586000	4.534738000	-1.576969000
1	-4.904333000	4.807793000	-1.751712000
1	-4.020194000	5.577063000	-0.421333000
1	4.848648000	-0.667515000	-0.002891000
1	5.074640000	-0.088505000	-1.647755000
1	7.204529000	-1.038755000	-0.851732000
1	6.593292000	-2.083191000	-2.142052000
1	-4.470742000	0.782701000	-2.968054000
1	-3.436799000	1.516107000	-4.240541000
1	-3.824778000	-0.730880000	-4.981719000
1	-2.165295000	-0.716140000	-4.361395000
1	-3.046093000	-1.780026000	-2.167566000

1	-3.416919000	-2.760995000	-3.624576000
1	-4.675884000	-1.740696000	-2.913907000
1	6.448583000	-2.584543000	-0.442562000
1	4.665489000	-2.000386000	3.044320000
1	4.564090000	3.411591000	2.961557000
1	3.126794000	-2.861598000	2.926092000
1	4.690695000	4.559683000	1.617978000
1	1.765465000	2.024852000	-2.406829000
1	0.210389000	1.488771000	-2.543933000
1	0.095577000	2.179979000	1.095196000
1	2.255626000	-4.235378000	-2.849871000
1	-1.592859000	-4.972275000	0.981337000
1	4.733670000	-3.729003000	-2.408405000
1	0.732611000	-2.365526000	-1.981227000
1	-0.342175000	-2.789326000	0.553387000
1	-4.130907000	-4.611951000	1.116021000

Curriculum Vitae - Jovan Livada

Education

Doctor of Philosophy in Chemistry

December 2019

The Pennsylvania State University, University Park, PA

Master of Science in Chemistry

December 2012

The Pennsylvania State University, University Park, PA

Bachelor of Arts in Chemistry and Theatre

May 2008

Hamilton College, Clinton, NY

Publications

- 1) **Title:** Spectroscopic Investigations of Catalase Compound II: Characterization of an Iron(IV) Hydroxide Intermediate in a Non-thiolate-Ligated Heme Enzyme

Author(s): Yosca, TH (Yosca, Timothy H.); Langston, MC (Langston, Matthew C.); Krest, CM (Krest, Courtney M.); Onderko, EL (Onderko, Elizabeth L.); Grove, TL (Grove, Tyler L.); **Livada, J (Livada, Jovan);** Green, MT (Green, Michel)

Source: JOURNAL OF THE AMERICAN CHEMICAL SOCIETY **Volume:** 138 **Issue:** 49 **Pages:** 16016-16023 **DOI:** 10.1021/jacs.6b09693 **Published:** DEC 14 2016

- 2) **Title:** Direct Measurement of the Radical Translocation Distance in the Class I Ribonucleotide Reductase from Chlamydia trachomatis

Author(s): **Livada, J (Livada, Jovan);** Martinie, RJ (Martinie, Ryan J.); Dassama, LMK (Dassama, Laura M. K.); Krebs, C (Krebs, Carsten); Bollinger, JM (Bollinger, J. Martin, Jr.); Silakov, A (Silakov, Alexey)

Source: JOURNAL OF PHYSICAL CHEMISTRY B **Volume:** 119 **Issue:** 43 **Pages:** 13777-13784 **DOI:** 10.1021/acsjpcb.5b04057 **Published:** OCT 29 2015

- 3) **Title:** Experimental Correlation of Substrate Position with Reaction Outcome in the Aliphatic Halogenase, SyrB2

Author(s): Martinie, RJ (Martinie, Ryan J.); **Livada, J (Livada, Jovan);** Chang, WC (Chang, Wei-chen); Green, MT (Green, Michael T.); Krebs, C (Krebs, Carsten); Bollinger, JM (Bollinger, J. Martin, Jr.); Silakov, A (Silakov, Alexey)

Source: JOURNAL OF THE AMERICAN CHEMICAL SOCIETY **Volume:** 137 **Issue:** 21 **Pages:** 6912-6919 **DOI:** 10.1021/jacs.5b03370 **Published:** JUN 3 2015

- 4) **Title:** A substrate radical intermediate in catalysis by the antibiotic resistance protein Cfr

Author(s): Grove, TL (Grove, Tyler L.); **Livada, J (Livada, Jovan);** Schwalm, EL (Schwalm, Erica L.); Green, MT (Green, Michael T.); Booker, SJ (Booker, Squire J.); Silakov, A (Silakov, Alexey)

Source: NATURE CHEMICAL BIOLOGY **Volume:** 9 **Issue:** 7 **Pages:** 422-+ **DOI:** 10.1038/NCHEMBIO.1251 **Published:** JUL 2013

- 5) **Title:** Reactive Intermediates in Cytochrome P450 Catalysis

Author(s): Krest, CM (Krest, Courtney M.); Onderko, EL (Onderko, Elizabeth L.); Yosca, TH (Yosca, Timothy H.); Calixto, JC (Calixto, Julio C.); Karp, RF (Karp, Richard F.); **Livada, J (Livada, Jovan);** Rittle, J (Rittle, Jonathan); Green, MT (Green, Michael T.)

Source: JOURNAL OF BIOLOGICAL CHEMISTRY **Volume:** 288 **Issue:** 24 **Pages:** 17074-17081 **DOI:** 10.1074/jbc.R113.473108 **Published:** JUN 14 2013

- 6) **Title:** Function of the Diiron Cluster of Escherichia coli Class Ia Ribonucleotide Reductase in Proton-Coupled Electron Transfer

Author(s): Worsdorfer, B (Woersdoerfer, Bigna); Conner, DA (Conner, Denise A.); Yokoyama, K (Yokoyama, Kenichi); **Livada, J (Livada, Jovan);** Seyedsayamdost, M (Seyedsayamdost, Mohammad); Jiang, W (Jiang, Wei); Silakov, A (Silakov, Alexey); Stubbe, J (Stubbe, JoAnne); Bollinger, JM (Bollinger, J. Martin, Jr.); Krebs, C (Krebs, Carsten)

Source: JOURNAL OF THE AMERICAN CHEMICAL SOCIETY **Volume:** 135 **Issue:** 23 **Pages:** 8585-8593 **DOI:** 10.1021/ja401342s **Published:** JUN 12 2013

- 7) **Title:** Do hydroxyl radical-water clusters, OH(H₂O)(n), n=1-5, exist in the atmosphere?

Author(s): Allodi, MA (Allodi, Marco A.); Dunn, ME (Dunn, Meghan E.); **Livada, J (Livada, Jovan);** Kirschner, KN (Kirschner, Karl N.); Shields, GC (Shields, George C.)

Source: JOURNAL OF PHYSICAL CHEMISTRY A **Volume:** 110 **Issue:** 49 **Pages:** 13283-13289 **DOI:** 10.1021/jp0644681 **Published:** DEC 14 2006

Awards and Honors

GOLD Scholar Award recipient, Clinton, NY

2008

Superior Poster Award recipient, Sanibel, GA

2007

McKinney prize in public speaking, Clinton, NY

2005